

EUR 15.154

Institute
FOR
Transuranium
Elements



JOINT
RESEARCH
CENTRE

COMMISSION OF THE EUROPEAN COMMUNITIES

COMMISSION OF THE EUROPEAN COMMUNITIES

Joint Research Centre

INSTITUTE
FOR TRANSURANIUM ELEMENTS
KARLSRUHE

Annual Report 1992

TUAR-92

1993

12 9376

EUR 15154 EN

Published by the
COMMISSION OF THE EUROPEAN COMMUNITIES
Directorate-General XIII
Telecommunications, information market and exploitation of research
Bâtiment Jean Monnet
LUXEMBOURG

LEGAL NOTICE

Neither the Commission of the European Communities nor any person acting on behalf of the Commission is responsible for the use which might be made of the following information

Reproduction is authorized, except for commercial purposes,
provided the source is acknowledged

Luxembourg: Office for Official Publications of the European Communities, 1993

Catalogue number: CD-NA-15154-EN-C
© ECSC-EEC-EAEC, Brussels Luxembourg, 1993
Printed in the Federal Republic of Germany

Abstract

In 1992, an electron-microscopic investigation of structural features occurring at the surface of LWR fuel after extended burn-up, the so-called rim-effect, was launched. Radiation damage in the oxygen sublattice of uranium dioxide and its recovery during annealing was studied, and new aspects of fission gas behaviour in UO_2 were discovered. A phase transition occurring in UO_2 near 2650K was studied in detail by sub-second pulse heating of small urania spheres in a high-pressure autoclave and the different mechanisms contributing to the heat capacity of solid and liquid urania were analysed.

Irradiations of mixed nitrides and of technetium metal (in view of its transmutation to a stable ruthenium isotope by neutron capture) to be carried out in the Petten high-flux reactor were prepared.

Studies of the mechanisms governing the transport of big aerosol particles in ventilation exhaust systems with high turbulent flow were continued.

The present situation and the technical possibilities of partitioning and transmutation were reviewed. New PIE results for uranium-neptunium oxide fuel irradiated in a fast flux (in the frame of the Superfact programme) became available.

"Hot" testing with real HAW demonstrated that the TRPO process is a prospective and competitive tool for actinide recovery and partitioning from high-active waste.

In an effort to characterise and test nuclear waste forms, a series of long-term oxidation tests with high burn-up nuclear fuels in air at 180 - 200°C was started. Electrochemical measurements were carried with non-irradiated fuel samples in order to identify key reaction steps in various aqueous solutions of technical relevance. Tests with UO_2 powder aiming at the identification of different leaching mechanisms in an autoclave were started. And a new non-destructive assay technique was employed to characterise individual fuel rods in terms of burn-up and radiotoxicity potential. The presence of granite has been seen to reduce the leach rate of certain waste glass constituents (actinides and fission products) except molybdenum.

Modelling activities of underground water contamination in a spent fuel repository were extended to the calculations of release probabilities of various fission products from different zones of the fuel rod which was assumed to be in contact with steam or water.

Basic investigations on actinides concerned the magnetic properties of certain actinide compounds. The Néel temperature of UO_2 was calculated. The effect of pressure on the optical response of Th_3P_4 and U_3P_4 and on the electrical resistance of USe was measured.

Under "Exploratory Research" an attempt was made to optimize acoustic cavities for aerosol scavenging, and the optimum conditions for acoustic aerosol scavenging at low frequencies were determined.

Major efforts in support of Commission Services concerned the preparations for the installation and the operation of on-site laboratories for safeguards analyses at La Hague and Sellafield.

Contract work in 1992 dealt principally with the conditioning, conversion, post-irradiation analysis and certain aspects of the reprocessing of nuclear fuels, as well as with studies for the transmutation of long-lived radioactive nuclides and the preparation of alpha-emitters for radiotherapeutical applications.

PARL. EUROP. di li.
N.C. EUR 15154
C1.

Commission of the European Communities
Joint Research Centre

TUAR 92

European Institute
for Transuranium Elements
Annual Report

January - December 1992

Table of Contents

Foreword	9
Executive Summary	11
MAIN ACHIEVEMENTS AND MILESTONES	
1. Specific Programmes	17
1.1 Basic Safety Research on Nuclear Fuels	17
Introduction	17
Structural investigations and basic studies on fuels	17
An electron microscope analysis of the microstructural "Rim effect" occurring in UO_2 fuel pellets following irradiation to high burn-up	17
Thermal conductivity of simulated high burn-up UO_2 fuel (SIMFUEL)	24
Radiation damage in the oxygen sublattice of UO_2 and its recovery during annealing	25
Fission gas bubble behaviour in uranium dioxide	27
Studies of problems related to reactor safety	29
Ultrasonic thermometers for the PHEBUS project	29
Differential pyrometry in the infrared	29
Modelling of whole-core LMFBR accidents using the TRANSURANUS code	30
Study of high-temperature properties	33
Introduction	33
Lambda transition in uranium dioxide	33
A model for order-disorder transitions in the UO_2 anion sublattice	37
Elementary contributions to the heat capacity of solid and liquid UO_2	41
Shielded Knudsen cell for fission product source-term analysis	44
Emissivity and melting point of thoria	47

Modelling work	50
Fuel performance code development (TRANSURANUS)	50
Atomistic simulation of Mo and Pd in UO ₂	51
1.2 Safety Aspects of Fuel Operation and Handling	55
Introduction	55
Optimisation of dense fuels	55
Duct transport of big particles (TRABI)	58
1.3 Actinide Determination and Recycling	61
Working group meeting on MA-containing targets and fuels (23 and 24 June 1992)	61
Present status of partitioning and transmutation	61
Irradiation in KNK II - MTE1 (Experiment KNK IIa)	68
Status of the Superfact experiment	68
EPMA results for americium in the Superfact fuel SF 16	73
EPMA investigation of an uranium-neptunium oxide fuel irradiated in the Superfact experiment (SF 15)	74
EPMA investigation of the products of cladding corrosion in the gaps of two Superfact fuel pins (SF 13 and SF 16)	77
Actinide partitioning by means of the TRPO process	80
1.4 Characterisation of Waste Forms and High Burn-up Fuel	87
Introduction	87
Basic studies on waste glasses	88
Leaching of UO ₂ and of SIMFUEL	89
Electrochemical techniques applied to natural UO ₂ corrosion in aqueous solutions	93
Influence of granite on the leaching behaviour of waste glass under dynamic conditions	99
Leaching behaviour of irradiated UO ₂ under highly oxidising conditions	101
Non-destructive characterisation of spent fuel	103
Oxidation of unirradiated UO ₂ pellets below 500°C	106

Low-temperature oxidation of high burn-up spent fuel	108
Origin of shaded zones in irradiated UO ₂ fuel cross sections after chemical etching	109
Hot cell annealing tests for fission gas release studies	115
Chemistry of the UO ₂ fuel periphery - Properties of Cs-U-O compounds	124
Modelling of the underground water contamination in a spent fuel repository	125
Non-destructive assay for spent fuel characterisation	128
1.5 Actinide Research	131
Introduction	131
Preparation and characterization of actinide metals and compounds	131
Magnetic compounds of the ThMn ₁₂ structure type	131
Study of a new family of actinide ternary intermetallic compounds	132
Compounds with the 1:1:1 composition	136
Characterisation of NpBe ₁₃ compounds	138
Synthesis and characterization of quasicrystalline materials	139
Structure of (L*Tc(CO) ₂) ₂ (-N ₂), with L* = HB(3,5-Me ₂ C ₃ N ₂) ₃	139
Solid state physics studies on actinide systems	140
Estimated magnetic ordering temperature of uranium dioxide	140
Neutron and synchrotron X-ray scattering	142
Photoelectron studies (UPS and XPS) of O ₂ , CO ₂ , CO, and C ₂ H ₄ adsorption on Pu metal	148
Mössbauer spectroscopy	150
High pressure studies on actinide systems	153
Effect of pressure on the optical response of Th ₃ P ₄ and U ₃ P ₄	153
The electrical resistance of USe under high pressure	154
Pressure induced phase transition in alpha-plutonium	156
Updated diagrams for pressure induced phase transitions in 5f and 4f metals	158
HPXRD study of AnCl ₄ (An = Th, U) single crystals	160

2. Exploratory Research	163
Acoustic aerosol scavenging	163
Attenuation of sound in fog and soot aerosols	163
Optimisation of acoustic cavities for aerosol conditioning	166
Infrasound scavenging of aerosol	171
3. Scientific-Technical Support to Community Policies	177
Introduction	177
3.1 Support to DG XIII	177
Acoustic aerosol scavenging	177
Introduction	177
Installation for agglomeration tests under dynamic conditions	177
Aerosol generation and measurement	177
Improvement of the separation efficiency of an ESP by means of acoustic pre-conditioning at a flow rate of 560 m ³ /hr	178
Acoustic agglomeration efficiency as a function of particle concentration and flow rate	179
Efficiency of the ESP and EAP as a function of flow rate	180
Conclusions	182
3.2 Support to DG XVII	182
On-site laboratories	182
Progress of the Sellafield on-site laboratory	182
Progress of the La Hague (LSS) on-site laboratory	186
Data transfer between mass spectrometers and PDP 11/73	187
Testing of components for the on-site laboratory	187
Maintenance of the hybrid K-edge apparatus at La Hague	188
International experiment to test the application of a neutron coincidence counter - gamma-detector for the measurement of PuO ₂ samples	188
Installation and applications of an ICP mass spectrometer coupled on-line to an ion chromatograph	191

Glow discharge mass spectrometer (GDMS): Installation	195
Verification of tank volume measurements by neodymium tracing and IDMS	196
4. Work for Third Parties	199
Introduction	199
Conditioning of C-containing MOX and carbide pellets	199
Conversion of uranyl and Pu nitrates in solution to oxides	199
Post-irradiation examination of LWR fuel rods	199
Post-irradiation examination of PHEBUS PF project fuel rods	199
Production of ^{225}Ac and ^{213}Bi for labelled monoclonal antibodies	200
Irradiation of minor-actinide containing alloys (CRIEPI)	202
Study of reprecipitation phenomena from dissolver solutions of highly burnt nuclear fuels	202
Development of a passive neutron detector for nuclear material measurements in the pilot conditioning plant Gorleben	204
Annexes	207
I. List of Publications	207
1. Conferences	207
2. Books and Periodicals	213
3. Reports	221
4. Patents	223
II. Collaboration with External Organisations	225
III. Human Resources	231
IV. Organisational Chart	233
V. Glossary	235
VI. List of Contributors	239
VII. List of Previous Reports	241

Foreword

to the Annual Progress Report 1992
of the European Institute for Transuranium Elements
by J. van Geel, Director

The role of one of the transuranium elements of great technological importance, plutonium, has changed dramatically during the past few years: From a fissile material of high esteem foreseen to gradually replace the limited natural resources in ^{235}U it has turned into an element of major public concern of which hundreds of tons have become available from reprocessing spent fuel and from the dismantling of nuclear warheads. The low market price of uranium and the delay in the introduction of fast reactors caused the value of plutonium to decrease drastically.

Today we are faced with the necessity

- to find means and ways for the safe and economic use of plutonium, either as MOX fuel in light water reactors or in dedicated plutonium burners
- and
- to reduce, if ever possible, the rate of production of plutonium and other actinides in power reactors.

Present and future work at the Institute for Transuranium Elements aims at contributing to an analysis and, if possible, to a solution of the above items.

Partitioning and transmutation of long-lived nuclides is a possible way of coping with the problem of long-term safety of nuclear waste. Here, again, the Institute has been involved in pioneering work and performed scoping experiments for a number of years. The present report contains an in-depth analysis of the present status and the perspectives of research in this field.

The results of basic actinide research, moreover, dealing with "unusual" elements, may help to better understand behaviour and properties of "usual" materials. We have learned, for example, that some actinide compounds exhibit unusual magnetic properties with extremely high coercive forces. Nobody would think of using permanent magnets containing highly radioactive transuranium elements in everyday life, but a better knowledge of how magnetism works in actinides might help to improve conventional magnet technology. Analogously, if we study the particular kind of superconductivity which some actinide compounds exhibit, we might come closer to a better understanding of the facets of this technologically highly interesting phenomenon.

Research on transuranium elements is thus highly relevant, and it will remain so, independent of the outcome of the ongoing nuclear debate.

Karlsruhe, May 1993

Executive Summary

In **Basic Safety Research on Nuclear Fuels**, studies of the fracture and evaporation behaviour of UO_2 , simulating different degrees of burn-up, were continued. A non-destructive technique to selectively detect defects in the oxygen sublattice made it possible to study damage ingrowth, damage recovery upon thermal annealing, and oxygen uptake during leaching of SIMfuel.

The lambda-transition, a phase change occurring in UO_2 at about 2650K, was experimentally investigated with laser heated specimens and employing a fast six-colour pyrometer developed at the Institute.

The phenomena leading to structural changes at the surface of UO_2 fuel pins at high burn-up were studied by high resolution transmission electron microscopy.

The Institute participated in a modelling benchmark exercise to predict the source terms for the first two PHEBUS PF experiments, using the code package FUTURE-MITRA and CHEMIF.

Continued international interest in the fuel performance code TRANSURANUS lead to cooperations with an increasing number of organisations and licensing authorities.

The **Study of Safety Aspects of Fuel Operation and Handling** dealt a) with a continued investigation of the operational limits of advanced fuels and b) with the transport and dispersion of radioactive aerosol particles in nuclear facilities.

a) The irradiations NILOC 3 and NILOC 4, carried out in the Petten High Flux Reactor, were completed. They had been designed to study possible contact phenomena between $(\text{U,Pu})\text{O}_2$ and UN pellets under irradiation and to investigate the behaviour of mixed nitride fuel at standard temperatures and at elevated off-normal temperatures. The fuel rods will be shipped back to Karlsruhe and undergo a thorough post-irradiation examination.

In the POMPEI experiment, mixed nitride and technetium pellets will be irradiated in HFR to high burn-up in a relative short time. The irradiation device was loaded and transported to Petten. For the fast flux experiment NIMPHE, a new capsule with fresh fuel pins (NIMPHE 1 bis) was prepared for irradiation in the PHENIX reactor.

b) An investigation of mechanisms governing the transport of large aerosol particles in ducts and chimneys (Project TRABI) was extended to highly turbulent flow conditions. The work is in progress.

Actinide Determination and Recycling activities were mainly concerned with an evaluation of the technical possibilities to transmute long-lived nuclear waste constituents (minor actinides) into shorter-lived fission products. The results of an earlier irradiation test (KNK IIa) were evaluated, and minor-actinide containing oxide fuel pins which had been irradiated in the PHENIX reactor were analysed.

A batch experiment with real HAW and a "cold" test with novel centrifugal extractors have demonstrated that TRPO (trialkyl phosphine oxide) is a promising and competitive extractant for the recovery and partitioning of

actinides from highly active waste. A test applying centrifugal extractors to real HAW is under preparation.

Progress was made in the **Characterisation of Waste Forms and of High Burn-Up Fuel**. In the context of efforts to model the consequences of water intrusion into an underground fuel deposit (Project COCAIN), existing ITU models (FUTURE, MITRA, CHEMIF) were adapted and used to characterise the initial state of an LWR fuel which had been subject to several irradiation cycles up to a burn-up of 50 GWd/t. In order to obtain further input data for COCAIN, the oxidation of UO_2 in air and under moist nitrogen was observed by gravimetry, and the reaction products were characterised ceramographically and via X-ray diffraction. From oxidation tests with high burn-up LWR fuel at elevated temperatures it was concluded that U_4O_9 formed at grain boundaries, preferentially in regions with large intergranular porosity, in contrast to unirradiated fuel where U_3O_7 or U_3O_8 may be formed upon oxidation, the limiting oxidation phase in irradiated urania seems to be U_4O_{9+x} with $x \leq 0.6$.

The uptake of oxygen dissolved in aqueous solutions by - unirradiated - UO_2 has been studied with an electrochemical technique which allows key reaction steps to be identified. The application of this technique to irradiated specimens is under preparation.

New autoclave leach tests on UO_2 powders - immersed in water or under vapour - were performed at temperatures up to 200° in order to identify mechanisms responsible for leaching. The work is in progress. Comparative measurements revealed that MOX leaches out slightly faster than pure UO_2 under otherwise identical conditions, and that the presence of granite reduces the leach rate (less for fission products, somewhat more for ^{99}Tc and actinides).

A method was developed to determine non-destructively the oxygen gradient at the surface of UO_2 and its variation during leaching.

In hot cell annealing tests for fission gas release studies, the effects of atmosphere, temperature history, and of the grain size were investigated in detail.

Equipment developed for the non-destructive assay of individual spent fuel pins was applied to pins with different initial enrichment and different final burn-up in order to determine, in association with the KORIGEN code, the build-up of higher nuclides in LWR fuel during irradiation - The neutron collar of the system has been equipped with an additional miniature semiconductor detector for simultaneous gamma spectrometry. - The possibility of performing gamma emission tomography on spent fuel in our hot cells is being examined. Tomography would yield information on the distribution of fission product activity across the fuel pin radius.

In **Actinide Research** the accent was on the preparation and on structural and physical studies of actinide compounds with heavy fermion properties and with a particular magnetic behaviour. ThMn_{12} -type compounds were studied as potential permanent magnets. A previously unknown group of compounds, $\text{An}_2\text{M}_2\text{X}$ ($\text{X} = \text{In}, \text{Sn}$), was synthesized and studied by magnetic methods and by Mössbauer spectroscopy. The study of AnMX ($\text{X} = \text{Al}, \text{Ga}$) compounds, of NpBe_{13} , and of quasicrystalline materials was continued.

The Néel temperature of UO_2 was calculated. Neutron and X-ray scattering methods were used to study hybridisation in URuAl and phase transitions in B1-

type compounds. The adsorption of gases on plutonium was investigated by photoelectron spectroscopy. Mössbauer spectroscopy was applied to study the electronic behaviour in NpPd_2Al_3 and, at ambient and elevated pressures, in NpIn_3 .

The optical response of Th_3P_4 and U_3P_4 to an applied pressure was measured, as well as the change in electrical resistance of USe with pressure. A novel pressure-induced phase transition in plutonium was found. General diagrams of the phase relations of f metals under pressure have been updated. For the first time, the effect of pressure on the structure of single crystalline actinide compounds was measured.

Experimental investigations on the attenuation of sound waves by aerosols and theoretical studies concerning the optimisation of acoustic cavities for aerosol conditioning were carried out during the reporting period under the heading **Exploratory Research**. In addition, the effect of low frequency sound on aerosol particles interaction was further investigated.

Possibilities of industrial applications of acoustic aerosol scavenging by sound waves were further explored in support of efforts of the **Directorate General XIII** (Telecommunication, Information Industry and Innovation) to transfer JRC research results to industry. Studies to increase the efficiency of industrial electrostatic filters by an acoustic pre-treatment were extended to flow velocities up to 1.7 m/sec in the acoustic module, corresponding to overall flow rates in our test rig of up to 1500 m³/sec, thus bringing the experimental scenario closer to technological requirements for an industrial environment. A formal application for support of this work by the "Forschungsstiftung der Vereinigung der Großkraftwerksbetreiber" has been filed. A decision is expected in 1993.

Support to the **Directorate General XVII** (Energy) on safeguarding fissile materials concentrated on the preparation of work in on-site analytical laboratories in Sellafield and La Hague. In this context, a portable compact K-edge absorption spectrometer was constructed and an expert system for the evaluation of safeguards measurement results was developed.

With the cooperation of workers from LANL, DCS Luxembourg, IRMM Geel and with the participation of observers from Canberra Electronics and from JRC Ispra, an apparatus was installed and tested to measure the total Pu content of a sample by a combination of neutron coincidence and gamma spectrometry, whereby the neutron coincidence counters would measure the ²⁴⁰Pu equivalent and the gamma spectrum would give information on the Pu isotopic vector. The system is to be used for on-site safeguards analysis.

Inductively-coupled mass spectrometry (ICP-MS) was applied to fission product analysis and a technique for the direct determination of fuel burn-up, based on ¹⁴⁸Nd determination without interference from ¹⁴⁸Sm, was proposed.

In the last quarter of 1992, an experiment was carried out at the La Hague UP2 plant in order to measure a reprocessing tank volume with a tracer technique: Natural neodymium was used as a tracer, with spikes of ¹⁵⁰Nd for isotope dilution mass spectrometry to be performed at the Institute. The results are presently being analysed.

In 1992, new contracts with **Third Parties** worth 441.6 kECU have been concluded. This brought the total volume of contract work under execution at the

Institute for Transuranium Elements on December 31, 1992 up to 17.107 MECU. Additional contracts totalling 662.9 kECU were under negotiation by the end of 1992.

The main subjects of ongoing contract research are the conditioning, conversion, post-irradiation analysis and reprocessing of nuclear fuels, the nuclear transmutation of long-lived nuclides, and the preparation of alpha emitters for radio-therapeutical applications.

As in the past, contract work was pursued with highest priority, and all deadlines were kept.

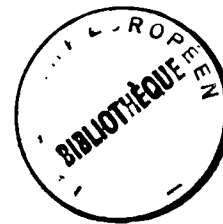
Work performed at the Institute for Transuranium Elements resulted in 114 publications in books and journals or in the form of reports (published or submitted in 1992) and 83 contributions of Institute staff to conferences and seminars held in the reporting period. Five patents were applied for or granted.

Close collaborative contacts were maintained in 1992 with 80 scientific and industrial institutions in 20 countries in Europe and abroad.

MAIN ACHIEVEMENTS AND MILESTONES

1 Specific Programmes

1.1 Basic Safety Research on Nuclear Fuels



Introduction

The aim of improving the safety of nuclear fuels was pursued by providing high precision basic experimental data supported by a broad modelling activity using different computer codes. Emphasis was placed on modelling and understanding the physical and chemical processes and mechanisms important for the behavior of LWR oxide fuels up to very long operation periods, i.e. up to high burnups reaching ~ 60 000 MWd/t. As previously, the successful working philosophy consisted in performing well-planned laboratory experiments to measure basic data in parallel with detailed post-irradiation analyses on LWR fuel irradiated under steady state, transient or accident conditions up to the above high burnup level. The different computer codes developed previously at ITU were further improved and the new basic data are constantly being added to their data banks to enable improved predictions of fuel behaviour over a wide range of conditions up to the case of accidents. As in previous years, important results were obtained, evaluated and published within the reporting period:

- The laboratory work of the previous reporting period, largely performed as so-called "single effect studies" and using UO_2 with different simulated burnups (so-called SIMFUEL) was continued. The thermal conductivity of UO_2 was shown to decrease already at a low simulated burnup of 1.5 at%. Further work was done on the fracture and evaporation behaviour of SIMFUEL. The radiation damage studies were continued employing the new non-destructive method to selectively detect defects in the oxygen sublattice developed last year. Both damage ingrowth, damage recovery upon thermal anneals and oxygen uptake during leaching of both UO_2 and SIMFUEL were successfully measured.
- The first experimental data on a phase transition (so-called λ -transition) in UO_2 at ~ 2650 K were obtained with laser-heated specimens and employing the fast six-colour pyrometer developed at the Institute.

- Basic experimental studies using accelerators and an extensive high resolution transmission electron microscope investigation on high burnup UO_2 fuel were performed to better understand the phenomena leading to the RIM-effect in UO_2 fuel at high burnup.
- Cooperation with the international reactor safety project PHEBUS PF was continued. Beyond else, the institute participates in a modelling benchmark exercise to predict the source terms for the first two tests FPT-O and FPT-1. To this end, the code package FUTURE-MITRA and CHEMIF was used.
- There was continued international interest in the fuel performance code TRANS-URANUS with cooperation with an increasing number of organisations and licensing bodies.

Structural Investigations and Basic Studies on Fuels

An electron microscope analysis of the microstructural "RIM effect" occurring in UO_2 fuel pellets following irradiation to high burnup

Introduction

It has been known for some time that significant micro-structural changes occur at the periphery of UO_2 fuel pellets which have been irradiated to high burn up [1,2]. There is a marked decrease in the apparent grain size, accompanied by an increase in porosity and fission gas depletion in the fuel matrix. These microstructural changes first occur when the average burn up exceeds about 40 GWd/tU and are usually confined to the outer regions of the

fuel to a depth of about 200 μm . The mechanism leading to the formation of this rim microstructure is not satisfactorily understood at the present time.

Transmission Electron Microscopy (TEM) and high resolution Scanning Electron Microscopy (SEM) have been used to make a detailed analysis of the microstructure of samples taken from the periphery of a UO_2 pellet irradiated to an average burn up of 7.6% FIMA, but with a local burn up at the rim of nearly 20% FIMA. This pellet was taken from the fuel rod AF21-2 irradiated in the Danish heavy water reactor at Risø.

Specimen preparation

The major difficulty in making an electron microscopy analysis of the rim region is to ensure that the material examined comes exclusively from the first 200 μm depth of the pellet. This effectively precludes specimen preparation by electropolishing, since it is not possible to control precisely the position of perforation, and consequently the area available for examination by TEM.

This problem was solved by taking very small pieces of fuel immediately adjacent to the cladding, extracted from a thin slice of the fuel cross section. An example of such a fragment of fuel still attached to the cladding is shown in Fig. 1.1. These pieces were then crushed under methanol, and drops of the resulting suspension were allowed to dry on thin carbon films supported on copper grids. The small pieces of fuel left on the films were often thin enough for transmission electron microscopy. The samples were examined in a Hitachi H700 200kV TEM which has been specially adapted for the analysis of radioactive samples, and is directly connected to a glovebox system [3,4]. This microscope is equipped with a secondary electron detector enabling very high resolution SEM images to be obtained, and with a Tracor Northern TN5500 energy dispersive X-ray analysis system. One advantage of this powder method of sample preparation is that the bulk of the specimen is small, thus minimising the background radiation level and permitting energy dispersive X-ray analysis to be performed. In addition the sample is not chemically affected by an electrolyte which might tend to dissolve out metallic fission product precipitates. The disadvantage of this method is that precise radial-positional

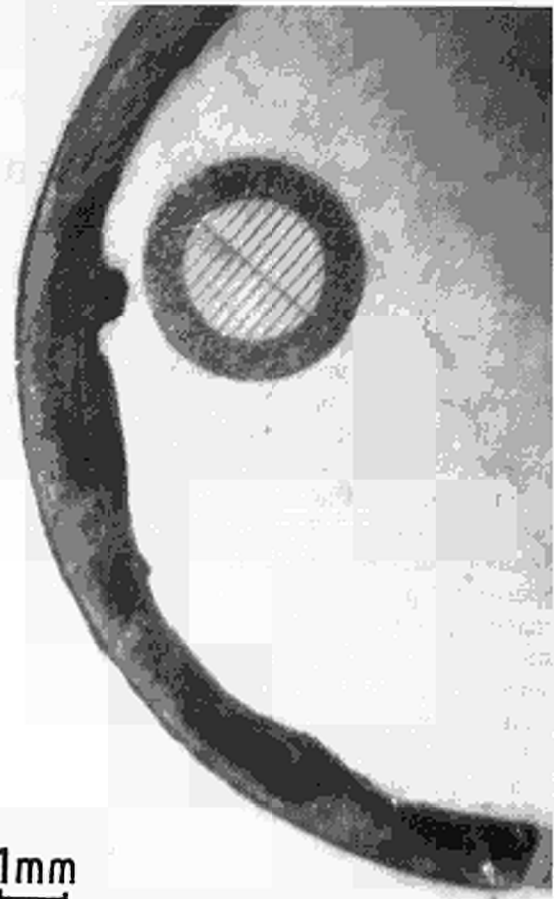


Fig.1.1 Optical micrograph showing a typical piece of fuel used as a specimen adhering to the inner surface of the fuel cladding.

information is not available for the fragments of fuel examined.

A further test was performed in which a fuel fragment from the rim which had been examined dry was immersed in distilled water, first for fifteen minutes, then for a total of 120 minutes, to check for possible effects on the microstructure.

In addition a sample from near to the fuel centre was examined for comparison purposes.

Experimental results

Both by TEM and SEM significant microstructural differences were found between the rim of the fuel and the inner regions. The rim sample showed the development of a subgrain microstructure with a typical grain size of 0.15 μm within the original coarse grain structure, a lower overall dislocation density

within the grains and a much lower density of intragranular fission gas bubbles and precipitates.

The electron diffraction patterns were those of UO_2 . In addition, semi-quantitative analysis using energy dispersive X-ray analysis showed no detectable change in the chemical composition of the fuel at the rim, neither within the grains nor on the grain boundaries. A quantitative determination of fission products contained in the rim structure with the EDX technique is difficult since the sensitivity is considerably reduced by the high background activity of the samples.

Immersion of the samples in water for up to 120 minutes resulted in no observable microstructural changes.

Unfortunately no sample of unirradiated as-fabricated fuel was provided for examination, which would have enabled a comparison to be made with the original fuel microstructure.

The subgrain structure

This was the principal microstructural modification, and could be observed directly by TEM, or by SEM on the fractured fuel surfaces and, particularly clearly, on the surfaces of exposed pores. Figs. 1.2 and 1.3 show examples of the typical rim microstructure as observed by transmission, with a diffraction pattern shown inset. The average subgrain size was measured by TEM as $0.16 \mu\text{m}$, and the misorientations between pairs of sub-grains to be typically 2 to 7 degrees. A histogram of the measured subgrain sizes as revealed by TEM is shown in Fig. 1.4a.

Figs. 1.5 and 1.6 are corresponding SEM images of the fracture surface of a fuel fragment, where the subgrain boundaries are visible. The structure is particularly clearly seen on the inner surfaces of large pores, and this is shown in Fig.1.7. Fig.1.4b presents the histogram of subgrain sizes determined from the SEM micrographs, which is comparable with Fig.

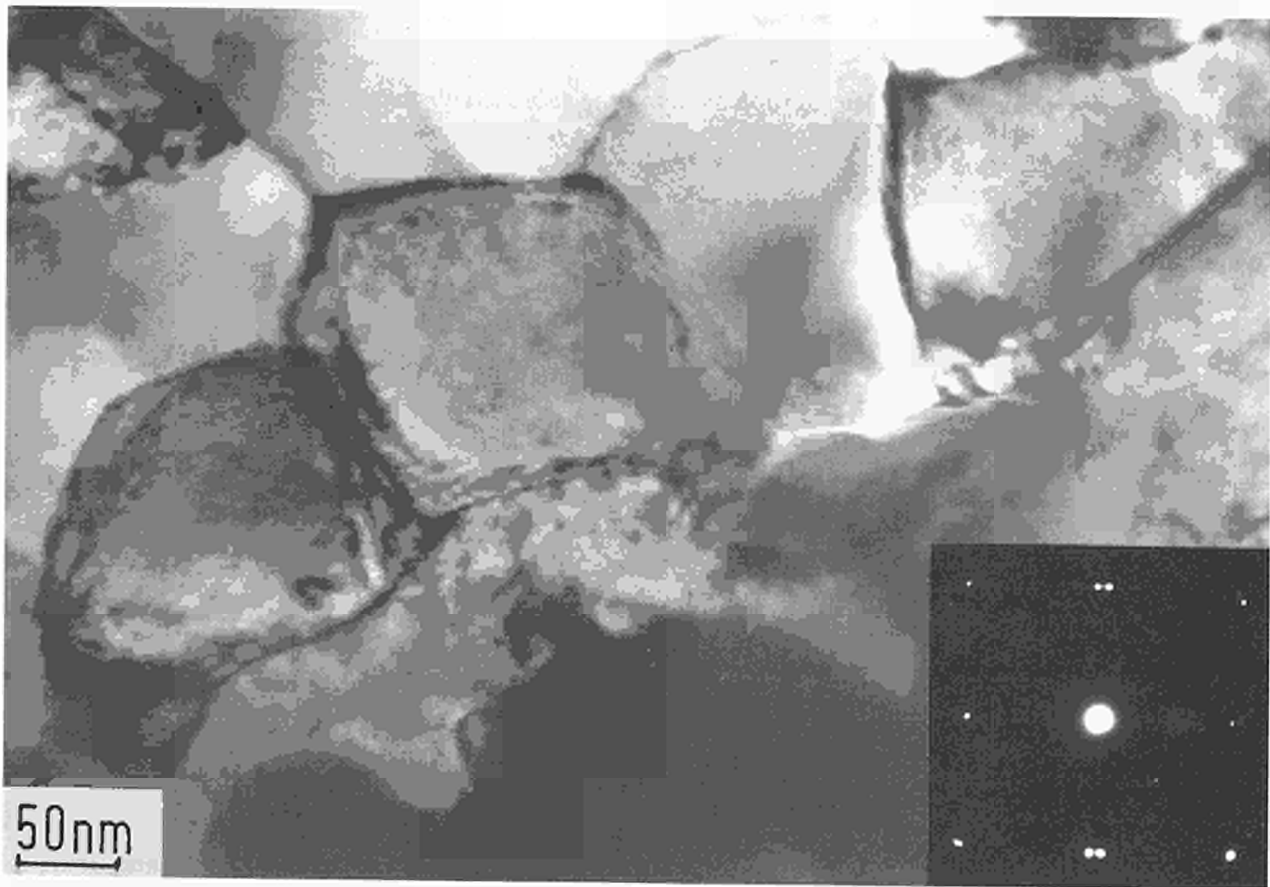


Fig.1.2 Transmission Electron Micrograph showing the fine scale subgrain structure at the fuel rim. The inset diffraction pattern shows the spread in subgrain orientations to be very small (< 5 deg).

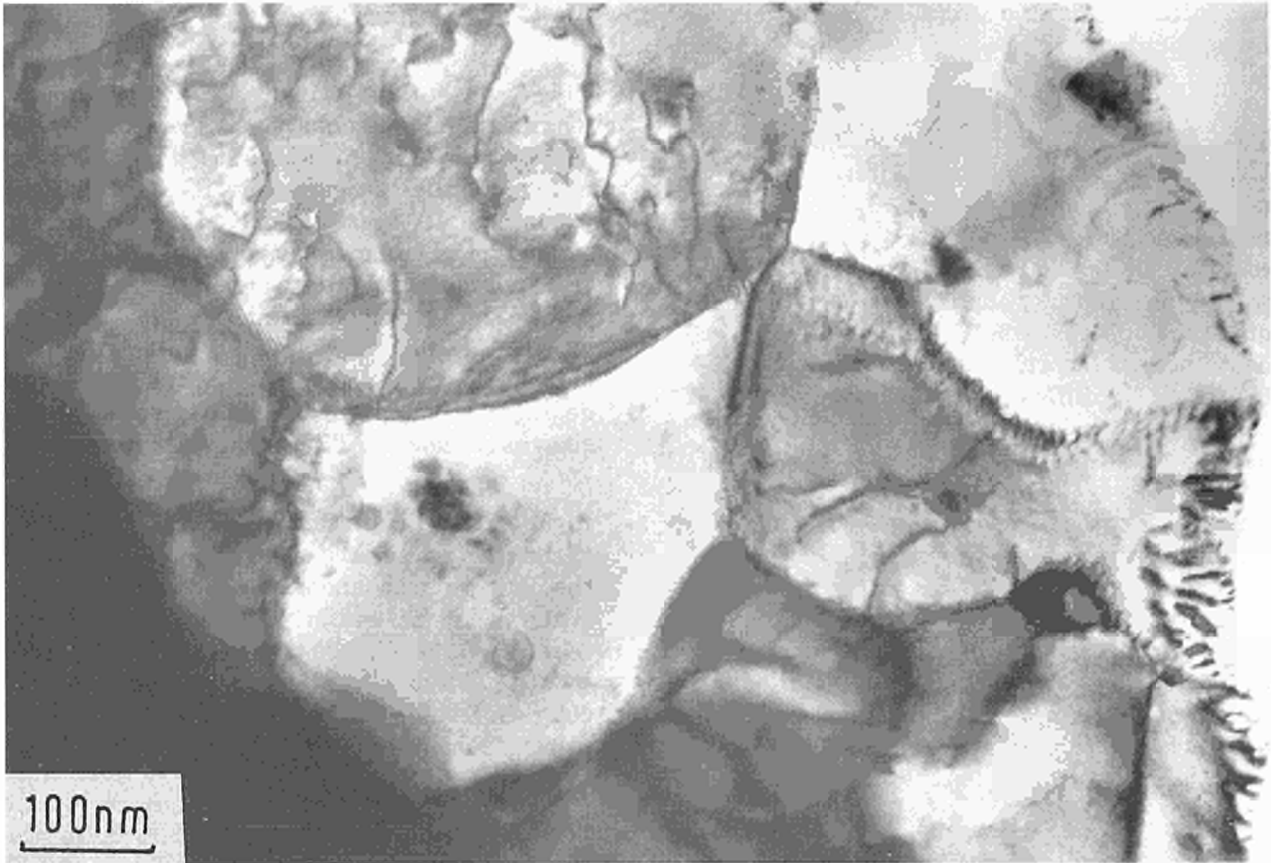


Fig.1.3 Transmission Electron Micrograph showing the subgrain structure at the rim of the fuel, demonstrating the low density of dislocations found within the structure. A low density of precipitates is found, but fission gas bubbles are absent.

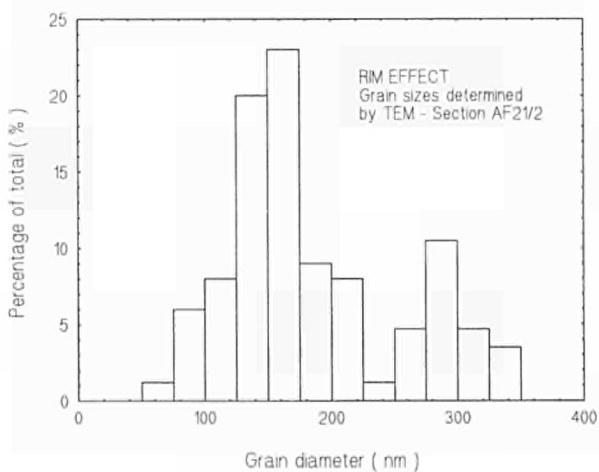


Fig.1.4a Histogram of the measured subgrain sizes as revealed by TEM.

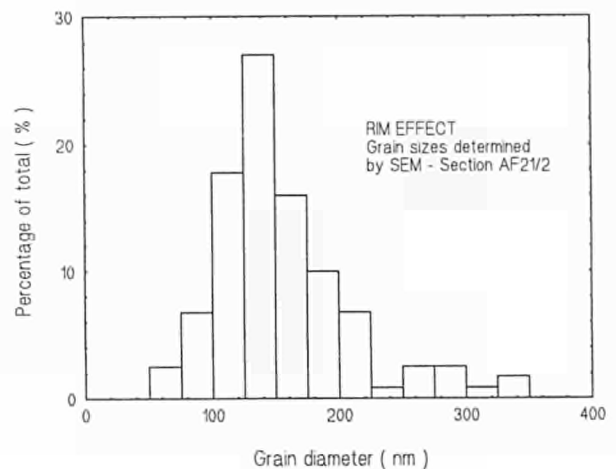


Fig.1.4b Histogram of the measured subgrain sizes as revealed by SEM.

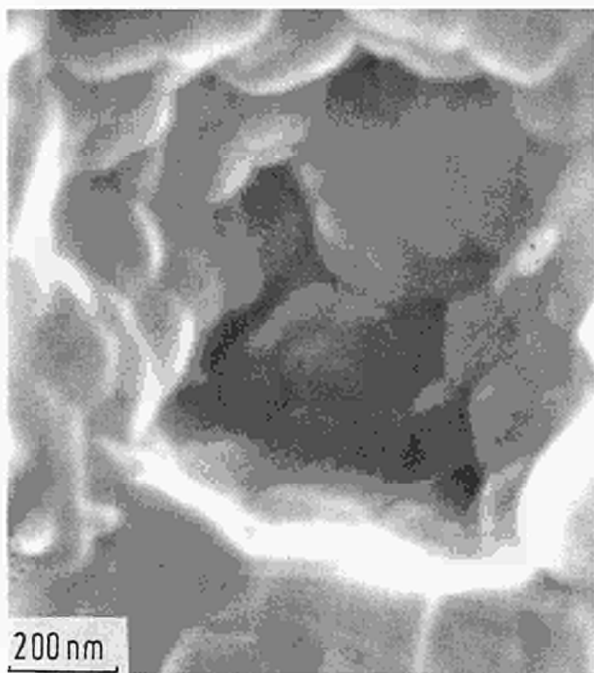


Fig.1.5 Scanning Electron Micrograph of a fractured fuel surface at the rim, showing the subgrain structure corresponding to the TEM micrographs.

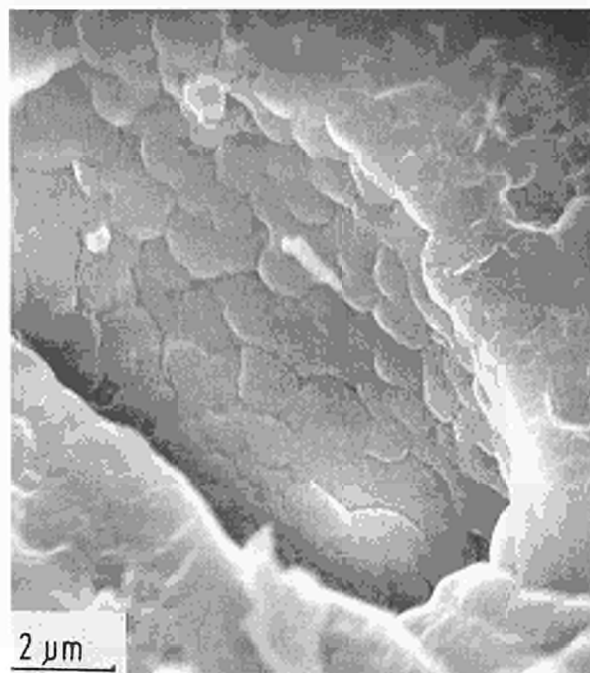


Fig.1.7 Scanning Electron Micrograph of a fractured fuel surface showing how the subgrain structure is particularly clearly visible on the inner surfaces of large pores.

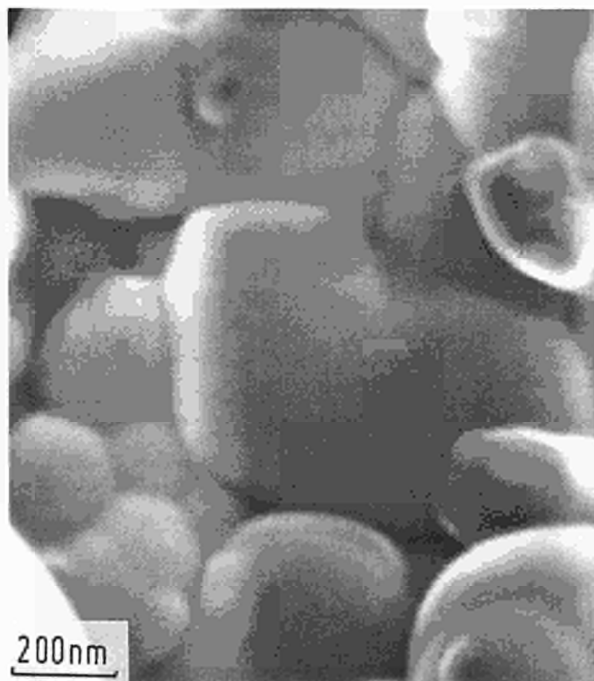


Fig.1.6 Scanning Electron Micrograph showing the subgrain structure at the rim of the fuel

1.4a, but with a slight displacement towards smaller values. This could result from the measuring technique because in the TEM case the grains are cut randomly, whilst in the SEM the exposed subgrain faces are directly imaged. Fig. 1.4 is based on measurements made on some four hundred grains. The measurements present the raw data without correction for the statistical effect of randomness, as is generally done in conventional ceramography.

The subgrain size histograms were approximately constant from one fuel fragment to another. However, in some areas a "two-tier" sub-grain system could be identified, in which the subgrains were clustered into units with an average size of $0.8 \mu\text{m}$, which is probably about one tenth of the average size of the original grains of the as-fabricated fuel. These units were separated by a high degree of porosity. Examples of this type of structure are shown in Fig. 1.8 and, at higher magnification, in Fig. 1.9.

The dislocation microstructures

Dislocation densities were measured in the TEM using the line intercept method [5,6], with care

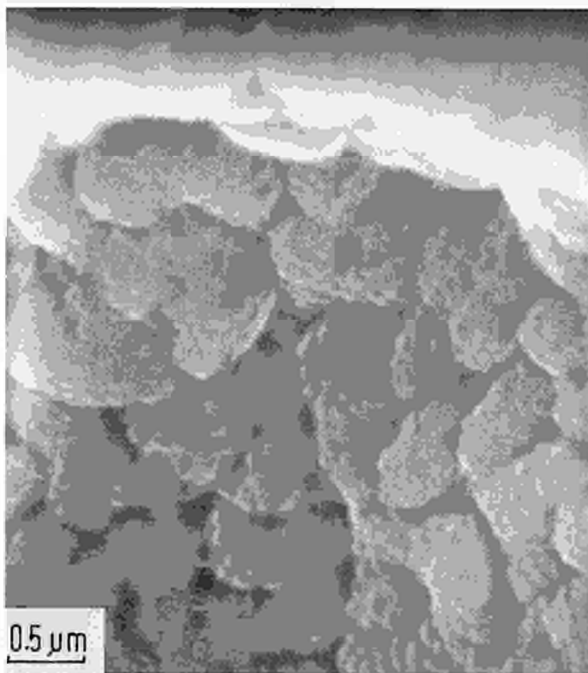


Fig.1.8 Scanning Electron Micrograph showing the "two-tier"-type structure of the subgrains clustered into units about one tenth the size of the original grains of the as-fabricated fuel.

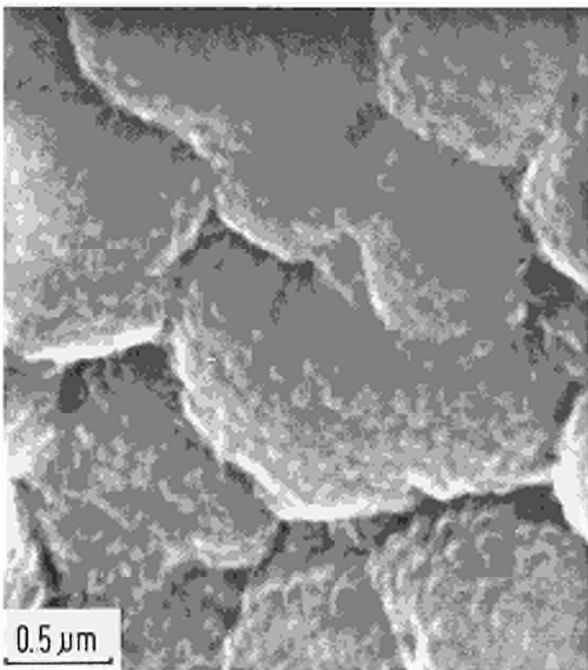


Fig.1.9 Part of Fig. 1.8 at a higher magnification.

taken to allow for diffraction contrast effects which can lead to dislocation invisibility under certain combinations of dislocation Burgers vector and diffraction conditions.

The subgrains show a much lower dislocation and defect density than the central regions of the fuel. Some of the smaller subgrains appear to be almost defect free, checked under a wide range of diffracting conditions in the TEM. The average matrix dislocation density in the rim material was measured to be $0.9 \times 10^{10} \text{ cm.cm}^{-3}$, inhomogeneously distributed, compared with a homogeneous value of $2.5 \times 10^{10} \text{ cm.cm}^{-3}$ in the central zones of the fuel.

The microstructure at the centre also contained a high density, measured to be $5.5 \times 10^{14} \text{ cm}^{-3}$, of large dislocation loops in the size range 12.5 to 50 nm. These loops were absent in the rim material. An example of the microstructure at the centre is shown in Fig. 1.10.

Fission gas bubbles and precipitates

The rim samples had no small intragranular fission gas bubbles in the size range $< 10 \text{ nm}$ in the subgrain structure, similarly no precipitates of the same size range were found. Under steady-state irradiation conditions up to a burn up of around 4% FIMA a high density of small fission gas bubble/precipitate pairs would be expected within the grains at the periphery of the fuel [7].

There was a low density of spherical metal precipitates with an average diameter of 35 nm on the grain boundaries. Occasionally much larger precipitates up to about 2 μm diameter were observed, but it is possible because of the crushing method used to produce the samples that these did not originate from the rim region.

At the fuel centre large five-metal particles up to 5 μm in diameter were found. In addition, a population of small fission gas bubbles linked to precipitates was present.

Conclusions

The examination of material taken from the rim region of this sample of high burn up fuel showed the microstructure to consist of low angle subgrains on a very fine scale. The development of this structure appears to involve

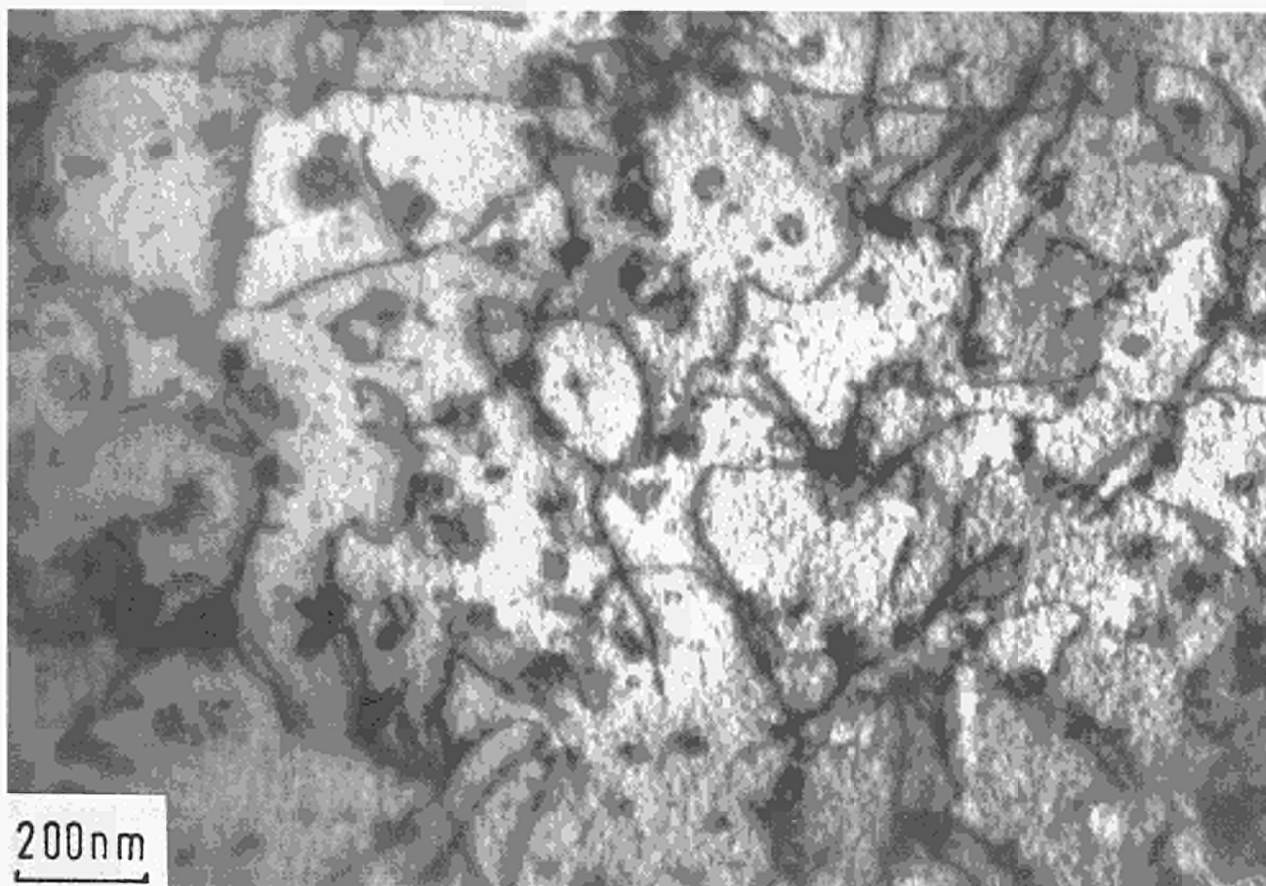


Fig.1.10 Transmission Electron Micrograph showing the typical microstructure of dislocations and dislocation loops at the fuel centre.

no change in the chemical composition of the fuel, and thus results from physical processes alone. The mechanism responsible for the appearance of this rim structure is still not clear following this investigation by electron microscopy. However, it is proposed to continue this TEM/SEM investigation on high burnup fuel. Also, a separate effect study using ion implantation to introduce high concentrations of fission products and radiation damage under well controlled conditions is pursued (see other contributions to this report) in order to elucidate the basic mechanisms contributing to the formation of the rim structure.

References

- [1] H. Stehle, "Performance of Oxide Fuel in Water-Cooled Power Reactors", *J. Nucl. Mater.* **153** (1988) 3
- [2] Hj. Matzke, H. Blank, M. Coquerelle, K. Lassmann, I.L.F. Ray, C. Ronchi and C.T. Walker, "Oxide Fuel Transients", *J. Nucl. Mater.* **166** (1989) 165
- [3] I.L.F. Ray, H. Thiele and H. Blank, "The Examination of Nuclear Fuel Samples by Scanning Transmission Electron Microscopy", *J. Physique*, **45** C2-849 (1984) 1
- [4] I.L.F. Ray and H. Thiele, "The Examination of Nuclear Fuel Samples by Electron Microscopy", Proc. Hot Cell Workshop, Karlsruhe (1981)
- [5] R.K. Ham, *Phil. Mag.* **6** (1961) 1183
- [6] P.B. Hirsch and J.W. Steeds, "Relation between the Structure and Mechanical Properties of Metals", N.P.L. Symposium No. 15. H.M.S.O. (1964)
- [7] I.L.F. Ray, H. Thiele and Hj. Matzke, "Fission Gas Behaviour During Power Transients in High Burn-up Nuclear Fuels Studied by Electron Microscopy", *Fundamental Aspects of Inert Gases in Solids*, Plenum Press, N.Y. Eds. S.E. Donnelly and J.H. Evans (1991) 457

Thermal conductivity of simulated high burnup UO_2 fuel (SIMFUEL)

The measurements of the thermal conductivity λ on UO_2 and 3 and 8 at% simulated burnup UO_2 reported in last report TUAR 91, p. 26 were extended to a further composition, i.e. to a 1.5 % burnup SIMFUEL, in order to cover the total range of interest in present LWR UO_2 fuels. The thermal properties of UO_2 at high temperature are among the most important parameters in assessing fuel behaviour at high burnup. Reduction in thermal conductivity occurs in the fuel during irradiation because of fission-gas bubbles, fission products (dissolved and precipitated) and (possible) oxygen to uranium ratio (O/U) increase.

SIMFUEL - **SIM**ulated high-burnup UO_2 , **FUEL** - provides a non-radioactive analogue to irradiated fuel. Extensive characterization [1] demonstrated the equivalence of the micro-structure and phase structure of SIMFUEL to irradiated high-burnup fuel (not including bubbles). All classes of fission products (except the fission gases and volatiles) are represented in SIMFUEL. The UO_2 matrix contained fully or partially dissolved oxides (e.g. Nd, La, Ce, Y, Sr, Zr). Spherical metallic Mo-Ru-Pd-Rh precipitates were uniformly dispersed throughout the matrix and a fine perovskite phase of the $(\text{Ba,Sr})_2\text{ZrO}_3$ -type precipitated at the matrix grain boundaries.

Previous measurements of λ have shown that the thermal conductivity of stoichiometric SIMFUEL at 3 and 8 % burnup is lower than that of the "pure" UO_2 [2]. In the reporting period, the thermal diffusivity α and specific heat C_p of 1.5 % burnup SIMFUEL was measured between room temperature and 1500 °C, and the data were combined to obtain the thermal conductivity by using the equation

$$\lambda = \alpha \cdot C_p \cdot \rho$$

where ρ is the density. The thermal diffusivity was measured by a laser-flash technique, and the specific heat was measured between 25 and 600 °C using Differential Scanning Calorimetry (DSC) and was calculated from enthalpy data for higher temperatures [3]. These new data, normalized to 95 % of the theoretical density match well the previously reported data for higher burnup. Thermal conductivities of UO_2 and 1.5, 3 and 8 at% equivalent burnup

stoichiometric SIMFUEL are plotted in Fig. 1.11 for various temperatures between 25 and 1500 °C. The effect of burnup is a significant

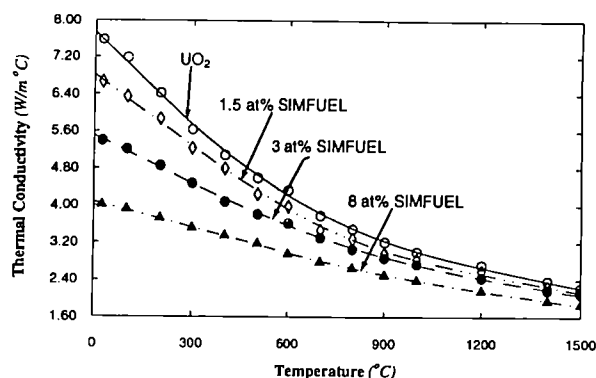


Fig.1.11 Thermal conductivity of UO_2 and SIMFUEL (1.5, 3 and 8 at% burnup), normalized to 95 % of theoretical density (TD), as a function of the temperature

degradation of the thermal conductivity of SIMFUEL compared to that of "pure" UO_2 . At room temperature, the thermal conductivities of 1.5, 3 and 8 at% burnup SIMFUEL are 89, 71 and 53 % that of pure UO_2 . At 1500 °C, the differences are smaller: 98, 94 and 85 % for 1.5, 3 and 8 at% SIMFUEL, compared to UO_2 . Most of the difference in thermal conductivity of SIMFUEL compared to fresh UO_2 is due to the decrease in thermal diffusivity: specific heat has only a small effect and it is in the opposite direction (see TUAR 91).

The thermal resistivities ($R = 1/\lambda$) of UO_2 and SIMFUEL are shown in Fig. 1.12. R varies

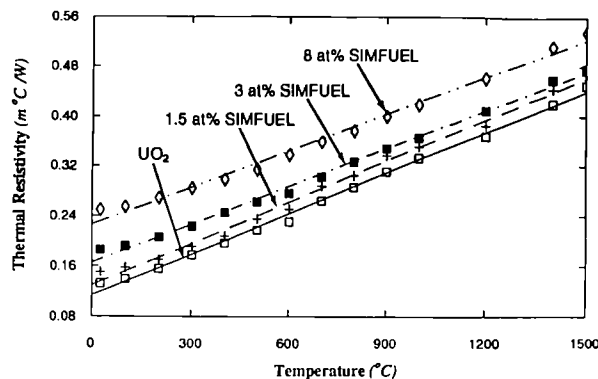


Fig.1.12 Thermal resistivity of UO_2 and SIMFUEL showing a linear dependence with the temperature

linearly with temperature for each SIMFUEL burnup:

$$R = A + BT$$

The new data confirm the linear dependence of the parameters with the burnup reported in TUAR 91:

$$R = [0.053 + (0.016 \pm 0.0015) b] + [- (0.005 \pm 0.002) b] \cdot 10^{-4} T$$

where R is expressed in $m \cdot K/W$ and b is the burnup in at%. Fig. 1.13 is a plot of the thermal resistivity versus burnup for three selected temperatures, showing linear variation.

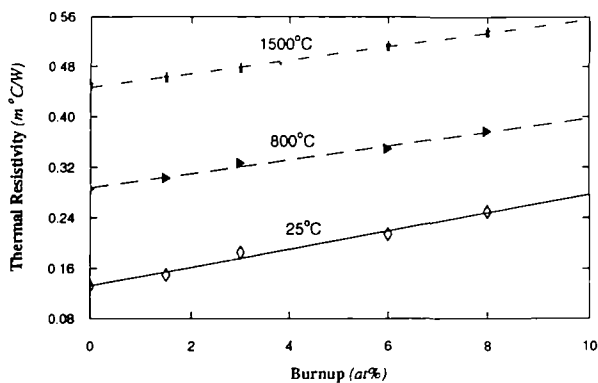


Fig.1.13 Thermal resistivity as a function of the burnup

From the thermal conductivity, the central temperature T_c of the fuel can be calculated for a given linear rating χ and a given surface temperature T_s from the conductivity integral:

$$X = 4 \pi \int_{T_s}^{T_c} \lambda dT$$

As an example, for a linear power of 45 kW/m and the 3 at % burnup SIMFUEL, the central temperature is about 200 °C higher than for the "pure" UO_2 . This increase in fuel operating temperatures due to the changes in the intrinsic thermal conductivity partially explains the enhanced gas-release observed at high burnup.

References

- [1] P.G. Lucuta, R.A. Verrall, Hj. Matzke and B. Palmer, "Microstructural Features of SIMFUEL - Simulated High-Burnup UO_2 -Based Nuclear Fuel", *J. Nucl. Mater.* 178 (1991) 48
- [2] P.G. Lucuta, Hj. Matzke, R.A. Verrall and H.A. Tasman, "Thermal Conductivity of SIMFUEL", in "Nuclear Materials for Fission Reactors", Eds. Hj. Matzke and G. Schumacher, *J. Nucl. Mater.* 188 (1992) 198
- [3] P.G. Lucuta, R.A. Verrall, Hj. Matzke and I.J. Hastings, "Characterization and Thermal Properties of Hyperstoichiometric SIMFUEL", presented at the Third Int. Conf. on CANDU Fuel, October 4-8, 1992, Pembroke, Canada

Radiation damage in the oxygen sublattice of UO_2 and its recovery during annealing

The application of ion scattering techniques to determine the lattice location of oxygen in UO_2 and of defects in the oxygen sublattice of UO_2 has been described in the last report TUAR 91, p. 31. Resonance scattering of high energy He ions on ^{16}O was developed to an extent that the signal due to oxygen was at least as large as that due to the much heavier uranium ions. In particular, the broad resonance between 7.3 and 7.7 MeV was shown to be very useful.

In the reporting period, this new non-destructive method was applied to determine gradients in oxygen content near the surface of leached UO_2 (see chapter 1.4) and to study build up of radiation damage and its recovery upon thermal annealing. To this end, UO_2 single crystals of good quality were selected, polished with diamond paste down to 0.25 μm and subsequently annealed at 1500 °C in Ar/8%H for 30 min, to recover the polishing damage. The samples were mounted on a 2-axis goniometer and analyzed using a 4He -ion beam at an incident energy of 7.57 MeV. The scattered 4He ions were detected by using a conventional silicon surface barrier detector located at 160°. The energy resolution of the experimental system was about 20 keV. The beam current varied between 10 and 30 nA. Two kinds of ions were implanted at 293 K: Xe ($M = 132$) and Kr ($M = 84$) representing typical elements of the two groups of heavy and light fission products. The implantation energies of Kr and Xe ions were chosen in such a way that their ranges

were approximately equal. These amounted to $R_p = 54$ nm for 200 keV Kr and to $R_p = 50$ nm for 300 keV Xe. The implanted samples were isochronally annealed in Ar/8%H at different temperatures for 15 min.

Random and aligned spectra for a $\langle 100 \rangle$ UO_2 single crystal are shown in Fig. 1.14. In order to analyze the oxygen sublattice, the O-portion of the spectra has to be separated from the measured spectrum. This was done by subtracting the U-background under the O-spectrum along the dotted line as shown in Fig. 1.14. The minimum yields just behind the surface peaks are $\chi_m^U = 0.02$ and $\chi_m^O = 0.12$.

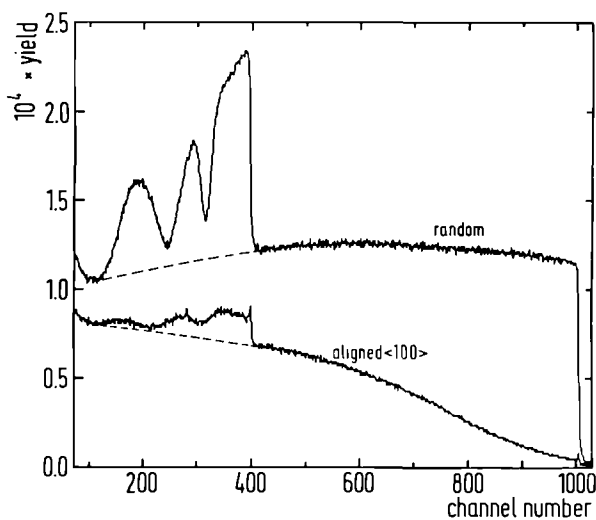


Fig.1.14 Random and aligned backscattering spectra for a virgin $\langle 100 \rangle$ UO_2 single crystal

Fig. 1.15 shows angular scans across the $\langle 100 \rangle$ axis in the tilt plane located 15° from the (100) plane. As expected the O dip is much narrower than the U dip. However, at large angles it follows the U dip until the random level for the U-sublattice is reached. This is apparently due to the much higher steering force of U rows as compared to O rows. He-ions which are dechanneled with respect to the weaker O rows still cannot break through the U rows. In such a case the O atoms can be regarded as "impurity" atoms located in the U channel. The critical angles, if converted using the $(1/E)^{1/2}$ Lindhard scaling, agree with previous data for UO_2 and U_4O_9 [1] measured for 1 and 2 MeV He-backscattering or the $^{16}\text{O}(d,p)^{17}\text{O}$ reaction.

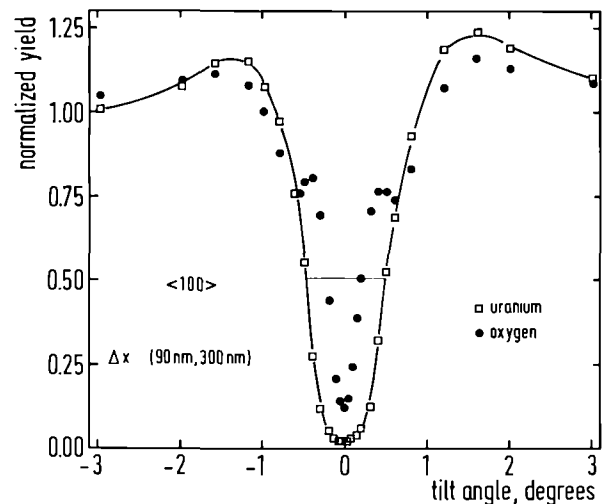


Fig.1.15 Angular scans across the $\langle 100 \rangle$ axis for U- and O-sublattice. The depth interval used is given as Δx in the figure

As a first step in studying damage ingrowth, the dose dependence of damage formation was measured. Fig. 1.16a shows the uranium portions of channeling spectra obtained for $\langle 110 \rangle$ UO_2 single crystals implanted with different doses of 200 keV Kr-ions. All these spectra were normalized to the random spectrum. One notes the increase of both damage peak (DP) and dechanneling yield with increasing dose. Similar results were obtained for the oxygen portions of the spectra. Fig. 1.16b shows the corresponding oxygen spectra obtained after subtraction of the uranium background followed by subtraction of an aligned spectrum of a virgin crystal and normalization to the random spectrum of such a crystal. Because of important defect clustering in ionic crystals leading to the formation of complicated defect structures, the area of the damage peak is not always a good measure of the amount of defects. The channeling minimum yield χ_m behind the damage peak is a more suitable parameter for this purpose. The variation of χ_m with increasing implantation dose for the U- and O-sublattices is shown in Fig. 1.17.

The common feature of both curves is the step increase of χ_m at low doses. For doses exceeding $2 \cdot 10^{15}$ at/cm^2 the slope rapidly levels off. The damage saturation below the random level confirms the fact that UO_2 cannot be amorphized by ion bombardment [2, 3].

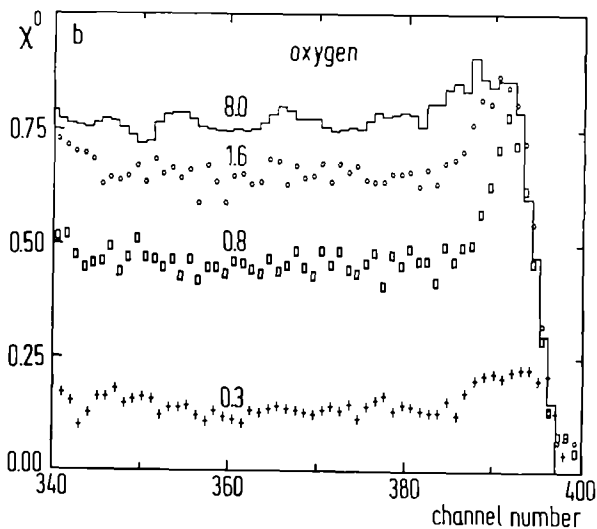
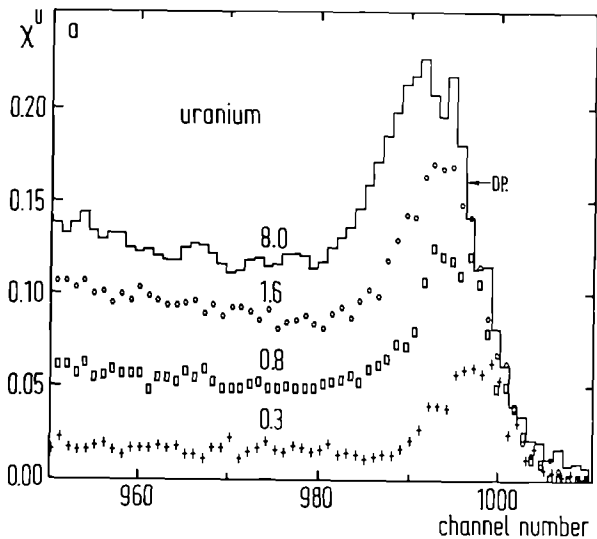


Fig.1.16 Aligned spectra for $\langle 100 \rangle$ UO_2 single crystals implanted with different doses of 200 keV Kr ions: a) U portion b) O portion after subtraction of U background

However, because of the great difference in the steering force of U- and O-rows (cf. Fig. 1.15), the O-channel can be much more easily obstructed than the U one. Thus, a much higher saturation value $X_m^O \approx 0.80$ was observed as compared to $X_m^U \approx 0.12$. Note also, that excess oxygen in uranium oxide is incorporated in such a way that the excess oxygen atoms largely block the $\langle 100 \rangle$ channel (see the extensive description of this fact in the channeling study of U_4O_9 in ref. [1]).

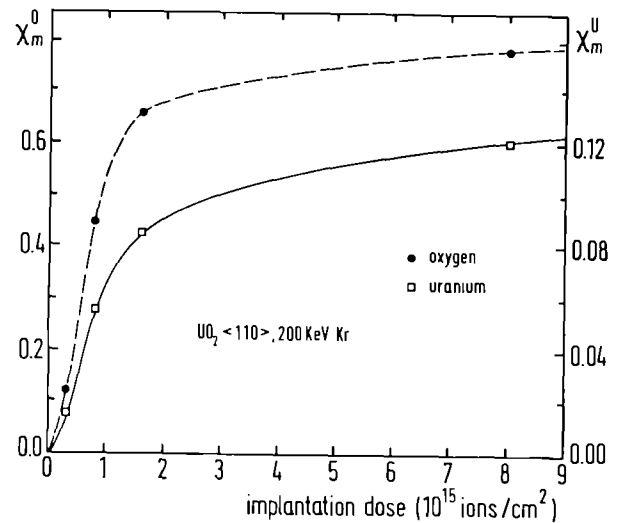


Fig.1.17 Minimum dechanneling yield for U- and O-sublattice as a function of the implanted dose

First results were also obtained on the annealing behavior of the defects in the oxygen sublattice. These will be summarized in the next report.

References

- [1] Hj. Matzke, J.A. Davies and N.G.E. Johansson, Can. J. Phys. **49** (1971) 2215
- [2] Hj. Matzke and A. Turos, J. Nucl. Mater. **188** (1992) 285
- [3] Hj. Matzke, Rad. Eff. **64** (1982) 3

Fission gas bubble behaviour in uranium dioxide

A theoretical model developed to study the gas bubble evolution in nuclear materials [1,2] has been used to analyze experiments on uranium dioxide irradiated to low burn-ups (0.1 and 0.4 at.%), in which fission gas bubble size distributions were measured following out-of-pile isothermal anneals [3,4]. Following irradiation, the UO_2 was annealed for 1 or 6 h each at temperatures between 1303 and 1973 K and then thinned for transmission electron microscopy observation of the bubble size distributions. The model is based on the assumption, that the co-

alescence of the moving bubbles is the main mechanism defining gas porosity development under these conditions. It is assumed that the gas bubbles are in equilibrium and their motion is caused by random migration.

The calculations show that the observed bubble size distributions may be reproduced on the basis of the bubble growth mechanisms considered. The joint action of bubble surface and volume diffusion mechanisms can explain both the general nature of the experimental distributions and their peculiarities, in particular the bimodal bubble size distribution observed after annealing at 1673 K.

In the calculations, the following material properties were used:

atomic volume $\Omega = 41 \times 10^{-30} \text{ m}^3$; diffusion coefficients for gas, g , for uranium volume diffusion, v , or surface diffusion, so :

$$D_g(\text{Xe}) = 5 \cdot 10^{-5} \exp(-3.9 \text{ eV}/kT) \text{ m}^2/\text{s} [5];$$

$$D_v = 1.09 \cdot 10^{-4} \exp(-4.56 \text{ eV}/kT) \text{ m}^2/\text{s} [6];$$

$$D_{so} = 5.64 \cdot 10^3 \exp(-5.24 \text{ eV}/kT) \text{ m}^2/\text{s} [7];$$

and surface energy $\gamma = 0.9 \text{ J}/\text{m}^2$ [8].

Here T is the temperature and k has its usual meaning. The D_v -values used have been shown before [9] to be not representative for bulk uranium diffusion in stoichiometric UO_2 , but rather to represent values describing U-atom rearrangement in layers near surfaces of UO_2 . They were chosen since such a process is possibly describing the conditions of volume diffusion around bubbles. In fact, to obtain a good fit of the experimental data, a D_v -value higher by a factor of 3 than the one given above was used. This is still within the range of reported values [9] for the uncertainties in literature results).

Figs. 1.18 and 1.19 show predicted bubble size distributions as a function of annealing time. For the calculations for both experiments, the same basic physical parameters were used, as given above. The agreement between calculations and experiments is seen to be good. The simultaneous action of volume and surface diffusion was assumed for the data of Fig. 1.18. In contrast, the data of Gulden [4] can be fitted without involving a contribution by surface diffusion (Fig. 1.19). A volume diffusion coefficient alone (with the above input parameters) can explain both the shape and the location of the observed bubble size distribution. The suppression of surface diffusion in these experiments may be due to the inclusions and impurities on the bubble surface, as suggested previously. One should note that the burn-up of

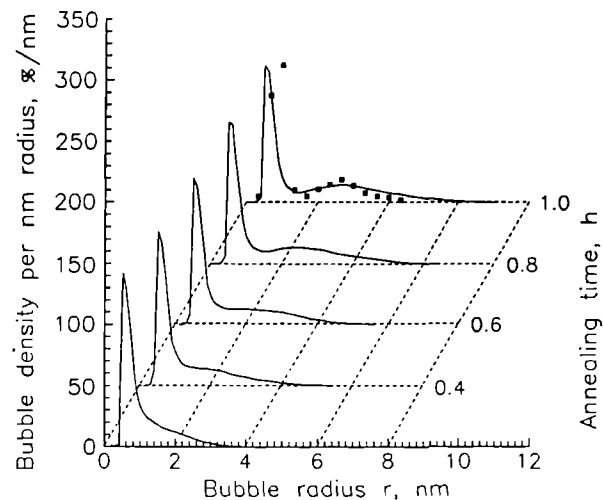


Fig.1.18 Calculated bubble size distribution in UO_2 at 1673 K as a function of annealing time. The black squares for $t = 1 \text{ h}$ show the experimental bubble size distribution [3]. Each bubble size distribution is normalized to the total number of bubbles.

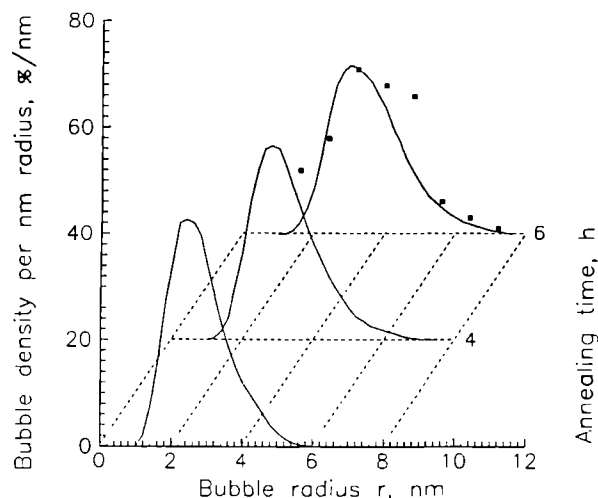


Fig.1.19 As Fig. 1.18, calculated for 1773 K. The black squares represent the bubble size distribution reported by Gulden [4].

these specimens was 4 times as high as that of the study of ref. [3].

Based on the comparison between model predictions and experimental data on bubble size distributions in lightly irradiated UO_2 annealed following irradiation, the following

conclusions can be drawn on fission gas bubble development in UO_2 :

- The evolution of bubble size distributions during post-irradiation annealing can be described by bubble migration and coalescence.
- The bimodal bubble size distribution observed by Matzke et al. [3] for low burn-up UO_2 is the result of operation of both the surface and the volume diffusion mechanisms.
- For higher burn-up, but very similar annealing conditions as in the experiments of Gulden [4], the dominant mass transfer mechanism changes to volume diffusion alone.

References

- V.F. Chkvaseli and E.Ya.Mikhlin, "Theoretical model of gas porosity development in nuclear reactor materials", Report FEI-1249 (Institute of Physics and Power Engineering, Obninsk, 1982) (in Russian)
- V.F. Chkvaseli, in "Nuclear Materials for Fission Reactors", Eds. HJ. Matzke and G. Schumacher, *J. Nucl. Mater.* **188** (1992) 258
- HJ. Matzke, C. Ronchi and C. Baker, *Eur. Appl. Res. Rept.- Nucl. Sci. Technol.* **5**, No. 6 (1984) 1105
- M.E. Gulden, *J. Nucl. Mater.* **23** (1967) 30
- HJ. Matzke, "Gas Release Mechanisms in UO_2 - A Critical Review", *Radiat. Eff.* **53** (1980) 219
- R.J. Hawkins, *J. Nucl. Mater.* **26** (1968) 112
- M.O. Marlowe and A.I. Kaznoff, *J. Nucl. Mater.* **25** (1968) 328
- HJ. Matzke, R. Warren and T. Inoue, *J. Nucl. Mater.* **91** (1980) 205
- HJ. Matzke, *J. Chem. Soc., Faraday Trans.* **86** (1990) 1243

Studies of Problems Related to Reactor Safety

Ultrasonic thermometers for the PHEBUS project

Ultrasonic thermometers were fabricated and delivered for the first irradiation test FPT-O. A detailed fabrication report [1] has been prepared, that includes validation tests of the

(difficult) brazed junction between AISI-347 and Zircalloy 4, as well as the calibration data.

A newly developed version of the control electronics, Black Box Mark III, is presently under construction [2, 3]. The previous concepts Mark I and Mark II perform the data reduction to echo time intervals immediately on the echo signal. This requires a substantial amount of dedicated electronics, which must be operated by highly trained personnel. The new concept uses a commercial 100 MHz 8-bit analog-to-digital converter, a standard personal computer (486/33 MHz), and a dedicated external pulse generator and amplifier (Fig.1.20). The echo signal is transferred to the computer memory as amplitude vs. time. The signal-to-noise ratio of the time resolution is improved by averaging data from 32 shots, and through cross correlation with the echo response from a single discontinuity. The echo positions are localised through parabolic fits around the extremes.

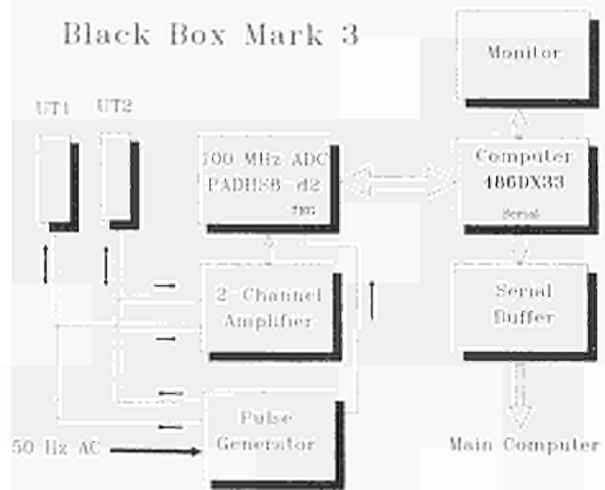


Fig.1.20 Block diagram of Black Box Mark III, for the simultaneous operation of two ultrasonic thermometers UT1 and UT2.

The Black Box Mark III is fully computer controlled, and requires a minimum of operator intervention after initial adjustment, thus permitting operation by untrained personnel.

Differential pyrometry in the infrared

Wide-band differential optical pyrometry in the wavelength range from 1.5 to 5 μm was studied

for application in a Laser Flash furnace in a shielded hot cell, where liquid nitrogen is not available for cooling [4]. Minimum object temperature and data quality depend crucially on the choice and temperature of the detector, on the efficiency of light collection, and on the layout of the preamplifier. The optics must be designed in such a way, that on the one hand as much light as possible is guided from the object onto the detector, whereas on the other hand the image should be so well defined that the detector itself limits the object field. For operation at 5 μm these goals are attainable with simple meniscus lenses out of Ge or ZnSe, for 1.5 to 2 μm with glass aspheric lenses or even standard achromats. The detectors tested comprise photoconductive PbSe elements and photovoltaic MCT diodes (for 5 μm), as well as photovoltaic Ge or InGaAs diodes (for 1.5 to 2 μm) and Si photodiodes (<1.05 μm). Amplifier noise depends crucially on the parallel impedance of the detector. The amplifier must be designed in accordance with the type of detector used. Measurement at 5 μm appears to be justified only below 200°C, and requires high aperture optics and/or additional noise reduction through averaging if detector cooling is limited to thermo-electrically attainable -30°C. The best performance in the temperature range 200° through 500°C is obtained with InGaAs detectors. Cooling InGaAs to -30°C only results in a modest improvement in the range 200° through 350°C.

References

- [1] H.A.Tasman, J.-F.Gueugnon, D.Pellotiero, C.Sari, C.-T.Walker: Ultrasonic Thermometers for PHEBUS-FPT0: Material Specifications, Fabrication, Test Results. Technical Note K0292162, August 1992
- [2] H.A.Tasman: Control and evaluation electronics for ultrasonic thermometry - a proposal for a Black Box Mark III. Technical Note K0292161, July 1992
- [3] H.A.Tasman: Black Box Mark 3: Neue Elektronik für Ultraschallthermometrie. Arbeitskreis Thermophysik, Herbsttreffen Dresden 5-6.11.1992
- [4] H.A.Tasman: Differential pyrometry in the infrared. High Temp.-High Pressures 23 (1991) 279

Modelling of whole-core LMFBR accidents using the TRANSURANUS code

Introduction

The European Accident Code-2 (EAC-2) [1] is a best-estimate code for the analysis to be performed of the initiation phase of unprotected whole-core accidents in liquid metal fast breeder reactors (LMFBR). Its development, done at JRC Ispra, was terminated at the end of 1991. In 1992 the EAC-2 code was released to interested parties in Europe. Since there was also interest in specific EAC-2 models for use in other codes, these models were also investigated in great detail. One of these models, the fuel rod behaviour code TRANSURANUS [2,3], constitutes a major improvement of the EAC code compared with other whole-core codes. It offers several distinct advantages:

1. TRANSURANUS allows a consistent steady-state and transient analysis to be performed. Many details of the fuel rod performance, such as the formation of the central void, the evolution of structural zones, swelling of fuel and cladding, grain growth, gas release, gap size, composition of the gas inside the fuel rod etc., are taken into account. In contrast to other more simplified whole-core accident codes we believe that these details are mandatory for any transient analysis, because they determine to a large extent the sequence and the final consequences of any accident.
2. The radial discretisation of fuel and cladding can be chosen to any degree desired. In view of the large temperature differences in the cladding (which may be possible) a detailed cladding analysis is essential for any failure analysis, which is of relevance in predicting failure time and location. We consider the minimum requirement of cladding nodes to be in the range of 20. This discretisation does not cause any problems to the TRANSURANUS code. It has to be stressed that the computer costs depend more or less only linearly on the number of nodes used.
3. Although a detailed fuel rod analysis is performed, the TRANSURANUS code is fast and reliable.

4. It can be employed in different versions (as a deterministic and as a statistical code).

The TRANSURANUS code was used [4] to analyse several experiments from the CABRI-1 program [5] which was initiated in 1973 by the Commissariat à l'Energie Atomique (CEA), France and the Kernforschungszentrum Karlsruhe (KfK), Federal Republic of Germany in cooperation with the Power Reactor and Nuclear Fuel Development Corporation (PNC) of Japan, the United Kingdom Atomic Energy Authority (UKAEA), and the U.S. Nuclear Regulatory Commission (NRC). The experimental programme was carried out at the CABRI facility at Caderache, France, between 1978 and 1986. The objective of the programme was to investigate the key phenomena in the initiation phase of severe accidents in LMFBRs. Single test pins located in a sodium loop were submitted to simulated unprotected loss of flow (ULOF or LOF), transient overpower (TOP), and transient undercooled overpower (TUCOP or LOF-TOP) conditions.

The following tests were selected for analysis:

TOP test with fresh fuel: A1R, A3
 TOP test with slightly irradiated fuel (< 1 a/o burn-up): AI1, AI2 and AI3
 LOF-TOP test with slightly irradiated fuel (< 1 a/o burn-up): BI1, BI2, BI3, BI4, BI5 and BI6

TRANSURANUS-URFRIC

The axial expansion of the fuel is an important negative reactivity feedback mechanism determining the severity of the accident. It is affected by the complicated interaction between fuel and cladding. Axial friction forces are created if the fuel is in contact with the cladding and if the axial strain component of the fuel exceeds that of the cladding. No axial forces are created if the fuel is in contact with the cladding and if the axial strain component of the cladding exceeds that of the fuel. In that case, the fuel which sticks to the cladding will be expanded and axial gaps between pellets will be formed.

Axial friction forces can only be calculated iteratively from the axial deformations of the whole fuel and cladding which means that the calculation of all fuel rod sections has to be embedded in an axial iteration loop which increases the computational costs. In order to avoid this axial iteration loop sometime so-called "simple local slip or noslip models" are

applied which substitute a calculation of the local friction forces at the expense of physically meaningful results.

The problem of calculating the friction forces arises from the very different modes of interaction between fuel and cladding. If the gap remains closed in a time step, it is necessary to determine whether the fuel and the cladding are so tightly wedged together that they move together (axially) during that time step (the static friction or the sticking condition), or whether the radial contact pressure is small enough to allow for a relative axial displacement (the sliding friction or slip condition). Sections without radial contact may be "trapped" by sections above them having radial contact. Additionally, no tensile forces exist in the fuel due to the pellet structure.

It is evident that the simple slip or noslip models suffer from severe limitations: the simple slip model underestimates the loading on the cladding, whereas the noslip model can account neither for a trapped fuel stack situation nor for a correct treatment if the fuel sticks to the cladding and the cladding expansion exceeds that of the fuel.

In order to avoid these limitations a theory was developed which allows the calculation of friction forces taking all different modes of interaction between fuel and cladding into consideration. The model to calculate the axial friction forces is the URFRIC model (TRANSURANUS friction model, [6]). It has been incorporated in the TRANSURANUS code but it can in principle also be used in any other fuel rod performance code.

Fig. 1.21 shows as an example (CABRI experiment AI3) the difference between the simple local slip, the simple local noslip and the detailed URFRIC model. Clearly, the URFRIC model gives the best agreement with experimental evidence.

TRANSURANUS statistical version

In view of the many uncertainties involved in complicated transients such as the CABRI experiments statistical analyses are indispensable: TRANSURANUS uses a simple Monte Carlo technique. The following quantities are treated as statistical variables, i.e. are varied in each Monte Carlo run:

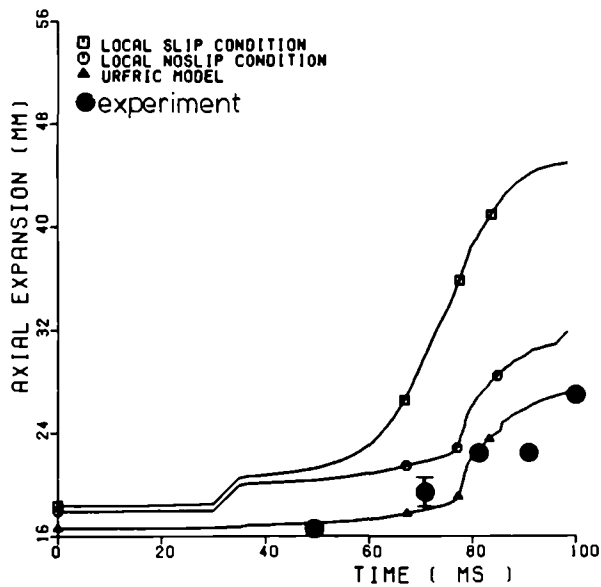


Fig.1.21 Axial expansion at top of fissile column during the TOP (CABRI experiment AI3); Comparison between the three different TRANSURANUS options and experimental evidence.

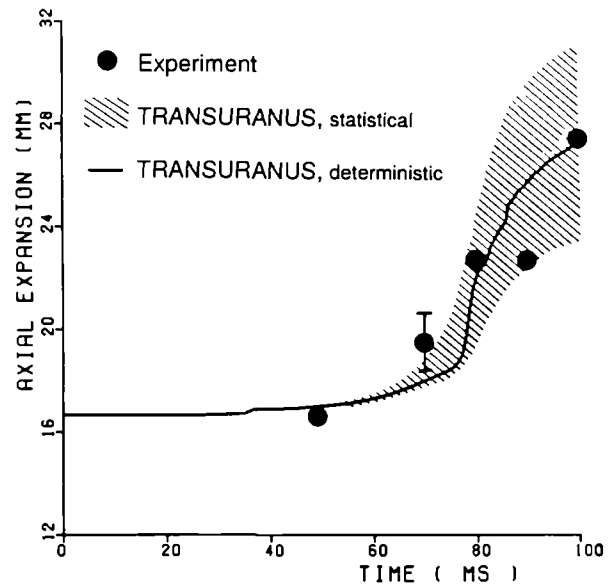


Fig.1.22 Axial expansion of the top of fissile column during the TOP (CABRI experiment AI3); Comparison between deterministic and statistical TRANSURANUS results and experimental evidence.

- Geometry of the fuel rod (fuel and cladding)
- Specific models, e.g. the gap conductance
- All material properties in fuel, cladding (thermal conductivity, thermal strain etc.) and coolant
- All prescribed quantities (linear rating, mass flow rate, boundary conditions etc.)

The statistical analyses performed in the context of this work serve as examples to demonstrate the potential of the TRANSURANUS code. To our knowledge, this is the first time that statistical analyses have been performed for LMFBR accidents.

Fig. 1.22 demonstrates the relevance of statistical analyses. Although the analysis was performed to demonstrate the TRANSURANUS capabilities, the agreement with experimental evidence is excellent.

Conclusions

The goal of this investigation was to summarize the status of the TRANSURANUS code at the end of the EAC-2 project by comparing code

results with selected experiments from the CABRI project. Emphasis was put on the important axial expansion of the fuel. It has to be stressed that the CABRI data evaluation and interpretation which was terminated and documented in 1989 was not completely available. Consequently, all results presented have to be considered as somewhat premature and need further clarification. All analyses were performed using identical code versions as well as consistent data and model options. The steady-state base irradiation and the transients were also analysed consistently. The following conclusions can be drawn:

1. The axial deformation of the fuel during the different transients (TOP, LOF, LOF-TOP) is in fair agreement with experimental evidence.
2. Despite a very detailed radial and axial discretisation used, the TRANSURANUS code runs fast and reliably: numerical problems did not occur.
3. To our knowledge for the first time statistical analyses of such complicated transients as those of CABRI were performed. These analyses serve as a demonstration of the capabilities of the TRANSURANUS code. De-

spite the lack of complete data they demonstrate already the relevance of such statistical analyses. We believe that a statistical treatment of transients will be indispensable in the future. They also prove the numerical robustness of TRANSURANUS.

4. The detailed TRANSURANUS URFRIC model to treat the complicated interaction between fuel and cladding and to calculate the axial friction forces cannot be substituted by simplistic models such as the so-called "local noslip model". The URFRIC model predicts that during the LOF phase axial gaps are created and that pellets fall down when the radial gap between fuel and cladding reopens before the TOP (experiments BI1, BI3, BI4, BI5 and BI6).
5. A detailed radial and axial discretisation is necessary to describe those complicated transients. This is especially true for the radial discretisation of the cladding where the minimum number of cladding nodes required are considered to be in the range of 20. The slower the transients, the more importance must be devoted to the cladding details.

References

- [1] H.U. Wider et al., The European Accident Code EAC-2: Overview and Status, International ANS Topical Fast Reactor Safety Meeting, 12-16 August 1990, Snowbird, UT (USA)
- [2] K. Lassmann, H.Blank, Modelling of Fuel Rod Behaviour and Recent Advances of the TRANSURANUS Code, Nucl. Eng. Des. 106 (1988) 291
- [3] K. Lassmann, TRANSURANUS: A Fuel Rod Analysis Code Ready for Use, J. Nucl. Mater. 188 (1992), 295
- [4] K. Lassmann, J. van de Laar, G. Peter, Analysis of CABRI experiments using the TRANSURANUS code and the coupled codes TRANSURANUS-CAMDYN, Tech. Note K 0292158 (1992)
- [5] K. Baumung and G. Augier, Quantitative Fuel Motion Determination with the CABRI Fast Neutron Hodoscope: Evaluation Methods and Results, Nucl. Techn. 96 (1991) 302-313
- [6] K. Lassmann, Treatment of the Axial Friction Forces in the TRANSURANUS Code, Nuclear science and technology, Transactions of two international seminars on the mathematical/mechanical modelling of reactor fuel elements, Commission of the European Communities, Report EUR 13660 EN (1991) 185

Study of High-Temperature Properties

Introduction

Work on the project in the reporting period was carried out along three action lines. The first regards the high temperature properties of nuclear materials, the second the fission product source term in irradiated nuclear fuels under accidental conditions, and the third the development of advanced thermometric techniques.

The following contributions pertain to the first two actions whilst the achievements of the third one, pursued in collaboration with industry, have been reported elsewhere [1].

Reference

- [1] ITU Technical Note: K0292 163 (1992), classified

Lambda transition in uranium dioxide

Introduction

New results are presented here, obtained from experiments employing subsecond pulse heating of small spheres of uranium in a high pressure autoclave, using a Nd-YAG laser.

The essential new feature is the discovery of a weak inflexion point or plateau in the cooling curve of nominally stoichiometric samples, initially heated to just below the melting point, near 2650 K. Thermal analysis of the cooling curve yields the heat capacity, which displays a sharp peak centred at the plateau temperature, the existence of which was first inferred by Bredig in 1969 [1]. However, the experimental evidence of this phenomenon was not universally accepted, as it was based on the numerical differentiation of the enthalpy curve $H=H(T)$ in a temperature interval where the experimental errors are relatively large [2]. Most interestingly, it is found that the occurrence of the heat capacity peak is sensitively dependent on the REDOX properties of the buffer gas in the autoclave.

The experiment

The sample, suspended by a thin tungsten needle, is positioned in the centre of an autoclave (Fig. 1.23), at the point of convergence of four Nd-YAG laser beams of equal power, whose size is approximately equal to the sample diameter. The specific power deposited on the sample is sufficiently homogeneous for enabling a one-dimensional thermal analysis to be carried out. The temperature is measured by a fast six-wavelength pyrometer positioned at 50 cm from the autoclave window, where a biconvex lense is mounted to provide an enlarged image of the measured area (0.15 mm diameter).

The sample (a nearly perfect sphere of 1 mm diameter) was heated up to 3000K within less than 50 ms. The input power was chosen in order to obtain a balance with the total heat losses (radiative, convective and conductive), at a temperature below the melting point of

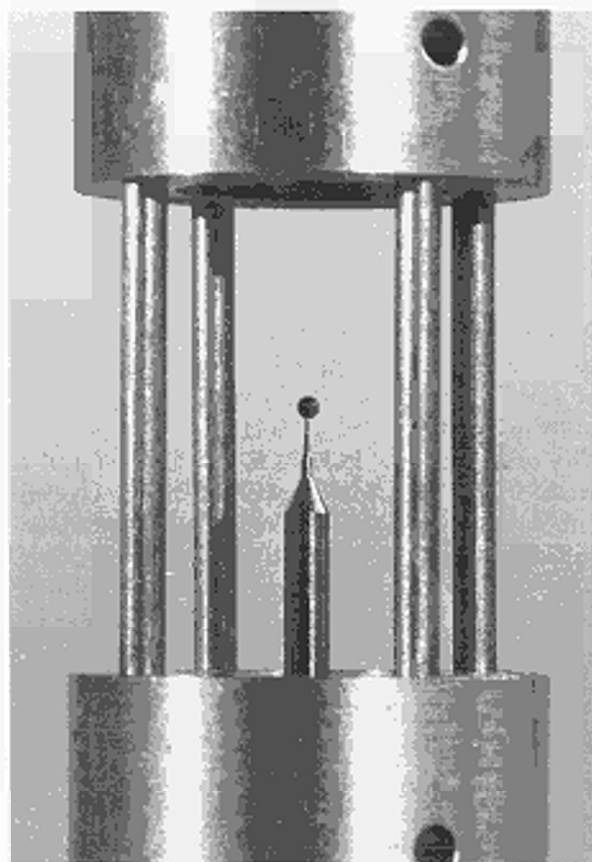


Fig.1.23 Specimen mounting. The sphere of UO_2 has a diameter of 0.8 mm.; the support is a tungsten needle.

urania. The steady state temperature was maintained for approximately 300 ms, after which the lasers were switched off. A computer code was used to calculate the heat propagation into the sample under realistic boundary conditions. The analysis shows that at the end of the heating stage the radial gradient in the sample was less than 100 K/mm.

The experimental cooling curve is normally smooth and reproducible and enables heat losses to be evaluated with a precision of 10-15%, if the heat capacity of the sample is known, or vice versa, the heat capacity can be deduced if the sample boundary cooling conditions are given. The thermal analysis of the extra contribution to the heat capacity in the region around the plateau is simple and accurate since it depends only on the ratio of the measured cooling rate to that predicted in the absence of a transition, i.e. calculated from an assumed baseline $C_p = C_p(T)$ in which the contribution of the transition is a priori not included.

The samples consist of spheres produced by a sol-gel method and sintered up to 85 to 97% of the theoretical density. Ceramographs made after pulse heating show that neither the grain size nor the porosity distribution were significantly affected by the thermal treatment (Fig. 1.24), confirming that melting had not occurred during the experiment.

Shots were made in inert, reducing (inert gas + 3% hydrogen), and oxidizing atmosphere (inert gas + 0.1 bar oxygen).

X-ray analysis showed that the lattice parameter of the samples treated in inert atmosphere ranged between 0.54703 to 0.54709 nm; a further increase above these values was observed after repeated shots, indicating a progressive reduction from an initially slightly hyperstoichiometric sample. After treatment in hydrogen, a lattice parameter of 0.54721 nm was measured. This corresponds to hypostoichiometric urania and, to our knowledge, is the highest lattice parameter of quenched f.c.c. uranium dioxide ever measured. No second phases could be observed by ceramographic and X-ray analysis, although it cannot be excluded that a rapid precipitation of metallic uranium may have produced sub-microscopic phases of a few nanometer size. Chemical determination of the O/U ratio could not be carried out due to the lack of a suitable microanalytical facility.

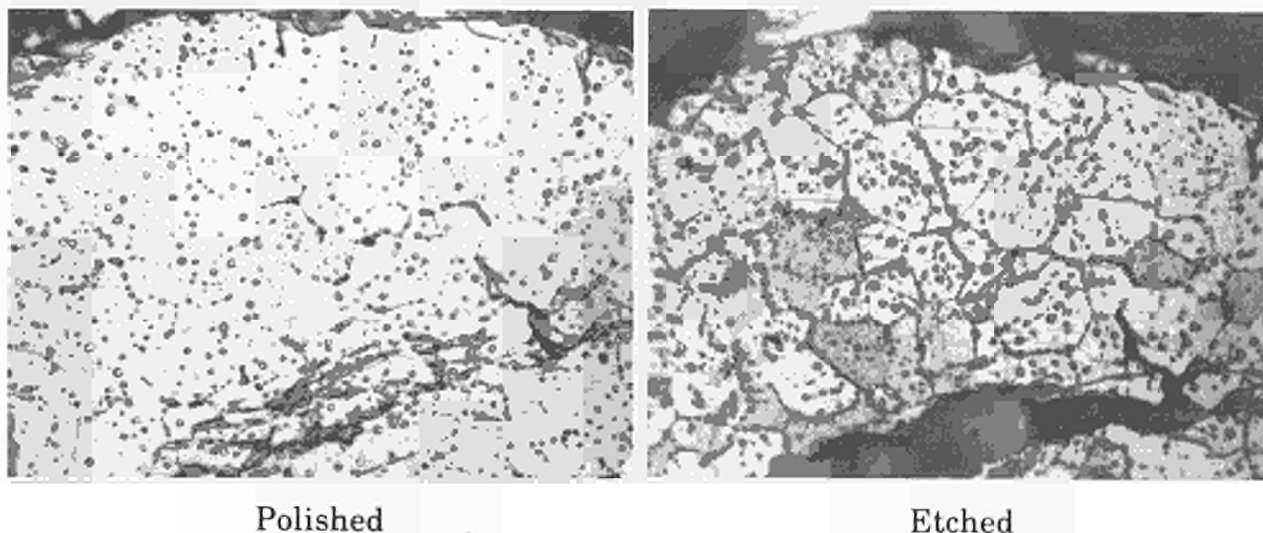


Fig.1.24 Ceramograph of the samples after heating in 25 bar He. The lattice parameter (0.54703 nm) indicates an approximately stoichiometric composition.

Results

The transition manifests itself as a weak inflection point of the cooling curve and passed unnoticed during preceding experiments. However, if the mean cooling rate is less than 10 K/ms the inflection point develops into a clearly shaped plateau (Fig. 1.25). Another point which made the identification difficult was the fact that slightly hyperstoichiometric samples did not produce a clear inflection unless repeated

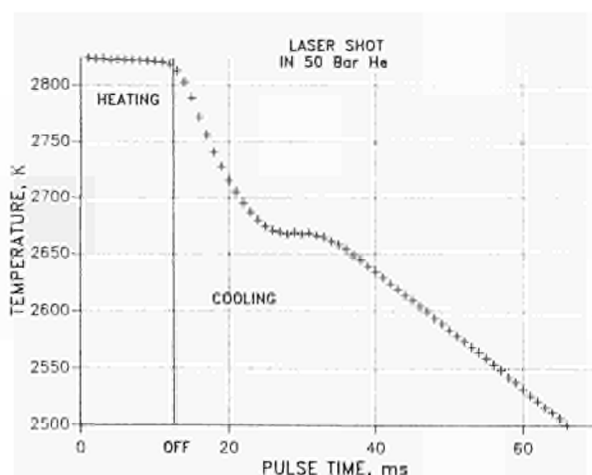


Fig.1.25 Pre-melting transition in UO_2 as revealed by the thermal analysis of a cooling sample, initially heated to 2850K, for 300ms, in 50 bar He.

shots led to a significant reduction. This occurred after the first shot in low-density samples, whereas dense samples needed up to ten shots to display a clear inflection. This is obviously due to the evaporation conditions in the different open pore and free surface structural configurations of the samples. The transition temperature in nominally stoichiometric urania is in the interval $T_c = 2670 \pm 30$ K, the scatter being approximately twice the experimental error in temperature. Interestingly, if the sample was initially quenched from temperatures above the melting point, no transition appeared in subsequent shots up to lower sub-melting temperatures.

It was soon realized that the transition temperature showed a systematic tendency to increase if a sequence of pulses was applied to the same sample. The effect was first detected in an inert gas atmosphere, but became much more pronounced if a reducing atmosphere (IG+3% H_2) was introduced into the autoclave (Fig. 1.26). The maximum detected transition temperature is 2950 K, corresponding to the above mentioned maximum value of the lattice parameter. Furthermore, it was observed that the transition at higher temperatures exhibits undercooling effects typical of first-order transitions (Fig. 1.27) (Undercooling in a thermodynamic phase transition is normally due to a time delay caused by the finite nucleation rate of the low-temperature phase).

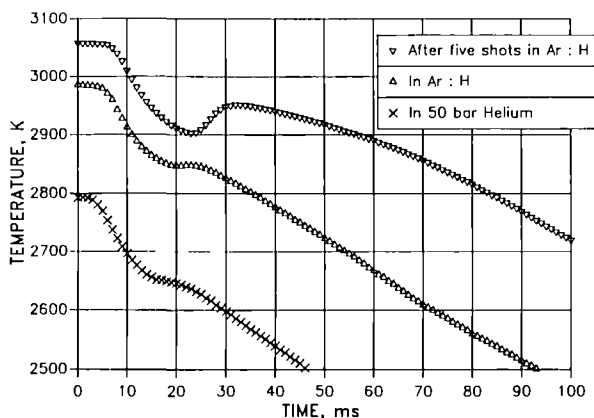


Fig.1.26 Cooling curves of samples heated in different atmospheres. The curve at the top was displayed by a sample repeatedly heated in a reducing atmosphere; an undercooling effect is clearly visible in the "plateau" region.

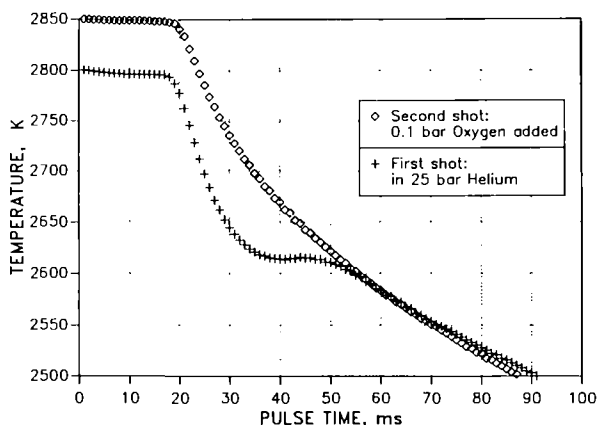


Fig.1.27 Cooling curves of samples heated in inert and oxidizing atmosphere, respectively; in the latter case, the transition plateau disappears.

The experiment was then repeated in an oxidizing atmosphere (IG+0.1 bar O₂), leading to even more dramatic results: the transition did in fact completely disappear, at least in the observed range (2300-3000 K). The results of the various experiments are collected in Tab. 1.1. The measured cooling curves have been analyzed with the above method to obtain the extra-contribution to C_p of the pre-melting transition. Fig. 1.28 shows that the heat capacity peak in nominally stoichiometric urania is localized around a temperature very

Tab.1.1 Summary of the experimental results obtained for different pressures and compositions of the autoclave gas. T_{trans} is the temperature at which the plateau occurs in the cooling curve of the identified samples, previously laser-heated to a temperature T_{max} (< T_{mel}).

Sample - shot - gas	T _{trans} (K)
1A - 45 - 75 bar He	2615
1A - 46 - 75 bar He	2678
1A - 47 - 75 bar He	2617
1A - 48 - 75 bar He	2727
1A - 49 - 75 bar He	2721
2A - 60 - 25 bar He	2648
2A - 62 - 25 bar He	2629
2A - 64 - 25 bar He	2614
2A - 65 - O ₂ +He*	
3A - 70 - 2 bar Ar+3%H ₂	2850
3A - 71 - 2 bar Ar+3%H ₂	2852
4A - 73 - 75 bar He	2866
4A - 74 - 75 bar He	2880
4A - 75 - 75 bar He	2880
4A - 77 - 75 bar He	2835
5A - 82 - 4 bar Ar+3%H ₂ *	2940
5A - 83 - 4 bar Ar+3%H ₂ *	
5A - 84 - 4 bar Ar+3%H ₂ *	
5A - 85 - 4 bar Ar+3%H ₂ *	
6A - 94 - 50 bar He	2648
6A - 95 - 50 bar He	2668
6A - 97 - 50 bar He	2734
7A - 100 - 4 bar Ar+3%H ₂	2755
7A - 101 - 4 bar Ar+3%H ₂	
7A - 102 - 4 bar Ar+3%H ₂	2847
7A - 103 - 4 bar Ar+3%H ₂	2838
7A - 104 - 4 bar Ar+3%H ₂	2918
7A - 105 - 4 bar Ar+3%H ₂	2950
8B - 114 - 40 bar He	2830
8B - 116 - 40 bar He	2840

* molten

close to that deduced by Bredig, however, the peak is in our case narrower and the value of C_p at the transition temperature does diverge, as the cooling rate at the transition temperature is effectively zero (This cannot be proved in the case of a regular plateau because the precision of the temperature measurement does not allow

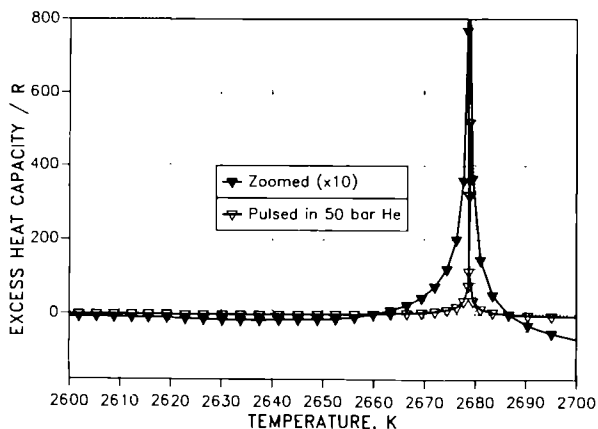


Fig.1.28 Excess heat capacity of UO_2 as a function of temperature due to the pre-melting transition, as deduced from the cooling curve. The curve with crosses corresponds to a ordinate scale reduction of a factor ten.

us to calculate temperature differences below a certain limit, but it is certainly the case when undercooling occurs, since a zero of dT/dt can be analogically inferred).

References

- [1] M.A.Bredig, Report ORNL 4437 (1969) 103
- [2] R.A. Hein, P.N.Flagella, Report GEMP-5789 (1968)

A model for order-disorder transitions in the UO_2 anion sublattice

Introduction

Our new results concerning the existence of a $C_p(T)$ peak at high temperature and its dependence on the UO_2 composition have been investigated, starting from a set of hypotheses and interpretations pertaining to similar transitions which occur in a class of compounds that crystallize in the fluorite lattice, and show superionic transitions, whose character is determined by a sharp (but continuous) increase of the point defect concentration across a critical temperature T_c . These phenomena, -customarily called "lambda"-transitions, from the shape of the corresponding $C_p(T)$ peak- are associated

with second-order thermodynamic phase transitions involving Frenkel disorder (in our case oxygen defects); their occurrence entails the divergence of the heat capacity at T_c , whilst both enthalpy and defect concentration do not exhibit discontinuities across the transition (as is the case of first-order transitions).

From a theoretical point of view second order transitions occur when the first, second and, for symmetry reasons, third derivative of the defect free energy ΔG , with respect to the defect concentration n , are zero at a distinct temperature T_c , and defect concentration, n_c . It is clear that once T_c is given, the model of a system undergoing a second-order transition should contain at least two free parameters which, together with n_c , should equate to zero the three derivatives of ΔG . Actually, since ΔG is normally expressed by a transcendental function, the existence of real solutions of the corresponding differential equations is not ensured, so that only particular systems can display second-order transitions.

We therefore constructed our model by starting from a set of physical hypotheses, which were finally translated into a mathematical formalism suitable for a reasonable fitting of the experimental observations:

- a) The first one concerns the configurational entropy S_c , of the Frenkel defects in UO_2 . At temperatures above 2500 K, complex clustering between oxygen vacancies and interstitials is likely to be much less pronounced than that observed at lower temperatures. However, the simplest (1 2 2) cluster produced by the displacement of two lattice oxygens adjacent to an interstitial towards the center of the neighbouring octahedral voids is probably stable even at high temperatures. In order to account for simple cluster formation due to repulsive interactions between lattice atoms and defects, we assumed that these entail a certain non-occupancy of defect sites neighbouring an already occupied site. This site blocking can be formulated in term of an effective cluster size, the defects themselves being randomly distributed, but over a reduced number of sites. In other words, the available sites for interstitials and vacancies in the f.c.c lattice are multiplied by suitable "blocking factors" calculated from the crystallographic properties of the cluster features. Finally, the configurational entropy can be expressed as a function of the

point defect concentration n , in which the blocking effect requires, mathematically, an upper variation limit for n . The assumed clustering model indicates that for interstitials this limit is 0.25, consistent with the phase boundary between UO_2 and U_4O_9 . Generally, it can be seen that the blocking model and the corresponding configurational entropy can be incorporated, without the introduction of any additional parameters, both for UO_{2+x} and UO_{2-x} .

- b) The non-configurational term of defect entropy S_{nc} is primarily due to the variation of the vibrational spectrum in the region surrounding the defect. A calculation of this term from atomic models is out of question. Even experimentally, if one deduces S_{nc} from the ΔG_{O_2} data, the uncertainty involved in separating the configurational from the non-configurational part of entropy is very high: one obtains $S_{nc} = (10 \pm 2)R$. In our case we have assumed an expression for S_{nc} with an explicit dependence on the defect concentration: $S_{nc} = S_0(1 + Bn)$, with $B > 0$, consistent with the positive frequency perturbations induced in the vicinity of an interstitial (One expects that the frequency perturbations due to vacancies are of opposite sign, but weaker than those produced by interstitials, whose sign eventually predominates in the total balance (see e.g. [1])).
- c) The formation enthalpy of defects W , is a key parameter for the model. It can be seen that with a constant partial formation enthalpy the system is inherently unable to display a second-order phase transition. The simplest model enabling such a transition to occur is that characterized by a linear variation of W with n , of type: $W = W_0 - Ln$. This expression provides the simplest description of a class of systems where the creation of defects is assisted by attractive potentials, so that by increasing the equilibrium concentration of defects, the energy necessary to create further defects decreases. This leads to cooperative effects which, for particular combinations of the parameters involved (i.e. entropy and temperature), may produce in the system phase transitions or conditions similar to thermodynamic critical states.

The parameter W_0 which represents the defect creation enthalpy at vanishing defect concentrations, can be obtained from

experimental data, yielding $W_0 = 3.6$ eV [2]. The defect interaction parameter L is a priori unknown, and in the model has to be formally treated as a variable to fit the observed features of the transition.

The case of stoichiometric UO_2

The basis hypothesis is the realization of a 2nd-phase transition in stoichiometric urania at a temperature $T_c = 2670$ K, which requires that at this temperature the first three derivatives of the free energy are zero and the fourth derivative is positive (Figs. 1.29a,b,c). In consequence, the three corresponding transcendental equations yield the defect concentration n_c , at the critical temperature, and the parameters L and S_0 . The following values are obtained:

$$L = 1.45 \text{ eV}, S_0 = 13.63R$$

With these values of the parameters the concentration of defects, $n(T)$, at arbitrary T , exhibits a vertical inflection point at $T = T_c$, entailing a divergent lambda-like heat capacity peak, which closely approximates the observed C_p -peak. At temperatures above T_c the defect concentration increases only very slightly with temperature (Figs. 1.30 and 1.31).

Predictions of the model away from stoichiometry

This is most simply achieved by utilizing the extension of the above treatment of the 2nd-order transition, with the obtained parameters to the case where an extrinsic defect concentration x is present, i.e. in the presence of a different expression of the configurational entropy. The qualitative predictions of the model for non-stoichiometric UO_2 can be summarized as follows:

- For the substoichiometric oxide UO_{2-x} the calculated defect concentration as a function of temperature displays a discontinuity at a temperature $T_t > T_c$, indicating the occurrence of a 1st-order phase transition at $T_t(x)$ (Fig. 1.30). For x tending to zero, $T_t(x)$ tends to $T_c = 2670$ K, and at $x=0$ the 2nd-order transition is to be regarded as the vestigial remnant of a 1st-order transition, which characterizes the anion order-disorder transition in UO_{2-x} .

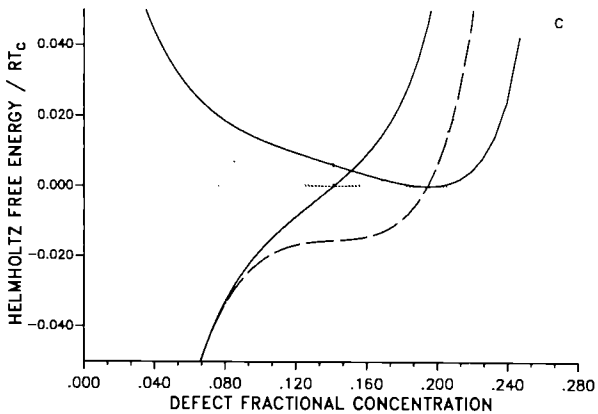
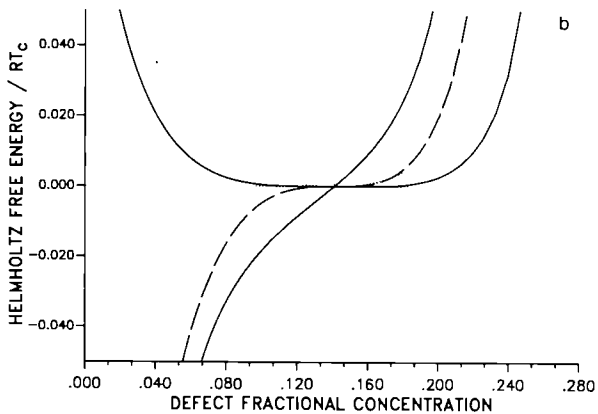
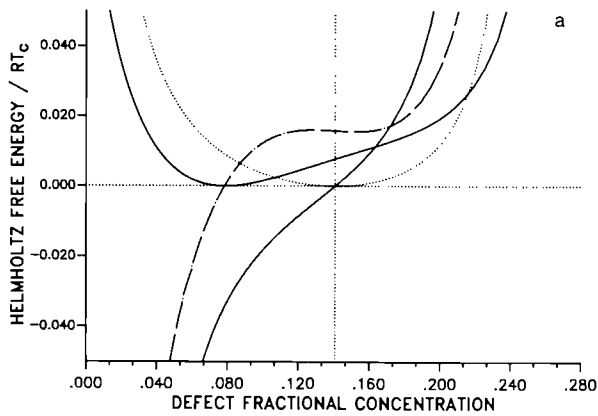


Fig.1.29a Calculated free energy as a function of defect concentration and its first, second and third derivatives, at 1% below the transition temperature. The minimum individuates an equilibrium defect concentration of circa 5%.

Fig.1.29b Idem as above, at the transition temperature. At this temperature all the derivatives up to the 3th order are zero.

Fig.1.29c Idem as above, 1% above the transition temperature. The equilibrium defect concentration is about 21%. A particularly "soft" blocking function was adopted in this calculation experiment to better emphasize the jump of $n(eq)$ across the transition.

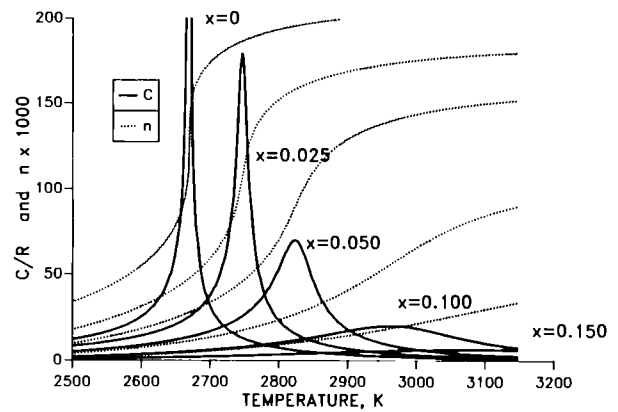


Fig.1.30 Calculated heat capacity peaks and defect concentration as functions of temperature at various super-stoichiometric deviations. The peaks in UO_{2+x} are due to diffuse transitions.

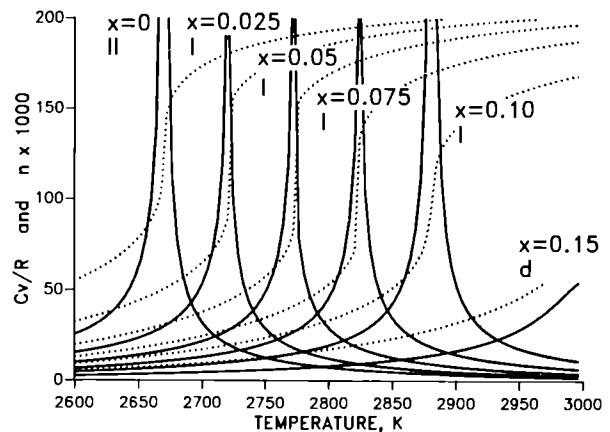


Fig.1.31 Idem as in Fig. 1.30, for sub-stoichiometric deviations. The peaks in UO_{2-x} are due to 1st-order transitions.

- The trend of the curve $T_t = T_t(x)$ is mainly defined by the assumed model for the configurational entropy, however, it can be seen that by varying the n-dependence of the non-configurational entropy (parameter B), the calculated transition temperatures in UO_{2-x} can be fitted to the experimental values. The complete exploitation of the physically allowed variability of model parameters is thus necessary and sufficient to explain the experiment.

- For superstoichiometric UO_{2+x} the calculated defect concentration $n(\bar{T})$ is a continuously increasing sigmoidal curve and the heat capacity exhibits a finite peak

at a temperature $T_p < T_c$, that is to say, in UO_{2+x} the Frenkel defect formation takes place as a regular thermally activated process with variable activation energy (Fig. 1.31) and with no critical point. In this context, it can be seen that the model is in qualitative agreement with the experimental results reported in the preceding section, where the variation of the transition temperature with stoichiometry and the clear appearance of a 1st-order transition in the substoichiometric samples are the most important observed features.

Implications for the Urania Phase Diagram

The experimental observation of the lambda-transitions in $\text{UO}_{2\pm x}$, together with the theoretical interpretation presented above, suggest some necessary refinements of the existing phase diagram of the material, although, given the uncertainty concerning the stoichiometry of the various samples used in our experiments, it is difficult to make definitive quantitative recommendations. However, it is clear that:

- i) The (x-T) phase field of UO_{2-x} is partitioned by a line of 1st-order phase transitions which starts at $T=2670$ at $x>0$, subsequently rising towards the solidus with increasing x (Fig. 1.32).
- ii) The hypothetical 2nd-order $T_t = T_t(x)$ line represents, in the assumed lattice defect model, a sort of discriminant: all order-

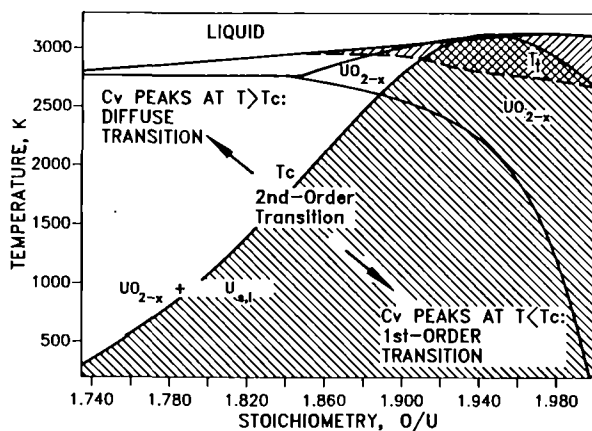


Fig.1.32 Phase diagram of UO_{2-x} including the calculated 2nd-order transition line and the predicted 1st-order phase transition line.

disorder transitions possibly occurring at temperatures above this line are of "diffuse type", i.e. do not exhibit singularities, whilst transitions occurring below this line have a 1st-order character.

- iii) Although no lambda-transition was detected in the superstoichiometric samples used in our experiments, it is physically significant to note that the predicted (but not realized) 2nd-order transition line $T_c(x)$ decreases with increasing x and crosses the U_4O_9 phase boundary at a point near 700 K (Fig. 1.33), where a diffuse order-disorder transition is observed [3] in the oxygen superlattice - suggesting that the 2nd-order lambda-transition in $\text{UO}_{2.00}$ (involving disorder in the fluorite oxygen sublattice) is the counterpart of this interstitial superlattice transition in U_4O_9 .

The experimental absence of any sharp C_p peak under oxidizing conditions is consistent with the calculated decrease in peak height (and increase in width) in diffuse transitions. The line of diffuse transitions predicted by the model for the above mentioned parameter values is shown as a dashed line in Fig. 1.33 the features of the

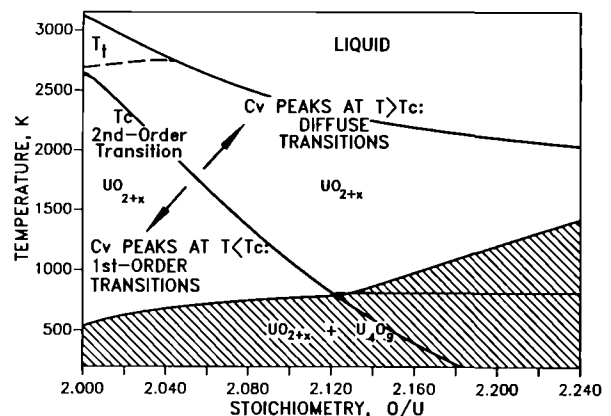


Fig.1.33 Idem as in Fig.1.32, for UO_{2+x} . The predicted diffuse transition is indicated with the dashed line.

corresponding peaks at selected compositions being given in Tab. 1.2.

These considerations cast new light on the superionic transitions and order-disorder phenomena in the fluorite oxygen lattice and superlattice of UO_2 . The obtained results indicate that, despite their apparent complexity, these effects can be described in terms of

Tab.1.2 Calculated premelting transition temperatures in UO_{2-x} , (assuming $T_c(x=0) = 2670$ K), together with details of the C_v peak associated with the diffuse transitions in UO_{2+x} .

Transition type	Stoichiom. 1000 x	Peak Temp. (K)	Peak C_v (R)	50% Peak width (K)
Diffuse	-150	3006	57	100
1st order	-100	2880	.	.
1st order	-75	2824	.	.
1st order	-50	2772	.	.
1st order	-25	2720	.	.
2nd order	0	2670	.	.
Diffuse	25	2746	180	30
Diffuse	50	2823	70	100
Diffuse	100	2963	20	350
Diffuse	150	3072	7	600

relatively simple hypotheses, and the corresponding mean field model is effectively able to provide a reasonable representation of the thermodynamic and thermophysical properties of the system.

References

- [1] N.F.Mott, R.W.Gurney, "Electronic Processes in Ionic Crystals", Dover (1966)
- [2] M.T.Hutchings, J.Chem.Phys. **C 17** (1984) 3903-40
- [3] H.Blank, C.Ronchi, Acta Cryst. **A24** (1968) 657-666

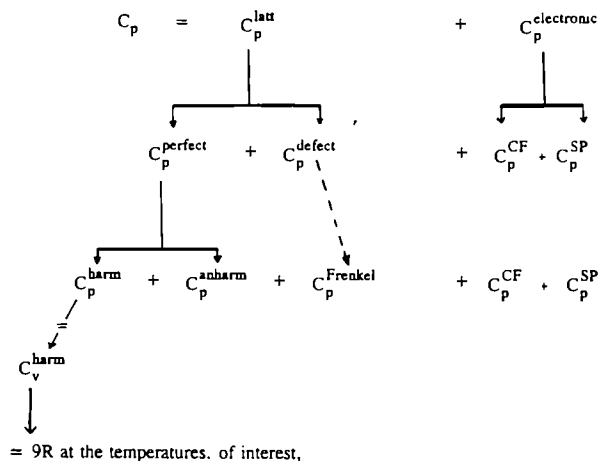
Elementary contributions to the heat capacity of solid and liquid UO_2

Introduction

In TUAR 91 an extensive contribution was published on the ITU experimental programme whose aim was the measurement of the heat capacity C_p of liquid uranium up to 8000K. The interpretation of the measured relationship between C_p and temperature over this wide range is related to the problem of breaking down the overall phenomenon elementary energy into exchange mechanisms and their relative weights, the assessment of the various heat capacity contributions being the fundamental step for a self consistent representation of the thermodynamic properties of the system.

Solid

The constant pressure heat capacity of solid UO_2 is analysed as follows:



$$C_p(UO_2) = 9R + C_p^{anh} + C_p^F + C_p^{CF} + C_p^{SP}$$

where

- C_p^F is the contribution arising from anion Frenkel disorder, which is effective at $T > 2000$ K. This point has been discussed in the preceding section.
- C_p^{CF} is the Crystal Field contribution due to thermal excitations over the crystal field levels of the localized electrons. For UO_2 there are experimental values for this contribution [1].
- C_p^{SP} is the Small Polaron contribution due to the disproportionation :

$$2U^{4+}(5f)^2 \rightarrow U^{3+}(5f)^3 + U^{5+}(5f)^1$$
 where the associated excess electrons/holes move by hopping as small polarons. In UO_2 this mechanism is active above 1200K and its parameters (activation enthalpy and entropy) can be deduced from d.c. electrical conductivity data [2] in the two temperature ranges where extrinsic and intrinsic defect regimes respectively are dominating the conductivity.

It is worthwhile noting that these three contributions are due to thermally activated processes and the pertaining partition functions are formally analogous. For this reason their

contributions to C_p have often been fitted by a single empirical function.

- iv) The harmonic vibration contribution, C_p^h , is suitably represented by Debye's model for a triatomic molecular lattice. In UO_2 , at temperatures above 1000 K, this contribution approaches the asymptotic Neumann-Kopp value of 9R.
- v) C_p^{anh} , arising from anharmonic lattice vibrations, can be empirically evaluated from a comparison with the heat capacity of thoria. In fact, ThO_2 at $T < 1200$ K does not exhibit neither Frenkel disorder nor electronic excitations, so that C_p is just given by the sum of the harmonic and anharmonic lattice vibrations. Therefore, in the temperature range where the harmonic vibrations are saturated and the polarons are not yet active, the heat capacities of thoria and urania differ only by the crystal field contributions. By evaluating experimentally the difference:

$$C_p^{CF} = C_p(UO_2) - C_p(ThO_2)$$

one obtains the figures reported in Tab. 1.3, which show that within an acceptable precision is

$$C_p^{anh}(UO_2) = C_p^{anh}(ThO_2) (= C_p(ThO_2) - 9R).$$

Tab.1.3 Heat capacity contributions due to crystal field in Uranid and Thoria.

$T \cdot 10^{-3}$	T_m scaled	T_m unscaled	C_p^{CF} (expt)
1.0	5.1	6.9	6.0
1.1	5.3	6.8	6.0
1.2	4.8	6.7	6.0
1.3	4.6	6.7	6.0

The five contributions to heat capacity have been evaluated as explained above, and are listed in Tab. 1.4. A few remarks are here in order:

1. The inability to accommodate C_p^{SP} at temperatures above 1400 K would indicate that either the anharmonic contribution or the small polaron peak obtained from the data of Bates [2] are overestimated. There are reasons to conclude that the least certain entry is the former.
2. The peak due to Frenkel disorder and the associated transition is too broad if compared to the experimental data at temperatures between 1800 and 2200 K. Above the lambda-transition, on the other hand, there is no such problem, the

Tab.1.4 Theoretical contributions to the heat capacity of solid UO_2 .

$T (10^{-3})$	$C_p^h = (C_v^h)$	C_p^{anh}	C_p^{CF} normalized to U^{4+}	S_1	C_p^{SP} $\times 10^{-3}$	C_p^F	S_2	$S_1 + S_2$	C_p^{exp} Hein & Flagella
1.0	74.8	2.5	6.0	83.3	-	-	-	83	84 ± 2
1.2	74.8	4.8	6.0	85.6	0.2	-	0.2	86	86 ± 2
1.4	74.8	6.9	6.0	87.7	1.2	0.3	1.5	89	88 ± 2
1.6	74.8	8.9	6.0	89.7	3.7	1.4	5.1	95	90 ± 2
1.8	74.8	10.9	6.0	91.7	8.3	4.8	13.1	105	93 ± 2
2.0	74.8	12.9	6.0	93.7	15.4	12.7	28.1	122	99 ± 3
2.2	74.8	14.8	6.0	95.6	23.8	29.3	53.1	149	109 ± 3
2.4	74.8	16.8	6.0	97.6	33.0	64.8	97.8	195	119 ± 4
2.6	74.8	18.8	7.0	100.6	40.3	223.8	264.0	365	PEAK
2.8	74.8	(20.8)	7.0	102.6	43.2	56.4	99.6	202	161 ± 4
3.0	74.8	(22.8)	7.0	104.6	47.0	15.3	62.3	167	161 ± 4
3.12	74.8	(23.8)	7.0	106.6	46.0	8.0	540	160	161 ± 4

calculated sum of the contributions being in agreement with the measurements (numerical derivatives of the enthalpy data of Hein and Flagella [7]). Independent of the remark in 1), it seems indeed that the Frenkel disorder peak calculated with the model mentioned in the preceding section has a too large tail compared to the experiment. Calculations show that a better agreement can only be obtained if a stronger (non-linear) defect interaction model is assumed. This study is still in progress.

Liquid

Each of the heat capacity contributions in the solid have been treated in turn, with respect to the likely changes entailed by melting.

- i) Harmonic contribution: an upper bound is given by the complete activation of both longitudinal and transversal activations of the triatomic molecule lattice, i.e. $9R$. The lower bound ($=3R$, due to longitudinal vibrations only) follows by suppressing the transversal modes; but the behaviour of most liquids shows that this can only be expected far above the melting point.
- ii) Anharmonic contribution: they are uncertain in the liquid. We shall return to this point which is currently being considered [3].
- iii) Crystal Field contributions: neglecting changes in the crystal field upon melting, Osborn [4] has calculated that this contribution decreases with temperature and attains 1 J/mol K at 7000 K .
- iv) Small polaron contribution: this contribution exhibits a maximum near the melting point and then falls, but slower than the experiment (Fig. 1.34). Two remarks should be made, however: first, although there is some evidence that UO_2 remains semiconducting in the liquid state [5], the activation enthalpy for polaron formation is experimentally uncertain, and it is very likely to decrease by melting: this would imply a steeper fall of the heat capacity contribution above T_m . Secondly, this contribution has been calculated in the absence of electron-hole interactions. As already noted for the "lambda" transition, such an interaction produces a narrowing of

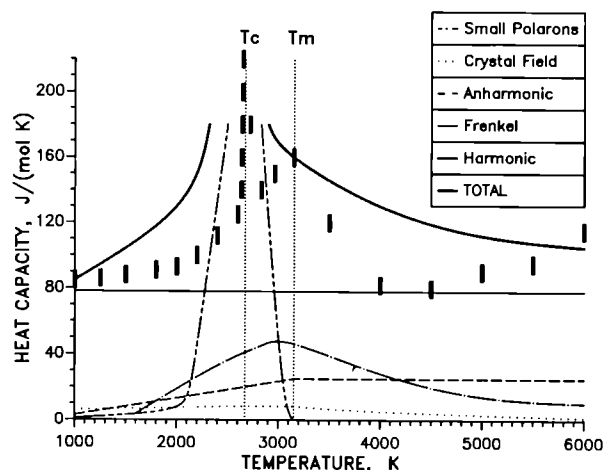


Fig.1.34 Calculated contributions to heat capacity in UO_2 . The bars represents the ITU experimental measurements.

the respective C_p -peak. Since the adopted small polaron formation parameters predict at T_m a $\text{U}^{(5+)}$ concentration of 17%, this interaction cannot be neglected. Considering that such an interaction term would lead to a similar formulation as in the case of the Frenkel disorder, an extreme consequence could be a phase transition from a Mott-insulating state to a metallic state, at a temperature near the melting point. Although there is at present no experimental evidence for such a (1st-order) transition, a "diffuse" transition in the sense explained in the preceding section is nonetheless possible, in which the heat capacity peak C_p^{SP} is sharpened up simply as a consequence of the saturation effects connected with the finite number of $\text{U}^{(4+)}$ ions available to participate in the polaron formation.

- v) Frenkel disorder contribution: unlike the small polarons, it is not clear whether the concept of Frenkel disorder is meaningful in the liquid state. In any case, the anion sublattice is already as disordered as it almost can be, even before melting occurs. Thus, in the absence of any contrary empirical indication, this contribution will be neglected above T_m . In conclusion, the trend of the theoretical contributions of the heat capacity in liquid UO_2 is in agreement with the experiment, predicting a decrease of C_p above the melting point, whereby a better quantitative agreement could be obtained if

more realistic models were assumed. Effectively, only harmonic and anharmonic vibrations contribute to the heat capacity up to temperatures as high as 4500 K, where the calculated C_p is only 15 J/mol K larger than the experimental value.

- vi) Finally, the upswing in the experimental C_p at $T > 5000$ K has to be considered as due to a new additional mechanism. It exhibits an activated T-dependence of the form:

$$C_p^{\text{act}}(T) = \text{const}/T^2 \exp(-E/kT)$$

where $E = 3\text{eV}$, indicating the existence of an energy gap of 6eV across which excitation occurs at these temperatures. Reference to the electronic energy scheme of solid UO_2 deduced from optical experiments [6] reveals that a gap of this magnitude exists between the 2p valence band (oxygen based) and the eg subband of the 6d band complex (uranium based). This strongly suggests that the increase in C_p above 5000K is electronic in origin. However, a more detailed analysis of this contribution is needed, paying more attention to the observed onset of saturation near 7000 K to a value of about 107 J/mol K.

References

- [1] G. Amoretti et al., Phys. Rev. **B40** (1989) 1856
- [2] J.L. Bates et al. J Amer. Ceram. Soc. **50** (1967) 652
- [3] R. Grimvall, Harwell, personal communication, December 1992
- [4] R. Osborn, Harwell, personal communication, December 1992
- [5] A.L. Wright et al. Trans. Amer. Nucl. Soc. **34** (1980) 551
- [6] J. Schoenes, Phys. Rept. **63** (1980) 301
- [7] R.A. Hein, P.N. Flagella, Report GEMP - 5789 (1968)

Shielded Knudsen cell for fission product source-term analysis

The current reactor and fuel cycle safety studies are centered on the problem of the release of radiotoxic fission products from the fuel in a variety of scenarios ranging from minor fuel rod failures, through hypothetical severe accidents, to spent fuel storage. The common aspect in the analysis of these events is the migration and the chemical reactions of the fission products in the presence of given thermal and chemical agents,

whereby the present trend of the risk analysis is to construct a groundwork of mechanistic models for the description of these processes, to be applied to different scenarios. This analytical program requires a substantial work of data collection and validation as well as original measurements on hitherto unknown multi-component systems.

Laboratory experiments on the fission product effusion rate from irradiated fuels are considered as particularly instructive both for checking existing models and for providing new indications on the relevant chemical species involved. In this perspective we have decided to construct a facility for the measurement of the Knudsen effusion of fission products from high burn up fuels. The construction, started in 1989, is now finished and the apparatus will be operative in spring 1993.

The apparatus was designed to perform accurate measurements of fission product effusion at constant temperature and under Knudsen conditions suitable for equilibrium vapour pressure evaluation. The experiments are performed either in vacuo or under a low pressure reacting gas atmosphere.

i) Samples and Radiation Protection

The instruments are installed in a standard alpha glove box, which is in turn protected by removable 5 cm thick lead walls (Fig. 1.35a,b). The transfer of the samples from the hot cells is made with a La Calhène transporter. The samples are small carrots of irradiated fuels of a few tens of milligrams, drilled out from a pellet cross section with a microsampling device; they are sealed in a tungsten cell with a conical aperture, which is then transferred to the laboratory and directly mounted in the furnace. The mounting and alignment of the cell are done manually through the gloves, whilst the following measurements are fully automated and are performed with closed lead walls.

ii) Measurements

The equipment consists of two water cooled ultra high vacuum vessels which can house two interchangeable furnaces.

The *first vessel* is of a cylindrical chamber, the top of which communicates with a second chamber through a slit that can be micrometrically aligned with the source of a quadrupole mounted horizontally in the top chamber. The chambers are independently evacuated by two Leybold turbomolecular

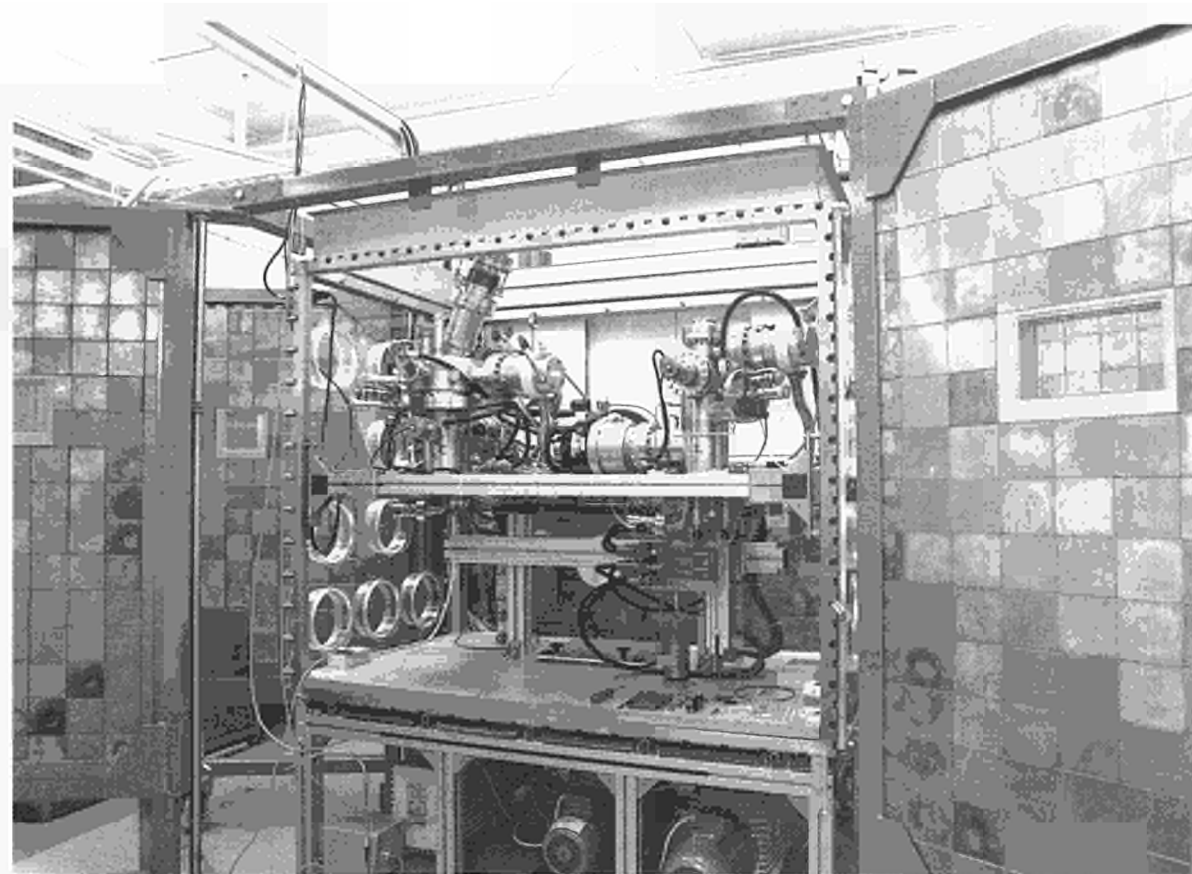


Fig.1.35a Shielded glove box for the investigation of fission product effusion from irradiated fuel.

pumps of 340 and 240 l/s, respectively. This enables the vessel to be operated as a differential pumping system, whereby in the Knudsen cell a pressure up to approximately 1 torr can be maintained, with a vacuum in the quadrupole of better than 10^{-5} torr.

The cell (Fig. 1.36) is a tungsten cylinder with a hole, of 0.3 to 0.8 mm in diameter and is positioned in the centre of an ohmically heated tungsten coil on the top of three supporting pins, which ensure a minimum of conductive heat losses. Furthermore, a small pipeline is connected to the base of the cell, to inject reactive gases during heat treatment. Radiation losses are reduced by a battery of seven tungsten and tantalum screens, enabling a maximum temperature of 3000 K to be reached in the cell, with an axial gradient of less than 1K/cm.

An x-y micrometric slide, operated from the outside, makes it possible to align the cell aperture with the vessel slit and the quadrupole source. This operation is made by means of a Helium-laser beam which, entering through a top window, defines the axial centreline of the vessel. In combination with a TV camera, the

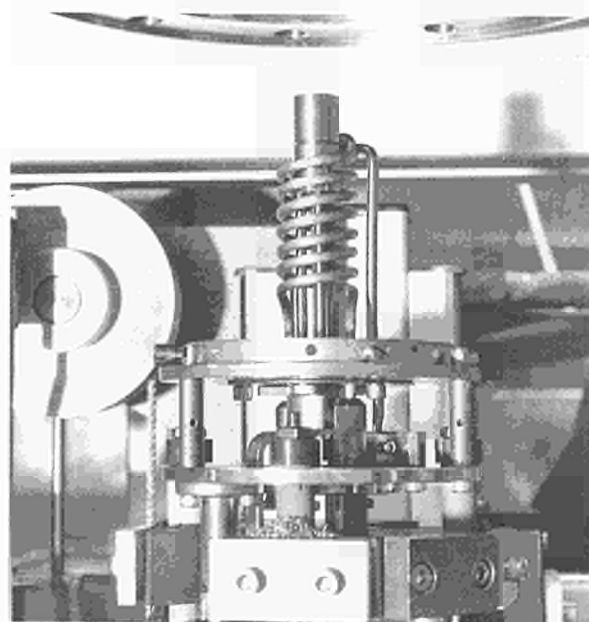


Fig.1.36 View of the tungsten Knudsen cell in its elevated mounting position above the heating coil.

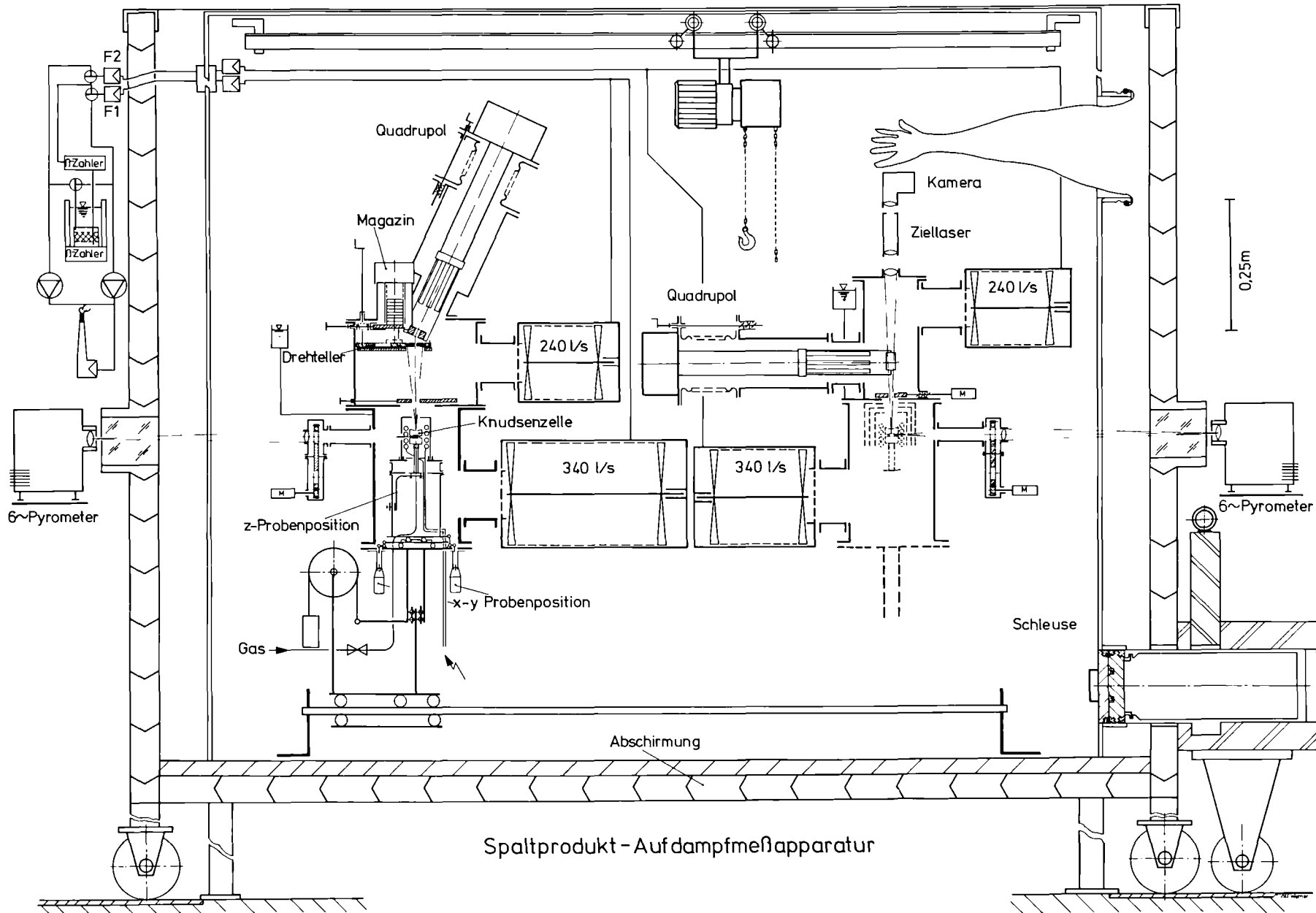


Fig.1.35b Scheme of the equipment for the F.P. effusion experiments.

spot of the beam is then used to align the system.

The temperature is measured by multichannel pyrometry in a "black hole" pierced in the cell; by this method errors due to vapour deposition on the window are avoided. For lower temperatures a thermocouple, fixed on the base of the cell, is available.

The molecular beam from the cell may be stopped by an intermediate shutter, so that the upper chamber is subjected to fission product contamination only during the measurement. The volatile fission products, except the gases, are either trapped on the water cooled parts of the housing or in the filters of the vacuum pipeline.

The Mass Spectrometer (MS) - a Balzers QMA150 with mass detection range from 1 to 500 - is positioned at approximately 50 mm from the cell aperture; this provides a good detection efficiency over a background of less than 1 pA.

Rare gases released from the specimen, after mass spectrometer measurement, are conveyed to a beta/gamma counter to measure their release rate (^{85}Kr) and are finally collected in a liquid nitrogen-cooled dewar, where a second counter measures the integral amount released.

The *second vessel* is designed to perform vaporization experiments under more severe gas reaction conditions. The bottom chamber of the vessel is identical to that of the first one, whilst the upper chamber is larger and is equipped with a mass spectrometer and with a battery of twenty cooled targets onto which the vapours may be collected by condensation and subsequently analyzed. The experiments may be run with both (hole) target deposition and mass spectrometric analysis or, if the gas pressure in the upper chamber exceeds the consented limit for MS operation, with target deposition only.

For heat treatments in the presence of a large reactive gas inlet, a second furnace is available with Ni cells, achieving temperatures up to 1300 K.

The characteristic and performances of the two vessels and furnaces are given in Tab. 1.5.

Emissivity and melting point of thoria

Measurements of the radiative properties of refractory oxides are continuing. The adopted technique is to heat small spheres of material in the laser autoclave with four tetrahedrally oriented Nd-YAG laser beams up to temperatures above the melting point and analyze the emitted thermal radiation with a multiwave pyrometer, enabling the spectral emissivities to be determined. The melting point is deduced by the position of the freezing plateau during cooling.

Differently from urania, which is always very dark in the composition range above and below $\text{O/U}=2$, stoichiometric sintered thoria is white; yet, in our experiments the samples assumed a dark colour when heated above 3500K in an inert or reducing atmosphere (Fig. 1.37), but remained unchanged, even after melting, in an oxygen atmosphere. It is therefore likely that the employed thoria was reduced under inert or reducing conditions below $\text{O/Th}=2$. It is uncertain whether the reduction was possible only in the presence of impurities.

The strong visible light absorption in UO_2 is due to the 5f electrons which occupy an energy band from 1.37 to 1.5 eV, whilst ThO_2 is characterized, in the Th^{4+} state, by a non-occupied 5f state: the absence of low energetic electrons in the valence band is the cause of the high transparency of stoichiometric thoria, and



Fig.1.37 ThO_2 samples after melting in oxidizing and reducing atmosphere, respectively. $\text{ThO}_{2.3}$ is dark compared to the white translucent stoichiometric compound.

	VESSEL I	VESSEL II
<i>Vacuum System</i>	Bottom: 1 Turbo 340 l/s Top: 1 Turbo 240 l/s Rotary Pump: 60 m ³ /h Vacuum limit: 10 ⁻¹¹ torr After 1 day degassing at RT : 10 ⁻⁸ torr With cell at 2500K: 10 ⁻⁸ torr	Idem
<i>Furnace</i>	Tmax = 3000K Knudsen Cell in tungsten Heating Resistance in tungsten Current Max.: 200 A Voltage Max.: 20 A 7 Cylindrical Heat Reflectors	Tmax = 1300K Knudsen Cell in nickel Heating Resistance in tantalum Current Max.: 200 A Voltage Max.: 20 A 3 Cylindrical Heat Reflectors
<i>Temperature Measurement</i>	Tmin = 1000K Multichannel Pyrometer With Wavelengths from 800 to 1800 nm	Tmax = 1300K Chromel Alumel Thermocouple
<i>Inlet Gas</i>	Gas or Steam from 10 ⁻¹⁰ to 10 ⁻¹ torr	Gas or Steam from 10 ⁻¹⁰ to 10 ² torr
<i>Mass Spectrometer</i>	Balzers QMS 150 Mass Range: 1-500 Detection Limit: 10 ⁻¹² A	Idem
<i>Target</i>	none	20-target cartridge of 30mm diameter on revolver.
<i>Radioactive Gas Detection</i>	Two plastic scintillators respectively on the pre-vacuum pipeline and in a LN-cooled Dewar.	idem

Tab.1.5 Characteristics of the shielded Knudsen-cells.

the spectral emissivity, like in all transparent materials, is correlated to the other optical properties and, in particular, to reflectivity, in a more complex way than that predicted by Kirchhoff's law. It is therefore difficult to construct a coherent picture with all the available experimental data, all the more because in the broad temperature range up to the melting point, the variation of the electronic properties of thoria is unknown.

In our experiments the samples, of 99% purity (approximately 1% Si) have been heated in 5 bar oxygen to maintain stoichiometry up to above the melting point, so that even after repeated shots they did not display any change in colour. Pulses have been applied with medium energy input rates and relatively long laser pulse times, in order to reach temperatures just above T_m and to obtain a clear and relatively long freezing plateau. The measured melting temperature of stoichiometric thoria was 3640 ± 20 K.

The emissivity at 960 nm is plotted in Fig. 1.38 as a function of temperature, compared with the lower temperature measurements by Clark and Moore [1] and those of the liquid by Bober [2]. At room temperature in the visible and near infrared spectrum the emittance of thoria is of the order of 0.1 and remains relatively low up to moderately high temperatures, as one can see from the curve in Fig. 1.38.

Between 500 and 1000 nm, our measurements indicate a strong increase in emissivity with temperature, from 0.25 at about 1200 K (Clark & Moore) up to 0.95 at the melting point, values

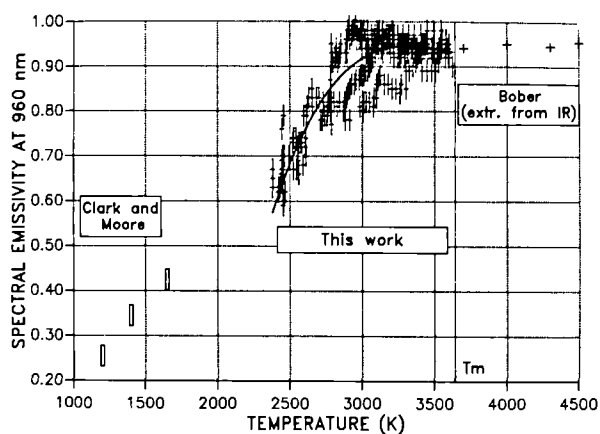


Fig.1.38 Spectral emissivity at 960 nm of ThO_2 as a function of temperature.

to which the liquid measurements of Bober can be matched perfectly. Unfortunately, due to the available detectors of our multiwavelength pyrometer, our measurements could be made only above 2500 K, i.e. 900K higher than the upper limit of the experiments of Clark; this leaves a significant temperature interval uncovered.

The marked increase of the spectral emissivity with temperature in the measured energy range of 1.5-2.4 eV (far above the phonon excitation energies) is unexplained in terms of the (low temperature) electron energy states of ThO_2 , on the basis of which the least energetic transitions should occur from the 2p valence band, through an energy gap of the order of 6eV. These results show that at high temperatures the optical properties of thoria undergo dramatic changes. Furthermore, at temperatures above 2500 K there is no significant difference in emissivity between the samples strongly darkened after heating in a reducing atmosphere, and those heated in oxygen, which at room temperature display a white translucent colour. In this respect, it is interesting to compare the emittance temperature coefficient with the heat capacity of thoria (see e.g. the review by Fink [3]): C_p also displays a sharp increase above 2500K, that can be attributed either to point defect formation, or to activation of electronic contributions (or to both ones). Up to now, in the absence of electrical conductivity measurements in ThO_2 at very high temperatures, one could not support this conjecture; now, the strong increase in emissivity above 2500K seems to provide evidence for substantial electronic excitations at these temperatures.

References

- [1] H.E.Clark, D.G.Moore, J. Res. Nat. Bur. Stand. A70 (1966) 393-415
- [2] M.Bober, H.U.Karow, K.Mueller, High Temp. - High Pressures 12 (1980) 161-168
- [3] J.K.Fink, Int. J. of Thermophys. 3 (1982) 163-200

Modelling Work

Fuel performance code development (TRANSURANUS)

Introduction

TRANSURANUS is a computer program for the thermal and mechanical analysis of fuel rods in nuclear reactors. The code consists of a clearly defined mechanical-mathematical framework into which physical models can easily be incorporated. Besides its flexibility for different fuel rod designs the TRANSURANUS code can deal with very different situations, as given for instance in an experiment under normal, off-normal and accident conditions. The time scale of the problems to be treated may range from milliseconds to years. The code has a comprehensive materials data bank for oxide, mixed oxide, carbide and nitride fuels, Zircaloy and steel claddings and different coolants. During its development great effort was spent on obtaining an extremely flexible tool which is easy to handle, exhibiting very fast running times. The total development effort is approximately 40 man-years. In recent years the interest to use this code has grown and the code is in use in several organisations, both in research and in private industry.

TRANSURANUS statistical version

The relevance of statistical analyses was discussed in the previous report (TUAR 91, p. 53). It was pointed out that the disadvantage of the Monte Carlo technique used in the TRANSURANUS code is the large computer time needed. Therefore, an attempt was made to perform statistical analyses with less expenditure. The method explored was the Numerical Noise Analysis [1], which offers the advantage that the computational costs are approximately identical with those for a deterministic analysis. The fundamental idea underlying this new approach is the following: analogous to standard noise analysis of measured quantities, which can be evaluated in many ways, the most important parameters of the fuel rod model are varied slightly on a Monte-Carlo basis in each time interval. These changes of model parameters result in changes of the different resulting quantities (such as for instance centreline temperatures) which can be regarded as artificially produced

"numerical noise". The known variation of model parameters and the resulting variation of the model results allow an analysis of the sensitivity of the model with respect to its parameters to be performed. Two limitations become apparent:

1. The changes of the parameters during a time interval should influence the unperturbed numerical solution only slightly, roughly within the numerical accuracy. This requirement is easy to meet since modern compilers have a possibility to automatically increase the accuracy. If a certain accuracy is sufficient for the unperturbed solution the perturbed computer model can be calculated with greater accuracy in such a way that perturbations will not influence the solutions in their previous accuracy, but further digits will be available for evaluation of the influence of parameters.

2. The numerical noise analysis can only be applied over several time steps (the evaluation interval) under the condition that the number of time steps is larger than the number of unknown parameters.

The evaluation of the parameters that influence the result is performed by the programme NNOISE which is a special postprocessor of the TRANSURANUS code. The Numerical Noise Analysis was implemented in the TRANSURANUS code and first test runs were performed. Fig. 1.39 gives an example.

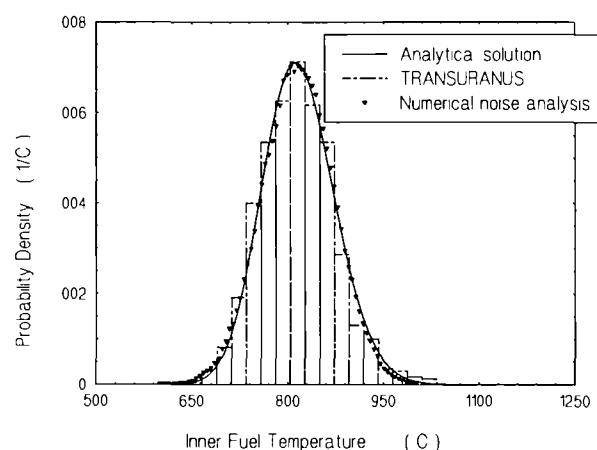


Fig.1.39 Comparison between different probabilistic techniques; in this analysis the linear rating and the thermal conductivity were treated as continuous random variables which are normally distributed.

High burn-up phenomena

Verification work at high burn-up started. Emphasis was given on the radial distribution of the power density which is governed by the Pu build-up in the outer rim of the fuel.

The standard TRANSURANUS model RADAR of Palmer et al. [2] was found to be limited to low burn-up. In addition, the recommended value for the resonance escape probability for PWR conditions, 0.6, is far too low and should be modified to approximately 0.8.

Because of the limitations it was decided to develop a new model which better describes the burn-up equations taking the build-up of the different Pu isotopes into account. The new model is called TUBRNP (TRANSURANUS burn-up model) and is in its verification state. An example is given in Fig. 1.40.

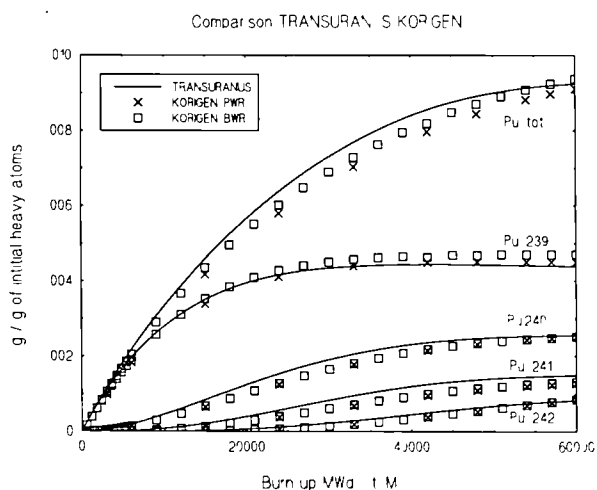


Fig.1.40 Pu build-up as a function of burn-up; compared are results from the new TRANSURANUS model TUBRNP with results from the KORIGEN code.

Maintenance work

The TRANSURANUS code consists of approximately 200 subprograms which have their own test programs. The total number of files to be maintained is more than 2000. In 1992 many subroutines have been carefully checked, revised and documented. The TRANSURANUS handbook is continuously updated.

Training courses and user support

Also in 1992, the TRANSURANUS code was transferred to other parties. Linked with this transfer were trainings courses and an extended user support. The subjects treated in the training courses were basically the same as described in the last annual report (TUAR 91, p. 51).

TRANSURANUS code release

The revised version 1 (modification 1), 1992 was released successfully to interested parties. The installation on different computers did not cause any problems.

References

- [1] K. Lassmann, Numerical Noise Analysis: A New Probabilistic Technique, *Computer Methods in Applied Mechanics and Engineering* **40** (1983) 111-119
- [2] I.D. Palmer, K.W. Hesketh, P.A. Jackson, A. Model for Predicting the Radial Power Profile in a Fuel Pin, *Water Reactor Fuel Elements Performance Computer Modelling*, Applied Science Publishers Ltd, 321-335

Atomistic simulation of Mo and Pd in UO₂

The presence of solid precipitates in high burn up UO₂ is of significance not only for its effects on the mechanical integrity of the fuel but also for its impact on fuel chemistry. Included among the precipitates are metallic phases consisting of Mo, Tc, Ru, Rh and Pd in variable proportions. Of these five metals, only Mo plays a significant part in oxide precipitates. This partitioning of Mo between the metallic and the oxide inventory is a result of the varying oxygen potential of the fuel with burn up and the degree of non-stoichiometry.

Given its high fission yield, it is clear that Mo can have an important role to play in regulating the fuel oxygen potential. This role will be diminished if significant quantities of Mo are effectively locked in phases which inhibit this function. The solubility of Mo in UO₂ then takes on an important aspect. The following summarises an investigation, using computer simulation techniques, of the behaviour of the most noble of the five metals, Pd and the least noble, Mo.

The interaction between two ions of charges q_1 and q_2 is described by a potential of the form

$$V_{12} = q_1 q_2/r + A \exp(-r/\rho) - C/r^6$$

where r is the separation between the ions. This potential consists of the sum of three parts modelling the Coulomb interaction, the short range electron repulsion and the van der Waals attraction, respectively. The calculation of the parameters A , ρ and C is the crucial step in the simulation procedure. The polarizability of the ions is incorporated into the calculation via the shell model formalism [1]. Here each ion is modelled as a charged core and shell, harmonically coupled together.

Employing the pair potentials described above, the perfect UO_2 lattice can be simulated and the change in energy upon introducing an isolated defect or defect cluster calculated. This is the approach adopted by the computer code CASCADE [2].

Using CASCADE, the energy required to place a fission product atom at a selection of possible trap sites in the fuel (the solution energy) was calculated. These trap sites range from simple vacancy and interstitial sites to di- (one O and one U), tri- (two O and one U) and tetra- (two O and two U) vacancy clusters. The effects of stoichiometry enter the calculation through the energy required to form such traps. Where the fission product is charged, an additional charge transfer term derived from tabulated ionization potentials is included. The exact nature of this term is, again, dependent on the fuel stoichiometry.

In Tab. 1.6 the behaviour of the neutral metal atoms is illustrated for the case of Pd. Although

Tab. 1.6 Solution energy of neutral Pd atom at various trap sites in urania. A positive energy indicates that the atom is insoluble at that site. All energies are in eV.

Trap site	UO_{2-x}	UO_2	UO_{2+x}
interstitial	11.00	11.00	11.00
O vacancy	7.97	11.37	14.77
U vacancy	15.94	9.14	2.34
di-vacancy	10.67	7.27	3.87
tri-vacancy	7.62	7.62	7.62
tetra-vacancy	18.40	11.60	4.80

the lowest energy site varies (it is a di- or tri-vacancy site in stoichiometric UO_2 for instance) the solution energies are always positive indicating a persistent insoluble character. The visible result of this insolubility is the presence of the metal precipitates. The calculated situation is also similar for neutral Mo.

In dealing with the charged ions of Mo, we have assumed that the starting state is the neutral metal atom. Calculations show that in UO_{2-x} and UO_2 charged Mo ions are still essentially insoluble. In the case of UO_{2+x} , however (Tab. 1.7) the solution of charged Mo at the uranium vacancy site becomes possible. By comparison with Tab. 1.6, it is possible to conclude that the preferred site for Mo^{n+} may be a di-vacancy. Unfortunately, this possibility could not be further investigated due to computational difficulties.

To summarise, the calculations indicate that oxidised Mo may be soluble in urania, but only

Tab. 1.7 Solution energy of Mo ions in UO_{2+x} . At the uranium vacancy site several of the solution energies are negative indicating that the oxidised ion is soluble. Energies in eV.

Trap site	Mo	Mo ¹⁺	Mo ²⁺	Mo ³⁺	Mo ⁴⁺	Mo ⁵⁺	Mo ⁶⁺
interstitial	20.64	14.27	10.89	9.58	16.54	25.82	28.82
O vacancy	24.40	20.35	19.82	19.99	27.52	36.82	39.47
U vacancy	3.42	-3.09	-7.24	-10.06	-3.67	6.14	10.23
tetra-vacancy	6.55	3.22	2.49	4.25	13.96	25.04	36.46

in the hyper-stoichiometric (oxygen excess) case. In connection with this, it is interesting to note that in high burn up or transient tested fuels, some metallic precipitates may exhibit depletion of Mo at their interfaces with the fuel. This may be evidence for a re-resolution of Mo, from such precipitates, back into the fuel, as burn up progresses.

References

- [1] Dick, B.G., and Overhauser, A.W., Phys. Rev. **112** (1958) 90.
- [2] Leslie, M., Daresbury Laboratory report, DL/SCI/TM31T (1982).

1.2 Safety Aspects of Fuel Operation and Handling

Introduction

The investigation of operational limits for advanced fuels was continued. The irradiation of the NILOC 3 and 4 TRIO-capsules in the HFR Petten, with an axial heterogeneous distribution of (U, Pu)O₂ and UN pellets and pins with mixed nitride fuels at standard and off normal fuel centre temperatures, were completed.

The high burn-up irradiation experiment POMPEI loaded with mixed nitride and technetium was prepared and transported to Petten. Three MN fuel pins, withdrawn from the NIMPHE 1 capsule, were replaced by fresh fuel pins and the capsule NIMPHE 1 bis was prepared for further irradiation in the PHENIX reactor.

The destructive examination of a 19 carbide-pin bundle, irradiated to 7 a/o burn-up in the KNK reactor, was executed by the Kernforschungszentrum Karlsruhe (KfK).

The investigation of the transport of large (>10 µm) aerosol particles in ducts and chimneys in the TRABI test installation was extended to highly turbulent conditions.

Optimisation of Dense Fuels

Introduction

During the reporting period the irradiation of the experiments NILOC 3, with a fuel pin for the heterogeneous fuel concept and two mixed nitride fuel pins, as well as NILOC 4, an irradiation of MN fuel pins at high - off normal fuel centre temperature, was accomplished. A short description of the first results is given below.

9 mixed nitride fuel discs and 3 technetium discs for the high burn-up irradiation experiment POMPEI were prepared, encapsulated and transported to Petten.

In collaboration with the French Commissariat à l'Energie Atomique (CEA) 6 new mixed ni-

tride fuel pins were assembled together with 8 irradiated fuel pins in the capsule NIMPHE 1 bis for further irradiation in the PHENIX reactor.

5 carbide pins which had been irradiated in the KNK II reactor in Karlsruhe were examined destructively in the KfK hot cells, and selected fuel parts were transported to ITU for further examination.

Irradiation experiments

BOL-irradiation experiments NILOC 3 and 4

The BOL (beginning of life) irradiation of NILOC 3 was started on July 2nd and went on until July 27th, it was continued on August 28th and was completed on September 21st, 1992 with 1 a/o burn-up. The experiment with 3 fuel pins with PHENIX pin geometry in a TRIO-capsule performed correctly.

Since the postirradiation examination is not yet finished, only some general remarks will be made here.

The axial gamma scanning performed by ECN Petten revealed a normal axial distribution of fission products. In the heterogeneous fuel pin no sign of centre fuel melting in the U-Pu-oxide fuel stack was observed by thermal and epithermal neutron radiography (performed by JRC Petten) and no restructuring nor severe reaction could be seen at the (U, Pu)O₂ - UN pellet interfaces.

Tab. 2.1 summarises the burn-up calculations for NILOC 3 and 4, based on mean values for the fissile power and the centre fuel temperatures attained.

The irradiation of the NILOC 4 experiment to investigate the operation limits of mixed nitride fuels started on December 17th, 1992 and was finished on January 12th, 1993 as planned at 0.5 a/o burn-up. No anomalies were observed during irradiation. First results are given in Tab. 2.1.

Tab.2.1 Burn-up calculations for NILOC 3 and 4

Expt	Niloc 3			Niloc 4		
cycle	92.06 & 92.07			92.11		
capsule	10	11	12	13	14	15
fuel pin	1	2	3	4	5	6
TRIOX leg	1	3	2	2	3	1
lin. fissile power (W/cm)	522	427	402	924	753	963
diam. (cm) (vol/mean)	0.545	0.545	0.542	0.714	0.716	0.716
area (cm ²)	0.233	0.233	0.231	0.400	0.403	0.403
density (g/cc)	11.61	11.75	10.32	11.63	11.57	11.57
burn-up (MW/t/day)	193.0	155.9	168.6	198.6	161.5	203.4
days irradi.	50.15	50.15	50.15	22.48	22.48	22.48
burn-up (at.% HM)	1.08	0.87	0.94	0.50	0.40	0.51
centre fuel temp. (K)	1910	1740	2470			

Both, NILOC 3 and 4, are expected to be transported to ITU - Karlsruhe mid 1993 for destructive PIE.

High burn-up irradiations POMPEI and NIMPHE 1 and 2

POMPEI (POM PEtten Irradiation) mixed nitrides and Tc

The aim of the POMPEI irradiation experiment is to study the evolution of structure, chemical behaviour, evolution of fission products at a high burn-up, 20 a/o, attained in less than 1 year.

POM (pellets oxides mixtes) capsules have already been used in the BR2 reactor (1967-1972) to produce high burn-up in fuels - MO₂, MC, MN, MCN - in the relative short time of about one year. Unfortunately, the fuels reacted with the capsule material SAP. Therefore the design had to be changed.

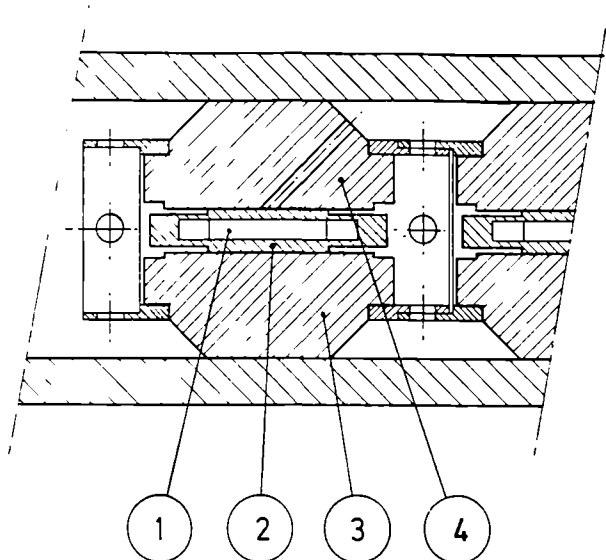
The fuel is in the form of discs ($\varnothing = 9$ mm,

height = 1.5 mm). Each disc is encapsulated and electron beam welded individually in the relevant clad material (steel DIN 1.4970).

During irradiation, the fuel temperature has to be kept < 900 °C, although the specific power is high (about 1000 W/g). In order to evacuate the high heat flux (about 800 W/cm²) the flat faces of the stainless steel boxes must be held in good contact with two massive pieces of a tantalum-zirconium-molybdenum alloy (TZM) (see Fig. 2.1).

This experiment was originally foreseen to be carried out with nitride fuels only, complementary to the joint investigation on mixed nitride fuels of the French Commissariat à l'Energie Atomique (CEA) and our Institute. A first irradiation of technetium specimens was included to obtain information on the irradiation behaviour of this material in view of its transmutation.

The Institute has studied the transmutation of actinides in fast reactors for a number of years. Besides the long-lived actinides, some fission products, notably ⁹⁹Tc (half-life T_{1/2} = 2.1x10⁵ yrs.) and ¹²⁹I (T_{1/2} = 1.57x10⁷ yrs.) contribute to the long term risk of storage of radioactive waste. If these fission products were separated from the waste to be stored and if they were de-



1. FUEL PELLETT (U,Pu)N or Tc-99 alloy
2. CAPSULE SS 1.4970
3. ANVIL TZM
4. ANVIL with T.C. TZM

Fig.2.1 Concept of the POMPEI irradiation experiment.

stroyed by transmutation in a nuclear reactor, the long term hazard could be significantly reduced. Of particular concern is ^{99}Tc because of its large fission yield, its many valence states and its migration behaviour in the geosphere.

^{99}Tc can be transmuted into stable ^{100}Ru by neutron capture. The capture cross section in a thermal neutron flux is about 3 times larger than in a fast flux. Tc metal is isostructural (hexagonal) with Ru and these two metals form solid solutions. Transmutation is thus slowly converting Tc into Ru with a continuous series of alloys being formed with continuing irradiation. At present, no irradiation results exist for Tc or Tc/Ru alloys for extended irradiation periods. In order to gain information on the irradiation behaviour during transmutation of Tc (swelling, possible anisotropy because of the hexagonal structure etc.) in one irradiation campaign, use was made of available irradiation space in an ongoing experiment with (U, Pu)N in HFR in Petten. The compositions selected were pure Tc-metal, an alloy of 50/50 Tc/Ru and an alloy of 20/80 Tc/Ru. These compositions represent the start of the transmutation process, its half completion and the state near completion. Discs of 9 mm \varnothing and 1.5 mm thickness of these alloys were prepared and mounted into the POMPEI irradiation device. A transmutation of about 10 % of the Tc into Ru is expected during the irradiation after which the specimens will be examined to determine their irradiation behav-

iour and to quantify the degree of transmutation achieved. The results will be reported in the next TUAR.

9 MN fuel discs, with an oxygen content varying from 500 ppm to 7000 ppm and prepared by two different fabrication processes (see Tab. 2.2), were individually sealed in small capsules and assembled together with 3 discs of technetium and technetium-ruthenium alloys.

The capsule was transported to Petten on December 10, 1992, where the final assemblage with thermocouples and flux detectors will be performed. Irradiation is scheduled for mid 1993.

Tab.2.2 Data for the POMPEI irradiation experiment

fuel-cladding-irradiation data	
Discs (9 + 3) ¹⁾	(U, Pu)N
Chemical composition	DP, K ²⁾
Fabrication method	22.5
Pu enrichment (Pu/U + Pu)	
Fissile contents of Pu & U	
Pu-239 (w/o)	85
Pu-241 (w/o)	1
U-235 (w/o)	92
Fuel density (% T.D.)	85 ± 1
C (w/o)	0.036 - 0.054
N (w/o)	5.515 - 5.070
(5 categories of pellets in this range)	
O (w/o)	0.046 - 0.749
Pellet diameter (mm)	9
Pellet thickness (mm)	1.5
<u>Cladding</u> ³⁾	
Material	1.4970
Thickness (mm)	0.75
Diameter (mm)	18
Height (mm)	3
Bonding	He
<u>Irradiation Condition</u>	
Specific power (w/g fuel)	980 - 720
Max. power per pellet (w)	1150
Goal burn-up (a/o)	20
Outer cladding temperature	660 - 550
Flux	thermal

1) 3 nitride pellets were replaced by 3 metal discs (Tc, Tc_{0.5}U_{0.5}, Tc_{0.2}Ru_{0.8}).

2) DP = direct pressing, K = conventional (with comminution)

3) Each disc is enclosed in a sealed capsule.

NIMPHE (NIture Mixte dans Phenix à joint HELium)

The NIMPHE irradiation experiments are carried out, with the aim to study and compare the behaviour of mixed nitride fuels with carbide and oxide fuels under fast flux neutron conditions at high burn-up (> 15 a/o), have reached about 7 a/o burn-up.

As both the non-destructive examination on 11 pins of the NIMPHE 1 experiment performed by CEA and the destructive PIE of 1 pin at ITU showed a good fuel behaviour it was decided to continue the irradiation to higher burn-up.

For this purpose 6 new mixed nitride fuel pins, 3 prepared by ITU and 3 by CEA, were assembled in the capsule NIMPHE 1 bis together with 8 mixed nitride fuel pins, already irradiated to 7 a/o, for further irradiation in the PHENIX reactor, scheduled during 1994.

The NIMPHE 2 irradiation experiment (3 mixed nitride and 2 carbide pins with Superphenix geometry), which has only reached 6.2 a/o burn-up, due to delay in the PHENIX irradiation programme, is foreseen to obtain the scheduled burn-up of 7 a/o during 1993. At this point a decision for further irradiation will be taken.

Fast flux irradiation in KNK II

Postirradiation examination of the 19 carbide pin bundle, fabricated for the German Carbide test programme by ITU, was continued. In the hot cells of the Kernforschungszentrum Karlsruhe (KfK) the destructive examination of 5 carbide pins was performed. Selected parts, especially of the carbide fuel prepared by the direct pressing process, have been transported to ITU for further examination.

The non-destructive PIE included dimensional controls, radiography, γ -scanning and eddy-current testing. The destructive examinations covered the determination of the fission gas content and ceramographic and metallographic analyses.

A correlation between released fission gas and oxygen content of the carbide fuel was observed. Fission gas release increased with increasing oxygen content from the carbides with 500, 2000 and 3000 ppm. In contrary the change of the fuel column length, observed by γ -radiography, decreased with increasing oxygen content.

More information will be available when the investigation is finished.

Duct Transport of Big Particles (TRABI)

Introduction

The transport mechanisms of big particles in ventilation exhaust systems with highly turbulent flow conditions were investigated further. The wind channel facility and attempts to prepare non-active test aerosols of high density, in monodisperse particle size fractions of 30 μm (geometric) and greater, were described in TUAR-91 p. 61.

Problem of the test aerosols

As explained in TUAR-91, ($\text{La}_{.49}\text{Bi}_{.50}\text{Eu}_{.01}$) oxide test aerosols were chosen for the first experiments. The SNAM sol-gel process yields apparently spherical and quasi-monodisperse particles in size ranges between 40 and 65 μm . These, however, turned out to be hollow (see Fig. 2.2 of TUAR-91 p. 62), so that their actual density is lower and consequently the aerodynamic diameter higher than expected. Further, they are broken to a great extent by the turbulent transport. During the reporting period, numerous attempts were made to improve the compactness and the mechanical stability by varying the La/Bi ratio and the sintering temperature, but the results were not satisfactory.

The use of a bismuth oxide aerosol (specific density of Bi_2O_3 : 8.5), generated by dispersion of commercial powder has also been considered. This powder can be divided by ultrasonic sieving into 4 fractions (< 30 , 30-40, 40-60 and > 60 μm geometric). It was expected that, in spite of their broader size ranges and their non-spherical shapes, these particles offer the advantage of hardness and compactness. In fact, SEM micrographs of original Bi_2O_3 samples, in all fractions resulting from sieving, show that the particles predominantly consist of compact three-dimensional aggregates of "primary particles" mostly 5 to 10 μm in size. Fig. 2.2 shows a typical example of a 30-40 μm fraction deposited on a Nuclepore filter (porosity 10 μm). Thus the problem of the uncertainty of the aerodynamic

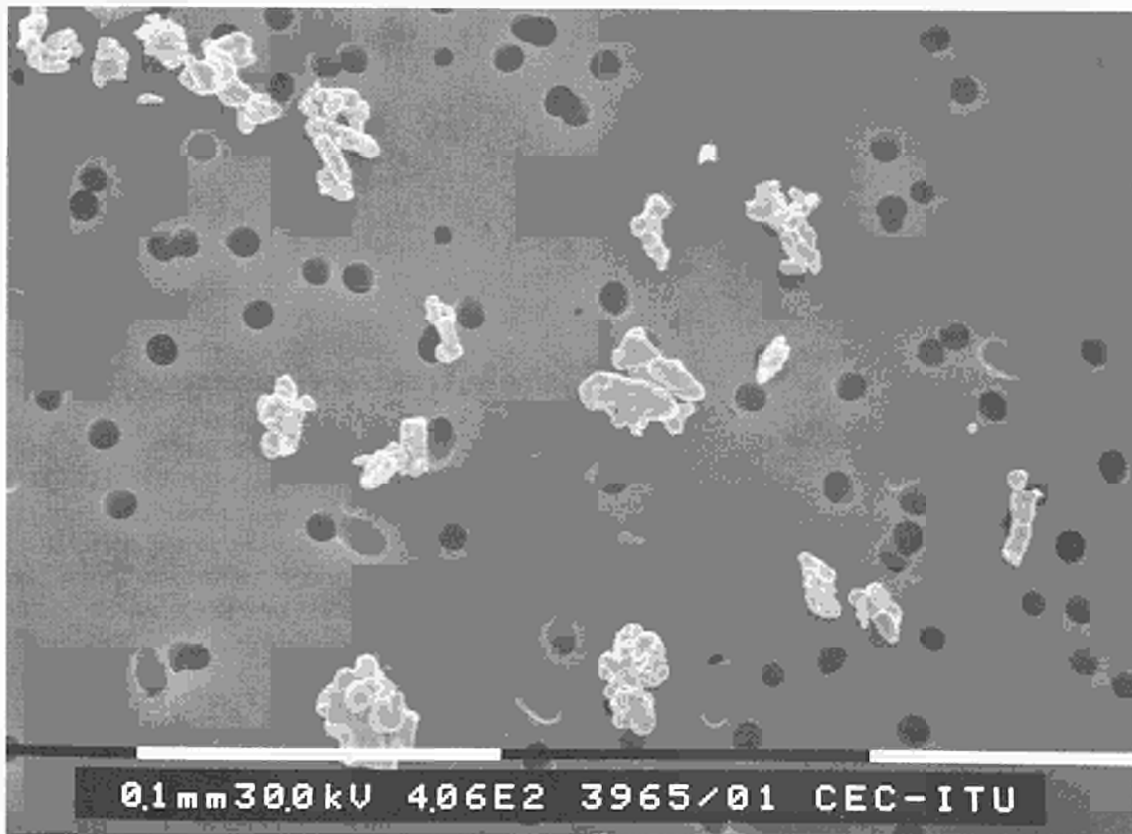


Fig.2.2 Electron micrograph of the Bi_2O_3 test aerosol impacted on a Nuclepore filter (porosity $10\ \mu\text{m}$)

diameter poses itself again, but to a lesser extent than in the case of the La-Bi-Eu oxide, used previously. With the advantage of mechanical stability, it was decided to use this aerosol, especially the fraction $30\text{-}40\ \mu\text{m}$, in the experiments from October 1992 onward.

Aerodynamic data and procedure

In a typical experiment, a turbulent air flow is forced into the channel (of a $0.2 \times 0.1\ \text{m}$ cross section) with a mean axial velocity of $15\ \text{m s}^{-1}$, resulting in a flow Reynolds number of 124000. Knowledge of the boundary conditions near the walls of the test duct is of importance to estimate the probability of deposition, traveling by creeping or bouncing, and reentrainment of the particles. Thus the depth δ of the laminar (or viscous) sub-layer was calculated and found to be about $110\ \mu\text{m}$ (the same order of magnitude as the particles). The roughness of the test duct inner surface, being less than $1.5\ \mu\text{m}$, can be neglected. Inside this sub-layer, the distribution of the fluid velocities is theoretically linear from zero at the wall to $3.5\ \text{m s}^{-1}$ (calculated value) at the distance δ .

For each experiment, a 100 mg sample of bismuth oxide powder of a definite size range is injected in the centre of the aerosol inlet section. Complete dispersion of the sample needs one second, so that the particle number concentration of the transported aerosol may be estimated between 2.0 and 2.8×10^6 particles m^{-3} for particle sizes of 40 and $30\ \mu\text{m}$ respectively. As described in TUAR-91, the particles leaving the test duct are collected on Nuclepore filters located (see Fig. 2.3) either on the axis of the duct

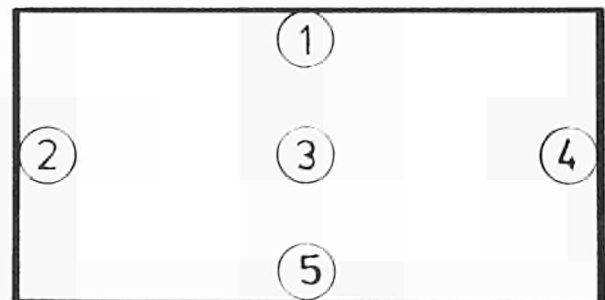


Fig.2.3 Locations of the particle collecting filters in the test channel cross section.

cross section (pos. 3) or against the inner surface of the duct wall (pos. 1,2,4,5). Further it was confirmed in a survey carried out by using SEM and EDAX, that no foreign particles (e.g. dust or filaments from HEPA filters) have been collected on the filters, so that optical microscopy and subsequent morphological quantimetry appear to be the most convenient methods to quantify the particles coming from the test duct.

Results and discussion

For reasons explained above, the experiments with La-Bi-Eu oxide spheres lead to erratic results and will not be further pursued. Using Bi-oxide aerosols, the first visual inspections and quantimetric evaluations of the filter micrographs from the various sampling locations suggest two findings:

- The agglomeration of the particles increases during the transport in a highly turbulent flow. Thus after injection of a 30-40 μm particle size sample, the particle number percent of aggregates larger than 40 μm , which is originally about 0.5, rises to 14, 9 and 6 in the upper (pos. 1), middle (pos. 3) and lower (pos. 5) collecting filters respectively. Agglomerates greater than 80 μm have even been detected (1 % in the upper filter). The mechanisms involved in this event have not yet been clarified, but mutual collisions may be considered, either in the core by turbulent diffusion or inside the viscous sub-layer, where particles deposited onto the wall are subsequently reentrained when the aggregate size becomes larger than the sub-layer depth.
- At a flow velocity of 15 m s^{-1} , gravitational settling practically does not influence the turbulent transport of the particulates up to 60 μm in size. Gravitational settling becomes effective at 9 m s^{-1} (flow Reynolds number: 75000) and below.

In the immediate future, we intend to confirm and explain these observations with measurements on smaller particle size fractions (20-30 μm). On the other hand, the problem of finding a convenient large particle test aerosol has not yet satisfactorily been solved.

1.3 Actinide Determination and Recycling

Working Group Meeting on MA-Containing Targets and Fuels (23 and 24 June 1992)

This was the second Meeting on Targets and Fuels that was setup following the Workshop on Partitioning and Transmutation of Minor Actinides, held in the Institute in October 1989 (TUAR 90, 71). The meeting was attended by 31 participants, including representatives from IAEA, CEC, JRC Ispra, and 6 from the Institute. The following countries were represented: Belgium, France, Germany, Japan, Netherlands, Spain and Switzerland.

The meeting offered a platform for the presentation of progress in the field and to arrange joint studies in developing targets and fuels for the transmutation of long-lived radiotoxic nuclides. Presentations included activities of national programmes, scientific matters in relation to different transmutation strategies and facilities offered by different laboratories for studies on fresh and irradiated targets.

The next meeting for the Working Group has been fixed for 29 and 30 June 1993 at the Institute.

Present status of partitioning and transmutation

Present situation

The public attitude towards any type of anthropogenic waste has led to a ranking of the proposed options according to recent polls in Germany and Japan (Tab. 3.1).

Any process which would generate less waste will - not surprisingly - meet the highest public acceptance. The option to recycle and possibly reuse waste would be the second choice. A partitioning and transmutation scheme of nuclear waste could be classified under this option as far as it applies to the fast type of reactor. Here minor actinides can be reused cost-

Tab.3.1 Public Acceptance and Classification of Processes

1. generating less waste		
2. recycle (and reuse) waste	P & T scheme	EFR/IFR with P & T
3. incinerate waste in special installations	U/Pu recycling	MAB, ADR
4. condition waste for geological disposal	direct storage	

effectively for energy production compared with other schemes relying on special minor actinide burners or accelerator-driven reactors where the energy balance is not so favourable. This latter option therefore should be classified as 'waste incineration using a special installation' (a similar concept is used for household waste) and is preferred to the conditioning of waste for geological disposal. The direct storage concept for spent nuclear fuel could be classified under last and least accepted category.

The situation of the back end of the nuclear fuel cycle in the European Community - though different in each of its states - is typically the application of interim storage of spent nuclear fuel for some decades. During this period sites will be explored for geological repositories which are planned to be in operation after the year 2010. Despite the newly built reprocessing plants in UK and France there remains fuel which cannot be (or is not intended to be) reprocessed during this period.

Hence there is still time to see whether research activities over the next 15 years will reveal that the option of partitioning and transmutation could be added to the present fuel cycle. So far two states, Netherlands and France, are conducting this type of studies, which in the case of France should come to a conclusion by the year 2007. The European Commission supports studies in its indirect and direct action programme in this field.

In the European Institute for Transuranium Elements minor-actinide containing fuels have been developed and irradiated in cooperation with the CEA France in the PHENIX reactor [1,

2]. This activity will be extended to other fuel concepts. Under a commercial agreement, minor actinide fuels based on a Zr-alloy are being studied for CRIEPI [3].

Objectives

In order to develop partitioning and transmutation schemes for radiotoxic nuclides the following questions need to be considered in order to define clearly the scope of the R & D work needed:

- Which nuclides and to what extent should be transmuted?

- Which of the proposed P & T schemes is the most promising one?
- How efficient can the P & T process be?

Nuclides to be transmuted

During a number of meetings [7-12, 35, 36] several candidate radionuclides for transmutations were identified, but not all of the listed radionuclides (Tab. 3.2) pose the same radiological hazard to the public when they eventually migrate out of the geological repository. If one assumes that such a repository will remain intact for several thousand years (as it is the experience for human made structures

Tab. 3.2 Candidate Radionuclides for Transmutation

Yearly uptake of elements [g]	Nuclide from nuclear waste	T ^{1/2} [a]	Annual limits of intake [Bq]	Isotopic abundance after dilution with natural elements [%]
1.1 E5	¹⁴ C 1	5.7 E3 ¹	1.5 E6 ¹	1 E-8 ¹
1.9 E3 ¹	³⁶ Cl 1	3.0 E5 ¹	1.3 E4 ¹	5 E-7 ¹
7.3 E-2 ¹	¹²⁹ I 1	1.6 E7 ¹	3.3 E2 ¹	7 E-2 ¹
3.6 E-3 ¹	¹³⁵ Cs 1	2.0 E6 ¹	5.1 E4 ¹	3 E1 ¹
	⁷⁹ Se 2	6.5 E4 ²		
	⁹³ Zr 2	1.5 E6 ²		
	⁹⁰ Sr 3	28.5 ³		
	¹²¹ Sn 3	50 ³		
	¹²⁶ Sn 3	10.5 ³		
	¹³⁷ Cs 3	30.17 ³		
	⁹⁹ Tc 4	2.1 E5 ⁴		
	²³⁷ Np 4	2.1 E6 ⁴		
	²³⁸ Pu 4	87.7 ⁴		
	²³⁹ Pu 4	2.4 E4 ⁴		
	²⁴⁰ Pu 4	6.5 E3 ⁴		
	²⁴¹ Pu 4	14.4 ⁴		
	²⁴² Pu 4	3.7 E5 ⁴		
	²⁴¹ Am 4	432 ⁴		
	²⁴² Am 4	141 ⁴		
	²⁴³ Am 4	7.3 E3 ⁴		
	²⁴⁵ Cm 4	8.5 E3 ⁴		
	²⁴⁶ Cm 4	4.7 E3 ⁴		
	²⁴⁷ Cm 4	1.5 E7 ⁴		
	²⁴⁸ Cm 4	3.4 E5 ⁴		

1 Nuclides forming monovalent ions with natural isotopic diluent.

2 Nuclides forming no monovalent ions.

3 Nuclides with half-lives below 100a decaying into stable nuclides.

4 Nuclides and parents forming monovalent ions with no natural diluent.

on earth) then nuclides with short half-lives like ^{137}Ce , ^{90}Sr , ^{137}Cs , ^{121}Sn , ^{126}Sn would decay to negligible levels. From the remaining only those which form monovalent ions would be transported back by water to the biosphere: ^{14}C , ^{36}Cl , ^{99}Tc , ^{129}I , ^{135}Cs and ^{237}Np . Since the latter nuclide has three parent nuclides: ^{241}Pu , ^{241}Am , ^{245}Cm all actinides have to be considered as potentially hazardous. During the migration through the geosphere the nuclides will be diluted with natural stable isotopes, which could reduce the specific activity to insignificant levels depending on the geological formation. To support this argument the annual average uptake of the natural element by the "ICRP-man" [4] is compared to the annual limits of uptake for each radionuclide [5]. From this the acceptable isotopic abundance for each of the considered radionuclides in the natural element can be calculated (Tab. 3.2). To what extent this isotope dilution will occur during the release from the repository is presently being investigated [6]. This concerns all nuclides except ^{99}Tc and the actinides. It follows from this that as first priority, the artificial elements should be transmuted: ^{99}Tc , ^{237}Np and its parent nuclides ^{241}Pu , ^{241}Am , ^{245}Cm .

Proposed partitioning and transmutation schemes

There are several nuclear processes under investigation which could transmute a radionuclide into a less toxic one (Fig. 3.1). Photons in the range of 10 MeV produced as Bremsstrahlung from accelerated electrons induce transmutation by (γ, n) -reaction and fission in actinides and can be employed for transmutation purposes [7-9]. The direct spallation of radionuclides by high energetic charged particles has been proposed [10] as well as the use of an inactive spallation source (e.g. Pb-Bi) to produce intense neutron fluxes [11-15]. The latter concepts are not very different from nuclear reactors - discussed below -- except that they can use subcritical arrangements with thermal [11, 13] or fast neutrons [12, 15] driven by accelerators. Included in the installations are reprocessing facilities which separate the remaining nuclides from the transmutation products (if needed). The radionuclides are introduced either continuously as aqueous slurries or solutions [11] or as molten salts [15] to the reactor or are added to fuel assemblies consisting of alloys [12] similar to the MA burner concept being studied by JAERI [16].

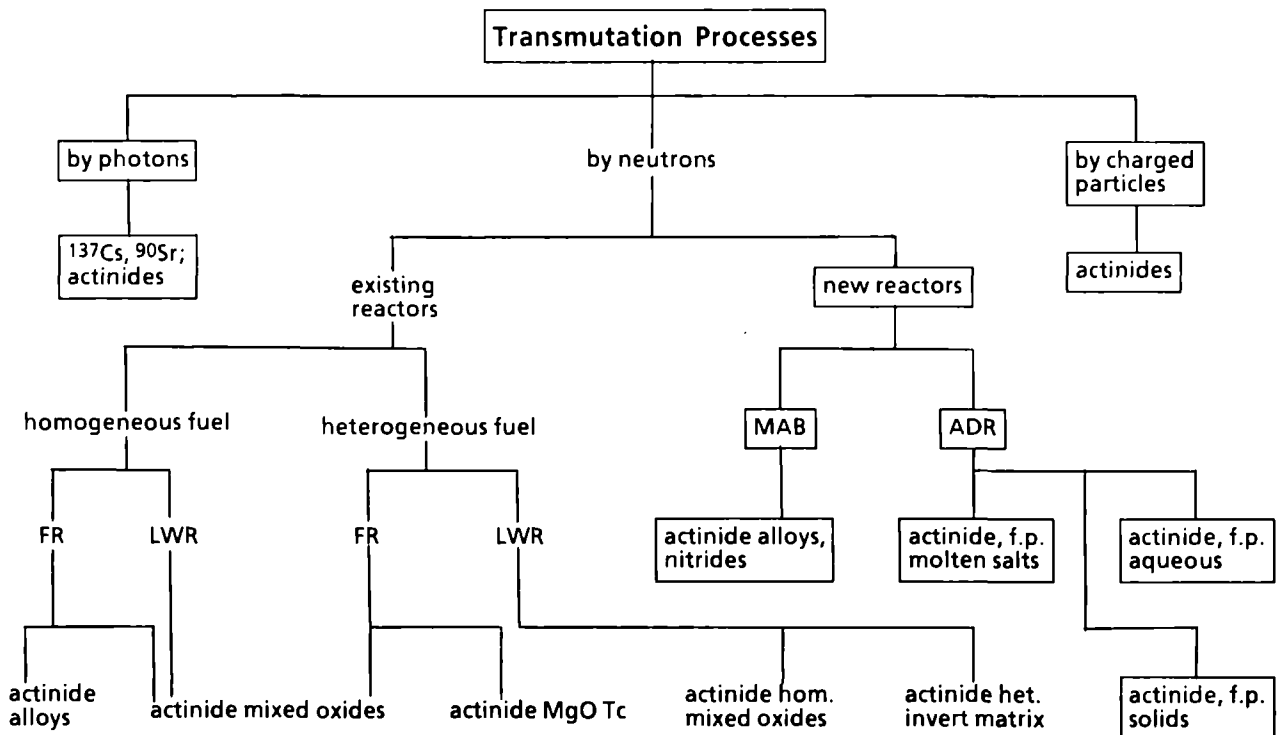


Fig.3.1 Scheme of proposed transmutation processes

Other concepts propose using existing LWR [17] and FR [1, 18, 19] or HWR [13] for transmutation. Not only Pu produced in the LWR fuel cycle but also the minor actinides could fuel fast reactors. Several years ago MA-containing mixed oxide fuels were developed and tested [1] (Tab. 3.3). The MA partitioned

Tab.3.3 Minor-Actinide Containing Fuels Irradiated in Fast Reactors

$(^{241}\text{Am}_{0.5}\text{U}_{0.5})\text{O}_{1.95}$	PFR
$^{241}\text{Am}_2\text{O}_3$	PFR
$^{244}\text{Cm}_2\text{O}_3$	PFR
$(^{241}\text{Am}_6^{244}\text{CmRE}_7)_2\text{O}_3$	PFR
NpO_2	KNKII
$(^{241}\text{Am}_{0.5}\text{U}_{0.5})\text{O}_{1.92}$	KNK II
$(\text{Np}_{0.45}\text{U}_{0.55})\text{O}_{2.00}$	PHENIX
$(\text{Np}_{0.2}^{241}\text{Am}_{0.2}\text{U}_{0.6})\text{O}_{1.95}$	PHENIX
$(\text{U}_{0.73}\text{Pu}_{0.25}\text{Np}_{0.02})\text{O}_{1.98}$	PHENIX
$(\text{U}_{0.73}\text{Pu}_{0.25}\text{Am}_{0.02})\text{O}_{1.98}$	PHENIX

from the spent LWR amount to about 10% of the Pu in that fuel. They can be either homogeneously mixed to the FR MOX fuel or concentrated in a few assemblies of the reactor. Their concentration would be about 2% of the fuel, well below the limit that would influence the Na void coefficient [3]. For higher MA concentrations the geometry of the core needs to be altered [20]. The partitioning of minor actinides (and selected fission products) from the spent fuel is not yet established. R & D work is under way to improve the Am recovery by electro-refining of Zr-based alloys [21], and the coextraction of Am, Cm is achieved by the TRUEX process [22]. Due to the similar chemical behaviour of lanthanides and Am and Cm, the products contain too much of the lanthanides to be directly used as fuels especially in the latter case. Studies are under way to develop new processes to separate the two groups of elements [21, 23].

Efficiency of P & T schemes

If one has agreed on the kind of nuclides to be transmuted, the question arises: to what extent should a P & T scheme reduce the radiotoxicity of a particular nuclide? Earlier answers to this question proposed "hazard reduction factors" of several orders of magnitude [24] which aimed at elimination of nuclides down to the "maximal permissible concentrations". Any realistic approach, however, has to consider losses during the P & T processes, which have still to be buried in a geological repository. How large these losses are, depends on the available technology and therefore one should retreat to the ALARA principle and reduce the radiotoxicity of a certain nuclide as low as reasonably achievable. For the existing fuel cycle - when extended to P & T - one could attain a reduction factor of 100 as shown by the following argument [25]:

Since one expects a reasonable reduction of the radiotoxic nuclides during the life-time of a reactor one can determine the lower limit of a cross-section for the neutron reaction causing the transmutation. The half-life, $T_{1/2}$, of this process is given by the equation

$$T_{1/2} = \frac{\ln 2}{\sigma \Phi} \quad (\sigma \text{ being the absorption cross-section in the neutron flux } \Phi)$$

If one assumes that the time of the minor-actinide-containing fuel in the core of the nuclear reactor is limited by the mechanical stability of its cladding (which is presently about 3 years in a fast reactor) and that during this period at least half of the minor actinides or fission products have to be transmuted, then the cross-section should be

$$\begin{aligned} \sigma &> 1.5 \text{ b} && (5 \cdot 10^{15} \text{ n/sec cm}^2, \text{ fast}), \\ \sigma &> 5 \text{ b} && (5 \cdot 10^{14} \text{ n/sec cm}^2, \text{ thermal}). \end{aligned}$$

The need to recycle the minor actinides due to the limitations of present claddings leads often to a wrong perception. If one expects a reduction of the radiotoxicity to 99.6% (which is equivalent to about 8 refueling cycles and which also corresponds to the life-time of the nuclear power station) then one can easily see that in total only twice the mass of the radionuclides was to be processed.

If N is the mass which is transmuted in a reactor of a refueling cycle length, t, assuming that t is about the same as $T_{1/2}$ (transmutation half-life

of the nuclide), then the decrease of the initial mass N_0 as a function of the number of cycles (n), can be described as:

$$\begin{aligned} N(nt) &= N_0 2^{-nt/T} \\ &= N_0 1/2^n \quad (\text{no feedback due to } \alpha\text{-decay} \\ &\quad \text{considered}) \end{aligned}$$

with

$N(t)$, the mass to be reworked for each cycle.

$\Sigma N(t)$, the total mass to be recycled is only 2 times the initial mass N_0

$$\begin{aligned} \Sigma N(t) &= N_0 (1 + \Sigma 1/2^n) \\ &= 2 N_0. \end{aligned}$$

Under such circumstances one can estimate the reduction factor of the radiotoxicity. The present reprocessing technology and subsequent fuel make-up has losses of minor actinides to the waste streams on the order of 0.3% per cycle. Hence the accumulated losses during all reprocessing stages would be 0.6% which together with the remaining 0.4% of the radionuclide after 8 cycles will sum up to 1% of the original radiotoxicity, i.e. the overall reduction of the initial radiotoxicity will be hundred times. This is still a significant reduction of an environmental hazard if compared to that of other noxes like NO_x , SO_2 (in the exhaust gases of automobiles and fossil fuel power stations) which are reduced on the average by only a factor of 3.

Fuel design constraints

The present discussion on the future of nuclear energy generation can be described by two extreme scenarios (Tab. 3.4).

Under the first scenario one assumes that nuclear energy production is phased out and that it is successfully replaced by another technology. During this phase the fissile material used for military purposes has to be treated as well. If under such a scenario

Tab.3.4 Scenarios

1. Phasing-out of nuclear energy production	Transmutation by LWR and/or ADR
2. Breeding of Pu for nuclear energy production	Transmutation by FRB

transmutation shall be employed it certainly would use the LWRs because funding to develop and deploy other reactor types would meet strong public resistance. However LWRs have limited capabilities for the transmutation of actinides and hardly any for fission products. Therefore accelerator-driven reactors (ADR) might be used as well. Some of them would have the ability to destroy the actinides even more rapidly than LWRs [26].

In the other scenario the generation of nuclear energy continues and because of limited low cost U resources, sooner or later breeding of Pu is needed to fuel future reactors. Since this breeding requires fast reactors, they could be used with advantage for transmutation purposes, too.

In this case the situation for the EC is quantified in Fig. 3.2, with assumed losses of 0.2% of Pu to the geological repository [27].

To develop a fuel for the purpose of transmutation, certain constraints have to be observed (Tab. 3.5). Because of reactor safety criteria, the concentration of minor actinides in any fuel matrix has to be limited for several reasons. For instance during irradiation a linear power increase will occur because of the build-up of fissile material with high fission neutron cross-sections. If the present cladding type is employed, its interaction with the new fuel has to be studied. In the case of cladding rupture, the

Tab.3.5 Constraints for Fuel Design

Reactor safety	linear power, fci, coolant compatibility, etc.
Fuel make-up	cost, occupational dose, etc.
Reprocessing	cost, losses, toxic waste, etc.
Nuclear materials Safeguards	diversion resistance, etc.

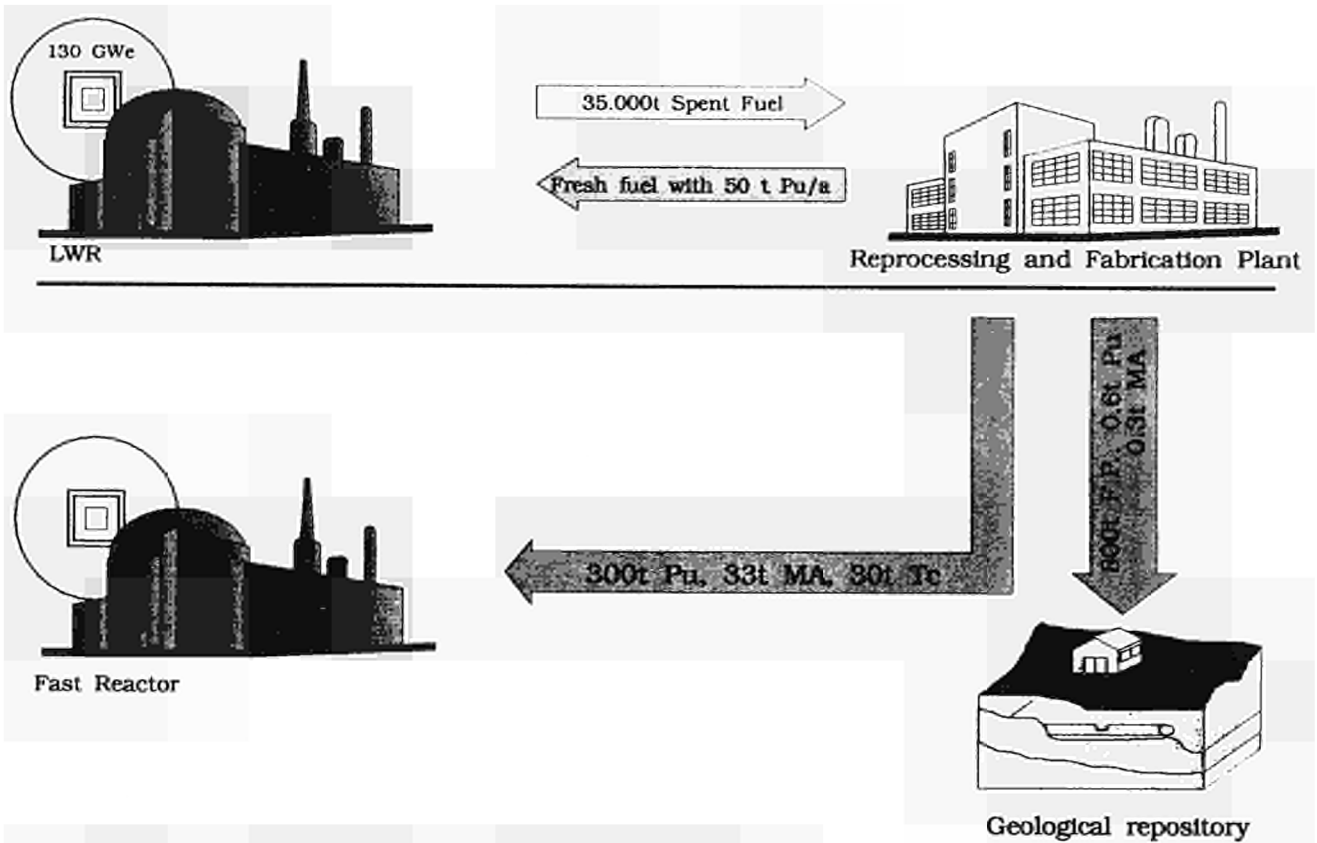


Fig.3.2 MA + F.P. Transmutation by transition from LWR to FR

minor actinide content of the fuel may affect the compatibility of fuel and coolant. In order to optimise the fuel fabrication, one has to consider the advantages and the disadvantages of the homogeneous and heterogeneous minor-actinide fuel concepts, e.g. to minimise the occupational dose. Already at an early stage, the impact of a new fuel type on the existing reprocessing schemes has to be assessed. In the past there have been several examples where fuel was developed and even used but which later turned out to be too difficult to be reprocessed (thorium-oxide fuel, carbide fuel, etc.). Since the success of any partitioning and transmutation scheme is strongly bound to the reprocessing losses, one has to pay the greatest attention to these problems. Finally the aspect of nuclear material safeguards has to be evaluated to see whether the new fuel concept would increase the diversion risk.

MA's together with Pu can be recycled in a self-generated mode in existing LWR and FR¹. The differences between the two reactor types are: The LWR in an equilibrium fuel cycle contains more than 10 times more transplutonium nuclides compared with a fast reactor fuel in equilibrium [28-31]. The neutron flux of present

LWR is too low to transmute ⁹⁹Tc and ¹²⁹I efficiently. This is not the case for the FR where in the blanket region a thermalised neutron flux of between $0.5 - 1 \cdot 10^{15} \text{n/sec cm}^2$ can be produced [32]. Inherent with the transmutation of MA is the build-up of ²³⁸Pu which further denatures Pu in the sense of nuclear material safeguards especially in case of FR with its low ²⁴⁰Pu content. However ²³⁸Pu in larger amounts would be a nuisance to the fabricator of mixed oxide fuels - although not of metallic fuel for the IFR where already remote fuel fabrication is foreseen. The latter concept eliminates the need of fuel transportation, which in case of oxide FR - and even more the LWR - fuels will be difficult, mainly due to the higher neutron radiation of ²⁴⁴Cm in fresh and of ²⁴²Cm, ²⁵²Cf in spent fuels.

MA actinides are a fuel for fast reactors, so that the additional energy generation and breeding rate would compensate for the extra costs in fuel make-up [1]. Since the energy generating costs of a LWR are considerably lower than that of a FR this argument is presently not applicable. The development of a P & T scheme (according to the present R & D programmes) will take more than 15 years: until then the uranium

prices will probably favour the LWR over the FR.

The FR with on-site reprocessing seems to be a viable concept for transmutation and presently the only existing reactor that can reduce its waste efficiently by recycling. It should not be forgotten, however, that an alternative fuel cycle based on the thorium molten salt reactor [33] could prove to be even more advantageous, since the MA production there is considerably lower and MA together with fission products can be transmuted as well. At present the technical feasibility of this type of reactor (despite extensive efforts at ORNL in the past) has not yet been proven.

Outlook

If nuclear energy generation is to be used by future generations then the limited supply of ^{235}U will renew the interest in the fast breeder concept. Regardless of what future fast reactors will look like, they will have the inherent potential to burn most radiotoxic waste. Therefore the development of the minor-actinide-containing fuel cycle for fast reactors is an essential task in keeping the nuclear energy option open.

Apart from basic research of more effective partitioning processes the basic physico-chemical properties of MA-containing fuels have to be studied and their irradiation behaviour tested.

For the IFR concept the electro-refining process has to be extended to extract all minor actinides from the spent fuel with sufficient decontamination from lanthanides and to isolate technetium which accumulates with other elements in the cadmium cathode. Investigations in these directions are under way, including the development of an appropriate fuel [21, 23]. This fuel is being developed in a joint effort between this Institute and CRIEPI and will be tested in a joint irradiation experiment with CEA in PHENIX.

For the oxide-fueled fast reactor, reprocessing covering minor actinides and technetium has not yet been developed to a comparable level as for the IFR. Nevertheless promising extraction schemes are under test which would not only extract these nuclides from the LWR spent fuel but also later could be used to reprocess the FR fuel [23, 34]. Minor-actinide-containing fuels have been tested in the PHENIX reactor (Tab. 3.3) [2]. The post-irradiation examinations revealed no unexpected behaviour under irradiation. A follow-up irradiation experiment

is presently under preparation which should lead to higher burn-ups. These fuels are being developed jointly by the CEA, France and the European Institute for Transuranium Elements and have been or will be irradiated in PHENIX.

References

- [1] KOCH, L., "Minor Actinide Transmutation - A Waste Management Option", *J. Less-Common Met.*, **122** (1986) 371-382
- [2] PRUNIER, C., et. al., "Transmutation of Minor Actinides: Behaviour under Irradiation of Americium and Neptunium Based Fuels", Proceedings of the 'Int. Conf. on Fast Reactors and Related Fuel Cycles "FR 91"', Kyoto, October 1991
- [3] INOUE, T., et. al., "Characterization of Fuel Alloys with Minor Actinides", ANS Winter Meeting, San Francisco, November 1991
- [4] REFERENCE MAN, ICRP 23 (1975)
- [5] Strahlenschutzverordnung, BRD Bundesgesetzblatt 1, (1977) 2905
- [6] Proceedings of the '1st Technical Meeting on the Nuclear Transmutation of Actinides', JRC Ispra, 16-18 March 1977, EUR 5897 (1978)
- [7] KASE, T., et. al., Specialists' Meeting on 'Accelerator-Driven Transmutation Technology for Radwaste and Other Applications', Stockholm, 1991
- [8] KHLEBNIKOV, S.V., et. al., Proceedings of the Workshop on 'Nuclear Transmutation of Long-lived Nuclear Power Radiowastes', Institute Nuclear Power Engineering Obninsk and Institute of Theor. and Exp. Physics Moscow, Obninsk, July 1991
- [9] TAKASHITA, H., et. al., OECD/NEA Specialists' Meeting on 'Accelerator-Based Transmutation', Würenlingen, March 1992
- [10] WENGER, H.U., et. al., *ibid.*
- [11] IRELAND, I., *ibid.*
- [12] TAKAHASHI, H., *ibid.*
- [13] KAZASITSKY, V.D., *ibid.*
- [14] TAKADA, H., et. al., Specialists' Meeting on 'Accelerator-Driven Transmutation Technology for Radwaste and Other Applications', Stockholm 1991
- [15] KAWATA, T., et. al., Symposium on 'Separations Technology and Transmutation Systems', Nat. Acad. of Sciences, Washington, January 1992
- [16] MUKAIYAMA, T., et. al., Proceedings of the 'Int. Conf. on Fast Reactors and Related Fuel Cycles "FR 91"', Kyoto, October 1991
- [17] LEFEVRE, J., Symposium on 'Separations Technology and Transmutation Systems', Nat. Acad. of Sciences, Washington, January 1992
- [18] CHANG, Y.I., *ibid.*
- [19] BALZ, W., et. al., Proceedings of the 'Int. Fast Reactor Safety Meeting', Snowbird, Utah, August 1990, Vol. 1 (1990) 153

- [20] THOMPSON, M.L., Symposium on 'Separations Technology and Transmutation Systems', Nat. Acad. of Sciences, Washington, January 1992
- [21] SAKATA, M., et. al., Proceedings of the 'Int. Conf. on Fast Reactors and Related Fuel Cycles "FR 91"', Kyoto, October 1991
- [22] HORWITZ, P., Symposium on 'Separations Technology and Transmutation Systems', Nat. Acad. of Sciences, Washington, January 1992
- [23] CECILLE, L., JAERI/OECD Meeting on 'Partitioning and Transmutation', Mito, Japan, November 1990
- [24] CLAIBORNE, H.C., "Nuclear Induced Transmutation of High-Level Radioactive Waste", ORNL/TM-3964 (1972)
- [25] KOCH, L., Proceedings of the 2nd Working Group Meeting on 'Targets and Fuels', CEC, JRC Karlsruhe, 23-24 June 1992 (to be published)
- [26] KOCH, L., "Status of Transmutation", IAEA Specialists' Meeting on 'Use of FBRs for Actinide Transmutation', Obninsk, September 1992
- [27] KOCH, L., "Transuranium Element Fuel Cycle in LWR - FR Symbiosis", Proceedings of the '5th Int. Conf. on Emerging Nuclear Energy Systems', ICENES, Karlsruhe, June 1989
- [28] KOCH, L., et. al., Proceedings of the '4. Int. Transplutonium Element Symposium', Baden-Baden (1975) 459-469
- [29] OLIVA, G., Proceedings of the '2nd Technical Meeting on the Nuclear Transmutation of Actinides', JRC Ispra, 21-24 April 1980, EUR 6929 (1980) 17
- [30] GUARDINI, S., SMITH, B.G.R., *ibid.*, p. 43
- [31] SCHMIDT, E., *ibid.*, p. 471
- [32] SALVATORES, M., et. al., Proceedings of the IAEA Advisory Group Meeting on 'Partitioning and Transmutation of Actinides and Selected Fission Products from HLW', Vienna, October 1991
- [33] FURNKAWA, K., Proceedings of the IAEA Advisory Group Meeting on 'Partitioning and Transmutation of Actinides and Selected Fission Products from HLW', Vienna, October 1991
- [34] MUSIKAS, C., et. al., "Results and Prospects for some Extractants in the Minor Actinide Partitioning", Proceedings of the Workshop on 'Partitioning and Transmutation of Minor Actinides', CEC, JRC Karlsruhe, October 1989
- [35] IAEA Specialists Meeting on 'Use of Fast Breeder Reactors for Actinide Transmutation', Obninsk, Russian Federation, 22-24 September 1992
- [36] Second General Meeting of the OECD/NEA, Chicago, USA, 11-13 November 1992

Irradiation in KNK II-MTE1 (Experiment KNK II a)

An irradiation experiment was launched in 1982 involving a series of capsules with actinides in milligram quantities and a selection of fission products in microgram quantities (TUSR 33, 62). Multifoil dosimeters were included for monitoring the neutron spectrum. The purpose of the irradiation experiment was to determine the neutron cross-sections of the various nuclides present, the local neutron energy spectrum and the integrated neutron flux. The samples, following irradiation and cooling, have now been delivered to the Institute and chemical analyses will start next year.

Status of the SUPERFACT Experiment

Four types of minor actinide containing oxide fuels have been irradiated in the Phenix reactor (see Tab. 3.3). Samples from irradiated pins have been analysed at the Institute.

Chemical analyses of dissolved samples

Isotopic composition studies were carried out on samples of approximately 1 g cut halfway along the active length of the fuel pins. Three of the samples, originating from the fuels containing 2% Np, 45% Np and 2% Am respectively, have been analysed. The concentrations of uranium, plutonium, americium and curium isotopes, and ^{148}Nd were measured by isotope dilution mass-spectrometry. ^{237}Np was measured by ICP-MS. Neodymium was used as a burnup monitor. The accuracies attained for these measurements and their relative standard deviations are shown in Tab. 3.6.

The burnup each fuel achieved during irradiation in PHENIX was calculated on the basis of the number of heavy metal atoms and ^{148}Nd measured for each sample. An effective fission yield was calculated in each case following the prediction from KORIGEN [1] of the contribution to total burnup from each of the fissile isotopes present. Cumulative fission yields for the fissile nuclides corresponding to a fast reactor were used [2]. The fission and capture cross-sections were adjusted for the

Tab.3.6 Techniques used in chemical analyses and their accuracies

	Technique used	Accuracy %
UPu isotope vectors	IDMS	< 0.7
AmCm isotope vectors	IDMS	1
Np-237	ICP-MS	5
Nd-148	ICP-MS	1
BU determination based	on Nd-148	1.5

calculations to PHENIX. The relative contributions to the total burnup, the effective fission yields and the burnup calculated from the ¹⁴⁸Nd concentration are shown in Tab. 3.7.

The experimental concentrations of actinides quoted as %IMA (% Initial Metal Atoms), are shown in Tab. 3.8. They have been calculated according to the equation:

$$\%IMA(X) = \frac{\text{No. of atoms X after irradiation}}{\Sigma X + \text{No. of atoms } ^{148}\text{Nd} / \text{Eff. fission yield}} \times 100$$

X : a nuclide e.g. ²³⁷Np

ΣX : total number of heavy atoms

The corresponding %IMA values obtained theoretically from the KORIGEN calculations are included in Tab. 3.8 for comparison. An agreement within 10% is generally observed between the experimental and theoretical predictions. Considering the transmutation of ²³⁷Np and ²⁴¹Am, a 30% and 10% reduction in their inventories is observed, following irradiation for 380 days in PHENIX, in fuels SF13 and SF15, and SF16 respectively. In order to assess the transmutation rate of these nuclides one has to differentiate in the neptunium and americium inventories the amounts that were formed during irradiation. Neutronic calculations for evaluation of data banks and transmutation studies are in progress under a separate study and will be reported in the next issue of TUAR.

Radiation dose levels of MA-containing fuels

The inclusion of MA in a fuel (SUPERFACT fuels) for subsequent transmutation, will increase the radiation dose levels of the fuel. Knowledge of these dose levels could allow cost penalties associated with the handling of these materials to be estimated. An indication of radiation dose levels encountered in the fabrication and discharge of MA-containing fuels, irradiated in a fast reactor (FR), is addressed here.

Tab.3.7 Contribution (%) to total burnup of the different fissile nuclides

	SF13 2% Np	SF15 45% Np	SF16 2% Am
U-235	2.5	1.2	2.4
238	7.8	8.6	8.2
Pu-238	1.2	19	1
239	67.8	11.3	67.6
240	6.8	—	6.7
241	12.5	—	12.34
Np-237	1.37	60	—
Am-241	—	—	1.7
Eff. fission yield for Nd-148	1.69%	1.77%	1.68%
Burnup (at%)	6.4	4.5	6.5

Tab.3.8 Experimental and theoretical %IMA values

	SF13 2% Np		SF15 45% Np		SF16 2% Am	
	%IMA (th)	%IMA (exp)	%IMA (th)	%IMA (exp)	%IMA (th)	%IMA (exp)
U-234	0.025	0.028	0.27	0.266	0.027	0.022
235	0.33	0.356	0.12	0.124	0.33	0.362
236	0.046	0.042	0.026	0.023	0.047	0.041
238	68.8	69.27	51.7	51.34	69.2	69.47
Np-237	1.12	1.325	32.6	32.77	0.034	0.033
Pu-238	0.54	0.68	7.6	8.4	0.53	0.57
239	13.3	12.82	2.9	2.45	12.95	12.75
240	5.73	6.03	0.11	0.1	5.6	5.93
241	1.4	1.34	0.022	0.004	1.37	1.36
242	1.12	1.1			1.14	1.15
Am-241	0.57	0.61	–	–	1.8	1.83
242m	0.006	0.012			0.045	0.058
243	0.07	0.064			0.075	0.067
Cm-242	–	–	–	–	0.0004	0.004
243					0.006	0.011
244	–	–	–	–	0.007	0.006
245						

Theoretical

Calculations were performed to predict the neutron and gamma outputs from the four SF fuels and a standard FR fuel (25% Pu, 62 GWd/tU) at charge, discharge, and 1y and 5y cooling times. The MOX fuel contained plutonium of the same isotopic composition as the SF fuels. The computer code KORIGEN was used for the calculations, with the fission and capture cross-sections adjusted to the conditions of the PHENIX reactor. The variation of the neutron and gamma outputs for the spent fuels are shown in Figs. 3.3 and 3.4.

The two americium fuels have the highest neutron and gamma outputs, in comparison to the standard FR-UPu fuel, at discharge, despite having the lower burnup. The fuel containing 2% ^{237}Np has a neutron output of the same order of magnitude, although still higher, as the standard fuel. The 45% ^{237}Np fuel presents the lowest neutron output due to lack of plutonium at charge and consequently lower production of curium isotopes. In general, ^{238}Pu , ^{242}Cm and ^{244}Cm dominate the neutron emission with the curium isotopes being the main radiation sources of the americium fuels.

Experimental

Measurements during fabrication

The surface dose rate of the SF fuel pins containing plutonium is highly dependent on the isotopic composition. The dose rate of freshly purified plutonium from a PWR stems from neutron emission: (α , n) reactions caused by the decay of ^{238}Pu and spontaneous fission of ^{240}Pu . The dose rate from plutonium is dominated, with increasing decay time, by the gamma dose rate due to build-up of ^{237}Np , and particularly, ^{241}Am from the decay of ^{241}Pu .

The gamma dose rate of the four SF fuel pins were measured during fabrication (TUAR 86, 82). The measurements were made using a portable ionisation chamber type 'Babyline' and thermoluminescence dosimeters in contact.

Measurements after irradiation

A qualitative analysis of the fission-product content of the irradiated mixed actinide oxides was performed by gamma-spectroscopy. The

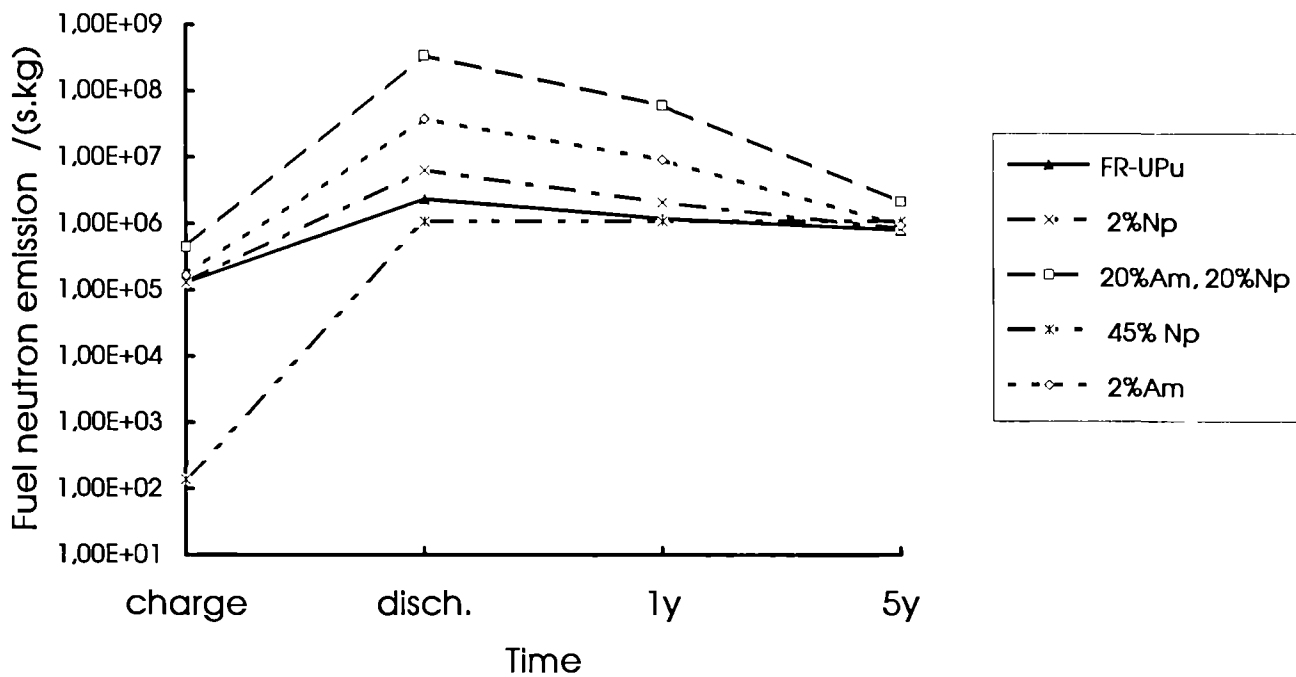


Fig.3.3 Neutron emission as a function of irradiation and cooling times

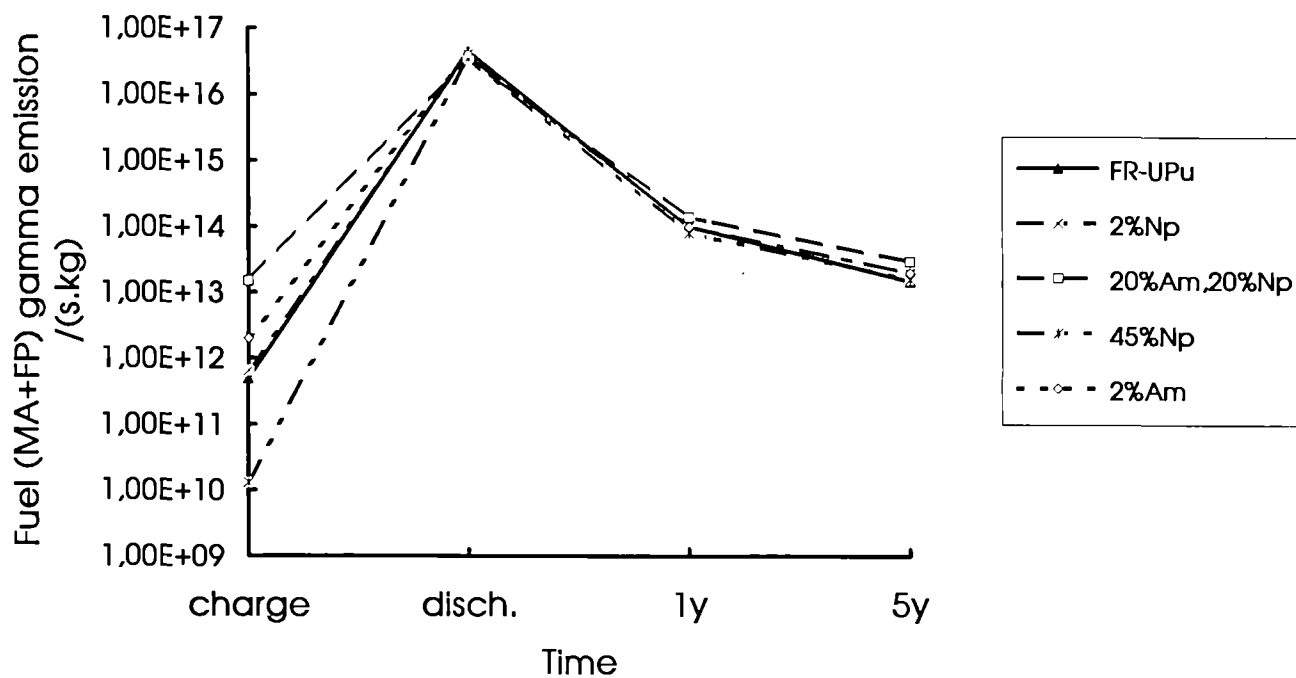


Fig.3.4 Gamma emission as a function of irradiation and cooling times

gross gamma and neutron dose rates after irradiation (cooling time 57 months), were measured inside a β - γ hot cell at the Institute. A compact array of neutron detectors and a Geiger-Müller (GM) counter embedded in a polyethylene moderator, were used for passive neutron and gamma interrogation of the fuel (TUAR 91, 121). The gamma dose rate was measured directly, with a precision of 5%, using the GM counter appropriately calibrated. The measurements were made with an absorber of 0.035 m lead between the fuel and the detector which were 0.06 m apart. The neutron dose rate was obtained from the measurement of the neutron emission of the fuel by spontaneous fission and (a,n) reactions. The neutron emission was then compared to the dose rate at 1m from a ^{252}Cf neutron source of known activity.

Results and Discussion

The addition of ^{241}Am increases the gamma dose of the fresh fuel and the neutron dose of the spent fuel. The radiation dose rates of MA-containing fuels in comparison to the standard FR fuel, can be assessed by comparing the source term nuclides which contribute to the gamma and neutron dose. The KORIGEN gamma and neutron outputs for fresh and spent fuels (5 years cooling time), normalised to the standard UPu FR fuel with the same irradiation exposure, are shown in Tab. 3.9.

In order to check the reliability of the KORIGEN predictions, the experimental and theoretical concentrations for the source term nuclides, i.e. ^{238}Pu , ^{240}Pu , ^{241}Am , ^{242}Cm , ^{244}Cm and fission products, have been compared (Tabs. 3.8, 3.10). The agreement is within 25% for the actinides and 50% for the fission products, sufficient for dose rate calculations but unsuitable for neutron physics studies. The

Tab.3.9 Calculated neutron and gamma outputs from the SF fuels normalised to a standard FR-UPu fuel (spent fuel cooling time 5 years)

Fuel	Neutrons		Gamma	
	fresh fuel	spent fuel	fresh fuel	spent fuel
SF13	1	1.07	1.3	1.4
SF14	3.4	2.7	30	2
SF15	1.10E-03	1.4	0.03	1.07
SF16	1.3	1.2	4	1.4

limitations of KORIGEN with respect to its fission yield and cross-section libraries should be considered when irradiation calculations are performed. The neutronic calculations will be followed up in a separate study.

The gamma dose rates during fabrication are given in Tab. 3.11. The neutron and gamma dose rates obtained experimentally for the SF fuel pins after discharge and 57 months cooling are shown in Tab. 3.12. The total radiation dose is determined by the gamma dose rate.

Tab.3.12 Radiation dose rates of spent fuel (cooling time 5 years)

Fuel	neutron dose rate nSv / (s. kg)	gamma dose rate mGy / (s. kg)
SF13	2.6	n.m.
SF14	5.5	0.5
SF15	3.1	0.4
SF16	2.6	1.4

n.m.: not measured

In conclusion, one can state that a cost penalty due to high radiation doses will be observed mainly during fuel fabrication whereas the

Tab.3.10 Experimental to theoretical FP concentrations (normalised to ^{137}Cs)

	SF13	SF14	SF15	SF16
Sb-125	0.7	1.02	0.6	0.7
Cs-134	1.8	1.6	2.1	2
Ce-144	1.6	—	1.4	1.7
Eu-154	2.1	2.4	1.6	2.1
Eu-155	1.4	—	0.4	0.4

Tab.3.11 Gamma dose rates ($mGy \cdot s^{-1}$) measured on fuel pins and pellets without shielding during fabrication

	SF13	SF14	SF15	SF16
Pellet (1.8E-3 kg):				
Contact	0.02	0.83	0.03	0.08
Fuel pin:				
Contact	0.12	5	0.4	0.5
0.5 m distance	5.00E-03	0.25	0.01	0.03

gamma radiation dose for the spent fuel increases by less than a factor of three even in the case of the heterogeneous (Am, Np) fuel. Consequently, additional means in order to reduce the occupational hazard dose from MA-containing fuels would be required only during fabrication.

References

- [1]U. Fischer and H.W. Wiese, 'Verbesserte konsistente Berechnung des nuclearen Inventars abgebrannter DWR-Brennstoffe auf der Basis von Zell-Abbrand-Verfahren mit KORIGEN', Kernforschungszentrum Karlsruhe, KfK-3014 (1983)
- [2]L. Koch, Radiochim. Acta 29 (1981) 61

EPMA Results for Americium in the Superfact Fuel SF16

In TUAR 91, preliminary EPMA results of the radial distribution of U, Pu and Am in the Superfact fuel SF16 were presented. The concentration of Am in the fuel was reported to be 1.9 wt%. Since the fuel initially contained just 2 wt% Am, this means that during the irradiation almost as much Am was produced by neutron capture as was burnt. However, gamma spectroscopy results given in the same report indicate that the concentration of Am in the SF16 fuel was much lower than the 1.9 wt% obtained by EPMA. According to the data in table 3.7 of TUAR-91 Am constituted 1.7% of the heavy metals in the fuel. Taking the fuel burnup to be 6.4 at%, this translates to a mass concentration of 1.4 wt%.

The source of the error in the EPMA results has recently been identified. It was found that the mass absorption coefficient (MAC) of the Am M_b X-ray line in U was wrongly calculated in the correction program. A value of $1172 \text{ cm}^2\text{g}^{-1}$ is obtained which is probably about a factor of two too high. This can be seen from the MACs for the Am M_b line in Np and Pu which in contrast are calculated to be 531 and $527 \text{ cm}^2\text{g}^{-1}$.

In the EPMA correction procedure currently in use at the Institute the MACs are calculated with the algorithms proposed by Heinrich [1]. It is acknowledged by Heinrich that between the M_{iv} and M_v absorption edges the data provide by these algorithms are unsafe. The energy of the Am M_b line is 3.63 keV and the energy of the M_{iv} absorption edge in U is 3.72 keV. Consequently, contrary to what is calculated no sharp increase in the level of absorption of the Am M_b is to be expected on going from Pu to U.

Fig.3.5 shows the EPMA concentration profile

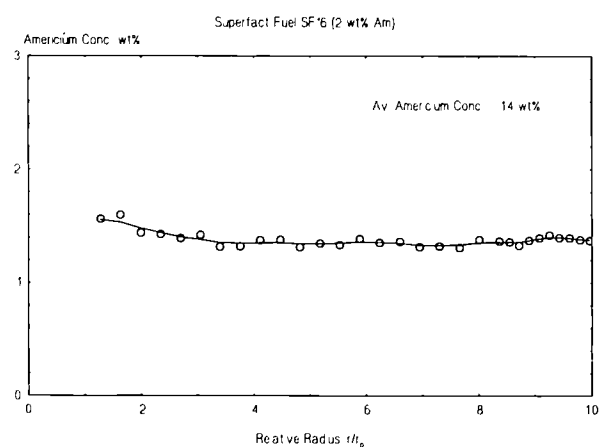


Fig.3.5 EPMA results for the radial distribution of Am in the Superfact Fuel SF16.

for Am in the fuel SF16 after the correction was made using a MAC for the Am M_b line in U of 520 instead of 1172 cm^2g^{-1} . The shape of the profile has not changed, but now the average concentration of Am has fallen from 1.9 to 1.4 wt% in agreement with the IDMS result.

References

- [1] K.F.J. Heinrich, Proc. 11th Inter. Congress on X-ray Optics and Microanalysis (J.D. Brown and A.H. Packwood eds.) Univ. of Western Ontario, 1986 p.67.

EPMA Investigation of an Uranium-Neptunium Oxide Fuel Irradiated in the Superfact Experiment (SF15)

Introduction

The fuel section analysed was cut from the Superfact pin SF15. The initial composition of the fuel was $(\text{U}_{0.55}\text{Np}_{0.45})\text{O}_2$ and the burnup, calculated on the basis of the ^{148}Nd concentration determined by isotope dilution mass spectrometry (IDMS), was 4.5 at%.

The objectives of the EPMA work were four fold:

1. To measure the concentrations of U, Np and Pu in the fuel, where plutonium results from neutron capture by ^{238}U and ^{237}Np .
2. To determine the release levels of Xe and Cs. The release of these fission products generally affects fuel performance. Further, there is a known link between the accumulation of Cs in the gap and stainless steel cladding corrosion.
3. To confirm the fuel burnup using the radial distribution of fission product Nd which is recognised as a burnup indicator.
4. To establish the nature of the material attached to the inner cladding surface at a number of places around the fuel.

Methods

Quantitative EPMA was carried out at an electron acceleration potential of 25 keV and a beam current of either 250 or 100 nA. The conventional microprobe correction procedure has been carried out using the Institute's QAUD2 program (see TUAR-91, p.128) which is based on the Quadrilateral Model of Scott and Love [1].

Xenon was analysed using the approach developed at the Institute [2]. For the UO_2 matrix this gives the concentration of gas in solution and trapped in intragranular bubbles smaller than 0.1 μm . Xenon contained in intergranular bubbles does not contribute to the measured X-ray intensity because point analysis was carried out away from grain boundaries. The confidence interval on the measured Xe concentrations at a significance level of 99% is about 5% relative at a concentration of 0.5 wt% and 10-20 % relative at 0.05 wt%. Similar levels of uncertainty are expected in the cases of Cs and Nd.

Plutonium was analysed using the M_b X-ray line. The measured intensity was corrected for X-ray contributions from the $M_{iii}N_{iv}$ line which lies only 0.011 \AA from the Pu M_b line. The correction was made as follows. The spectrometer was positioned on the Pu M_b line and the X-ray intensity obtained from the UO_2 standard at this setting was recorded. About 8 counts/sec were registered which corresponds to 0.76 wt% Pu. The true percentage of Pu at each spot analysed was then obtained by multiplying the reference concentration of 0.76 wt% by the fraction of UO_2 present and subtracting the result from the measured Pu concentration.

Radial concentration profiles were obtained from point analysis along the fuel radius at intervals of 50 and 150 μm . At each location six measurements were made. These were up to 10 μm apart and were placed away from grain boundaries thereby avoiding pores, large gas bubbles and cracks. The specimen current image (absorbed electron current) was used to obtain information about the disposition of the pores and gas bubbles at the locations where point analysis was carried out.

Results

Concentration and distribution of uranium, neptunium and plutonium

The concentrations of U and Np in the fuel decreased during the irradiation. Fig.3.6 and 3.7 show their radial distributions in the fuel. As seen, U and Np were reasonably uniformly distributed in the fuel. Their average concentrations in the fuel section were 46.1 wt% and 28 wt%, respectively.

Plutonium was created during the irradiation by neutron capture. The radial distribution of this constituent is shown in Fig.3.8. It is seen that the concentration of Pu increased slightly in the central region fuel. Between $r/r_0 = 0.5$ and the fuel centre 10.8 wt% Pu was measured

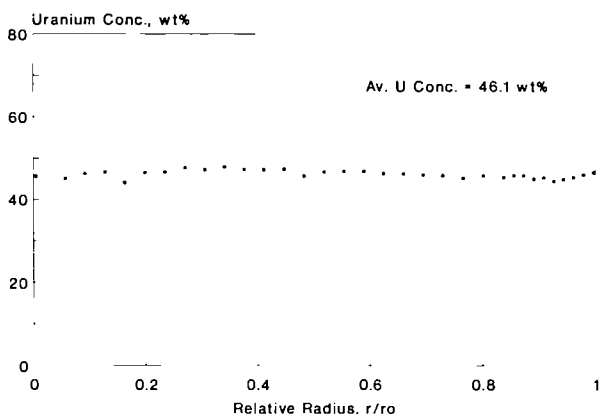


Fig.3.6 EPMA results for the radial distribution of uranium in the Superfact Fuel SF15.

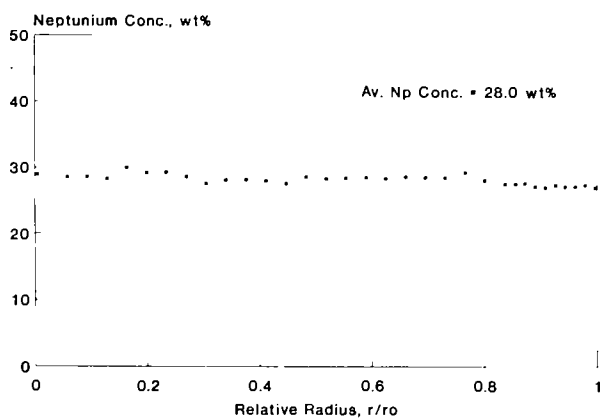


Fig.3.7 EPMA results for the radial distribution of neptunium in the Superfact Fuel SF15.

which represents a 4% increase compared with average Pu concentration of 10.3 wt%.

The radial distribution of the actinide elements in the fuel is shown in Fig.3.9. In this figure the sum total of the concentrations of U, Np and Pu is plotted. It is evident that the actinide concentration profile increases gradually with distance from the fuel surface which suggests that the neutron flux had decreased slightly. It was found that the average concentrations of U, Np and Pu in the fuel cross-section summed to 84.5 wt%.

As seen from Tab.3.13 the concentrations of U, Np and Pu measured with the microprobe are in good agreement with those obtained by mass spectrometry. In addition to U, Np and Pu the fuel also contained about 0.04 wt% Am (see TUAR-91, p.76) which was not measured by EPMA.

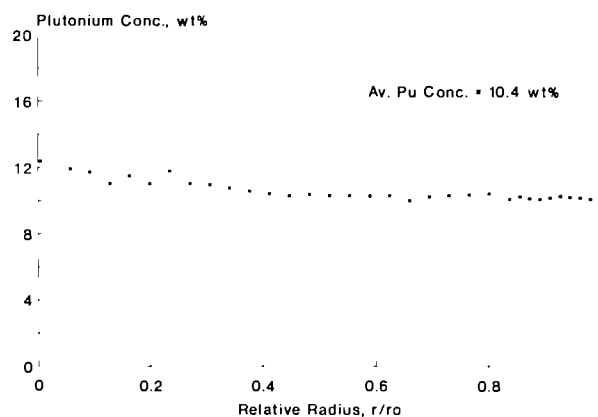


Fig.3.8 EPMA results for the radial distribution of plutonium in the Superfact Fuel SF15.

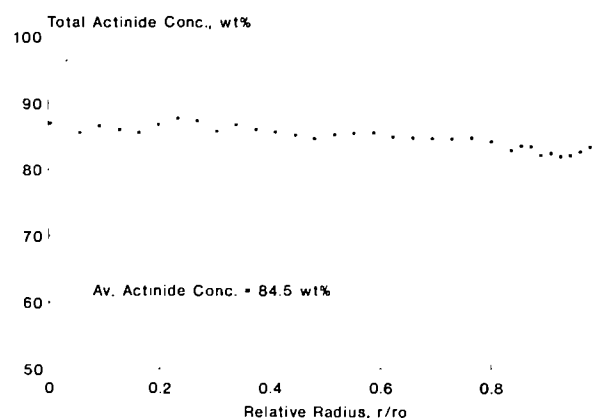


Fig.3.9 EPMA results for the radial distribution of the actinide elements (sum of the local concentrations of U, Np and Pu) in the Superfact Fuel SF15.

Tab.3.13 Concentrations of U, Np and Pu in the Superfact Fuel SF15

Element	Concentration (% Heavy Metal)	
	EPMA	Mass Spectrometry a)
Uranium	54.5	54.2
Neptunium	33.2	33.9
Plutonium	12.3	11.8

a) ICP-MS and TIMS

Fuel burnup

The fuel burnup was derived from the radial distribution of fission product Nd. A value of 4.5 at% was obtained.

The Nd concentration profile is shown in Fig.3.10. It is seen that the concentration of this fission product climbed noticeably in the central region of the fuel. From the profile the average Nd concentration in the fuel was found to be 0.48 wt%. The burnup was calculated on the premise that 0.105 wt% Nd corresponded to 1 at% burn-up. This correlation was derived from the cumulative fission yields of the stable Nd isotopes, which for ^{237}Np sum to 0.173 [3], and from the amount of Nd formed by the radioactive decay of Pm during the five year period since the fuel was discharged from the reactor. The latter is taken as equivalent to a yield fraction of 0.023.

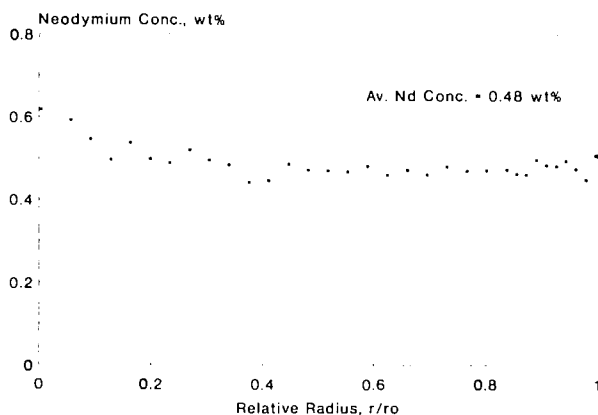


Fig.3.10 EPMA results for the radial distribution of neodymium in the Superfact Fuel SF15.

The burnup can also be determined from the total concentration of the actinides remaining at the end of the irradiation. The measured concentrations of U, Np and Pu in the SF15 fuel summed to 84.5 wt% which indicates that 4.2% of the heavy atoms had been burnt. A higher burn-up of 4.4 at% is obtained however, if the increase in the actinide concentration in the central region of the fuel is neglected. This can be justified on the grounds that the increase could be due to a general depletion of fission products.

Release of xenon and caesium

The radial distributions of Xe and Cs in the fuel are shown in Fig.3.11. Both fission products show a sharp fall in concentration in the outer part of the fuel and low retention (< 0.1 wt%) in the region between $r/r_0 = 0.6$ and the fuel center. Interestingly, similar levels of Xe and Cs were measured at the pellet surface. Moreover, in the central region of the fuel, more Xe than Cs was detected, whereas usually the opposite is found.

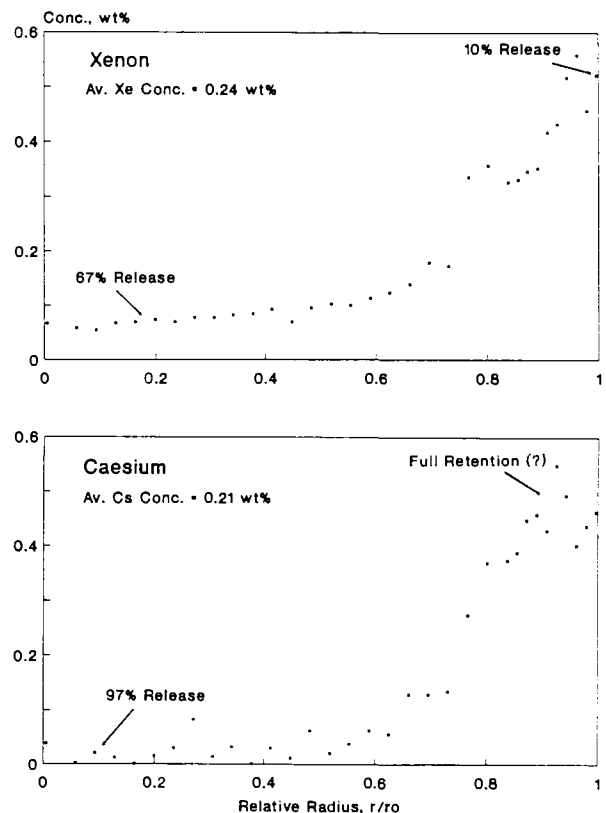


Fig.3.11 EPMA results for the radial distribution of xenon and caesium in the Superfact Fuel SF15.

Xenon release had evidently occurred over the entire fuel cross-section. The local level of release ranged from roughly 10% at the pellet surface to about 90% at the pellet centre. The average integral release for the fuel cross-section was close to 60%. These release figures were calculated assuming a Xe inventory of 0.58 wt% which is based on a cumulative yield fraction of 0.26.

The Cs profile indicates complete retention at the pellet surface. It is possible, however, that the high concentrations measured at this location are a consequence of radial migration, rather than of the absence of release. The concentration peak at about $r/r_0 = 0.9$ would seem to support this hypothesis. In the central region of the fuel the release level approached 100% which pushed the average integral release value for the entire cross-section to 54%. In the calculation of these release figures a cumulative Cs yield fraction of 0.203 was assumed.

Composition of the material in the gap

The material attached to the inside of the cladding and described as "an oxide layer deposited a few tens of microns thick" (TUSR-91, p.73) was identified as fuel. In Tab.3.14 its composition is shown together with the composition of the fuel at a distance of 10-20 μm from the pellet rim. It is seen that the analysis results are very simi-

Tab.3.14 Composition of the material attached to the inner cladding surface and the composition of the fuel at the pellet rim

Element	Composition, wt %	
	Material in the gap	Fuel at pellet rim
Uranium	45.84	46.50
Neptunium	27.89	27.00
Plutonium	10.10	10.11
Iron	0.76	
Chromium	0.03	
Caesium	1.60	0.46
Xenon	0.11	0.52
Neodymium	0.45	0.51
Oxygen ^{a)}	12.00	12.00

Not all constituents have been analysed.

a) Fixed concentration

lar. The fuel on the cladding surface, however, contained about 1% Fe which had presumably diffused out of the stainless steel cladding. It also differed from the fuel proper in that it contained about four times as much Cs, but less than a quarter of the amount of fission gas. It is thought that fuel-cladding mechanical interaction caused this thin layer of fuel to be detached from the pellet. The high Cs concentration may be explained by the condensation of this fission product in the gap.



References

- [1] V.D. Scott and G. Love, X-ray Spectrom. 21 (1992) 27.
- [2] C.T. Walker, J. Nucl. Mater. 80 (1979) 190.
- [3] L. Koch, Radiochimica Acta 29 (1981) 61.

EPMA Investigation of the Products of Cladding Corrosion in the Gaps of Two Superfact Fuel Pins (SF 13 and SF 16)

Introduction

Cladding corrosion products were observed at a number of places in the gaps of fuel pins SF13 ($(\text{U}_{0.74}\text{Pu}_{0.24}\text{Np}_{0.02})\text{O}_2$) and SF16 ($(\text{U}_{0.74}\text{Pu}_{0.24}\text{Am}_{0.02})\text{O}_2$). Both these fuels contained 24 wt% Pu. The material in the gap is a mixture of two phases; one metallic, the other an oxide (TUAR-91, fig. 3.5a). In the Am containing fuel, SF16, the duplex mixture was so fine that neither point analysis nor X-ray line scanning could be trusted to provide reliable information about the composition of the individual phases. Therefore, only the composition of the corrosion product phases in the gap of pin SF13 is given. In addition to data on the composition of the cladding corrosion product results are reported for the depth of penetration of Fe and Ni in the SF16 fuel. It has been suggested [1] that these cladding constituents can migrate large distances in LMFBR mixed oxide fuel by a mechanism that is similar to the van Arkel-de Boer process. According to this mechanism, a chemical reaction with fission product iodine results in the gas phase transport of Fe, Ni and Cr to higher temperature regions. Briefly, it is postulated that iodine reacts with the stainless steel cladding to

form the metal di-iodide which then diffuses across the gap to the fuel where the reaction is reversed. The iodide decomposes at the higher temperature to release the metal and the liberated I_2 diffuses back to the cladding to pick up more metal.

Cladding corrosion product phases in fuel pin SF13

Fig.3.12 shows X-ray distribution maps for the main constituents of the material in the gap of fuel pin SF13. It is seen that Cr and Pu have collected in the oxide phase, whereas Fe, Ni and U have accumulated in the metallic phase. Further, at the cladding surface a layer of Cs several microns thick is evident. Directly below this

in the cladding there are several points exhibiting Cr enrichment. From the electron absorption micrographs it appears that the position of the Cs layer coincides with a narrow band of chemical attack at the cladding surface. The areas of Cr enrichment could indicate islands of Cr_2O_3 .

The compositions of the metallic and oxide phases in the gap are given in Tabs.3.15 and 3.16, respectively. In both cases, the compositions of the phases in the SF13 fuel pin are compared with the compositions of similar phases analysed in a LMFBR mixed oxide fuel pin, AU07 [2]. This pin contained fuel of composition $(U_{0.7}Pu_{0.3})O_2$ and was irradiated in the MOL7B experiment. The analyses were made on pin section AU07-10 which had a burnup of 13 at%.

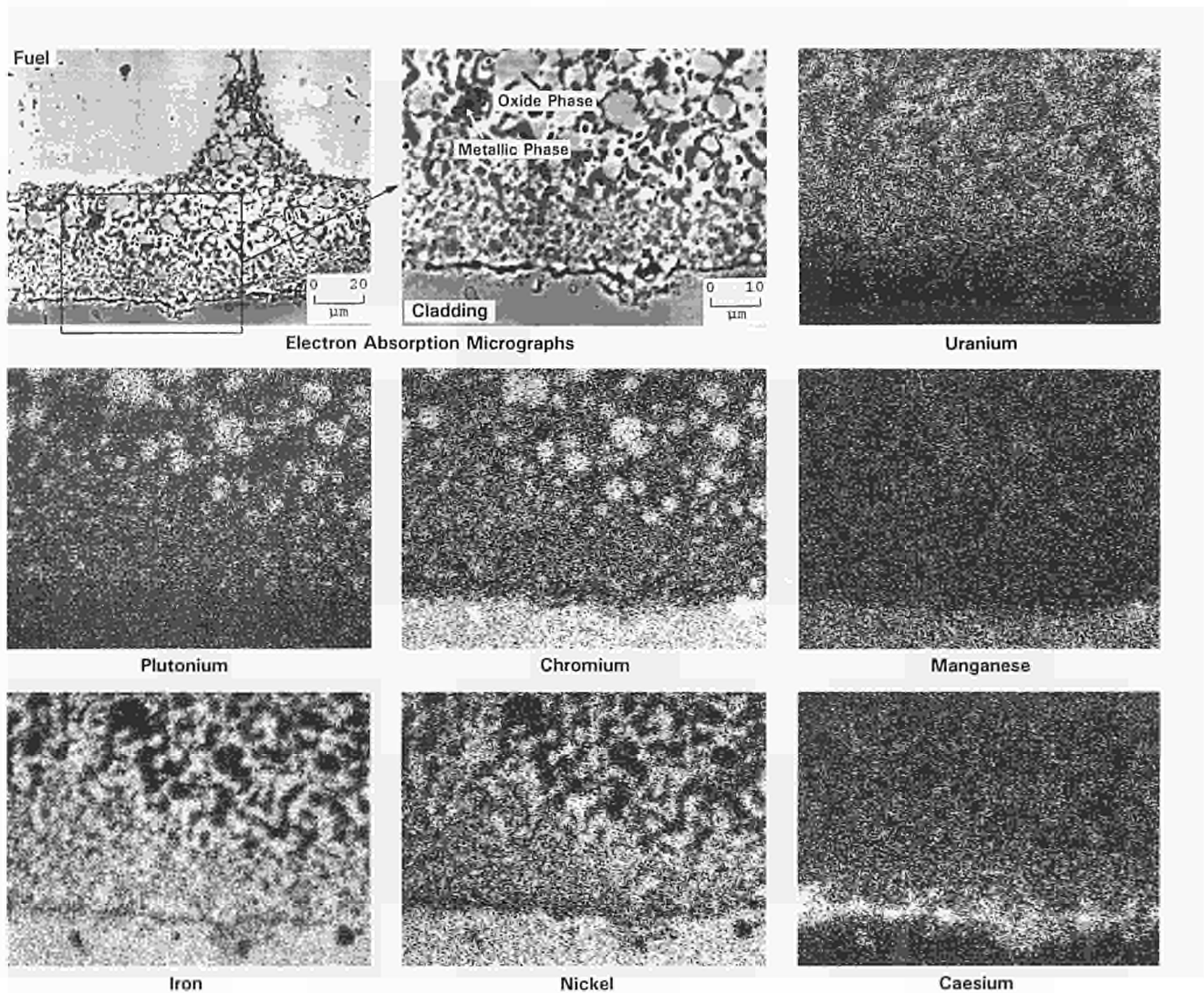


Fig.3.12 X-ray maps showing the local distributions of the main constituents of the corrosion product phases in the gap of the superfact fuel pin SF13.

Tab.3.15 Composition of the metallic phase in the gap of the Superfact Fuel SF13 and in the gap of an LMFBR mixed oxide fuel

Element SF13	Concentration	
	(U _{0.7} Pu _{0.3})O ₂	wt %
Chromium	1.9	1.5
Manganese	0.1	0.1
Iron	68.2	78.2
Nickel	18.9	18.0
Uranium	7.5	...
Neptunium	0.1	
Plutonium	1.3	...
Palladium	1.0	2.1
Tellurium	0.3	...
Caesium	0.7	...
Tin	...	0.1

Tab.3.16 Composition of the oxide phase in the gap of the Superfact Fuel SF13 and in the gap of an LMFBR mixed oxide fuel

Element	Concentration, at%	
	SF13	(U _{0.7} Pu _{0.3})O ₂ ^{a)}
Chromium	22.2	24.7
Manganese	1.1	1.3
Iron	0.7	0.5
Nickel	0.2	0.4
Uranium	4.7	0.8
Neptunium	0.4	
Plutonium	7.4	0.1
Molybdenium	...	1.0
Palladium	0.1	...
Tellurium	...	1.5
Iodine	...	0.1
Caesium	0.4	4.5
Oxygen	62.8	64.2

a) Grey phase in ref. [2]

It is seen from the tables that in the Superfact fuel pin and the LMFBR fuel pin the metallic and the oxide phases were broadly similar in composition. In both pins, Fe and Ni were the most abundant elements in the metallic phase (Tab.3.15). Together their concentrations sum to more than 85 wt%. In the Superfact pin, however, about 9 wt% Fe had been replaced by the actinide elements U, Np and Pu. Apparently, chromium sesquioxide, Cr₂O₃, is the main constituent of the oxide phase. This is clearly seen from Tab.3.16 where the concentrations of the component elements are given in at%. In the case of the Superfact fuel, the concentrations of Cr, Mn and O in the oxide phase amount to 86.1 at% and the O/Cr ratio is 2.7, which is considerably higher than that for Cr₂O₃ (1.5). Most of the excess oxygen comes from the presence of UO₂ and PuO₂ in the phase. When this extra oxygen (24.2 at%) is deducted, the O/Cr ratio decreases to 1.7. It is to be noted that the phase contained only 0.4 at% Cs. This means that if a ternary oxide, such as caesium chromate, caesium molybdate or caesium uranate, had formed it was present in only small amounts (2-3 wt%).

Depth of penetration of iron and nickel in the SF16 fuel

Fig.3.13 shows how the concentrations of Fe and Ni in the fuel changed with distance from the pellet rim in pin SF16. It is seen that initially the concentrations of both elements fall sharply within 50 µm of the fuel surface before leveling-off at around 100 ppm. This concentration is slightly higher than the limit of detection for both Fe and Ni which was 90 and 70 ppm, respectively. However, the detection of Fe and Ni at depths greater than 50 µm is very probably not due to their migration, but rather to the fact that the fuel contained Fe and Ni as impurities (98 ppm and 32 ppm, respectively). It would appear, therefore, that the greatest depth to which Fe and Ni penetrated in the SF16 fuel was around 50 µm.

References

- [1] C. E. Johnson and C.E. Crouthamel, J. Nucl. Mater. 34 (1970) 101.
- [2] C.T. Walker, J. Nucl. Mater. 74 (1978) 358.

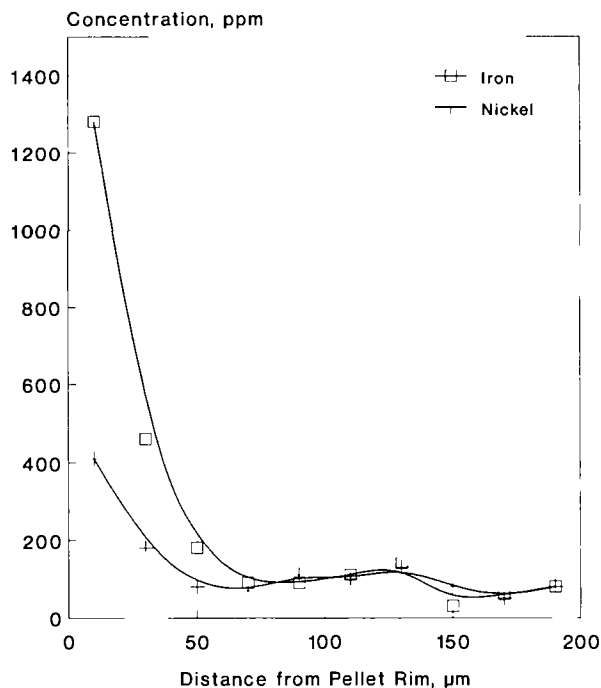


Fig.3.13 Depth of penetration of the cladding constituents Fe and Ni in $(U_{0.74}Pu_{0.24}Am_{0.02})O_2$ fuel (pin SF16).

Actinide partitioning by means of the TRPO process

Introduction

The highly active waste (HAW) from the PUREX process contains, together with the fission products, significant amounts of actinides, i.e. 0.5 % of U and Pu, a large percentage of Np and almost all Am and Cm. These actinides determine the long term radiological hazard of HAW. Their separation would therefore reduce considerably the hazard. Similar to the TRUOX process [1], a process has been developed in the P.R. of China, the so-called TRPO process [2], in which a trialkyl (C6-C8) phosphine oxide is used to extract the above actinides from HAW solutions.

The co-operation between the Tsinghua University of Beijing and the Transuranium Institute started in 1989 with a study of the extraction capabilities of the TRPO (TUAR-90, 82). This work has continued with two experiments to determine the distribution coefficient as a function of nitric acid concentration and to investigate the radiation stability of TRPO. Both experi-

ments were made with real HAW on a batch scale. A simulated waste was used to study the process in a continuous operation scheme by means of centrifugal extractors.

Continuous TRPO process in a centrifugal extractor

The TRPO process conceived for the removal of actinides from HAW was verified in a continuous counter current mode in miniature annular centrifugal extractors [3]. A simulated HAW solution is prepared (see Tab.3.17), where Nd is used as stand-in for Am, Zr should simulate Pu and Np.

Tab.3.17 Composition of the simulated HAW solution (0.7 M HNO_3)

element	added, g/l	analysed, g/l
Cr	0.082	0.052
Fe	0.379	0.236
Ni	0.070	0.079
Sr	0.147	0.155
Zr	0.337	0.284
Mo	0.315	0.216
Ru	0.197	0.197
Rh	0.036	0.030
Pd	0.131	0.112
Cs	0.446	0.435
Ba	0.306	0.293
Ce	0.450	0.459
Nd	1.555	1.450

The composition in Tab.3.17 corresponds to a HAW solution with a specific volume of 5000 l/t U. Zr, Mo, Ru, Rh and Pd were reduced to 50 % in consideration of their precipitation during fuel dissolution and HAW storage. A comparison between the analysis of the waste solution by ICP-MS with the theoretical composition shows that some elements (Zr, Mo, Fe, Cr and noble metals) must have precipitated.

The centrifugal extractor equipment consists of a 12 stage set, divided into three benches with 4 extractors each (Fig.3.14).

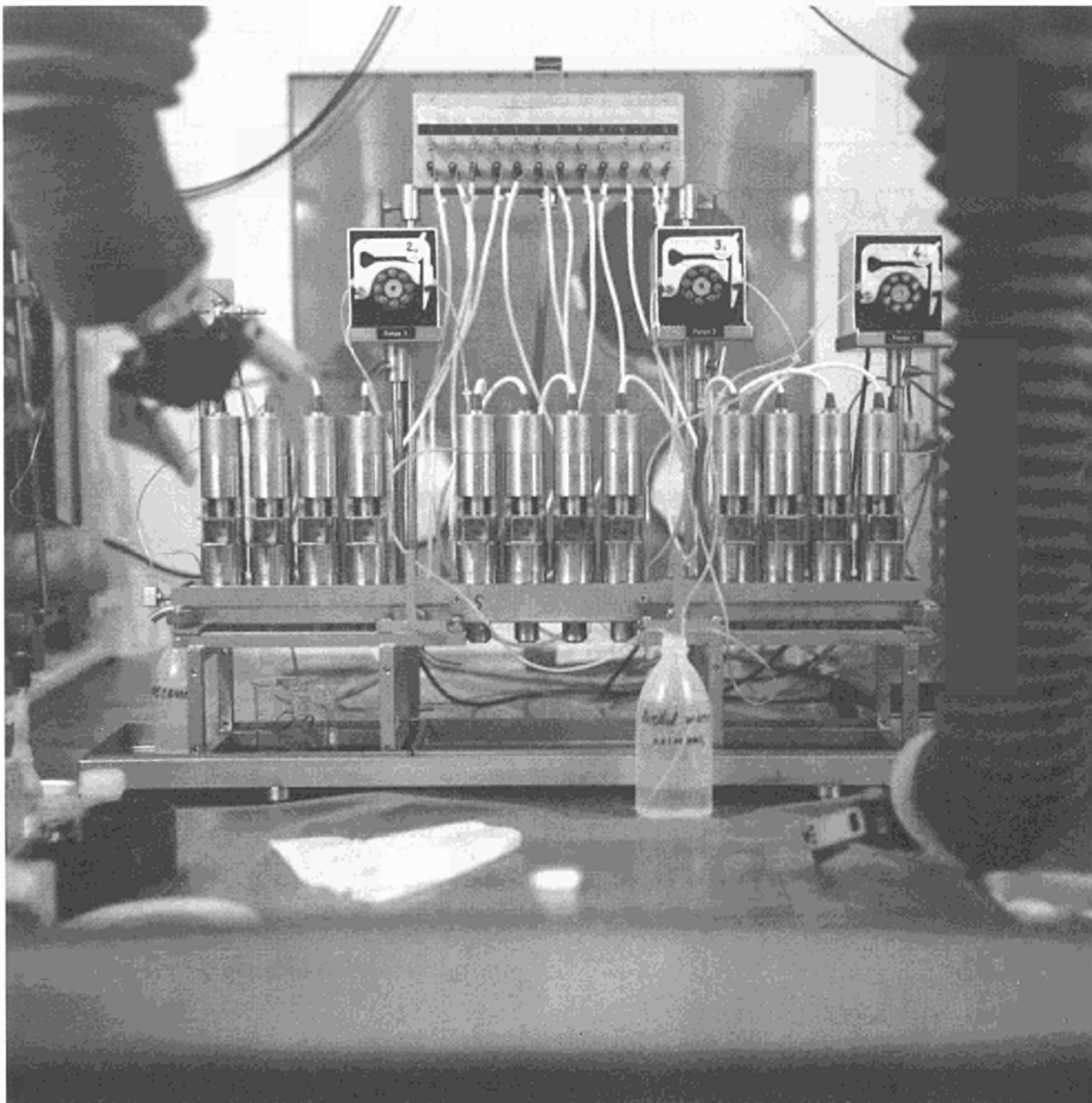


Fig.3.14 Centrifugal extractor equipment

To get a satisfactory partitioning of actinides 22 stages are needed; thus the process has been divided into two parts. In the first step extraction and back extraction of Nd with 5.5 M HNO_3 takes place, the organic phase is collected and fed a second time into the equipment (after cleaning) for stripping of Zr with 0.6 M oxalic acid and 5% sodium carbonate. The schematic operation mode of the process is shown in Fig.3.15.

The acidity in the raffinate was used to monitor for the steady state in the equipment. A stable

value of 0.4 M was reached in less than 1 hour. From here about 200 ml of organic phase were collected. Samples were taken at each outlet stream and the experiment was stopped. At each stage a sample with organic and aqueous phase was taken and analysed. For the second part the procedure was similar.

The distribution of the elements in the process streams is presented in Fig.3.16.

The distribution between different streams is very clear except for Mo and Ru. As can be seen

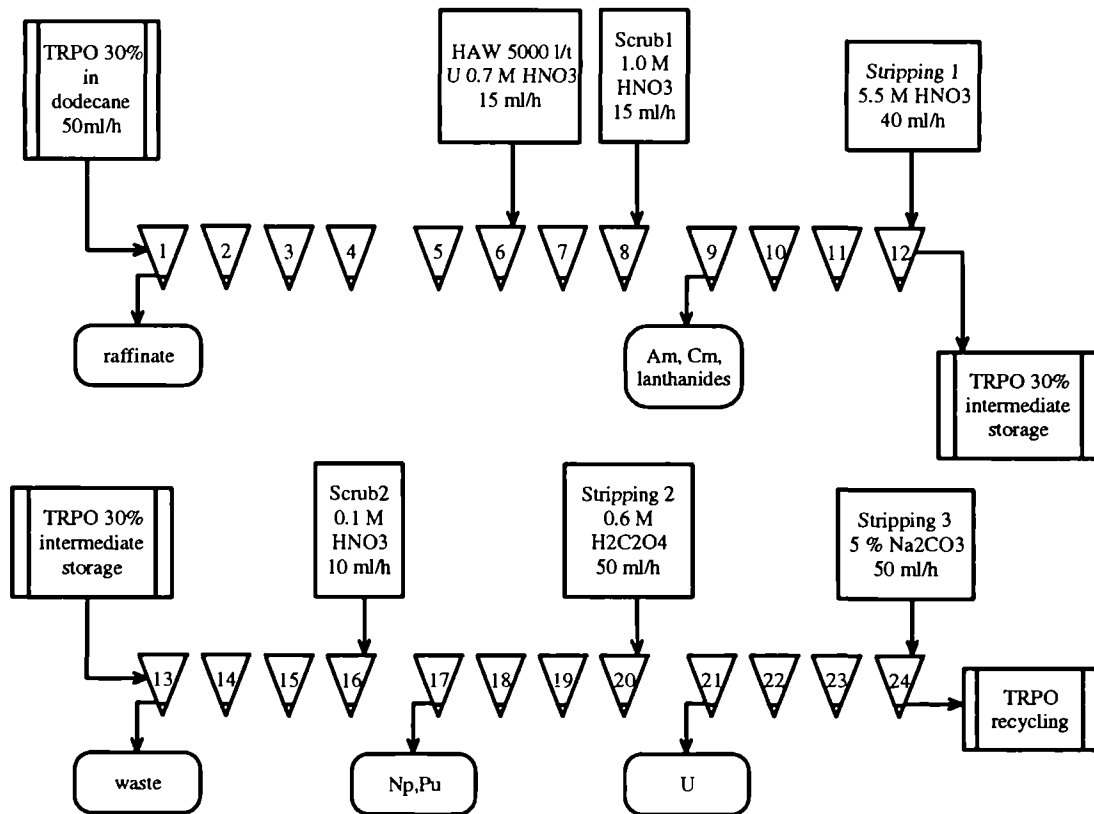


Fig.3.15 Schematic operation mode for the TRPO process in centrifugal extractors

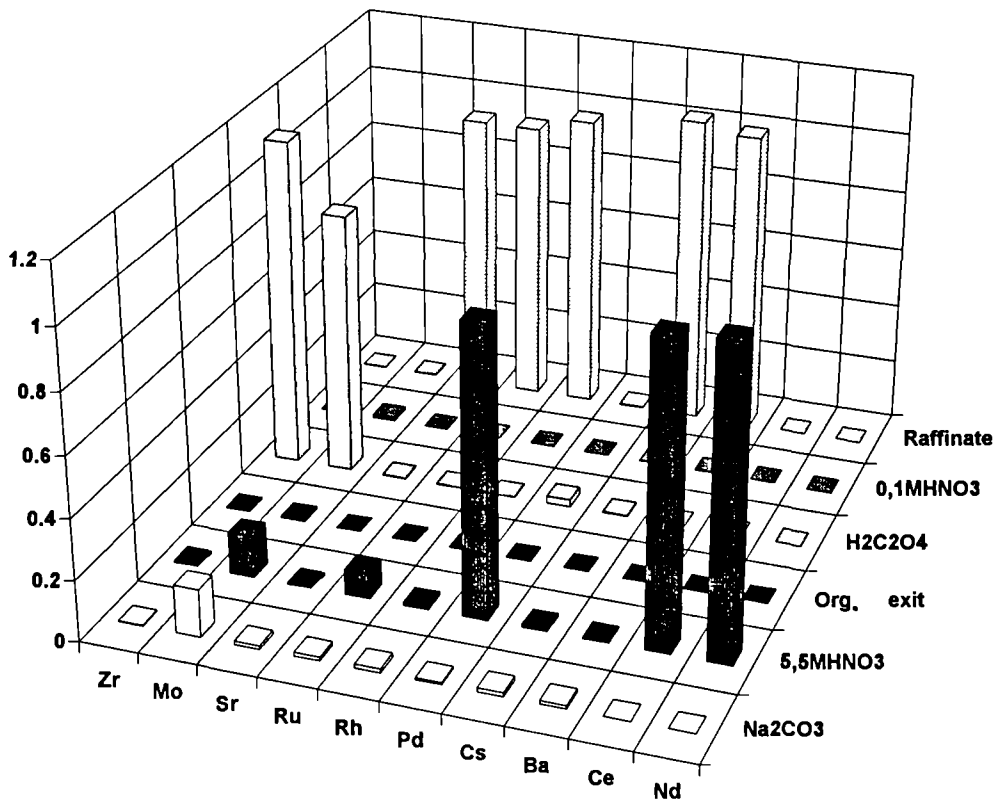


Fig.3.16 Relative distribution of waste elements in the different streams of the TRPO process in %

Tab.3.18 Relative distribution of waste elements in the different streams of the TRPO process in %

element	Na ₂ CO ₃	H ₂ C ₂ O ₄	HNO ₃ 0.1 M	HNO ₃ 5.5 M	TRPO	raffinate	recovery
Cr	1.5	0.3	0.3	4.6	0.3	95.2	102.2
Fe	1.3	6.5	0.8	8.9	0.2	84.8	102.4
Ni	1.1	0.9	0.3	47.8	0.3	45.0	95.6
Sr	1.1	0.1	0.1	0.6	0.0	94.5	96.5
Zr	0.2	109.9	0.1	0.6	0.6	0.2	111.7
Mo	15.7	87.7	0.8	14.0	0.7	0.2	119.2
Ru	1.2	0.2	0.1	8.7	0.2	94.5	104.9
Rh	1.2	0.2	0.1	1.2	0.0	99.2	101.9
Pd	0.7	2.4	0.1	95.5	0.2	0.3	99.3
Cs	1.4	0.2	0.1	1.2	0.0	104.0	107.0
Ba	1.1	0.1	0.1	0.5	0.0	101.2	103.2
Ce	0.0	0.0	0.0	100.2	0.0	0.0	100.2
Nd	0.0	0.0	0.0	101.8	0.0	0.0	101.8

from Tab.3.18, the recovery of Nd is excellent within the detection limits of ICP-MS analytical method.

The material balance of the experiment is good, especially for the lanthanides. Cs, Ba, Sr, Rh and Ru are almost completely retained in the raffinate.

The profiles of Zr and Nd in the 22 extractor stages are shown in Fig. 3.17.

The extraction in the first six stages works well especially for Nd, where more than 99.9% of Nd are extracted by TRPO and where the Zr concentration in the raffinate is low. Also the back extraction with 5.5 M HNO₃ for Nd (stages 9-12) and with oxalic acid for Zr (stages 15-18) gave satisfactory results; for Zr the concentration in the organic phase was of about 10 ppb, i.e. the detection limit of the analytical method. For Nd a slight contamination was observed between stage 14 and 20, most probably because the cleaning of the equipment prior to the second part of the process was not sufficient.

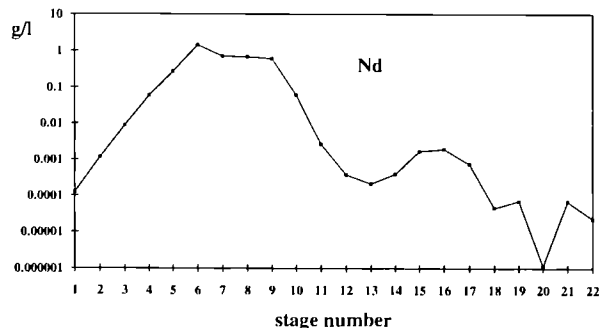
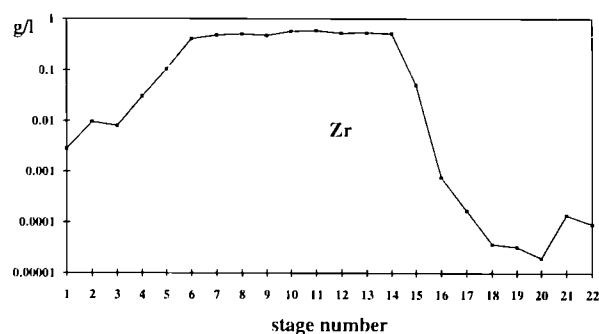


Fig.3.17 Profiles of Zr and Nd in the centrifugal extractors

Influence of HNO₃ concentration on the TRPO extraction behaviour

In order to see the influence of nitric acid on the extraction behaviour of TRPO, a batch experiment was carried out with real HAW solution. The initial composition of the concentrated HAW was determined by ICP-MS (Tab. 3.19).

This solution was then diluted 10 times in order to reach a specific volume of about 5000 l/ t U. The acidity range investigated was from 0.3 to 5 M HNO₃. The flow sheet of the experimental procedure is shown in Fig.3.18.

Tab.3.19 Composition of the real HAW concentrate, HNO₃ concentration 3.09 mol/l

element group	element	concentration, g/l
corrosion products	Cr	1.10
	Mn	0.41
	Fe	10.13
	Ni	2.56
	Co	0.01
fission products	Rb	0.53
	Sr	1.18
	Y	0.78
	Zr	0.22
	Mo	2.07
	Tc	1.36
	Ru	2.99
	Rh	0.60
	Pd	0.57
	Ag	0.00
	Cd	0.45
	Sn	0.05
	Te	0.14
	I	0.00
	Cs	3.71
	Ba	3.90
	La	2.25
	Ce	4.32
	Pr	2.16
Nd	7.32	
Sm	1.56	
Eu	0.21	
Gd	0.42	
actinides	U	6.82
	Np	0.45
	Pu	0.15
	Am	0.47
	Cm	0.02

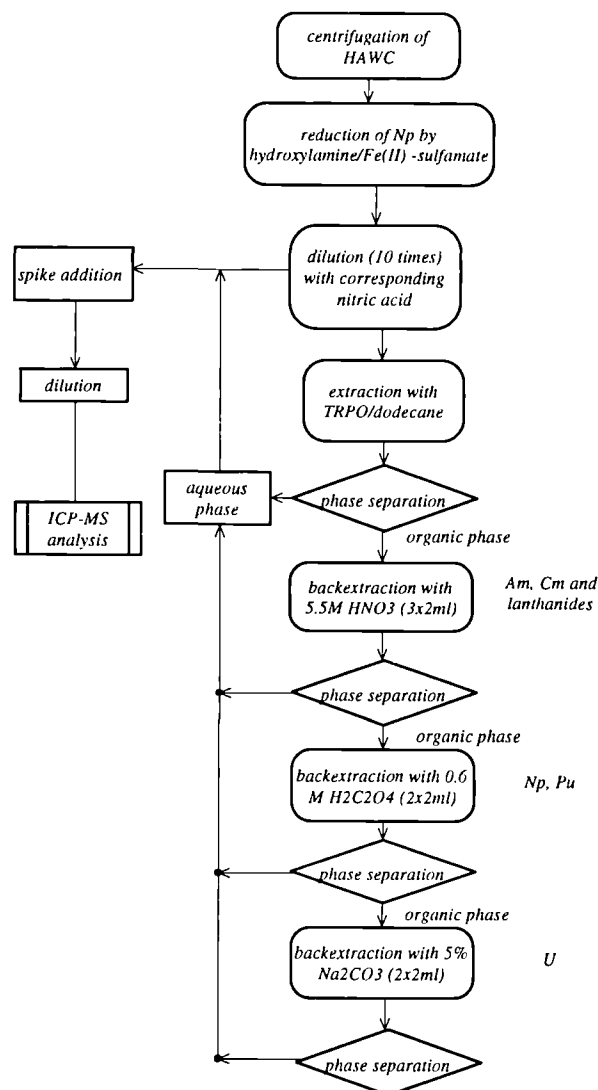


Fig.3.18 Flow sheet for the TRPO extraction

The HAW concentrate was added immediately after adjustment of the Np-IV valency to the reaction tube containing 2 ml of the corresponding nitric acid and 2 ml of the organic phase (30 % TRPO in dodecane, in order to avoid reprecipitation from HAW especially for the low nitric acid concentrations).

Fig.3.19 gives the distribution ratio of the main fission products as a function of the nitric acid concentration.

Cs and Sr have always very low distribution ratios, also for Ru, Rh and Pd. At least at HNO₃ concentrations above 1 M the distribution ratio is low. Only Zr, Mo and Tc show an increased extraction especially at low acidity (< 1M).

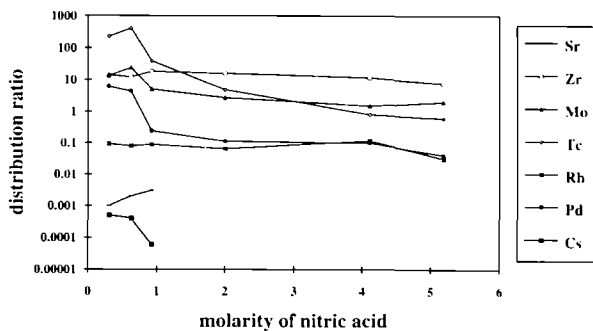


Fig.3.19 Dependence of the distribution ratio of main fission products on the HNO_3 concentration

The actinides form two groups with different extraction behaviour (Fig.3.20). The minor actinides Np, U and Pu have high distribution ratios independent of the nitric acid concentration,

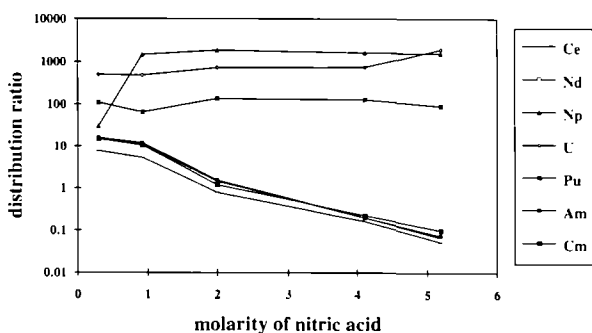


Fig.3.20 Dependence of the distribution ratio of the actinides on the HNO_3 concentration

the higher actinides Am and Pu have a much lower distribution ratio which decreases with increasing nitric acid concentration and which is unfortunately very similar to that of the lanthanides, making the separation between the two element groups impossible at least in the above described process scheme.

Fig.3.19 and 3.20 also show, that in order to have a reasonably good extraction of Am and Cm and to avoid a too high extraction of fission products, a HNO_3 concentration of 1 M or just below seems to be the best suited acidity.

The cross contamination between Np and Pu (back extracted with 6 M $\text{H}_2\text{C}_2\text{O}_4$) on one hand and Am and Cm stripped with 5.5 M HNO_3 on the other hand is very low. Unfortunately the U

recovery was surprisingly low. A possible explanation could be the uncompleted phase separation. U would be back-extracted by Na_2CO_3 ; the analysis of the solution requires acidification. If the aqueous phase is contaminated even with very small amounts of organic phase, this leads to important U losses (cf. high distribution ratio). From the fission products, lanthanides, Zr, Mo and Tc are co-extracted with the actinides.

Both experiments, i.e. the batch experiment with real HAW and the cold test of the centrifugal extractors have shown, that the TRPO process is a prospective and competitive process for actinide recovery and partitioning from HAW. A test with the extractors with real HAW will start very soon.

References

- [1] G. Bidoglio, M. D'Alessandro, EUR 11914 (1988) 43
- [2] E.P. Horwitz, D.G. Kalina, H. Diamond, Vandegrift, W. Schulz, Solvent Extr. Ion. Exch. 3 (1985) 75
- [3] Y. Zhu, C. Song, Recovery of Np, Pu and Am from Highly Active Waste, in Transuranium Elements, L.R. Morss and J. Fuger eds., ACS, Washington, DC (1992)
- [4] Y. Zhu, C. Song, J. Xu, D. Yang, B. Lie, J. Chen, Chinese J. Nucl. Sci. Eng. 9 (1989) 141

1.4 Characterisation of Waste Forms and High Burn-up Fuel

Introduction

The studies on radioactive wastes carried out at the Institute for Transuranium Elements are centered on the characterization of the waste forms (non-processed spent fuel and vitrified high level waste), with respect to properties relevant to their behaviour under conditions of long term storage.

Properties to be investigated include thermal conductivity, thermal and mechanical stability, redistribution of actinides and fission products within the waste materials, radiation damage, resistance to corrosive agents and leaching behaviour with various leachant compositions.

In the particular case of the leaching of spent fuels a computer code, COCAIN, is being developed. The aim is to model the underground water contamination in a fuel repository, should water accidentally leach the fuel.

At present time the ITU codes (FUTURE, MITRA, CHEMIF) to be used for the characterisation of the initial fuel state are operational. The fuel restructuring resulting from irradiation representative of a LWR-fuel (fuel moved at every cycle into different power core zones and burned out up to 50.000 MWd /t) has been calculated by means of FUTURE. From this fuel restructuring the nuclide migration to the grain boundary was determined by means of MITRA and the probability for a volatile isotope to come in contact with the leachant has been calculated.

An additional information which aims at the determination of the chemical compounds formed by these nuclides as a function of the oxygen potential will be gained by using CHEMIF.

The validation of the code COCAIN needs experimental data not restricted to leaching tests but, furthermore, on the fuel state, the fission product inventory, the migration of fission products to the grain boundaries and the corrosion mechanism.

The latter aspect could be very sensitive to the fuel oxidation state; therefore, more precise in-

formation concerning the oxidation kinetics of irradiated UO_2 and MOX fuels when in contact with water or vapour have to be gained.

A study of the oxidation of unirradiated UO_2 in air and in moist N_2 , carried out by thermogravimetry, is completed. The final compounds of this reaction (U_4O_9 , U_3O_8) have been characterized by ceramography and X-ray diffraction. An Arrhenius function and an equation for the rate constant were determined. Similar studies on irradiated UO_2 (and MOX) are on the way in hot cells in order to check the oxidation mechanisms under realistic conditions.

A series of long term oxidation tests has been started with high burn-up LWR fuels (50 GWh/tU) in air at 180-200°C. In agreement with previous American studies on PWR fuels (25 GWh/tU), first metallographic results indicate the formation of the U_4O_9 phase at the grain boundaries, with growing direction towards the grain centre and with faster reaction kinetics in the fuel regions with larger intergranular porosity. Our observations show that U_4O_9 does not form coherently along the grain boundaries but precipitate in the form of interlinked needles and platelets as in oxidized unirradiated UO_2 . Contrary to unirradiated fuel the limiting oxidation phase does not seem to be U_3O_7 or U_3O_8 , but a U_4O_{9+y} -type phase (probably metastable), whose homogeneity range seems to extend up to $\text{O}/\text{U} = 2.4$.

Electrochemical measurements (potential-time, linear polarisation and ac impedance techniques) have been used in experiments with natural (non-irradiated) UO_2 pellets in aqueous solutions (3 % NaCl, 3 % Na_2CO_3 and 0.1M NaClO_4). The aim has been to characterise the behaviour of fuel in known solutions and identify key reaction steps.

UO_2 takes up oxygen very readily from aqueous solutions to give UO_{2+x} , which results in potential changes. Above a certain potential of about $\sim +100$ mV (versus a saturated calomel electrode), oxidative dissolution is predicted to commence whereas under reducing conditions dissolution rates remain low. This accelerated dissolution under anodic (oxidising) conditions has been observed with ac impedance techniques. Longer

term (500h) tests at rest potentials in 3% Na₂CO₃ have shown a slow dissolution rate; electron microscopy has also revealed an accompanying deposition process of needle clusters of an hydrate of uranium oxide (probably schoepite UO₃·xH₂O).

In this preliminary phase the results will be used for comparison with future work with irradiated UO₂ fuel to be carried out in the hot cells. Techniques for electrode preparation with active UO₂ are currently being tested.

New leaching tests on UO₂ powder in an autoclave at 200 °C in the presence of H₂O or H₂O/30%H₂O₂ either in vapour or in immersion have started. This study should establish the different mechanisms of leaching.

Under H₂O or H₂O₂ immersion conditions at 200 °C, the leaching rate of U is about 10⁻² and is controlled by the oxidation of U⁴⁺ and the high solubility of U⁶⁺ in H₂O. The Np leaching rate is not negligible and points to an unexpected partial oxidation of Np in the fuel to Np⁵⁺. On the contrary, Pu as Pu⁴⁺ in the fuel remains unleached. The leaching under vapour condition appears ineffective.

Finally, a non-destructive assay technique was used to characterize individual fuel pins in terms of burn-up and radiotoxicity potential. A study of the influence of the starting enrichment in U-235 on the minor actinide build-up is on the way.

Leaching tests on fuel rod segments with pre-set defects are foreseen for 1993. These fuel rod segments have to be fabricated from BR3 UO₂ fuel rods irradiated to 50.000 MWd/t. A prerequisite condition for these leaching tests is the availability of characteristic data concerning the fuel and the fuel rods. At the present time, only the NDT examinations are completed.

The leaching behaviour of R7T7 glass in the presence of granite has been studied. The influence of granite seems to reduce the leaching rate of the analysed glass constituents, of actinides and fission products, except Mo, whose leaching rate is accelerated.

Basic Studies on Waste Glasses

The laboratory work on basic physical processes, radiation damage and leaching of simulated HLW waste glasses was concentrated in 1992 on the French reference glass for LWR fission product solutions, SON 681817, generally referred to as R7T7 glass, since this is the glass to be used in the future. This work led to an invited contribution to a special volume of *J. Nucl. Mater.* [1]. The work on the other glasses studied previously, the US product MCC 76-68 and the German glass GP 98/12 was terminated (see e.g. TUAR 91, p. 89) because these glasses will not be technologically used in the near future since reprocessing will not be done with US fuel and reprocessing of German fuel will not be done in Germany.

A hot hardness test apparatus, received from IMF, KfK, was put into operation to measure the temperature dependence of Vickers hardness *H* and radial crack length *c* at Vickers indentations and to deduce fracture toughness values *K_{IC}* up to 500 °C, thus extending previous measurements up to 200 °C (for R7T7) and 300 °C (for GP 98/12) [2, 3]. The results for R7T7, which has a transformation temperature of 502 °C [1], show a continuous decrease in *H* with temperature *T* (see Fig.4.1). The crack lengths *c* increased up to 350 °C, and there was a very pronounced decrease above 450 °C. Whereas at the load used (*P* = 19.6 N), 20 cracks were found for 5 indentations between room temperature and 450 °C, only 12 cracks were seen at 500 °C. Correspondingly, the calculated fracture toughness, *K_{IC}*, increased significantly. To calculate *K_{IC}*, the relation

$$K_{IC} = 0.057 \cdot H \cdot a^{1/2} \cdot (E/H)^{2/5} \cdot (c/a)^{-3/2}$$

was used (see refs. [2, 3]). Here, *a* is the half diagonal of the Vickers indentation. This relationship has a theoretical basis in terms of the elastic/plastic indentation fracture mechanics of a center-loaded half-penny crack [e.g. 2, 3]. To evaluate *K_{IC}* at increased temperatures, the assumption has to be made, that the empirical constant of 0.057 necessary to convert the proportionality to an equality and obtained at room temperature is not a function of temperature. This assumption has some experimental support [2, 3].

For GP 98/12 which has a higher transformation temperature (543 °C) [1], a similar continuous

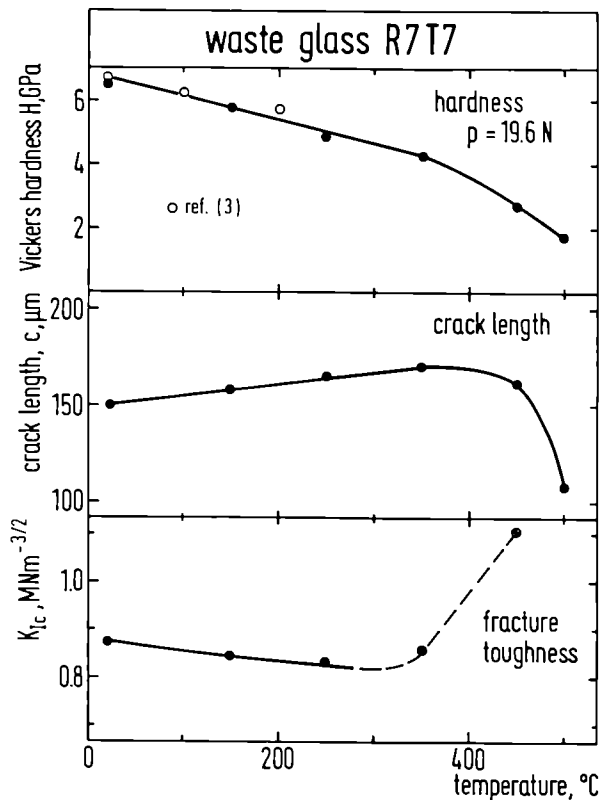


Fig.4.1 Hardness, crack length at Vickers indentations and fracture toughness of R7T7 glass as a function of temperature

decrease in H with T was found. Only 12 cracks at 5 indentations were seen at 500 °C as with R7T7, but the crack length increased up to 450 °C, in contrast to R7T7. For the base glass VG 98/12 (without added simulated waste), it increased even up to 500 °C thus yielding a smaller variation of K_{Ic} with T than observed for R7T7.

The extensive work on the effects of radiation damage on leaching, volume changes and fracture behavior reported before (TUAR 90, p. 87; TUAR 91, p. 89) was terminated with measurements of leach rates at low temperatures (20 and 50 °C), again using R7T7 and GP 98/12. A typical result for R7T7 is shown in Fig.4.2.

If leach rates measured at elevated temperatures $T \geq 90$ °C are extrapolated to room temperature, an activation enthalpy of 60 kJ/mol is usually used [1]. The calculated mass losses at 20 °C are of the order of a $\mu\text{g}/\text{cm}^2$ day, or less. To get quantitative information for such small changes, radiotracer measurements are useful (see Fig.4.2). The glasses were implanted with

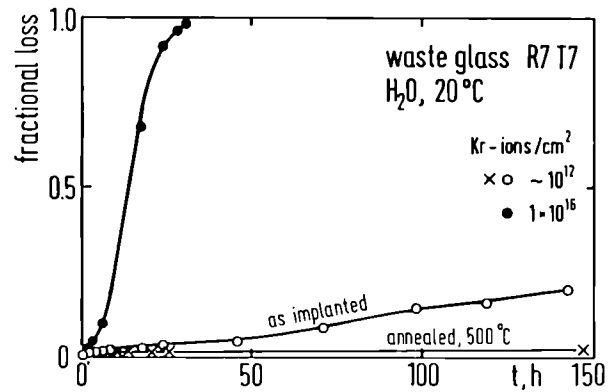


Fig.4.2 Tracer experiments with R7T7 glass implanted with 40 keV ^{85}Kr ions to two doses to measure the slow kinetics of leaching at room temperature. For the low dose, one specimen was preannealed to 500 °C before leaching.

^{85}Kr , either as trace amount, or with a large gas concentration adding a stable ^{84}Kr beam. The loss of ^{85}Kr was measured with progressing leaching time in H_2O at 20 or 50 °C with a glass surface to water volume ratio, S/V , of 20m^{-1} . The median range of Kr at the energy used (40 keV) is 25 nm, i.e. 50 % of the implanted Kr are located within the first 25 nm. Since the Kr-concentration is peaked at the median range, the curves of fractional loss of Kr are not completely linear with time. The fact that leaching is significantly increased for high Kr-doses (high damage levels) is due to conditions imposed by ion implantation (radiation enhanced Na mobility biased in the electric field set up during implantation and sputtering (see TUAR 91, p. 90)). It is not found in glasses doped with short-lived actinides (e.g. Cm-244, see TUAR 90, p. 88) and is thus not likely to occur in real waste glasses. It is interesting to compare the results for glasses as-implanted with the trace amount of ^{85}Kr (showing a leach rate of ~ 10 nm/week) with the glass implanted with the same dose but annealed at 500 °C following implantation and before leaching, in order to recover all possible radiation damage. This shows that the intrinsic leach rate of R7T7 is very low indeed at room temperature, i.e. ~ 1 nm/week, and that a small damage effect exists even at the low dose of $\sim 10^{12}$ ions/ cm^2 .

Following a first round robin test of the Technical Committee 19 (Physical Methods for Studying Glass Surfaces) of the International Commission on Glass, in which different techniques (RBS, ERDA, NRA, XPS, SIMS) were compared and in which the Institute participated [4], a sec-

ond round robin test to measure thin coatings on glasses and possible interdiffusion phenomena was performed. The techniques used in the TU-work, i.e. Rutherford backscattering RBS, and elastic recoil detection analysis, ERDA, were shown to be powerful and reliable. The results were presented at the Int. Congress on Glasses, Madrid, Oct. 5-9, 1992 [5].

References

- [1] Hj. Matzke and E. Vernaz: "Thermal and Physicochemical Properties Important for the Long Term Behavior of Nuclear Waste", invited contribution to 8. Int. Symp. on Thermodynamics of Nuclear Materials, Snowbird, Utah, Aug. 1992, *J. Nucl. Mater.*, special volume 201 (1993) 295
- [2] Hj. Matzke, E. Toscano, J. Routbort and K. Reimann: "Temperature Dependence of Fracture Toughness and Elastic Moduli of a Waste Glass", *J. Amer. Ceram. Soc.* **69** (1986) C-138
- [3] R. Dal Maschio, E.H. Toscano and Hj. Matzke: "Fracture Toughness of Waste Glasses at Elevated Temperatures" in *Indentation Fracture and Mechanical Properties of Ceramic Fuels and of Waste Ceramics and Glasses*, Ed. Hj. Matzke, *Europ. Appl. Res. Reports* **7** (1987) 1203
- [4] G.W. Arnold, G. Della Mea, J.C. Dran, H. Kawahara, P. Lehuède, Hj. Matzke, P. Mazzoldi, N. Noshiro and C. Pantano: "Surface Analysis of Coated Flat Glasses: Comparison of Various Techniques", *Glass Technology* **31** (1990) 58
- [5] K. Bange, F. Bauke, G. Della Mea, J.C. Dran, G. Emiliani, F. Geotti-Bianchini, P. Lehuède, Hj. Matzke, P. Mazzoldi and P. Polato, to be published in *Glass Technology*

Leaching of UO_2 and of SIM-FUEL

Introduction

The studies on leaching, hydration and surface analysis of UO_2 and of SIMFUEL, described in TUAR 90, p. 33 and TUAR 91, p. 102 were continued and extended. The previous work had been aimed at developing methods to accurately and nondestructively measure thickness and kinetics of formation of layers of higher oxides on UO_2 , the prerequisite of leaching since UO_2

shows a very small solubility and has to be oxidized in order to become soluble in water [1]. This previous Rutherford backscattering/channeling work was focused on the analysis of distortions in the U-sublattice due to leaching. A direct measurement of the oxygen content in these thin layers (typically a few to some 10^2 nm thickness) by conventional Rutherford backscattering techniques is not possible in the presence of the heavy U-atoms since the Rutherford scattering cross section σ_R is proportional to the atomic number, Z , square, hence $\sigma_R \propto Z^2$. Therefore, the signal of U is larger by $(92/8)^2 = 132$ times than the signal for oxygen. Small changes in the O-content can thus not be measured quantitatively with conventional Rutherford backscattering.

However, two new resonance scattering methods were recently successfully developed (see TUAR 91, p. 32) using high energy He-ions [2]. In particular the broad resonance of the (α, α) scattering of O-16 between 7.3 and 7.7 MeV allows accurate nondestructive direct analysis of the oxygen content in surface layers of up to about a μm to be performed [3].

Leaching of UO_2

A typical example is shown in Fig.4.3, where two random spectra obtained for a virgin, hence stoichiometric UO_2 crystal and for a leached crystal (pH = 6, 180 °C, 32 h) are presented. The only difference between these two spectra is in the first oxygen peak (hatched area). This

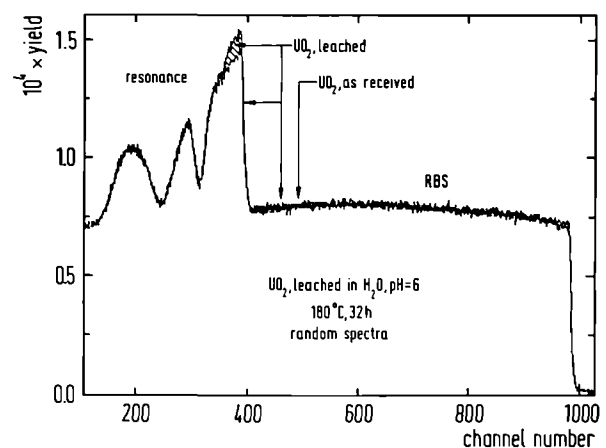


Fig.4.3 Comparison of two random backscattering (Rutherford and resonance) spectra for virgin (stoichiometric) UO_2 and UO_2 leached in water of pH = 6 at 180 °C for 32 h

proves unambiguously oxygen uptake of UO_2 upon leaching. Fig.4.4 shows the oxygen content and gradient between the surface exposed to the water and a depth of 800 nm. Additional chan-

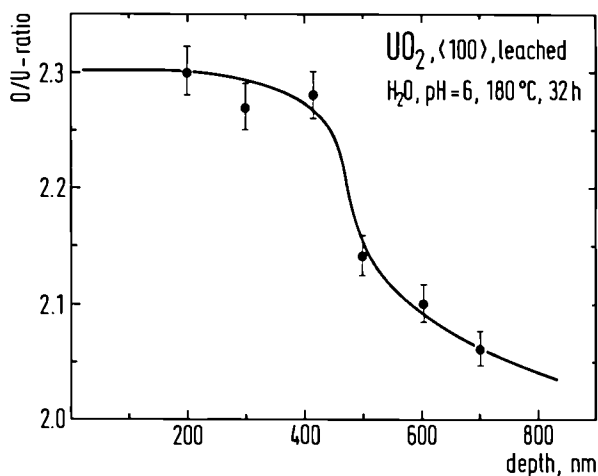


Fig.4.4 Oxygen content as a function of depth of the leached UO_2 specimen of Fig.4.3

neling measurements showed that the oxygen atoms are strongly displaced from the sites they occupy in the UO_2 lattice within the region of uniform O-content, hence the region corresponding to $\text{U}_3\text{O}_{7(x)}$. The displacement of the oxygen atoms decreased at greater depth (> 400 nm), as expected, since the composition of the layers went through U_4O_9 and approached UO_2 again.

A number of similar measurements was performed for other leaching conditions. These indicated that stresses were built up in the oxidized surface layer whenever they exceeded a thickness of ~ 200 nm.

Leaching of SIMFUEL

Leaching experiments were performed with SIMFUEL with 3, 6 and 8 % simulated burnup. This SIMFUEL replicates high burnup LWR fuel to a large extent [4] (and TUAR 90, p. 28) and is therefore used nowadays in many laboratories in different countries (see TUAR 91, p. 103): A larger number of researchers wanted to participate in leaching tests: the countries involved include Finland (K. Ollila), Spain in different laboratories (A. Sandino, I. Casas, J. Bruno and coworkers), Sweden (D. Shrive, L. Werme) and Canada (D. Shoesmith, E. Sunder). Other laboratories doing research on SIMFUEL are JAERI (Japan), Grenoble and Orsay (France).

Since chemical analysis of the leaching solutions is performed in many of these laboratories, and because of difficulties in getting access to ICP analyses in TUI, emphasis of the present investigations was placed on analysing the leached surfaces of SIMFUEL, applying nuclear techniques (RBS, ERDA etc.) and SEM with EDAX.

Leaching with UO_2 , 3 %, 6 % and 8 % SIMFUEL was performed in H_2O at either 150°C (for so far 1884 h) or at 200°C (for so far 102 h). Measurements were made at 8 time intervals to follow the time dependence of the leaching process, after 8, 174, 333, 476, 1213 and 1884 h for 150°C , and after 4, 14, 29, 54 and 102 h for 200°C . Besides RBS, ERDA and SEM/EDAX measurements, the total weight changes were recorded. The measurements for 174 h, 150°C and 4 h, 200°C showed the expected surface oxidation of all specimens and caused the formation of a layer of composition near to U_3O_7 (see above and Fig.4.4). Further leaching revealed differences in the behavior of the 4 types of specimens. For UO_2 , the layers grew and the total loss of matter by dissolution amounted to \sim one third of the oxidized layers.

For 3 and 8 % SIMFUEL, oxidation and leach rates of U were less pronounced than with UO_2 , due to the effect of fission products dissolved in the UO_2 lattice. In addition, redeposition of fission-rich crystalline matter (see Figs.4.5 and 4.6) occurred covering up to 30 % of the surface. The redeposited matter often had a needle-shape. The needles started growing in pores or at other faults in the surface. EDAX analysis showed that they contained Ba. Zr was also found at the surface locally enriched. This was supported by RBS which showed a characteristic shoulder for the masses of heavy fission products (Ba, Nd). A shift of a part of the U-shoulder to lower energies confirmed the enrichment in fission products or otherwise the depletion in U. The layers were too thin to be analysed by EDAX.

The 3 % and 8 % SIMFUEL gained weight during leaching, in contrast to UO_2 , thus supporting the above statement of reduced leach rates in SIMFUEL as compared with UO_2 . An apparent exception was the 6 % SIMFUEL which, due to its larger porosity, showed more grain boundary attack. This caused some grains to become separated thus giving an untypical weight loss. Apart from this effect, the 6 % SIMFUEL fitted well into the sequence UO_2 - 3 % - 6 % - 8 % SIMFUEL showing decreased leach rates and increasing coverage of the surface with crystalline



Fig.4.5 SEM picture of 8 % burnup SIMFUEL following leaching at 150 °C in H₂O for 1213 h. First redeposition of matter rich in fission products is seen

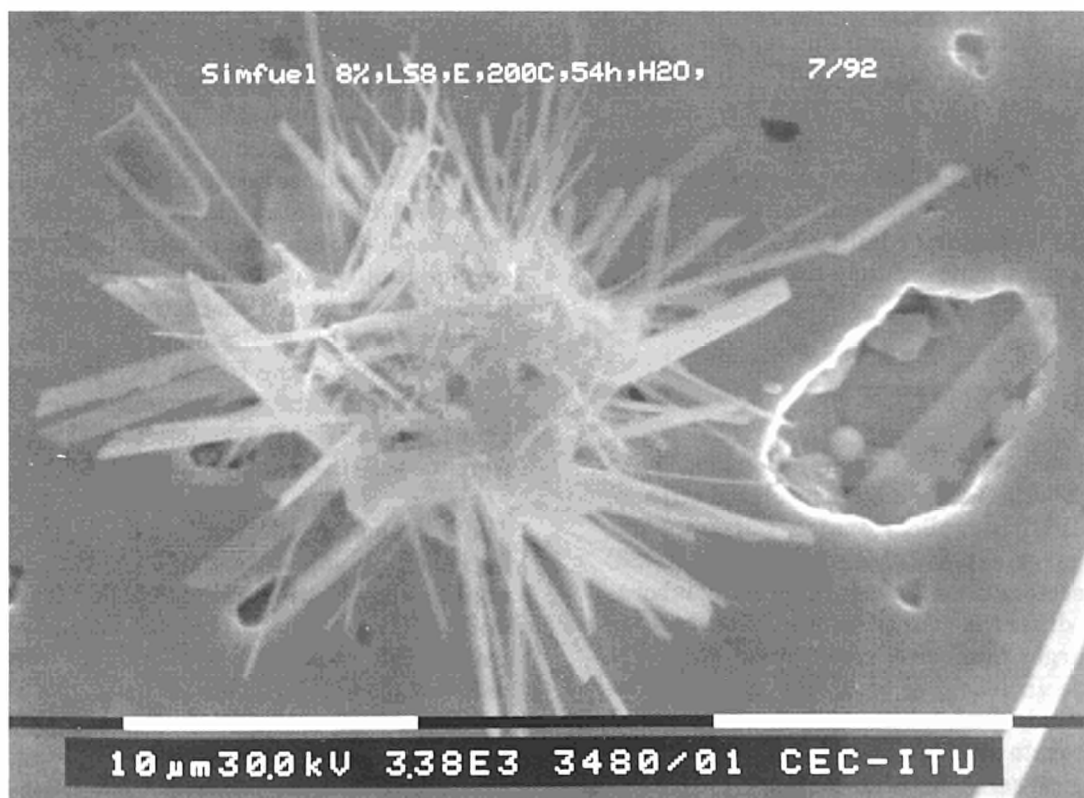


Fig.4.6 SEM picture of 8 % burnup SIMFUEL following leaching at 200 °C in H₂O for 54 h. Re-deposition starts in pores and leads to coverage of a significant fraction of the surface

deposits rich in Ba and Zr. The conclusion is therefore that fission products dissolved in UO_2 reduce aqueous corrosion.

References

- [1] Hj. Matzke and A. Turos, "Mechanisms and Kinetics of Leaching of UO_2 in Water", *Solid State Ionics* **49** (1991) 365
- [2] A. Turos, Hj. Matzke, J. Chaumont and L. Thomé: "Location of Oxygen Atoms in UO_2 Single Crystals by Resonant Scattering of He Ions", *Nucl. Instrum. Methods in Phys. Research* **B66** (1992) 280
- [3] A. Turos, Hj. Matzke, M. Wielunski and L. Nowicki, "Radiation Defects in the Oxygen Sublattice of UO_2 Single Crystals", *Nucl. Instrum. Methods in Phys. Research*, in print
- [4] P.G. Lucuta, R.A. Verrall, Hj. Matzke and B.J. Palmer: "Microstructural Features of SIMFUEL: Simulated High Burnup UO_2 Based Nuclear Fuel", *J. Nucl. Mater.* **178** (1991) 48

Electrochemical Techniques Applied to Natural UO_2 Corrosion in Aqueous Solutions

Introduction

The solubility of uranium dioxide in natural waters and the mechanisms of its dissolution is of interest in the event of engineered barriers being breached when fuel is in final storage in an underground repository. The objective of electrochemical testing, however, is to investigate the initial dissolution mechanisms in aqueous solutions and to pinpoint key species or rate-determining steps in this process.

This characterisation of natural UO_2 in aqueous solutions will be followed by corresponding hot cell experiments with irradiated UO_2 .

Experimental method

Electrode preparation

3 mm thick sections were cut from a pellet of natural UO_2 of 7.5 mm diameter and a 94.5 %

theoretical density (provided by Nukem, Germany). Details of electrode preparation are given in TUAR 90.

Potential-time experiments

The techniques for measuring open circuit rest potential of UO_2 in 3 % Na_2CO_3 , 3 % NaCl and 0.1 M NaClO_4 against saturated calomel electrode, have also been reported in TUAR 90.

Polarisation curves

The 3 % Na_2CO_3 solution was de-aerated by purging with N_2 (99.996 % purity) for 30 to 60 min. The polished electrode (1200 SiC grit and 1 μm diamond paste) was inserted along with the saturated calomel reference electrode and the platinum foil auxiliary electrode in the solution. The electrodes were then connected to the potentiostat (Autostat 251) with a SIS 386 PC provided with Autostat software to control the sweep and to collect and analyse data. The electrode's surface oxidation was removed by precathodisation at -2000 mV (vs SCE) for 5 minutes, then sweeping anodically to +1000 mV and then returning to 0 mV at 30 mV/min. AC impedance measurements were then carried out on the sample at various anodic potentials. The sweep was repeated after reabrasion of the electrode and precathodisation at -2000 mV for 5 min. The sweep rose to +1000 mV and was held at this potential for 1 hour. Then it was removed, rinsed in distilled water, and mounted for examination under the scanning electron microscope (SEM Philips 515) with a Tracor energy dispersive analysis (EDX) system.

AC impedance measurements

A UO_2 electrode (polished as in section 2.3), was inserted in an 3% Na_2CO_3 solution open to laboratory air in the same 3 electrode arrangement as for the polarisation sweeps and the rest potential monitored for up to 700 h. AC impedance measurements were performed at intervals using a potentiostat/electrochemical interface (Capcis March) linked to a frequency response analyser (Capcis Voltech CV 2001) with a computer to control the sweep and collect the data. The voltage input was a 20 mV sine wave and the sweep was performed from 100 kHz down to 10 mHz in logarithmic steps. Linear polarisation tests were also performed on the electrode polarising to ± 10 mV at 10 $\text{mV}\cdot\text{min}^{-1}$ using

the Autostat 251. Polarisation resistance (R_p) values were evaluated from the slope ($\Delta V/\Delta I$) of the data. After 700 h in solution the sample was removed, rinsed in distilled water and prepared for examination by the SEM-EDX.

Results and discussion

Potential-time measurements

Comparison of potential-time measurement with $UO_2 - H_2O - CO_2$ stability diagrams

A summary of results reported in TUAR 90 for the effect of aeration in demineralised water are given in Tab.4.1 and for the effect of pH in NaCl and Na_2CO_3 solutions in Tab.4.2. A stability (E-

Tab.4.1 Influence of deaeration on the UO_2 corrosion potential in demineralised water (pH 8.0 - 9.0)

	Condition	Potential after 60 mins (mV _{SCE})
1	oxygenated before measurement in open vessel	+ 167
2	deaerated before measurement in open vessel	+ 10
3	deaerated before and during measurement in closed vessel	- 238

pH) diagram for the $UO_2-H_2O-CO_2$ system is given in Fig.4.7 based on a data review from Grenthe, Fuger et al. [7] for total $[CO_3^{2-}] = 0.3$ M (approx. 3 %) and total $[U] = 10^{-5}$ M. The domain in which Schoepite ($UO_3 \cdot 2H_2O$) can precipitate out is also outlined.

The UO_2 corrosion potential in demineralised water ($< 0.1 \mu S.cm$) falls with decreasing O_2 levels by upto 400 mV.

Tab.4.2 Potential-time measurements of UO_2 in aqueous solutions

Solution	Aeration (O_2/N_2)	pH	final potential/ mV _{SCE}
3 % Na_2CO_3	N_2	11	-10
"	O_2	11	-10
3 % NaCl	N_2	1	+160
"	N_2	4.6 - 6.4	+40

Using the thermodynamic data from Grenthe et al. the $[UO_2^{2+}]$ equilibrium potentials with $UO_{2.25}$, $UO_{2.333}$ and $UO_{2.667}$ (assuming a $[UO_2^{2+}] = 10^{-6}$ M and a typical pH of 8.5) range from +86 to +424 mV_{SCE}; these are 250 mV more positive than the measured potentials -238 mV to +167 mV_{SCE}. Changes in the value of $[UO_2^{2+}]$ or pH will not account for these differences; assuming these are potential determining and at equilibrium, the measured potentials represent non-stoichiometric UO_{2+x} with x considerably less than 0.25 in continuously de-aerated solution, x approaching 0.25 in the de-aerated solution, and $0.333 < x < 0.667$ in the aerated condition (i.e. at least U_3O_7 in aerated solutions).

Sunder, Shoesmith et al. [1,4] (from XPS Data) have proposed that O_2 uptake by UO_2 occurs rapidly from -400 mV_{SCE} in aqueous solutions, later forming a film of $UO_{2.33}(U_3O_7)$ at the potential of -100 mV to +100 mV_{SCE}. This result would also suggest that $UO_{2.33}(U_3O_7)$ film formation is attained under open and aerated conditions. Sunder and co-workers also note that oxidative dissolution can then take place via an adsorbed UO_2^{2+} intermediate.

In de-aerated 3% sodium chloride (pH 4-6) solution the potential (+40 mV_{SCE}) is slightly higher than that of de-aerated demineralised water (pH 8-9) (+10 mV_{SCE}) but this is attributable to the difference in pH between the solutions and suggests that, as in the case of demineralised water, there is some oxidation of the UO_2 (to less than $UO_{2.25}$) despite de-aeration. In addition, the similarity indicates that no complexation of the UO_2 by chloride ions occurs; chlorides are generally poor ligands of actinide elements [7,8]. At pH=1 a more noble and stable potential of (+160 + 242 =) +402 V_{SHE} is measured. This compares with an extrapolated value for the $UO_2^{2+}/UO_2(cr)$ equilibrium of +410 mV_{SHE};

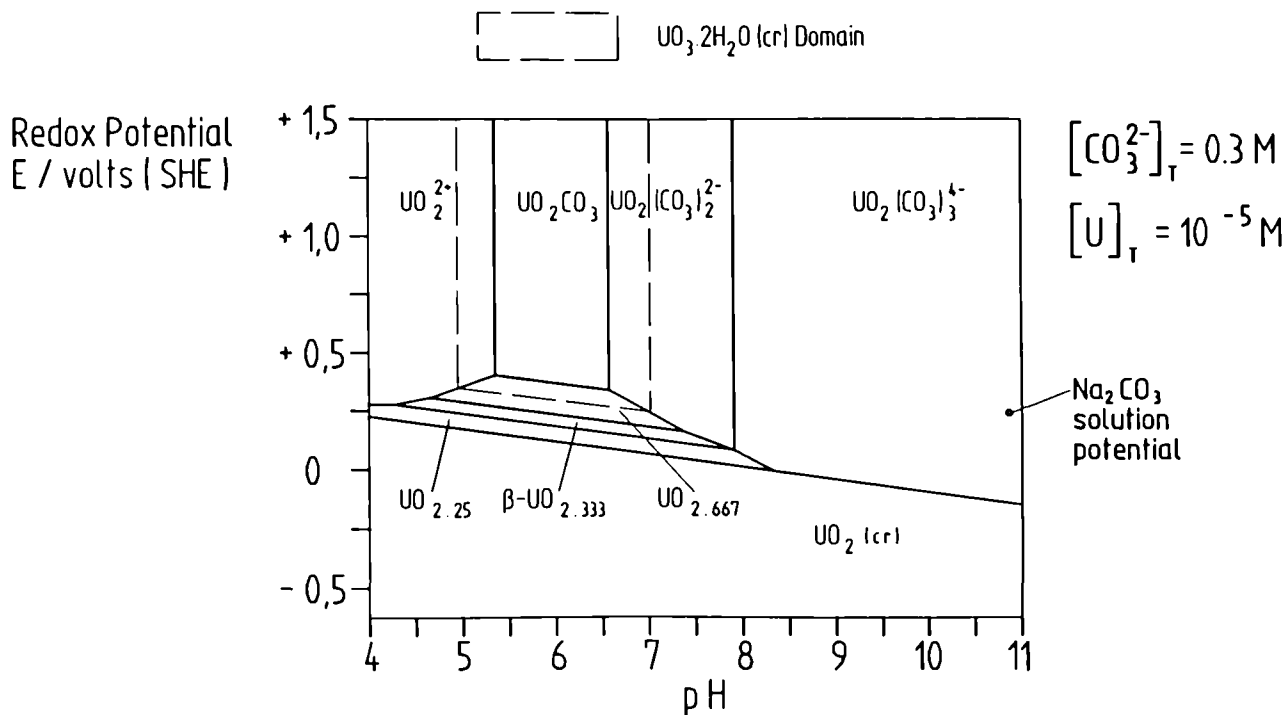


Fig.4.7 Stability (redox potential vs pH) diagram for the $UO_2-H_2O-CO_2$ system at 25 °C [7]

the agreement implies this equilibrium is rapidly attained in acid solutions.

The rest potential of UO_2 in 3% Na_2CO_3 is noticeably more negative but this difference may be due to direct action of complexation by the CO_3^{2-} ion (as they are known complexants of uranium ions [9]) or more likely, due to the alkaline pH of 10.8. The difference corresponds to about 60mV/pH and implies a reaction involving a single proton transfer. Such a fall in the alkaline region (pH > 8.2) would be expected from the stability diagram in Fig.4.7. Sunder et al. [2] also noted a linear fall in UO_2 rest potential with pH in the alkaline region between pH 10 and 14 and in the strongly acid region pH < 2 for chlorate solutions. However it can also be seen that the 3% Na_2CO_3 potentials lie above the equilibrium potentials: measured potentials are 0 to -50 mV_{SCE} (i.e. +242 to +192 mV_{SHE}) at pH 10.8 - 11 compared to -180 to -200 mV_{SHE} for the $UO_2(CO_3)_3^{4-}/UO_2(cr)$ equilibrium. This indicates that oxidation of the UO_2 has taken place (assuming all important species are included on the diagram).

Polarisation curves in 3% Na_2CO_3

The polarisation sweep after pre-cathodisation is seen in Fig.4.8 and shows a corrosion poten-

tial value of -600 mV_{SCE}, (and corrosion current i_{corr} of 170 nA·cm⁻²). Thereafter the current rises showing two points of inflexion at +15 mV ($i = 1.5 \mu A \cdot cm^{-2}$) and at +590mV_{SCE}. During the reverse sweep, the curve down to +590 mV matches that of the upward sweep indicating a reversible reaction, thereafter the anodic current rapidly declines and becomes cathodic. This suggests that the oxide film layer is not directly reduced and this initial oxidation is not reversible.

The stability diagram does not indicate the higher oxides UO_{2+x} as being stable in Na_2CO_3

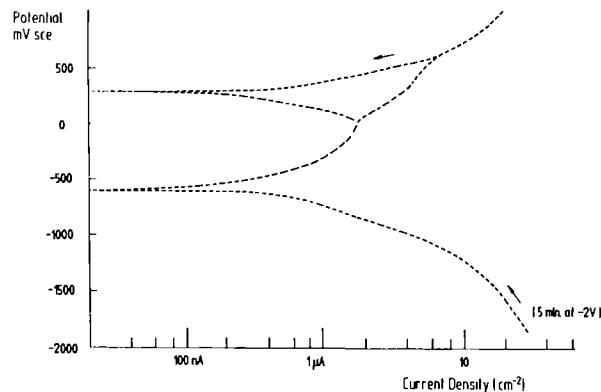


Fig.4.8 Polarisation sweep of UO_2 in 3% Na_2CO_3 solution

solutions above pH 8. However this curve, and other results [6], imply the opposite. Possibly slow dissolution kinetics enable oxide layers to be formed in practice.

Given that higher uranium oxides form in aerated solutions [1,2,4], then this can be interpreted as an initial E_{corr} at -600 mV to -800 mV_{SCE} for $\text{UO}_2 \rightarrow \text{UO}_{2+x}$ ($x \leq 0.10$), and then at +15 to +75 mV_{SCE} the transition to UO_{2+x} to $\text{UO}_{2.33}$ (U_3O_7) occurs, and which is not, or only slowly, reversible. The final reversible transition at +590 mV_{SCE} could be a transition to $\text{UO}_{2.67}$ (U_3O_8) at which point the anodic film may undergo dissolution.

AC Impedance spectra

The impedance spectra for a UO_2 electrode held at various anodic potentials and at rest potentials in 3 % Na_2CO_3 are shown in Fig.4.9. One

can see at the high frequency end ($\omega = 10^4$ Hz - 100 Hz) a low flattened arc with a diameter (i.e. charge transfer resistance (R_{ct}) value) of approx. 2-3 $\text{k}\Omega\cdot\text{cm}^2$ present at all potentials. In the spectrum taken at +2 V_{SCE} this is followed directly by a second low arc (in 0.1 Hz -20 mHz range) of 4 $\text{k}\Omega\cdot\text{cm}^2$ diameter. In the +1 V_{SCE} anodic spectrum a larger arc at slightly lower frequencies compared to the +2 V_{SCE} spectrum is visible (R_{ct} value = 9 $\text{k}\Omega\cdot\text{cm}^2$). This implies the rapid dissolution at +2 V_{SCE} is replaced by another rapid reaction for anodic dissolution, (e.g. $\text{UO}_2 + \text{H}_2\text{O} \rightarrow \text{UO}_3 + 2\text{H}^+ + 2\text{e}^-$ is replaced by UO_2 complexation by carbonate ions [2]).

As the potential is lowered further to +400 mV_{SCE}, the low frequency 0.1 Hz -10 mHz shows a larger arc indicating a slowing of this process ($R_{\text{ct}} \approx 80\text{-}100 \text{ k}\Omega\cdot\text{cm}^2$). At a rest potential value of -74 mV_{SCE}, the low frequency arc has become linear indicating a diffusion-limited pro-

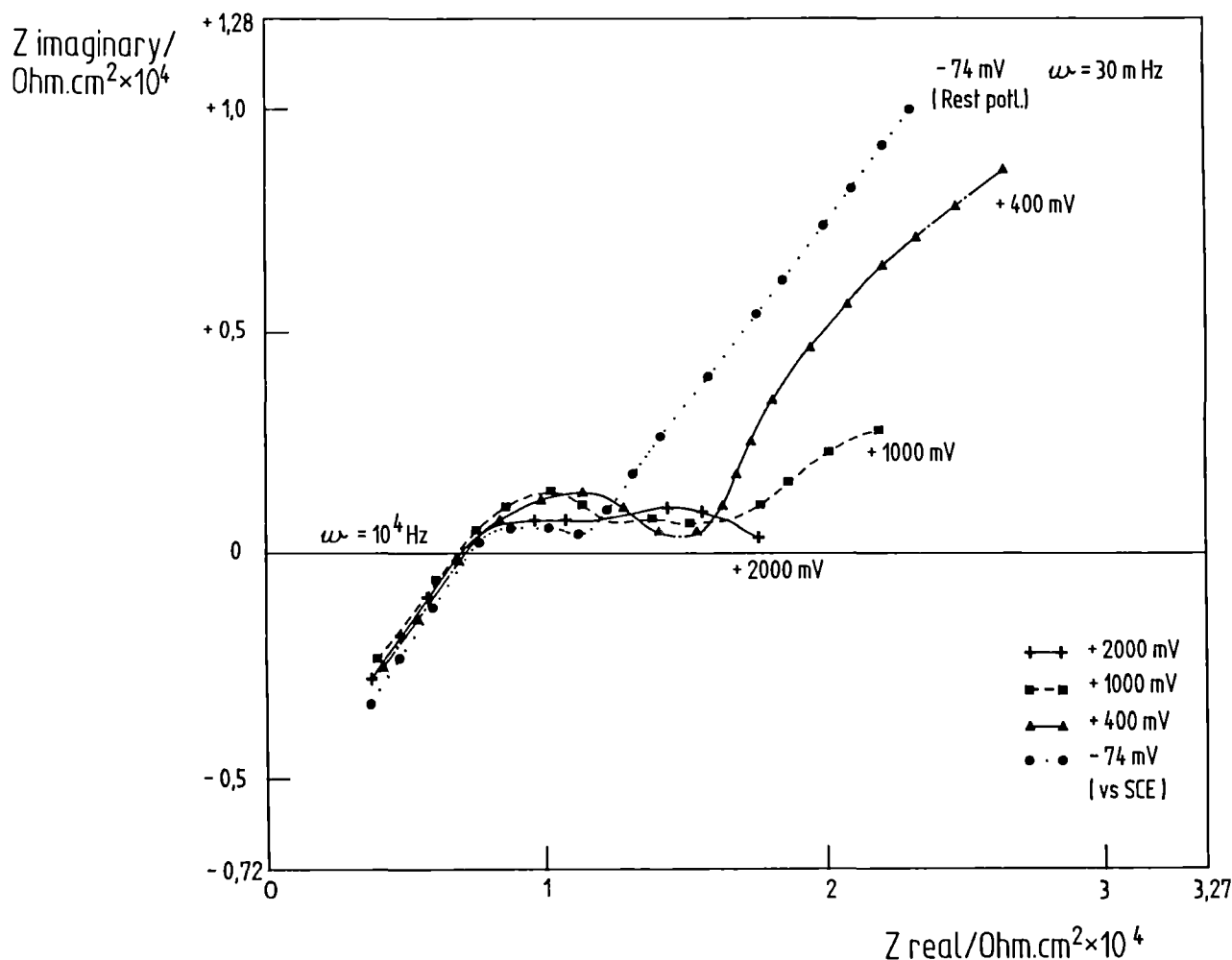


Fig.4.9 AC Impedance spectra of UO_2 in 3 % Na_2CO_3 at various (anodic) potentials

cess, e.g. diffusion of a soluble species (such as HCO_3^-) to the electrode surface. The faster reaction observed at higher frequencies may be one of the initial steps of the carbonate complexing of UO_2 :

$$\text{UO}_2 + (\text{HCO}_3^-)_{\text{ads}} \rightarrow (\text{UO}_2\text{-HCO}_3)_{\text{ads}} + \text{e}^-$$

as all reacting species are adsorbed on the electrode surface [2].

The UO_2 rest potential electrode generally showed a similar profile to that of the polarised electrode at rest potential with a rapid process (high frequency arc with a diameter (R_{ct}) of 2 - 4 $\text{k}\Omega\cdot\text{cm}^2$) and a slow reaction step (with a R_{ct} of 2 - 8 $\times 10^5 \Omega\cdot\text{cm}^2$). Other traces sometimes showed a linear diffusion arm at low frequencies. The polarisation resistance (R_p) from the linear polarisation tests was between 1 and 3 $\times 10^5 \text{ k}\Omega\cdot\text{cm}^2$ which agrees with the R_{ct} values. Using the Stern-Geary equation [5], the depth penetration was calculated as 1 - 4 μm p.a. assuming Faraday's Laws and a conservative factor of 3 to account for the effective surface area of the 94.5 % dense UO_2 .

Leach tests reported by Matzke and Turos [3] at 170-200 $^\circ\text{C}$ attacked layers of UO_2 specimens of 0.4 μm thickness after only 10 - 16 h refluxing (i.e. 200 $\mu\text{m}/\text{year}$) but only very thin layers below 130 $^\circ\text{C}$. The electrochemical measurements indicate the rates of attack at ambient temperatures. Gray and Wilson [6] also noted that the presence of $\text{CO}_3^{2-}/\text{HCO}_3^-$ in 'soft' well-water considerably increased the dissolution of UO_2 particles (from unused fuel pellets) compared to the well water only.

Electron microscopic examination

A micrograph of the starting material is given in Fig.4.10 and of the 700 h rest potential specimen in 3 % Na_2CO_3 solution in Fig.4.11. Two main features can be seen on the exposed specimen. Firstly, small parallel cracks usually at right angles to the polishing striations (Fig.4.11a). These appear to be stress-assisted attack, since these cracks were not present in a control, as-polished UO_2 specimen. The second feature is tufts of needle-like crystals growing from various points (Fig.4.11b). The points of dissolution and crystal deposition are sometimes adjacent to each other. The local surface energy may determine which process dominates at any one site. EDX indicated only uranium present in the crystals which had the crystal habit of schoepite ($\text{UO}_3\cdot 2\text{H}_2\text{O}$) [3].



Fig.4.10 SEM Micrograph of UO_2 electrode as-polished - 5000 x

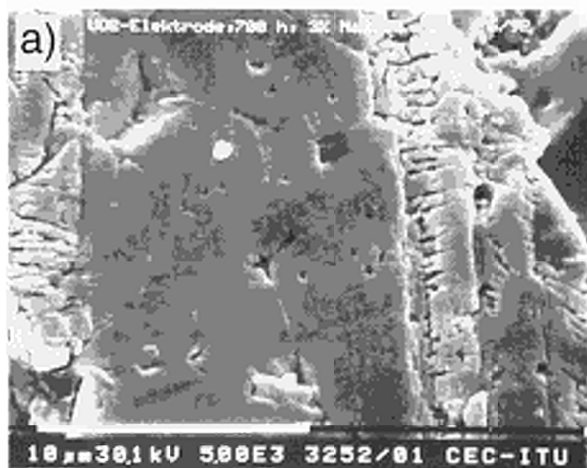


Fig.4.11 SEM Micrographs of UO_2 electrode surface after 700 h at rest potential in 3 % Na_2CO_3 a) 5000 x, b) 3100 x

By contrast in Fig.4.12 (electrode anodised 1 h at +1.0 V_{SCE} in 3 % Na₂CO₃) no needle-like deposits (schoepite) were seen. However grain

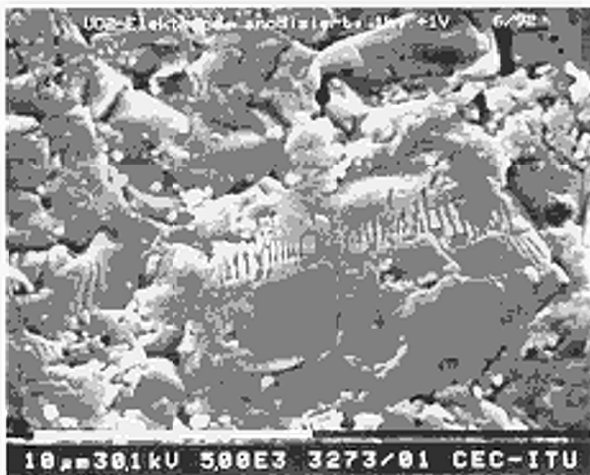


Fig.4.12 SEM Micrograph of UO₂ electrode surface after anodising for 1 h at +1000 mV (SCE) in 3 % Na₂CO₃ - 5000 x

boundaries were clearly visible and pores enlarged as if etched. The parallel stress-assisted attack at right angles to the polishing orientation was also very evident. Sometimes their form suggested that some deposition had occurred. However using the mechanisms proposed by Sunder, Shoesmith and others [1,2,4] it would be expected that under forced dissolution of the UO₂ in Na₂CO₃ solution, the positively-charged intermediates (e.g. UO₂²⁺) would be repelled and slow down the UO₃·2H₂O redeposition compared to rest potential specimens.

Conclusions

The following observations regarding UO₂ corrosion in aqueous solutions may be made:

1. UO_{2+x} is a material whose composition varies in close equilibrium with the oxygen concentrations in aqueous solutions (at least up to UO_{2.33} in oxygenated solutions); its composition is also affected by the solution pH and composition.
2. The polarisation curves imply that UO₂ oxidation initiates at very low potentials with subsequent oxidation to UO_{2.33} and possibly to UO_{2.667}.
3. AC impedance measurements indicate both a more rapid and a slower reaction. The rate-determining step is driven anodically and is replaced by another dissolution reac-

tion at the most anodic potentials. At rest potentials the rate-determining step is diffusion-limited, probably through a species in solution.

4. UO₂ displays localised dissolution at high stress features (i.e. at 90° to polishing marks). The rest-potential UO₂ specimens also showed adjacent needle-like deposits of uranium oxide (presumably hydrated UO₃·Schoepite). This deposition is suppressed at anodic potentials.

References

- [1] S. Sunder, D.W. Shoesmith, M.G. Bailey and G.W. Wallace, *J. Electroanal. Chem.* **150** (1983) 217-228
- [2] S. Sunder, D.W. Shoesmith, M.G. Bailey and G.W. Wallace, 2nd Int. Conf. on Radioactive Waste Management, Sept. 7-11, 1986, Winnipeg, Manitoba
- [3] H.J. Matzke, *A. Turos Solid State Ionics* **49** (1991) 189-194
- [4] S. Sunder, D.W. Shoesmith, H. Christensen, N.H. Miller, B. Leger and M.G. Bailey 1990 Spent Fuel Workshop, Gull Harbour Resort and Conference Centre, Manitoba.
- [5] European Federation of Corrosion Publication No. 4 Guidelines on electrochemical corrosion measurements - Inst. of Metals London 1990
- [6] W. Gray and C. Wilson, 1990 Spent Fuel Workshop, Gull Harbour Resort and Conference Centre, Manitoba
- [7] OECD NEA Chemical Thermodynamics Vol. 1 The Chemical Thermodynamics of Uranium, I. Grenthe, J. Fuger, R. Konings, R. Lemire, A. Muller, C. Nguyen-Trung and H. Wanner Edit. H. Wanner and I. Forest. North Holland-Elsevier 1992.
- [8] S.P. Awasthi, S. Sundaresan, *Indian J. Chem* **20A** (1981) 378-381
- [9] R.J. Lemire, P.R. Tremaine, *J. Chem. Eng. Data* **25** (1980) 361-370

Influence of Granite on the Leaching Behaviour of Waste Glass under Dynamic Conditions

Introduction

It is known that in a repository the leaching of a high-level radioactive waste glass is significantly influenced by the environment (backfill-, canister material and host rock) due to an increased ionic strength and the presence of foreign chemicals such as carbonates and humic acids [1,2].

Although soxhlet extractors are mainly used to obtain results on the leaching of waste forms under standardised conditions [3], an experiment was carried out with the equipment described in TUAR-88, 176, to see the influence of granite on the leaching behaviour of waste glass under dynamic conditions. The French R7T7 glass was leached for 100 days together with different amounts of granite. Tab.4.3 summarises the experimental parameters.

Tab.4.3 Leaching of vitrified waste in the presence of granite (experimental conditions). Test duration: 100 d

soxhlet number	granite powder weight, g	position of granite powder	glass sample	
			weight, mg	estimated surface, cm ²
1	2	sample container	-	-
2	no	-	475	2.35
3	0.2	sample container	447	2.21
4	2	sample container	457	2.26

Experimental results

ICP-MS was used for the determination of the elemental and isotopic composition of the leachate.

The glass components Li and B are mainly found in the leachate. About 10 % of these elements are found in the wash solution of the sample container only if granite is present (Fig.4.13).

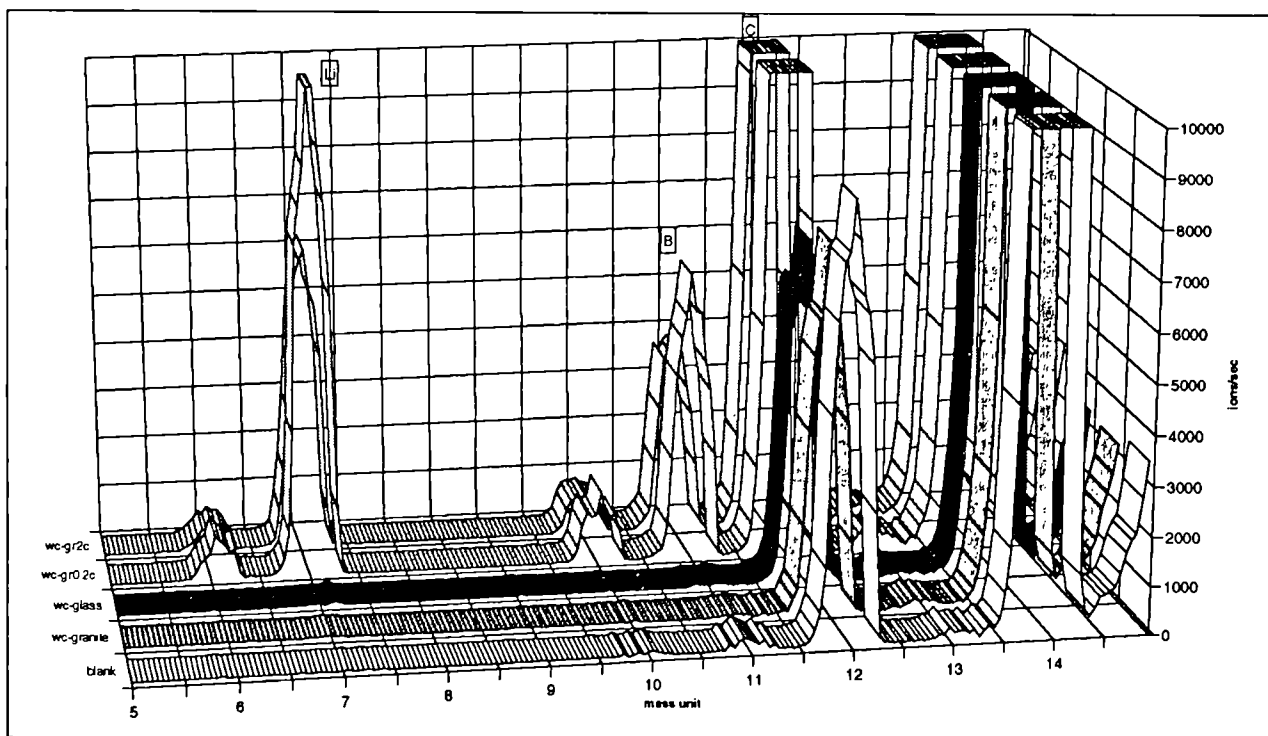


Fig.4.13 Mass spectra of the wash solution of the sample container
 wc: wash solution of the container
 v: heating vessel
 c: sample container
 gr: granite (the number refers to the amount of granite in c)

At the same time an increase of carbon (mass 12) is observed. A very similar result is obtained for Mo (20 % adsorbed on the sample container). The presence of granite has decreased the leaching from waste glass; only for Mo an increase of up to 30 % was observed (Tab.4.4)

Tab.4.4 Influence of granite on the leaching of vitrified waste

element group	element	relative change of leached amount in the presence of granite (2g)	% adsorbed			
			sample container		heating vessel	
			glass	glass + granite	glass	glass + granite
glass components	Li	-48 %	0	10	0	0
	B	-34 %	0	10	0	0
soluble f.p.	Sr	-47 %	1	1	66	89
	Cs	-48 %	1	1	2	45
	Ba	-53 %	2	1	92	98
	Mo	+30 %	0	20	12	1
lanthanides	La	> -90 %	76	18	21	67
	Ce	> -90 %	94	13	3	67
actinides	U	-43 %	34	8	63	89
	Pu	> -90 %	~100	0	0	0
	Np	> -90 %	0	0	~100	0

Sr and Ba are adsorbed on the heating vessel, especially in the presence of granite. The Cs amount adsorbed on the walls of the heating vessel has increased from 2 to 45 % with granite.

Significant amounts of lanthanides were only found in the absence of granite and most of it was adsorbed on the walls of the sample container.

The leaching of U was also reduced in the presence of granite and uranium was found to be mainly adsorbed on equipment walls. Without granite, 1/3 was found in the sample container and 2/3 in the heating vessel, with granite, most of the U is adsorbed on the heating vessel.

Np and Pu could be detected only with glass alone, Np in the wash solution of the heating vessel and Pu in the sample container.

The analysis of the wash solution of the granite powder did not reveal the presence of leached elements.

The quantitative results are summarised in Fig.4.14.

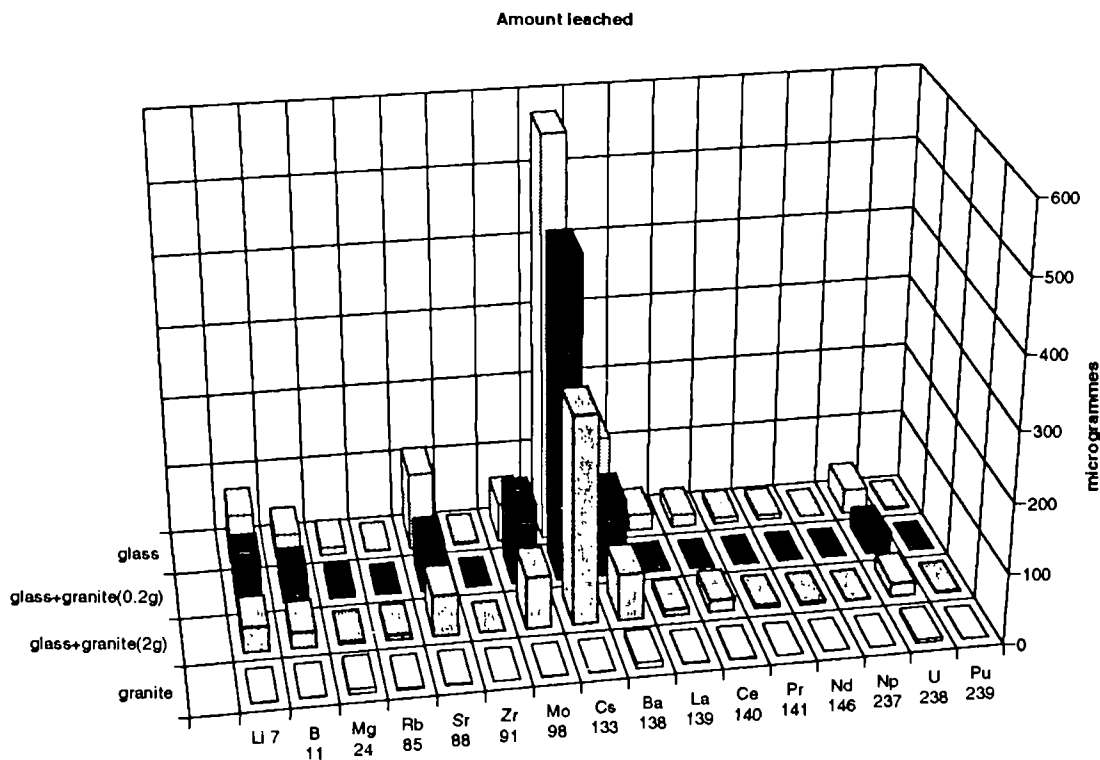


Fig.4.14 Dynamic leaching (soxhlet) of R7T7 glass in the presence of granite (quantitative results)

Conclusions

In contrast to experiments carried out under static conditions [4] where no influence of granite was observed, granite induces under pseudo-dynamic conditions a reduction of the leaching rates of U and of fission products by about 50 % except for Mo, whose leaching rate increases by 30 %. A similar reduction was seen for the glass components Li and B. Low amounts of lanthanides, of Pu and Np are detected in the absence of granite. Pu is almost completely adsorbed on the sample container walls, whereas Np was found in the heating vessel. This could indicate a difference in the chemical behaviour of the leachate inducing a difference in mobility for these two elements which was already observed in migration studies of these elements in different geologic formations [5].

Leaching Behaviour of Irradiated UO₂ under Highly Oxidising Conditions

Experimental conditions

As described in TUAR-91, p. 96, a possible way of studying the influence of the oxidation state of spent fuel on its leaching behaviour is to leach irradiated UO₂ powder in presence of hydrogen peroxide. A second experiment was conducted for a test duration of up to 4 weeks in parallel, with and without immersion. The test conditions are given in Tab.4.5.

The experiment was not completely successful, because the experimental set-up for the oxidation in the vapour phase (cf. TUAR-91, 99) was made of Teflon which could not resist the high

Tab.4.5 Experimental parameters of oxidation of spent fuel (30% H₂O₂ solution) at 200 °C

solution	10 ml H ₂ O ₂		10 ml H ₂ O	
experimental conditions	vapour phase	immersion	vapour phase	immersion
test duration	7 and 28 d	7 and 28 d	28 d	28 d
mechanical behaviour of sample holder	embrittlement of the sample container		embrittlement of the sample container	

gamma radiation level. The Teflon in direct contact with the fuel become brittle and the presence of holes was observed. As a consequence, sample particles were found in solution in some cases. The formation of fluorine species can be assumed, modifying the chemistry during the leaching process. Furthermore, important losses of solution were observed probably as a consequence of the embrittlement of the Teflon containers. Moreover, SEM examinations lead to suspect an interaction between fuel and Teflon. Despite these problems it was possible to recover in each case fuel samples for analysis by SEM and solutions for ICP-MS analysis. However, the malfunctioning of the autoclave has to be taken into account and a new autoclave must be designed. The test will be repeated with the new equipment.

Results

As to be expected no fuel components were found in the leachate, when the fuel was oxidised by vapour, except in some cases, where fuel and, surprisingly, also cladding particles were found, due to the above mentioned problems with the Teflon containers (Fig.4.15).

The quantitative results are summarised in Tab.4.6.

The results of Tab.4.6 were normalised with respect to the initial content in the fuel, the geometrical surface area and the test duration.

$$R_n = \frac{a_{il}}{a_{if}} \cdot \frac{1}{S_a \cdot t} \cdot 100$$

R_n: normalised leach rate in %

a_{il}: content of element i in the leachate in µg/g fuel

a_{if}: calculated content of element i in the fuel in µg/g fuel

S_a: geometrical surface area of the sample in cm² determined from SEM analysis

t: test duration in d

The leach rates of the main components of the leachate are given for samples treated under immersion conditions (Tab.4.7)

According to the low confidence level of the experiments conducted in the vapour phase the results of this report is restricted to the ICP-MS analyses of the leachate and SEM examination of the UO₂ powder leached under immersion conditions.

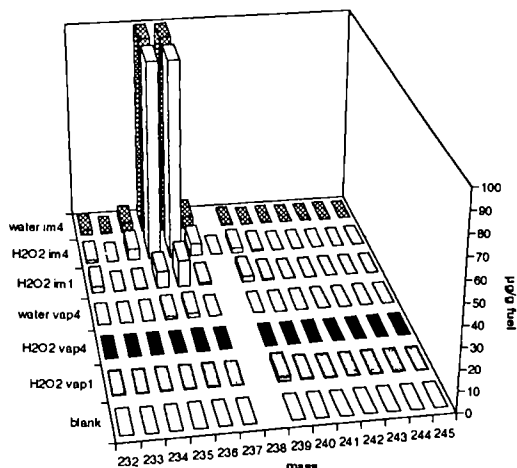
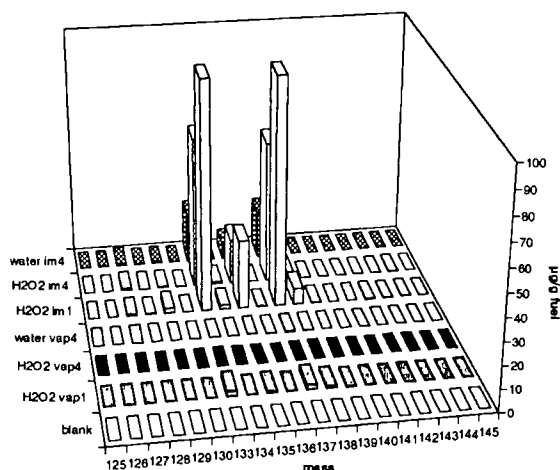
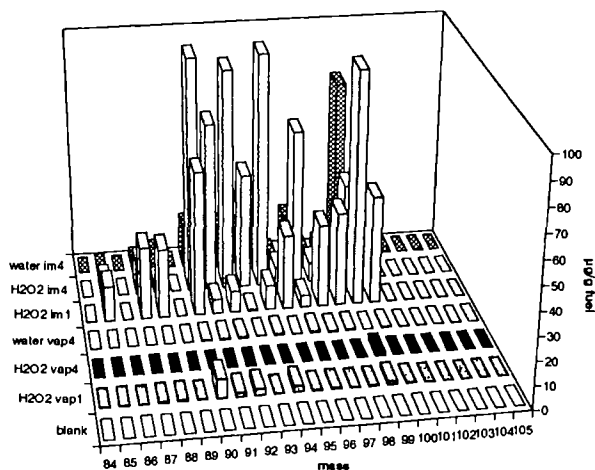


Fig.4.15 Mass spectra of leachates
vap: vapour phase
im: immersion conditions
numbers indicate the test duration in weeks

Tab.4.6 Main components in the leachate in $\mu\text{g/g}$ fuel

element group	element	H ₂ O ₂ im1	H ₂ O ₂ im4	H ₂ O im4
soluble f.p.	Y	0.04	0.04	0.01
	Sr	45.32	6.55	9.41
	Zr	75.77*	547.38	97.37
insoluble f.p.	Rb	45.17	20.11	4.86
	Cs	214.13	132.65	43.40
	Ba	31.06	17.77	4.87
ϵ metals	Tc	327.76	41.37	77.66
	Mo	151.59	35.17	14.81
	Rh	0.14	0.04	0.09
	Ru	0.90	0.30	0.43
	Pd	2.87	6.02	3.02
lan- thanides	La	0.11	0.04	0.07
	Pr	0.05	0.02	0.02
	Ce	0.09	0.06	0.05
	Nd	0.08	0.05	0.13
	Sm	0.12	0.05	0.08
actinides	Np	0.69	3.70	3.57
	U	1500.46	15183.38	18330.59
	Pu	2.05	2.26	0.59
	Am	0.06	0.09	0.02
	Cm	0.02	0.01	0.03

* this Zr has a natural isotopic composition and results from the chemical interaction between fuel and cladding or from impurities of the fabrication

Tab.4.7 Leaching rates of the main components in $\%/cm^2 \cdot d$

element group	element	H ₂ O ₂ im1	H ₂ O ₂ im4	H ₂ O im4
soluble f.p.	Y	0.0002	0.0000	0.0000
	Sr	0.1187	0.0043	0.0062
	Zr	0.2487	0.4492	0.0799
insoluble f.p.	Rb	0.2813	0.0313	0.0076
	Cs	0.2462	0.0079	0.0125
	Ba	0.0552	0.0381	0.0022
ϵ metals	Tc	1.0759	0.0339	0.0637
	Mo	0.1289	0.0075	0.0031
	Rh	0.0015	0.0001	0.0002
	Ru	0.0014	0.0001	0.0002
	Pd	0.0073	0.0039	0.0019
lan- thanides	La	0.0002	0.0000	0.0000
	Pr	0.0001	0.0000	0.0000
	Ce	0.0001	0.0000	0.0000
	Nd	0.0001	0.0000	0.0000
	Sm	0.0005	0.0001	0.0001
actinides	Np	0.0030	0.0040	0.0039
	U	0.0037	0.0094	0.0114
	Pu	0.0006	0.0002	0.0000
	Am	0.0003	0.0001	0.0000
	Cm	0.0021	0.0002	0.0008

As shown by SEM, the fuels analysed were sometimes porous and the geometrical area was not representative of the real area, the former giving a too low value. Thus, the real normalised leach rate will be lower than the leach rate calculated above; although absolute values might not be correct, a comparison between the leach rates of the different elements analysed can be attempted. From this analysis the following conclusions can be drawn:

- The leach rate of U increases with time and is likely to be very sensitive to the oxidation progress of the fuel (see oxidation of UO_2 pellets below 500 °C, this report); no difference appears between H_2O and H_2O_2 leaching. This observation suggests that O_2 in the solution plays a similar determining role in the oxidation process.

The oxidation of UO_2 favours the transfer of uranium to the leachate as U^{6+} which is highly soluble in water. On the contrary, the low Pu^{4+} solubility in H_2O should explain the low leaching rate which we have found experimentally.

Np should exist as Np^{4+} in the fuel and the measured leach rate of this element suggests an unexpected partial bulk oxidation to Np^{5+} .

- Whatever be the leachant
 - the rare earths are not affected
 - the alloying metals Mo, Te, Ru, Rh, Pd display a specific behaviour. As already noticed Tc is very sensitive to the leaching process and, at a lower degree, Mo as well; considering the oxygen potential likely to be reached by the fuel, oxidation of Tc and Mo can be expected; Ru, Rh, Pd appear to be only slightly affected.

- The analyses of the other fission products seem to be incoherent and no correlation between each other or with U could be found. This can be partially explained in the case of Cs, Ba, Rb which are not soluble and show a heterogeneous distribution in the fuel; on the other hand, soluble fission products were not leached concurrently.

- Furthermore, white precipitates, apparently $\text{UO}_4 \cdot x\text{H}_2\text{O}$, were found in the leachate (leaching under H_2O_2 immersion condition) (Fig.4.15).

- Assuming that the experimental conditions are such, that a comparison between leaching tests under vapour and under immersion conditions is possible, then the UO_2 powder seems to

remain unaffected by the preceding leach tests.

References

- [1] R.J. Lemire, F. Garisto, *Radiochim. Acta* **58/59** (1992) 37
- [2] W. Lutze, B. Grambow, *Radiochim. Acta* **58/59** (1992) 3
- [3] Material Characterisation Centre, MCC-5S Soxhlet Leach Test Method, PNL-3990 (1981)
- [4] N. Godon, E. Vernaz, J.H. Thomassin and J.C. Touray, *Mat. Res. Soc. Symp. Proc.* **127** (1989) 97
- [5] G. Bidoglio, M. D' Alessandro, *EUR* **11914** (1988) 43

Non-Destructive Characterisation of Spent Fuel

Introduction

UO_2 and MOX-fuel rods irradiated in the BR3-reactor in Belgium will be used to carry out leach tests on fuel rod segments with pre-set defects. Five UO_2 and five MOX fuel rods were delivered to the Institute for this purpose in 1992.

The characterisation of these materials has started and this report describes the results of NDT examinations of the UO_2 fuel rods.

Fuel data

The fuel was fabricated by the company Franco-Belge de Fabrication de Combustible (FBFC) in Dessel, Belgium. UO_2 was obtained from UF6 by the process ADU. The initial enrichment was 8.26 wt %. The main fuel characteristics are given in Tab.4.8.

Tab.4.8 Fuel and pellet data

Fuel pellet	Mean diameter [mm]	8.04
	Height [mm]	12.22-12.41
	Weight [g]	6.323-6.419
Fuel	Mean density [g/cm^3]	10.34-10.35
	[% TD]	94.3-94.6
	Boron equivalent [ppm of B]	0.6
	Stoichiometry [O/M]	1,997
	Mean grain size [μm]	11

Cladding data

The Zry-4 tubes were produced by VDM-AG, Werk Duisburg (FR of Germany), from an ingot provided by Teledyne Wah Chang, Albany, Oregon, USA. The tubes were heat treated at 540 °C for 2.5 h. The main characteristics of the cladding are given in Tab.4.9.

Tab.4.9 Cladding data

Alloy	Zry-4
Outer diameter [mm]	9,50
Internal diameter [mm]	8,24
Wall thickness	0,58

Irradiation conditions

The 5 UO₂-fuel rods were irradiated in the same assembly, in four cycles corresponding to 31544 effective full power hours (EFPH), from June 22, 1979 to June 30, 1987.

The mean and the maximum calculated burn-ups reached by the 5 rods are given in Tab.4.10.

Tab.4.10 Calculated burn-up

Rod No.	Burn-up [GWd/t] (Average)	Burn-up [GWd/t] (Maximum)
1 - 556	41.5	51
1 - 650	41.8	51.4
1 - 854	42.3	52
1 - 820	41.6	51.1
1 - 551	43.3	53.2

Post-irradiation examinations

Visual examination

The visual examination of the outer surface of the cladding displayed an uniform adherent black oxide films and the absence of macroscopic defects.

Defect determination by eddy current

No cladding defects were detected.

Profilometry

All the rods showed a smooth profile with a slight decrease in the mean diameter in the middle of the rods indicating creepdown. The nominal diameter was 9.5 +/- 0.01 mm. In Tab.4.11 the creepdown has been calculated from the outer diameter value and the oxide layer thickness.

Tab.4.11 Outer diameter variation and creepdown

Rod No.	Outer diameter variation $\Delta d/d$, [μm]	Average creepdown, [μm]
1 - 556	-40	-66
1 - 650	-32	-60
1 - 854	-35	-61
1 - 820	-28	-57
1 - 551	-25	-51

Rod length

All the rods presented a slight radiation induced growth. The results of the measurements are presented in Tab.4.12.

Tab.4.12 Rod length and irradiation growth of the rods

Rod No.	Length [mm]	Growth [%]
1 - 556	1139.05	0.27
1 - 650	1139.58	0.32
1 - 854	1139.65	0.32
1 - 820	1139.30	0.29
1 - 551	1139.55	0.31

Axial fission product distribution (gamma scanning)

The isotopes detected were: Cs-134, Cs-137, Ru-106 and Ce-144. The axial distribution of burn-up estimated from the Cs-137 distribution agrees well with the calculated values by Belgonucléaire. The axial profile of each rod shows a reduced activity in the vicinity of the spacers (central zone).

Oxide layer thickness

All rods showed a uniformly distributed oxide layer whose average thickness is given in Tab.4.13.

Tab.4.13 Oxide layer thickness

Rod No.	Oxide Layer Thickness [μm]
1 - 556	40
1 - 650	42
1 - 854	40
1 - 820	43
1 - 551	40

Gas analysis (puncturing)

The results of the elemental and isotopic composition of the filling gas He are collected in Tab.4.14a and 4.14b. The results include helium

Tab.4.14a Composition of the filling gas

Pin Nr.	Composition of the filling gas [%]												
	He	N ₂	O ₂	Ar	CO ₂	Kr-83	Kr-84	Kr-85	Kr-86	Xe-131	Xe-132	Xe-134	Xe-136
1-556	98.8	0.05	0.05	0.05	0.03	0.02	0.05	0.01	0.08	0.1	0.18	0.28	0.36
1-650	98.5	0.17	0.08	0.03	0.09	0.02	0.05	0.01	0.08	0.11	0.21	0.31	0.38
1-854	98.9	0.12	0.08	0.03	0.04	0.01	0.03	0.01	0.06	0.08	0.16	0.23	0.28
1-820	98.9	0.09	0.06	0.05	0.04	0.01	0.03	0.01	0.06	0.08	0.15	0.22	0.28
1-551	98.7	0.07	0.05	0.03	0.04	0.02	0.05	0.01	0.08	0.1	0.2	0.31	0.38

Tab.4.14b Normal gas volume of the filling gas, Xe/Kr-ratio, free volume and relative gas release

Pin No.	Gas Vol. (NTP) [cc]	Xe-Vol. (NTP) [cc]	Kr-Vol. (NTP) [cc]	Xe/Kr ratio	Free volume [cc]	Gas release ratio [%]
1-556	150.18	1.37	0.22	6.19	6.65	0.3
1-650	143.56	1.44	0.23	6.38	6.67	0.35
1-854	136.38	1.02	0.15	6.87	5.8	0.21
1-820	150.03	1.10	0.17	6.50	6.66	0.25
1-551	145.42	1.44	0.24	6.1	6.46	0.36

and N₂, O₂ and CO₂ as impurities resulting from the filling gas procedure. Argon was used during the welding process during fabrication.

Future work

The values found for the fission gas release ratio are similar to those measured on BR3 fuel rods irradiated to a burn-up of 25000 MWd/t and a higher release could be expected. The fuel microstructure examination will already bring information on the thermal behaviour of the fuel; an additional Xe, Nd determination by EMPA will be carried out in order to confirm the results of the filling gas analysis.

Non-destructive testings suggest the absence of cladding defects. The next step of the characterisation study will be a fuel microstructure analysis as a function of the burn-up distribution.

The fuel rods will be cut in segments, 15 cm in length, with pre-set defects for leach tests.

Due to the strong axial burn-up variation, only the fuel rod zone located between the maximum burn-up and 0.80 max. burn-up is suitable for the leaching experiments.

The refabrication of these fuel rod segments including fuel retrieval, inner and outer surface cleaning, end plug TIG welding, pre-set defect fabrication and their characterisation is under way.

Oxidation of Unirradiated UO₂ Pellets below 500 °C

The investigation of the oxidation in air of unirradiated UO₂ pellets was continued. Details of the starting material and of the operational conditions can be found in Ref. [1]. The results of isothermal oxidation runs in a thermobalance were obtained in the form of weight changes as a function of time and were related to the heterogeneous reaction:

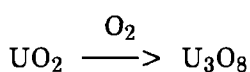


Fig.4.16 represents the oxidation ratio α (ratio between the weight change at the time t and the

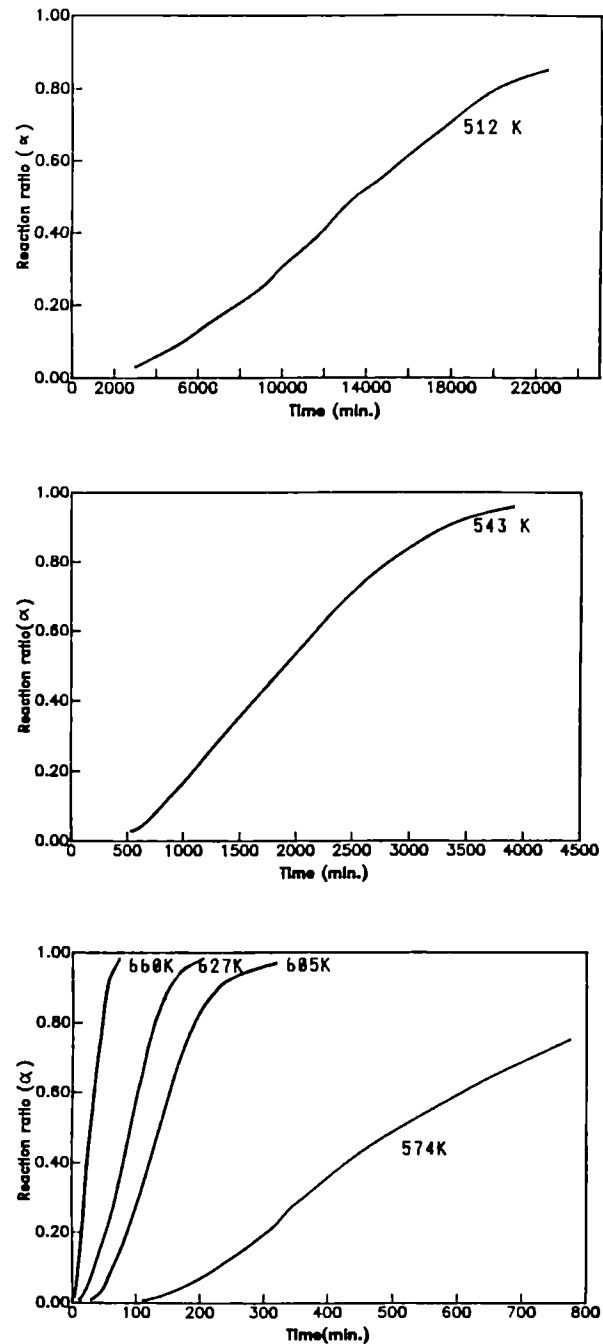


Fig.4.16 Reaction ratio as a function of time for various temperatures

total weight change) as a function of time for various temperatures.

Metallographic, X-ray and TEM analysis of the oxidised material showed that the reaction interface (between uranium oxide and oxygen) was represented by a layer, 50 to 100 μm thick, in which oxygen diffusion controlled processes first caused the nucleation of U₄O₉ at the grain boundaries and then bulk diffusion and nucleation of a U₃O₈ phase. The transition from U₄O₉

to U_3O_8 was accompanied by a large volume variation which caused the disintegration of the reaction layer. In this manner, the oxidation interface was continuously renewed, the specific surface of the oxidising material increased and finally the pellet decreased in size and disintegrated before the oxidation reaction was completed. The intermediate oxidation products consisted of UO_2 , U_4O_9 and U_3O_8 whereas the final product was U_3O_8 powder. Similar results were obtained by oxidation of polycrystalline UO_2 in water vapour at temperatures between 170 °C and 387 °C.

The oxidation reaction sequences are rather complicated and the evaluation of the results would require the use of sophisticated models and calculation procedures not available at present. For this reason the results were currently interpreted on the basis of simple conventional first order kinetic plots. The reaction rate was calculated from the plots of

$$\log_{10} \frac{1}{(1-a)}$$

vs. time. Each graph in Fig.4.17 consists of two straight lines and the "knee" between them is an indication that the overall reaction can be divided at least into two stages in which the oxidation process occurs at different rates. This is in agreement with the results reported in Ref. [2] concerning the oxidation in air of natural UO_2 spheres (120 μm in diameter) at temperatures between 320 °C and 380 °C. It is not the aim of this study to investigate the relationship between the stages and the reaction type. The Arrhenius plot of the rate constant k of the first

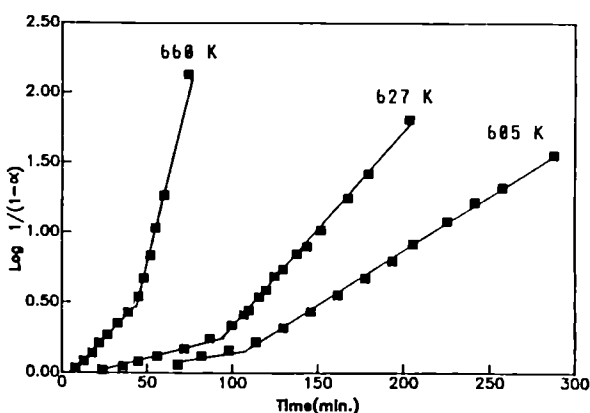


Fig.4.17 Example of plot of $\log_{10} \frac{1}{(1-a)}$ as a function of time (example,

and the second reaction stage are represented in the Fig.4.18. The equations of the rate constant are:

$$k = 2.954 \cdot 10^8 \exp \left(\frac{-31000}{RT} \right)$$

for the first stage (before "knee") and

$$k = 2.705 \cdot 10^8 \exp \left(\frac{-29445}{RT} \right)$$

for the second stage. The values of the activation energies, 31 and 29 Kcal/mole respectively, indicate that the lines are almost parallel and therefore that the oxidation processes occurring in the two stages are essentially the same and proceed only with different rates.

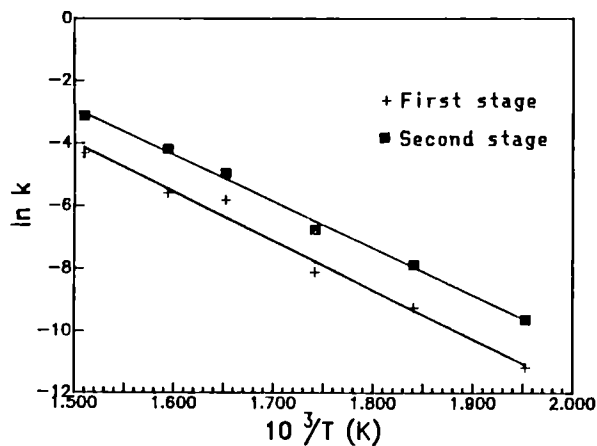


Fig.4.18 Arrhenius plot of the reaction rate constants

The results of this work allow the following conclusions to be drawn:

- grain boundary diffusion controlled processes largely contribute to the transport of oxygen, in addition of bulk diffusion, during the oxidation of polycrystalline uranium dioxide.
- oxidation of UO_2 pellets in dry air or in water vapour at temperatures between 170 °C and 390 °C takes place in a less than 100 μm thick interface and causes the formation of U_4O_9 and U_3O_8 at the grain boundaries and the disintegration of the oxidising material before oxidation is complete.
- the final product of the oxidation in air and water vapour is U_3O_8 . Intermediate products are mixtures of UO_2 , U_4O_9 and U_3O_8 .

References

- [1] TUAR-91 (1991) 104
- [2] K. Harrison, *J. Nucl. Mater.* **23** (1967) 121

Low-Temperature Oxidation of High Burn-up Spent Fuel

Introduction

During the last years the problem of the low-temperature oxidation of spent fuels has been thoroughly treated in the literature especially by American [1-3] and Canadian authors [4-5], in relation with the potential risks of fission gas release in dry-repositories, when cladding breaches appear during fuel disposal. In this case UO_2 will react with air at temperatures ranging between 50 and 300 °C [5], where a matter of concern is the potential formation of the U_3O_8 phase, which due to its large volume increase (36 %) would exert a considerable mechanical stress on the cladding, thus enhancing the risk of fission gas release if cladding rupture occurs.

In this respect however, long-term oxidation tests with CANDU spent fuel (30 GWd/tU) have shown that in the temperature range 175 - 200 °C no U_3O_8 -phase is formed, at least up to exposure times as long as 40000 hours [6]. At these temperatures, the only oxidation product formed was a U_4O_{9+y} -phase, which grew coherently along the grain boundaries, and whose homogeneity range extended up to O/M ~2.4 [1,2]. The lack of U_3O_8 nucleation can be attributed to the extremely slow formation kinetics of this phase in the temperature range considered [4].

This last point is however in contradiction to results of other oxidation tests in air with unirradiated UO_2 performed worldwide and at ITU (see preceding chapter of this report), which indicate that at temperatures of about 200 °C, though the phase U_4O_9 appears at an intermediate step, the final oxidation step leads to the formation of the U_3O_8 phase.

Therefore, in order to elucidate the causes for the apparently different oxidation processes in irradiated and non-irradiated UO_2 , new low-temperature oxidation tests (air, 200 °C) with high burn-up fuel have been started. Goals of these experiments will be the determination of

the crystal structure, density and morphology of the oxidation phases appearing, and the assessment of the oxidation kinetics, with consideration of the influence of the prior fuel microstructure (porosity, grain size and grain restructuring) and burn-up.

Preliminary results

First results of preliminary tests performed with a LWR fuel of 40 GWd/tU burn-up, show that after exposure to air at 180 °C during 1 week, the only phase formed was U_4O_9 . This phase nucleated at the grain boundaries and grew towards the grain interiors in the form of inter-linked needles and platelets (Fig.4.19).

Central regions of the fuel with larger porosity and more grain boundary decoration (pores) showed a larger fraction of U_4O_9 -phase formed, indicating that the oxidation rate is enhanced as the intergranular porosity increases. Similar results were found with CANDU fuel [1].

Tests under performance

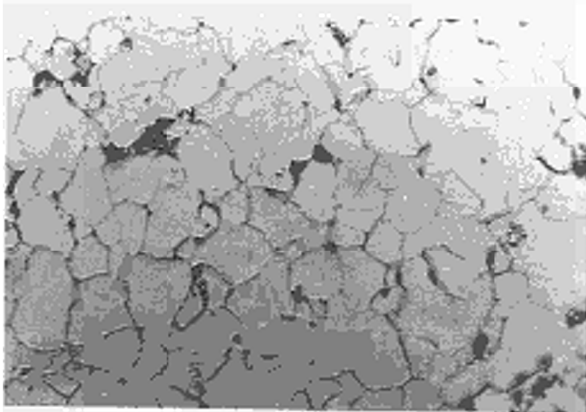
Long-term oxidation tests with LWR fuels of 50 GWd/tU burn-up (200 °C, 1 - 3 months) are still under evaluation. During these tests samples are retrieved from the apparatus every week and the corresponding weight gain, density, X-ray structure and microstructure are determined.

It is also planned to perform thermogravimetric analyses (continuous weight variation) under controlled p_{O_2} conditions, in order to determine the composition limits (O/M) of the oxidation phases. The phase characterisation will also be completed by XRD-analysis as a function of temperature and p_{O_2} . In this context, a point of interest will be the determination of the possible metastability range of the phase U_4O_9 , as it is suggested in Fig.4.20.

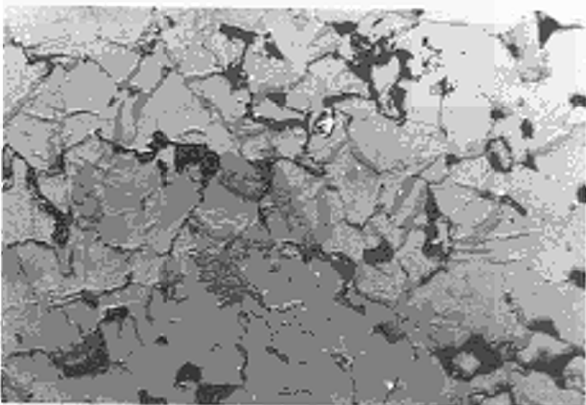
References

- [1] L.E. Thomas et al., *J. Nucl. Mater.* **184** (1991) 117
- [2] L.E. Thomas et al., *J. Nucl. Mater.* **166** (1989) 243
- [3] R.E. Woodley et al., *Nucl. Technol.* **85** (1989) 74
- [4] P. Taylor et al., *J. Nucl. Mater.* **189** (1992) 116
- [5] P. Taylor et al., *J. Nucl. Mater.* **168** (1989) 70
- [6] P. Taylor et al., *J. Nucl. Mater.* **183** (1991) 105
- [7] R.E. Einziger et al., *J. Nucl. Mater.* **190** (1992) 53

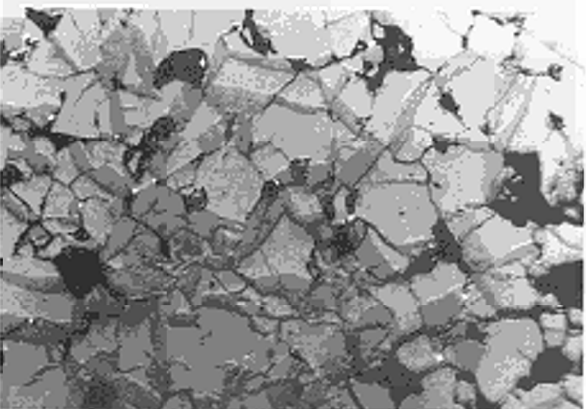
UO_{2+x} -phase starts to form at grain boundaries



$r/r_0=0.5$



$r/r_0=0.3$



$r/r_0=0.0$

Fig.4.19 Formation of U_4O_9 -phase at different radial positions in an air-oxidated fuel cross section (180 °C/1 week)

Origin of Shaded Zones in Irradiated UO_2 Fuel Cross-sections after Chemical Etching

Introduction

A typical feature of irradiated fuels at high burn-up (above 30 GWd/tU) is the appearance of shaded concentric zones in the ceramographic cross-sections after etching, showing an intense fine intragranular porosity or pitting at high magnifications, which does not affect however the grain boundaries (denuded zones) [1-4]. These dark regions whose radii are burn-up dependent, are attributed to the existence of intragranular fission gas bubbles, which become evident after chemical attack due to their increase in size. In addition, since any measurable local Xe, Cs release is concentrated within these dark zones, they are used also as temperature indicators for the onset of gas-bubble precipitation and fission gas release [1-3].

However, it is not completely clear whether these shaded zones are caused by interaction of the etching solution with preexisting submicroscopic bubbles, or with subsized second phase precipitates or structural defects accumulated during irradiation, like, for example, dislocation loops.

To clear up this point, new detailed SEM examinations were performed at the Institute on a BR3 fuel (BU ~ 27 GWd/tU), the results of which are described below.

Material selection and sample preparation

BR3 fuel with a burn-up of 27 GWd/tU was selected for this study because of its rather extended central shaded zone appearing after etching at positions $r/r_0 = 0$ to $r/r_0 \sim 0.35$ (Fig.4.21). An enlarged view of this zone is shown in Fig.4.22, where the as-etched intragranular substructure becomes evident.

To elucidate whether the intragranular substructure was present before etching or not, a fracture surface analysis was necessary. An important point of the sample preparation was to provide a fracture surface with as large a fraction of transgranular fracture mode (cleavage) as possible, in order to investigate the grain interiors. For this purpose, a remotely controlled

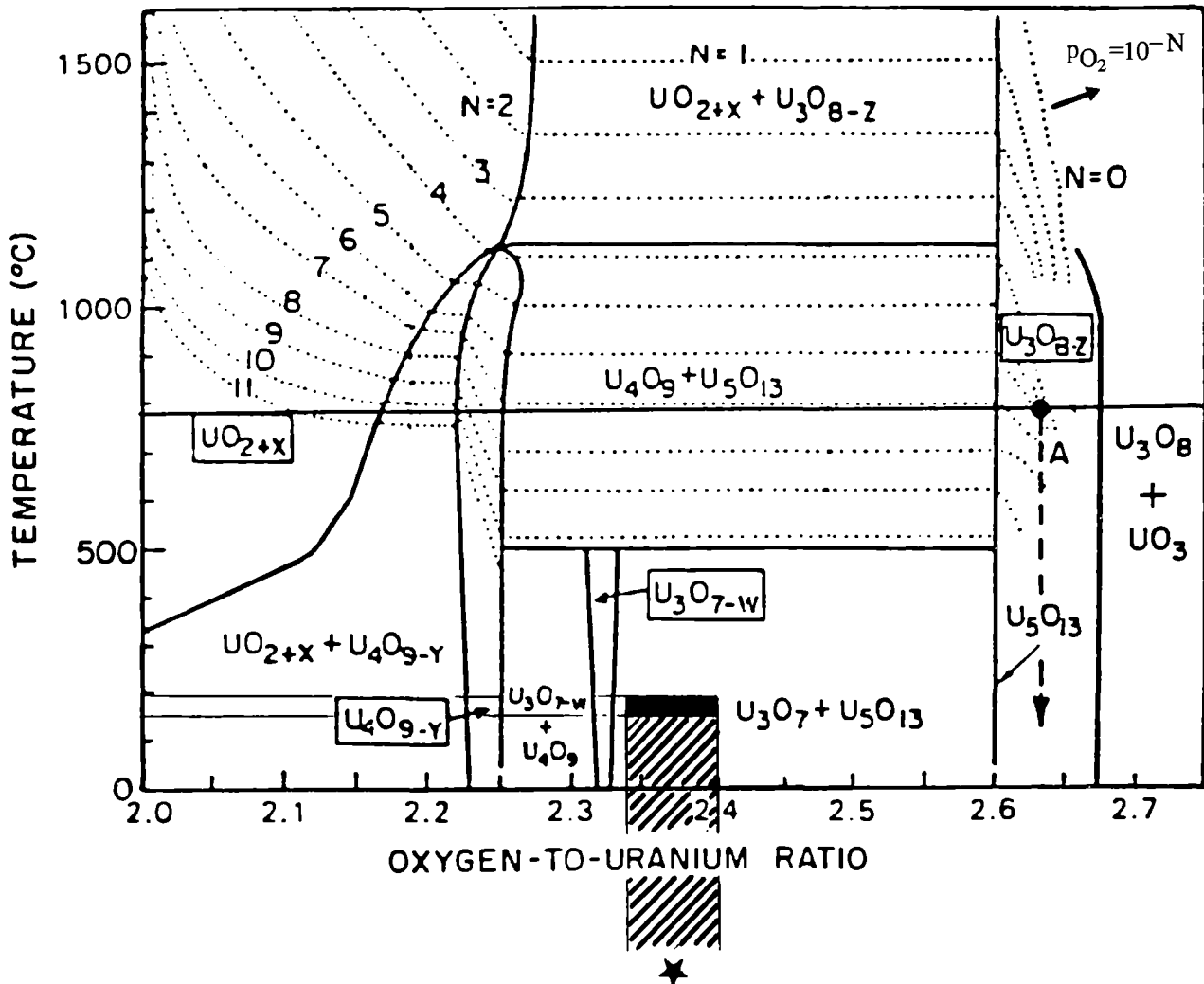


Fig.4.20 Phase diagram of unirradiated UO_2 . Effect of temperature and oxygen partial pressure on the degree of oxydation of uranium

* Composition range of final oxidation-products after exposure of irradiated UO_2 ($\sim 30 \text{ GWd/tU}$) to air (1 atm) at 175-195 °C (test duration : 8000 to 40000 hours) XRD structure : U_4O_9 - Ref. [7]

fracturing device was developed (Fig.4.23) which is able to release an instantaneous load of up to 25 kg/mm² to the surface of a metallographic sample via a hard alloy chisel, producing a localized impact fracture.

Since the applied impact load was far above the fracture strength of UO_2 ($\sim 14 \text{ kg/mm}^2$ [5]), at least 80 % of the fracture obtained was of transgranular nature (Fig.4.24). The polished and the fractures surfaces were then thoroughly inspected by SEM in the as-received condition. After cleaning and flash immersion of the sample in a $\text{H}_2\text{O} : \text{H}_2\text{O}_2 : \text{HNO}_3$ etching solution, in order to promote the intragranular attack, a second SEM inspection of both surfaces was performed.

Results

As can be seen in Fig.4.24, the transgranular fracture surface of the central part of the fuel (dark zone), did not reveal any intragranular fine porosity before etching, at least within the limits of resolution of the SEM equipment (500Å).

However, after a slight chemical etching, fuel regions inside the dark zone showed grains affected by etch-pitting (Fig.4.25) whereas outside the dark zone no etch-pitting was observed (Fig.4.26). The etch-pitting effect was evident not only on polished surfaces (Fig.4.25), but also on transgranular (cleaved) fracture surfaces

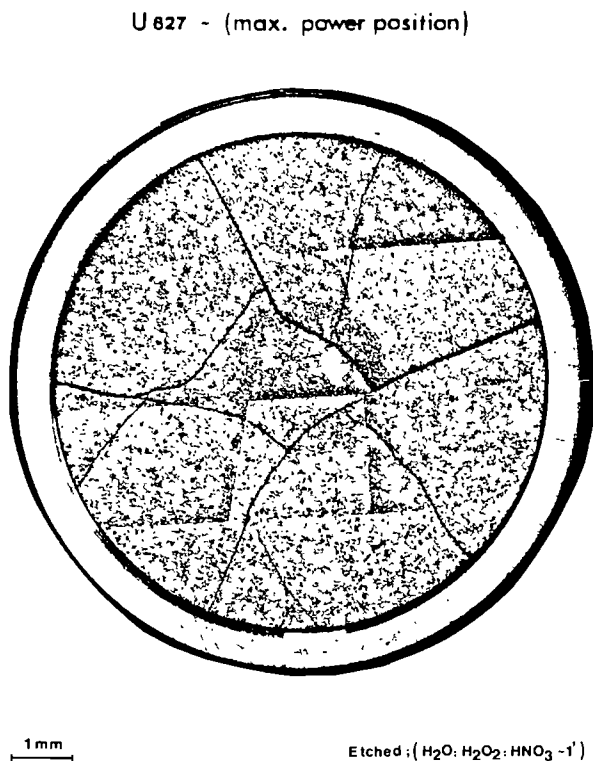


Fig.4.21 Ceramographic cross-section of a BR-3 fuel ($BU \sim 30 \text{ GWd/tU}$). Dark zone in central position ($r/r_0 = 0$ to $r/r_0 = 0.35$) appearing after chemical etching with $H_2O:H_2O_2:HNO_3$ solution

(Fig.4.27). The pits inside the grains were preferentially oriented, constituting a regular array which seemed to depend on the crystallographic orientation of each grain (Fig.4.28,4.29). They appear as equilateral triangles, a morphology which is typical of the dislocation etch-pits in the CaF_2 structure [6].

Regarding the fracture type, it is necessary to point out that the main fracture mode was transgranular, but at the periphery of the fuel pellet it was predominantly intergranular. When this part of the fuel was exposed to acid etching, a grain boundary decoration became evident, indicating the possible presence of a second phase growing up on the grain faces (Fig.4.30).

Discussion

According to our observations the origin of the dark zones in high burn-up fuels after etching is to be attributed to an etch-pitting effect, which does not necessarily denote the presence of intragranular fission gas bubbles, as previously assumed in the literature [4]. In our opinion, the

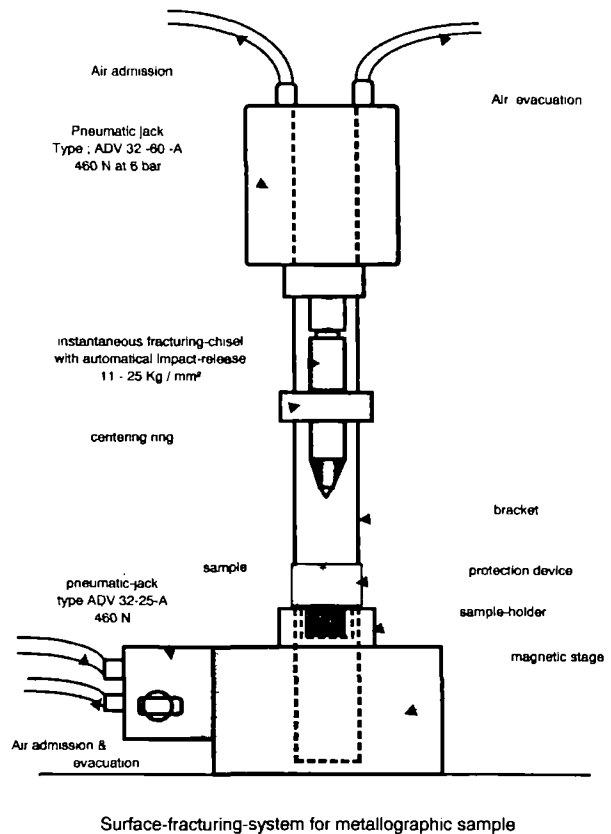
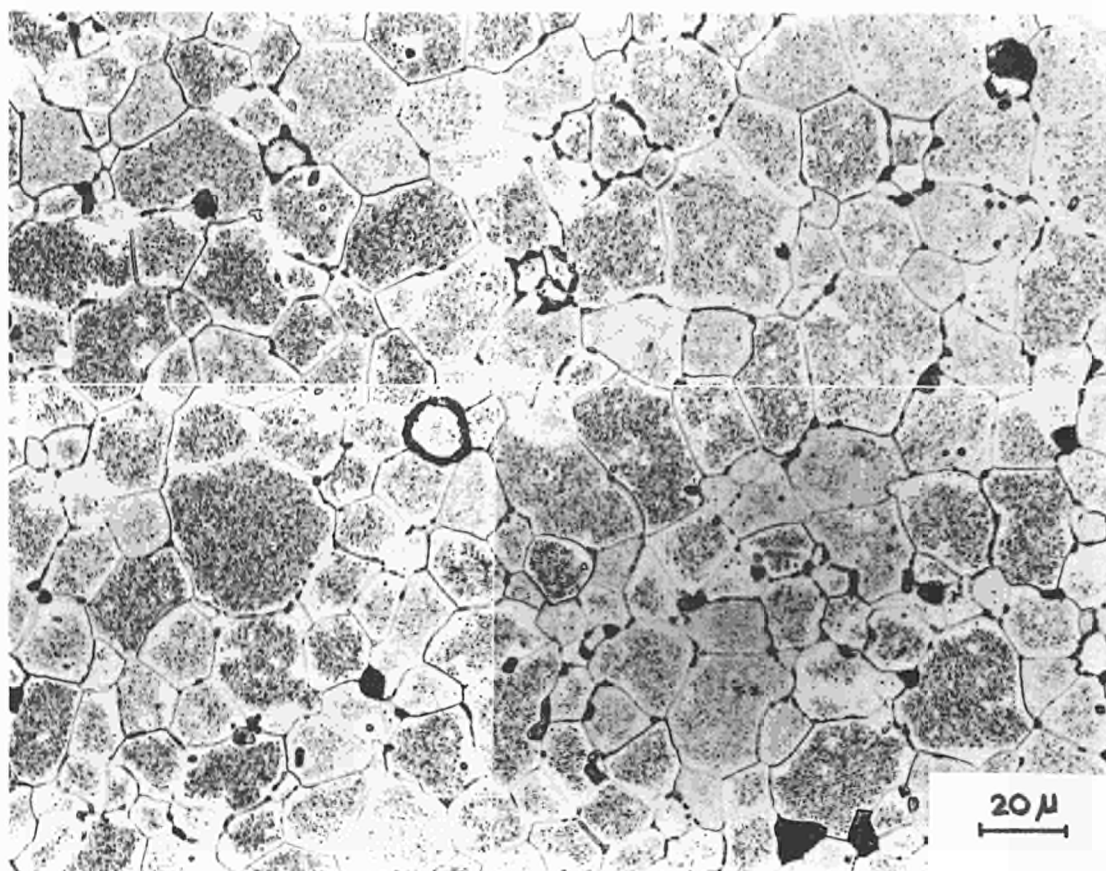


Fig.4.23 Remote controlled apparatus for the localized impact fracture of polished fuel cross-sections

described effect is caused by the interaction of the etching solution with dislocation lines or loops existing within the UO_2 grains. In this respect it is worthwhile to note that the obtained etch-pit pattern is similar to that of dislocation etch-pits in CaF_2 , an ionic crystal whose structural space group is the same as that of UO_2 . Another possible cause for this effect could be the interaction of the acid with coherent second-phase precipitates [6]. Complementary TEM examinations would bring additional information to these hypotheses.

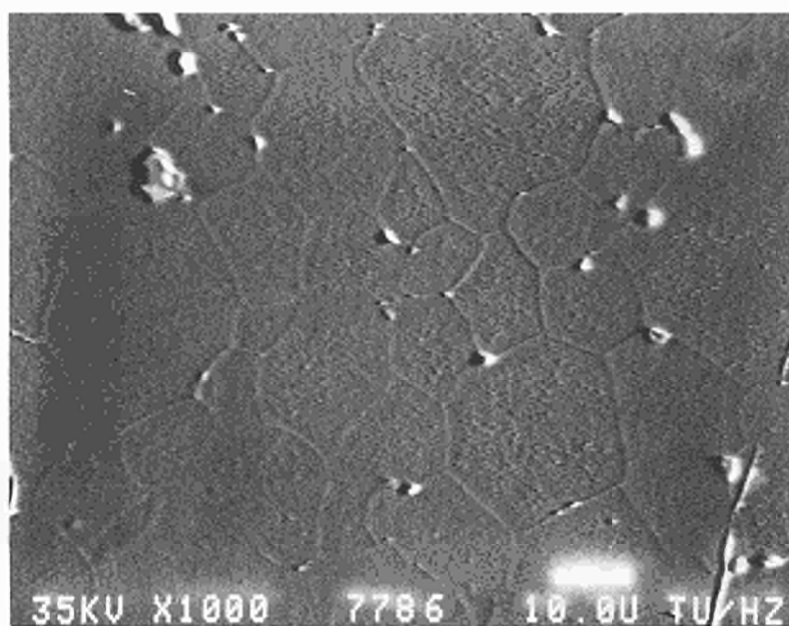
The intergranular mode of fuel fracture at the pellet periphery is to be associated with a change in mechanical strength at the grain interfaces resulting from chemical modifications. We think that this effect can be related to the burn-up increase in this region (caused by Pu-enrichment due to neutron capture), and to a preferential concentration of volatile fission products (Cs) along the grain faces. Additional chemical microanalyses of the etching solution and some complementary EMPA determinations will be performed in order to elucidate the nature of this intergranular deposit (Fig.4.30).

after chemical etching ($\text{H}_2\text{O} : \text{H}_2\text{O}_2 : \text{HNO}_3$)



20 μ

$r/r_0 = 0.25$



SEM-BEI image

Fig.4.22 Fuel microstructure within the dark zone in Fig.4.21 (as-etched condition)

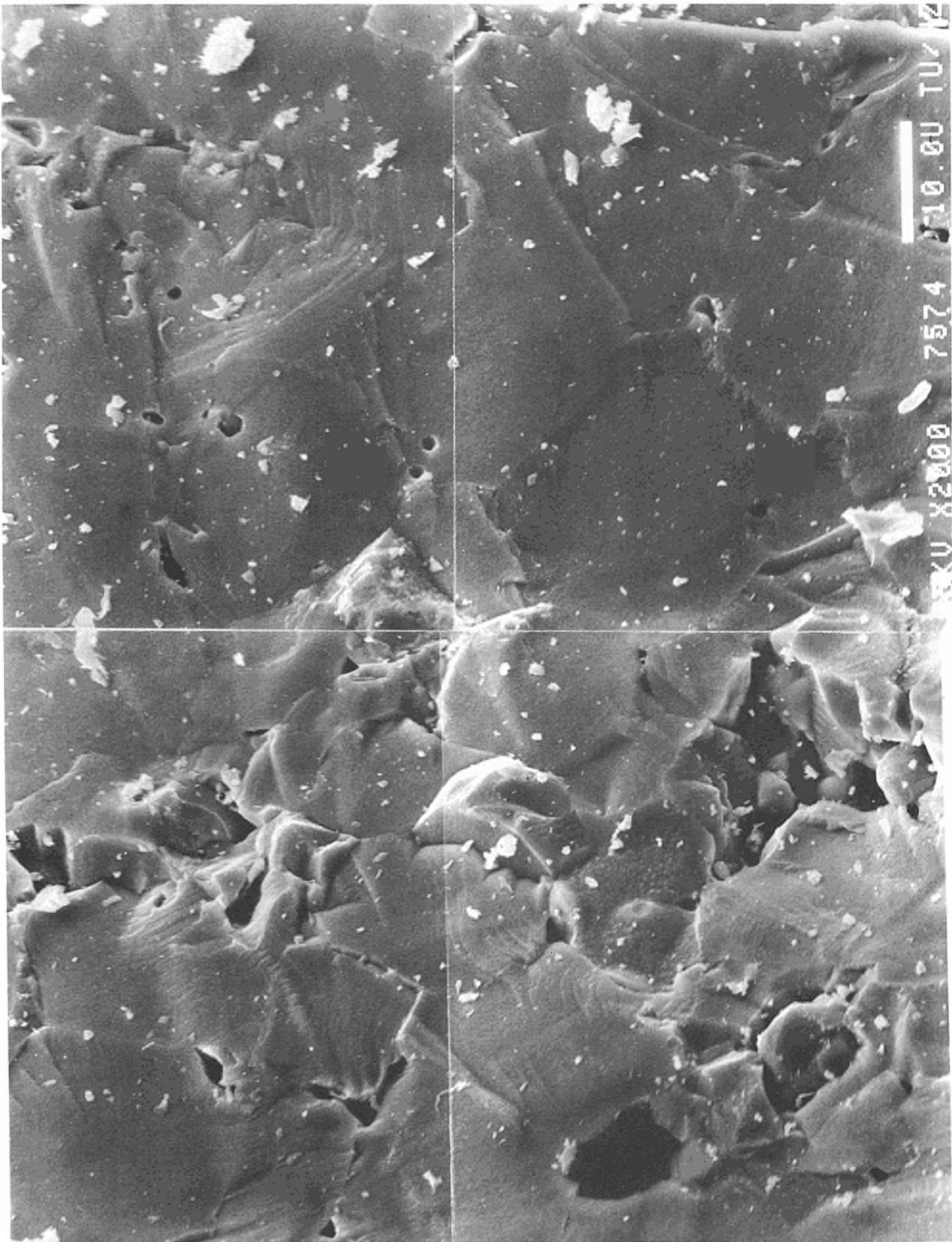
$r/r_0 = 0.00$ 

Fig.4.24 Transgranular fracture surface of a fuel region within the dark zone in Fig.4.21 (non-etched condition)

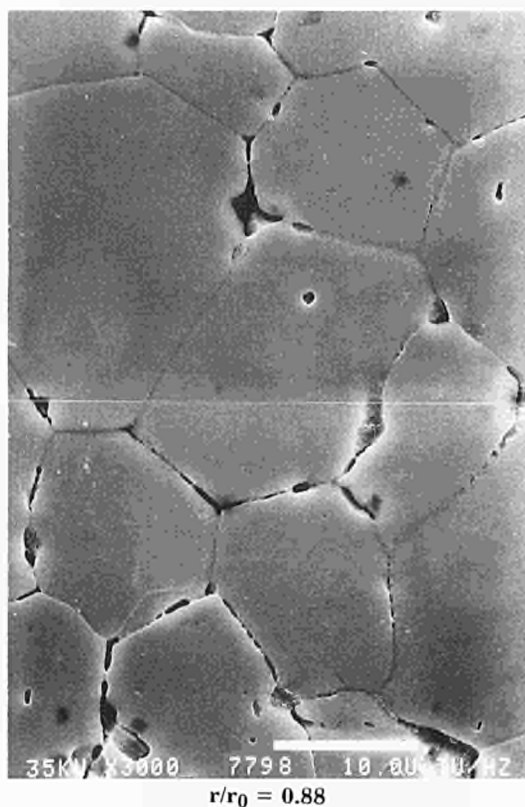


Fig.4.25 Fuel microstructure outside the dark zone in Fig.4.21 (as-etched condition)

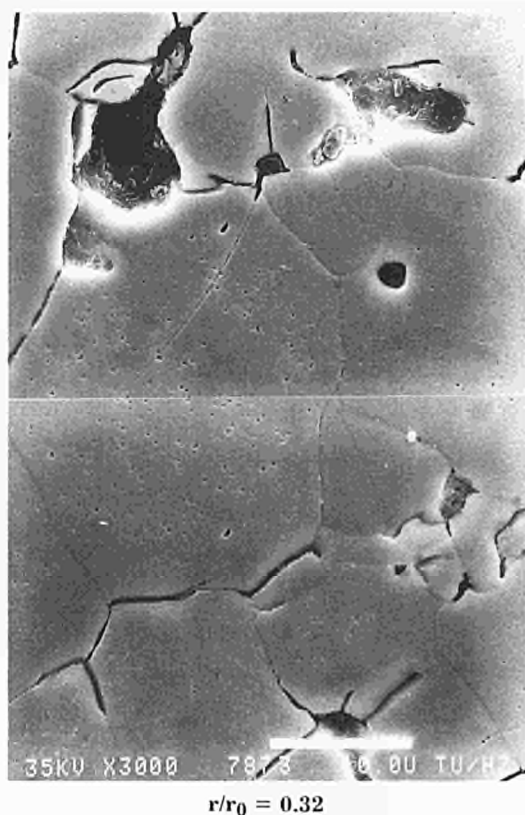


Fig.4.26 Fuel microstructure inside the dark zone in Fig.4.21. Appearance of intragranular triangular pits (denuded grain boundaries) after light etching with $H_2O:H_2O_2:HNO_3$ solution.

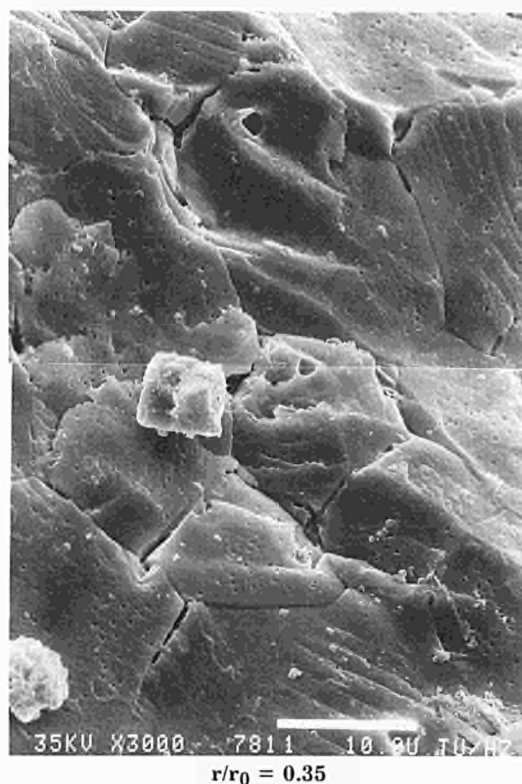


Fig.4.27 Transgranular fracture surface of a fuel region within the dark zone in Fig.4.21. Appearance of intragranular triangular pits after light chemical etching.

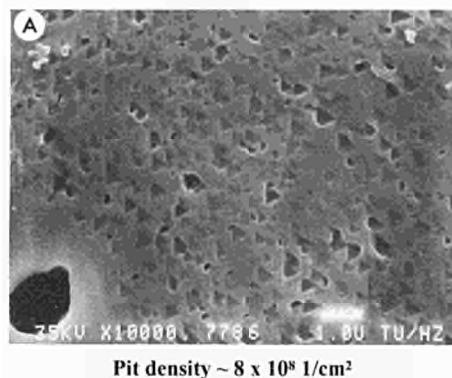
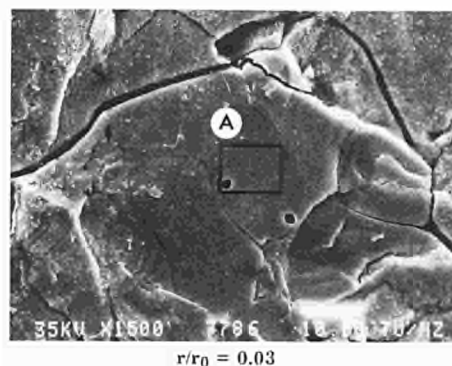


Fig.4.28 Preferentially oriented triangular pits on the cleaved surface of a fuel grain inside the dark zone of Fig.4.21., appearing after light chemical etching.

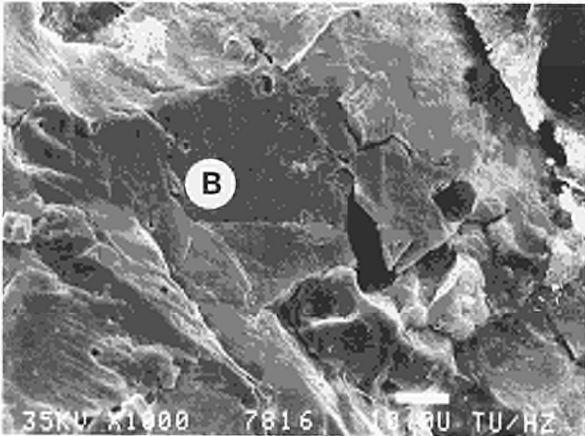


Fig.4.29 Change of preferential orientation of triangular etch-pits between neighbour fuel grains inside the dark zone of Fig.4.21 (cleaved surface after light chemical etching).

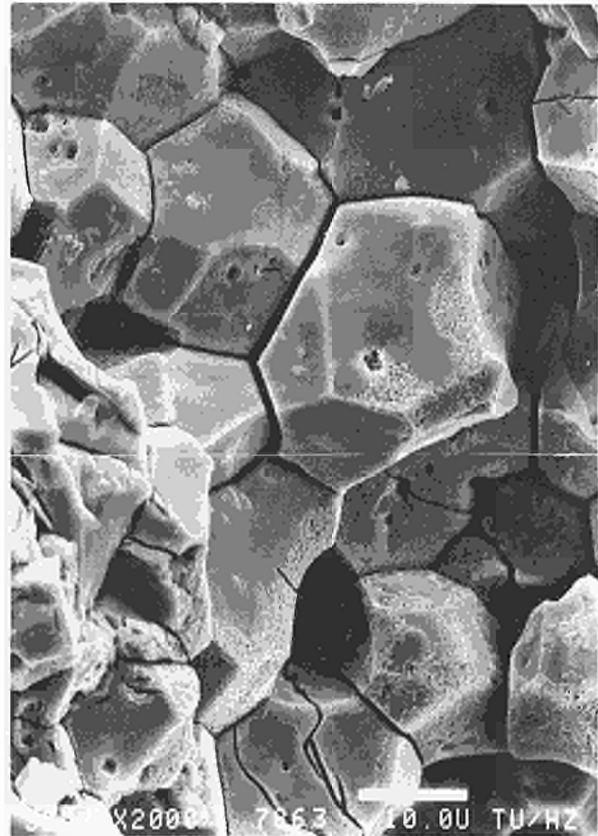


Fig.4.30 Intergranular fracture surface at the fuel periphery after light chemical etching

References

- [1] H. Stehle, *J. Nucl. Mater.* **153** (1988) 3
- [2] F. Sontheimer et al., *IAEA-IWGFPT/25*, Karlsruhe 1985, 108
- [3] R. Manzel et al., *LWR Fuel Performance*, International Topical Meeting, Avignon, France, 1991, 528
- [4] P. Guedeney et al., *ibid.*, 627
- [5] D.R. Olander, *Fundamental Aspects of Nuclear Fuel Elements*, TID-26711-P1, 1976, 339
- [6] W.G. Johnston, *Dislocation Edds. Pits in Non-metallic Crystals*, *Progress in Ceramic Science*, Vol. 2, 1962, 1

Hot Cell Annealing Tests for Fission Gas Release Studies

Introduction

Among the technical considerations related to LWR fuel performance at extended burn-up, the need to define fission gas release behaviour is probably the most important. This is principally because large internal fuel rod pressure and high fuel temperature may not allow the maximum possible burn-up to be obtained. For this reason, annealing tests were proposed as part of the HBC programme to be carried out by ITU, Karlsruhe. The goal of these annealing tests is to obtain information on the role played by parameters such as grain size, and oxygen potential of the atmosphere for high burn-up fuel.

Experimental equipment and conditions

Fuel rod data

The fission gas release of highly irradiated UO_2 fuels supplied by two different fuel manufacturers (BN and ABB) was studied by annealing segments of fuel pellets in the hot cell and by comparing their behaviour as a function of grain size, and atmosphere. The analysed fuels had been irradiated to burn-ups of 58 and 53 GWd/tU in the Belgian BR-3 reactor (BN) and in the Ringhals reactor (ABB), respectively.

Fuel and irradiation data are given in Tab.4.15.

Tab.4.15 Fuel pellet and rod design characteristics

Fuel	BN	ABB
Pellet density (%TD)	94.25	95.2
Grain size (μm)	11	40
Stoichiometry (O/M)	1.997	2.02
Pellet diameter (mm)	8.04	10.52
Burn-up (GWd/T)	58	53

The hot cell annealing of fuel took place under controlled oxygen potentials (ΔG_{O_2} values), during which the fission product release was monitored by measuring ^{85}Kr evolved from the fuel. The changes in fuel microstructures after annealing were also examined.

Hot cell annealing and fission gas analysis equipment

The equipment, consisting of a high frequency induction furnace linked to analysis circuits in a glove box has been described in TUAR 91. The analyses circuits have a β -flow counter for measuring ^{85}Kr release rates followed by a γ -counter for measuring accumulated ^{85}Kr releases in a liquid nitrogen cold trap.

Annealing procedure

The fuel samples of 0.1 - 0.3 g weight were selected from a 3 mm cut of the fuel to be as representative as possible of the fuel structure.

Tests treated BN fuel, and for selected examinations, ABB fuel, under reducing conditions ($\text{H}_2\text{O}:\text{H}_2 = 1:10$) or oxidizing conditions ($\text{CO}:\text{CO}_2 = 1:10$) at flow rates of $560 \text{ cm}^3\cdot\text{mn}^{-1}$ and $220 \text{ cm}^3\cdot\text{mn}^{-1}$ respectively. The fuel samples were heated to 1500°C directly for 1 hour (single step) or to 1000°C and rising in 100°C steps (10 mins. rise time then 50 mins. hold time) up to 1500°C (staircase profile).

These anneals were, also repeated with 'pre-cooking' at 1000°C for 48 hours before rising to 1500°C by single step or staircase profiles. In addition, there was a baseline test of BN fuel at 1000°C for 48 hours under reducing conditions. The test matrix is given in Tab.4.16.

Tab.4.16 HBC annealing programme

No.	Fuel	Atmos.	Pre-cooking (48 h/1000°C)	Annealing (1500°C)*
1	BN	reducing	yes	-
2	"	"	"	single step
3	"	"	"	staircase
4	BN/ABB	"	no	single step
5	BN/ABB	oxid.	no	single step
6	"	"	"	staircase
7	BN	reducing	no	staircase

* single step 1 h at 1500°C
staircase 1000-1500 $^\circ\text{C}$ in 100°C steps 1 h hold time

Residual gas determination

The thermal annealing runs were performed in duplicate so that annealed samples could also be analysed for residual gas, and the fission gas release ratio obtained.

The annealed sample was placed in a low melting point salt bed of sodium nitrate, sodium peroxide and sodium hydroxide (55 g : 4.5 g : 6 g) in a stainless steel crucible. The specimen was then gently heated in a reducing atmosphere ($\text{H}_2\text{O}:\text{H}_2 = 1:10$) with a flow-rate of $560 \text{ ml}\cdot\text{min}^{-1}$. Heating was from room temperature ($\sim 20^\circ\text{C}$) to 300°C in 30 minutes. Thereafter to 600°C in 2 hours. Gas releases were generally seen at $\sim 550^\circ\text{C}$.

Controls using non-annealed fuel did not yield release values any higher than those of the annealed fuel although the fuel appeared to have been dissolved. A possible explanation is that the molten salt attacks the fuel intergranularly and releases the grain boundary gas but only partially the intragranular fission gas. The non-annealed specimens have a lower intergranular porosity and also may be attacked more slowly as they have no interconnected intergranular porosity and channels created by annealing

Microstructure analysis

Ceramographic examination (including porosity measurements) were made of cross-sections of the as-received material. In addition the heat-treated samples were examined by scanning electron microscopy (SEM). Energy dispersive analysis (EDX) will be performed on selected samples. The specimens were re-mounted and polished for examination under the optical microscope.

Experimental results

Fission gas release during annealing

Form of results

Total ^{85}Kr releases evaluated per gram of fuel during annealing are summarised in the left half of Tab.4.17 (Annealing). The residual gas results are seen in the second part of Tab.4.17 (Residual Gas Dissolution) as impulses/g and then as percentage release of the total annealing and salt dissolution releases. This total has been taken as an estimation of the grain boundary ^{85}Kr inventory. The values calculated from the multichannel analyser (MCA) are approximately twice the values derived from the cold trap. The cold trap is the more accurate method and has been quantitatively calibrated for ^{85}Kr .

There are only MCA values for the oxidising (CO/CO_2) atmospheres since the liquid N_2 cold trap would be blocked by the CO_2 (which is solid at -78.5°C). However an average ratio of percentage releases obtained under reducing atmospheres from MCA and from cold trap (0.48) has been used to obtain an approximate value

for the cold trap releases for CO/CO_2 atmospheres.

Under reducing conditions, a small release was observed during the initial heat up at $700 - 850^\circ\text{C}$. This usually represented from 2 % to 10 % of the total release annealing (see Annealing Tab.4.17). Thereafter with the direct (single step) heating to 1500°C , a second and major release (i.e. $> 80\%$ of total) was observed at approximately $1350^\circ\text{C} - 1450^\circ\text{C}$ (see Fig.4.31).

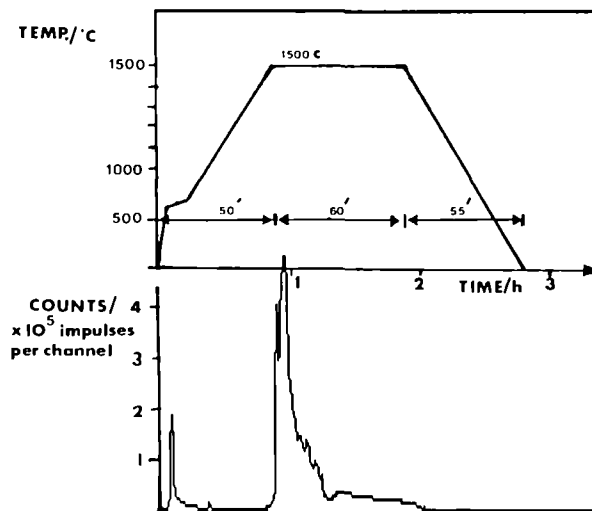


Fig.4.31 Fission gas release profile of BN 3-241 fuel during direct heating to 1500°C under reducing ($\text{H}_2\text{O}/\text{H}_2$) conditions.

The determination of the temperature of release was not exact because of the rapid ramp: $\sim 50^\circ\text{C}/\text{min}$. For the staircase profile the major releases occurred at $1300-1400^\circ\text{C}$ and $1400-1500^\circ\text{C}$ steps (see Fig.4.32). The releases reached a sharp peak on attaining the hold temperature and then died away asymptotically.

On some occasions secondary, smaller outbursts were noted during the decay phase of the release at hold temperature (see Fig.4.31). These may result from microcrack formation which sporadically modifies the simple diffusion process.

Effect of oxidising atmosphere

Under oxidising conditions similar forms of release were seen; a small, low temperature release at $700-800^\circ\text{C}$, and then, under single step heating to 1500°C , a major release at $1400-1450^\circ\text{C}$. The oxidising condition, single step releases were similar in ratio and total amount to those

observed during reducing conditions. By contrast, the staircase anneals under oxidising conditions for BN fuel showed a five times greater (MCA) total release compared to single step anneals and these appeared to commence approximately 100 °C lower (i.e. on rising to 1300 °C) (Compare Fig.4.32 (reducing) with Fig.4.33 (oxidising)). This shows that the longer (6 h) staircase heating is required before the influence of oxidation on release is apparent.

The residual gas determination confirmed these increased releases under oxidising atmospheres. Estimations of the cold trap % releases (made by

using the mean MCA/cold trap ratio) suggest an increase for single step heated BN fuels from 20 % to 25 % release of ^{85}Kr grain boundary inventory, while staircase heating under oxidising atmospheres caused a threefold increase (from 10 % to 34 % release). ABB fuel was even more susceptible to oxidising atmospheres with a tenfold increase in % release of the grain boundary gas from 3.3 % to 29 %.

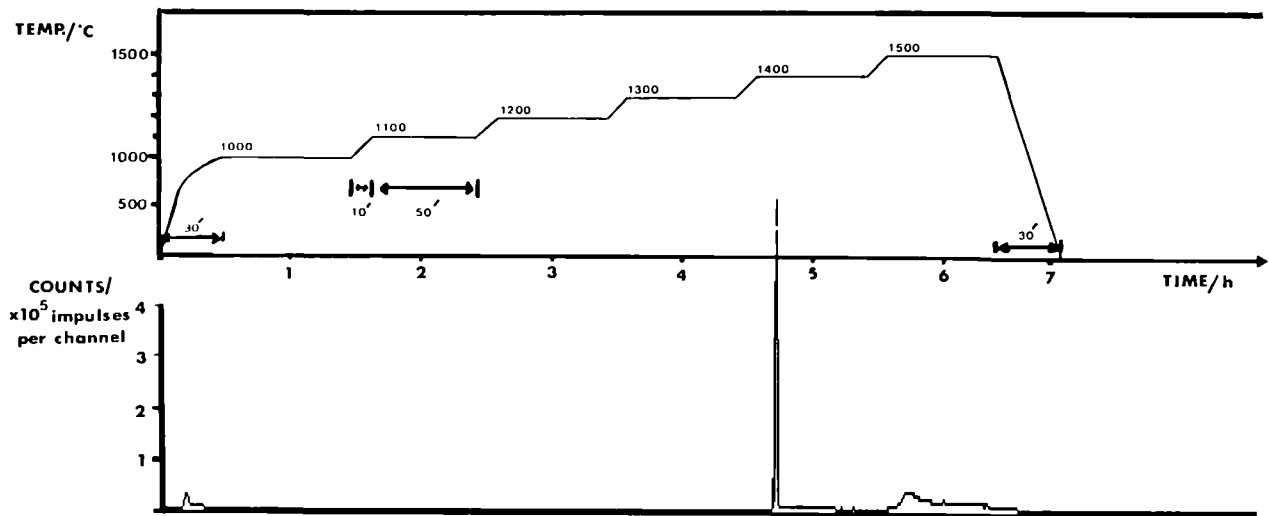


Fig.4.32 ^{85}Kr gas release profile of BN 3-241 during a staircase anneal (1000-1500 °C) in 100 °C steps under reducing ($\text{H}_2\text{O}/\text{H}_2$) conditions.

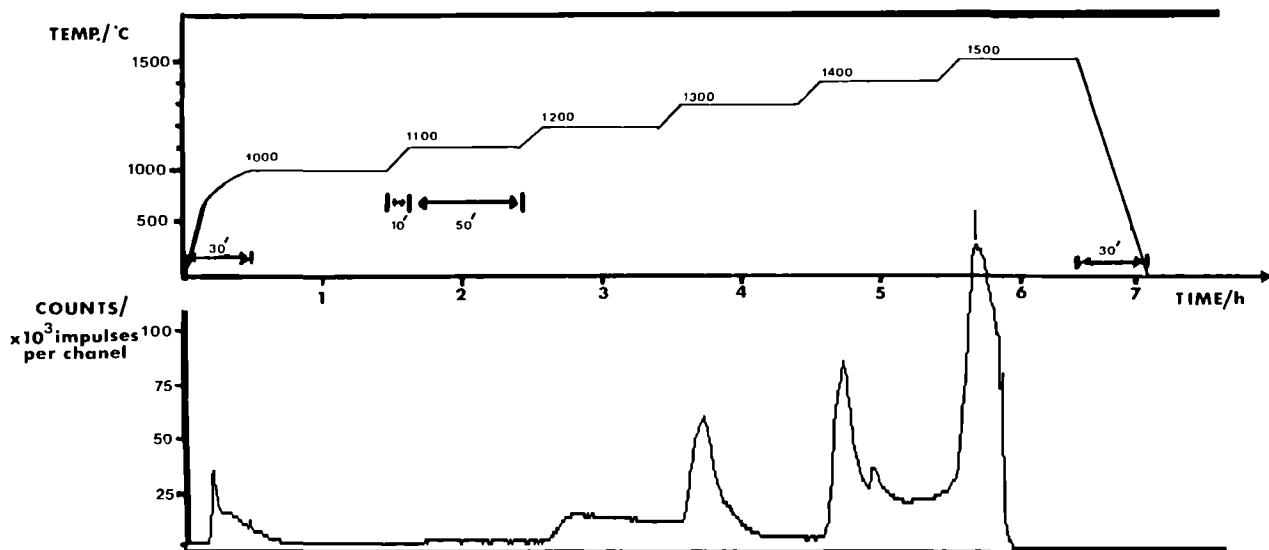


Fig.4.33 ^{85}Kr gas release of BN 3-241 during a staircase anneal (1000-1500 °C in 100 °C steps) under oxidising (CO/CO_2) conditions.

Tab.4.17 Comparison of 'released' vs. 'retained'⁸⁵Kr during thermal anneals

				Annealing		Residual Gas (Dissolution)		% Release during thermal annealing		Ratio Release Trap/ Rel. MCA
				MCA imp/g	Trap imp/s/g	MCA imp/g	Trap imp/s/g	MCA imp/g	Trap imp/s/g	
H ₂ O/H ₂	1. BN	precooking only	⊙ ⊗	- 1.26x10 ⁶	2,050 1,609	60.31x10 ⁶	137,358	- 2.0 %	- 1.2 %	0.57
		precook + 1 h/1500°C	⊙ ⊗	88.4x10 ⁶ 32.5x10 ⁶	72,728 31,188	83.63x10 ⁶	190,609	51.4 % -	27.6 % -	
		precook + 1000-1500°C 100 °C step	⊙ ⊗	- 15.7x10 ⁶	25,067 19,344	- 120.5x10 ⁶	- 229,025	- 11.5 %	- 7.8 %	0.48
		1 h/1500 °C	⊙	47.7x10 ⁶	32,714	67.55x10 ⁶	134,709	41.4 %	19.5 %	
		1000-1500 °C 100 °C step	⊙ ⊗	28.7x10 ⁶ 25.8x10 ⁶	21,917* (*1200-1500 °C) 16,724	- 55.35x10 ⁶	- 153,420	- 31.8 %	- 9.8 %	0.31
2. ABB	1 h/1500 °C	⊙	5.08x10 ⁶	4,333	41.26x10 ⁶	128,856	11.0 %	3.3 %	0.30	
		⊗	11.1x10 ⁶	(ramped) 7,500	-	-	-	-		
CO/CO ₂	1. BN	1 h/1500 °C	⊙ ⊗	48.2x10 ⁶ 37.7x10 ⁶	-	34.26x10 ⁶	83,300	- 52.4 %	- 25.1 % (1)	
		1000-1500°C in 100 °C steps	⊙ ⊗	152.7x10 ⁶ 80.0x10 ⁶	-	35.8x10 ⁶	103,989	- 69.1 %	- 33.1 % (1)	
	2. ABB	1 h/1500 °C	⊙ ⊗ ⊗	10.3x10 ⁶ 8.13x10 ⁶ 31.2x10 ⁶	- -	- 19.86x10 ⁶	- -	- 61.1 %	- 29.3 % (1)	
Controls	BN	not annealed	⊙	0	0	82.3x10 ⁶	131,750			
			⊗	0	0	50.7x10 ⁶	127,200			
Controls	ABB	not annealed	⊙	0	0	47.27x10 ⁶	104,840	620 °C (2)		
			⊗	0	0	7.83x10 ⁶	23,560			
			⊗	0	0	55.10x10 ⁶	128,300	830 °C		
			⊗	0	0	51.47x10 ⁶	110,252	795 °C		

Abbrand BN: 58 GWd/t
ABB: 56 GWd/t

(1) estimated using the mean Trap/MCA release ratio of 0.48
(2) Max. temps. of residual gas analysis

Effect of heating profile (single step vs. staircase)

Fission gas releases appeared to be slightly higher for the 'single step' BN specimens heated under reducing conditions compared to 'staircase' BN specimens. This comes out more clearly when the % releases of grain boundary inventory are compared. The releases are doubled for non-precooked samples (10 % to 20 %) and tripled for precooked samples (8 % to 28 %). This indicates that the thermal stresses from the more rapid heat up lead to a more effective venting of the grain boundaries.

Effect of pre-cooking

The effect of pre-cooking alone under reducing conditions appears to be nominal and corresponds to only 1 % of the estimated grain boundary inventory (see Tab.4.17). Precooking under reducing conditions before a staircase profile appears to cause a decrease in the % release of the grain boundary inventory. This contrasts with the pre-cooking with single step profile for BN fuel which shows a 25 % (cold trap) increase in the release of grain boundary fission gas.

Pre-cooking appears to affect the fuel microstructure and aid fission gas nucleation. This could reduce release during subsequent slow heating by increasing intragranular nucleation but could aid fission gas release during rapid (single step) heating when there is thermal cracking.

Comparison of fuels: effect of grain size

However the greatest differences were those observed between fuels. BN fuel releases 5 times more ^{85}Kr than ABB fuel under single step heating profiles (compare Fig.4.31 with Fig.4.34). This finding is confirmed by the release of grain boundary inventory which indicates a sixfold difference (3.3 % for ABB and 19.5 % for BN fuel). The very different grain size of the two fuels (BN 11 μm , ABB 40 μm) clearly has a very significant difference on the release [2,3].

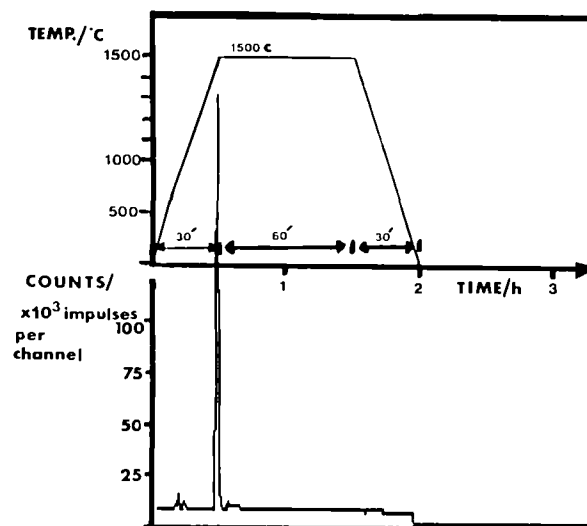


Fig.4.34 ^{85}Kr gas release of ABB 9K2-1 during a direct heating to 1500 °C under reducing ($\text{H}_2\text{O}/\text{H}_2$) conditions.

Microstructural analysis

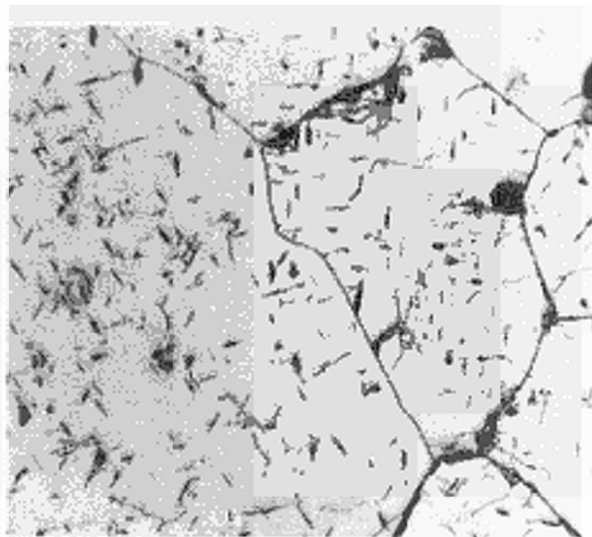
Grain size

The two fuels have differing microstructures. BN fuel has 13 μm mean grain diameter but with a binodal distribution at $\leq 5 \mu\text{m}$ and 15-20 μm mean diameters. ABB fuel has a mean grain diameter of 20.5 μm (ranging from 9 μm upto 65 μm diameter). BN fuel displayed no porous outer rim which was present in the ABB fuel upto a maximum depth of 50 μm .

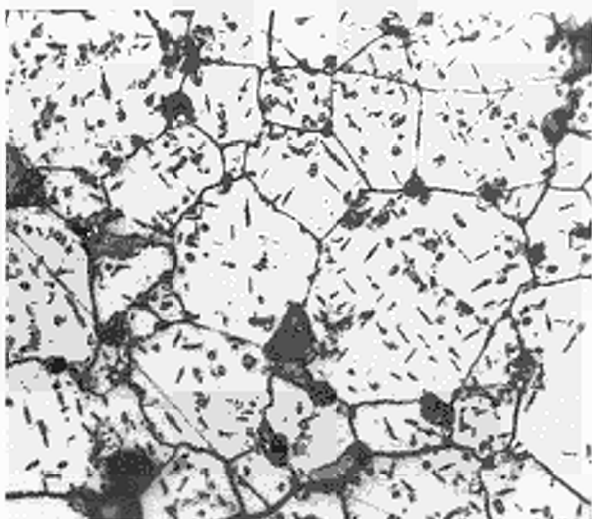
UO_2 stoichiometry

Etching specifically for the U_4O_{9-x} phase was carried out, and an acicular phase appeared along two preferential orientations in the colder (outer) part of the fuel (e.g. in BN for $r/r_0 > 0.87$) (see Fig.4.35). This acicular phase disappeared after pre-cooking for 48 h at 1000 °C under reducing conditions.

The Free Energy (Ellingham) Diagram shown in Fig.4.36 indicates the oxygen potential of the atmospheres compared to the UO_2 and its superstoichiometric forms. It is seen that pre-cooking in $\text{H}_2\text{O}/\text{H}_2 = 1:10$ atmosphere would have reduced the fuel at equilibrium to approximately stoichiometric UO_2 (i.e. $\text{UO}_{2.0001}$ or lower), and would have removed the higher oxides (e.g. U_4O_9). This implies that the fuels are slightly



a) ABB 9K2-1 (1100x), $r/r_0 = 0.92$



b) BN3-241 (1100x), $r/r_0 = 0.99$

Fig.4.35 Optical micrographs (H_2SO_4/H_2O_2 etched) of ABB 9K2-1 and BN 3-241 fuels showing the acicular phase present in the outer part of the received fuel.

hyperstoichiometric after irradiation as would be expected. By comparison CO/CO_2 (oxidising) atmospheres are able to increase the UO_2 stoichiometry to approximately $UO_{2.05}$ at 1500 °C at equilibrium.

Porosity

The pre-cooking appears to have no effect on the

visible porosity which remains unchanged at 6.5 % (see Tab.4.18). This compares with 5.25 % porosity for manufacturers specifications (see Tab.4.15).

Tab.4.18 Porosity measurements of BN and ABB fuels before and after annealing tests.

Fuel	Thermal Treatment	intergranular ¹⁾ vol. %	intragranular ¹⁾ vol. %	Total vol. %
BN	As-received		6.5	6.5
	Red/Pre-cooking		6.5	6.5
	Red/Pre-cooking/1h-1500 °C	9.1		9.1
	Red/Pre-cooking/staircase			7.8 ²⁾
	Red/1h-1500 °C	7.6		7.6
	Red/staircase	6.5		6.5
	Oxid/1h-1500 °C	9.6	3.0	12.6
ABB	As-received		1.83	2.5 ²⁾
	Red/1h-1500 °C		1.7	1.7
	Oxid/1h-1500 °C		2.1	2.1
		9.6	2.7	12.3
		9.6		12.6

¹⁾ estimated
²⁾ sintering porosity also present

After heating BN fuel under reduced conditions this usually rises to 7 - 9 % with only slight intragranular porosity. Rapid one-step heating under reducing conditions appears to result in larger grain boundary pores compared to staircase heating. Oxidising heat treatments compared to reducing treatments of BN fuel caused increased porosity of 12 % but with noticeably more intragranular porosity and increased coalescence (i.e. fewer but larger grain boundary pores).

ABB fuel has much less starting porosity (of 1.8 %) which is only slightly changed after reducing heat treatment. However in oxidising atmospheres an increase to 2.1 % is observed, particularly in intragranular porosity.

Pre-cooking at 1000°C for 48h under reducing conditions causes the disappearance of the U_4O_{9-x} type-phases in the as-received material. Pre-cooking appears to nucleate fission bubbles that grow to intergranular porosity in subsequent 1500°C heat treatments.

The pre-cooking and staircase profiles may cause a memory effect with the low temperature annealing steps allowing more nucleation to occur and high temperatures enhancing the pore growth compared to nucleation. Therefore staircase heating results in the more numerous and finer pores observed on the grain boundaries compared to direct heating (see Fig.4.37). The

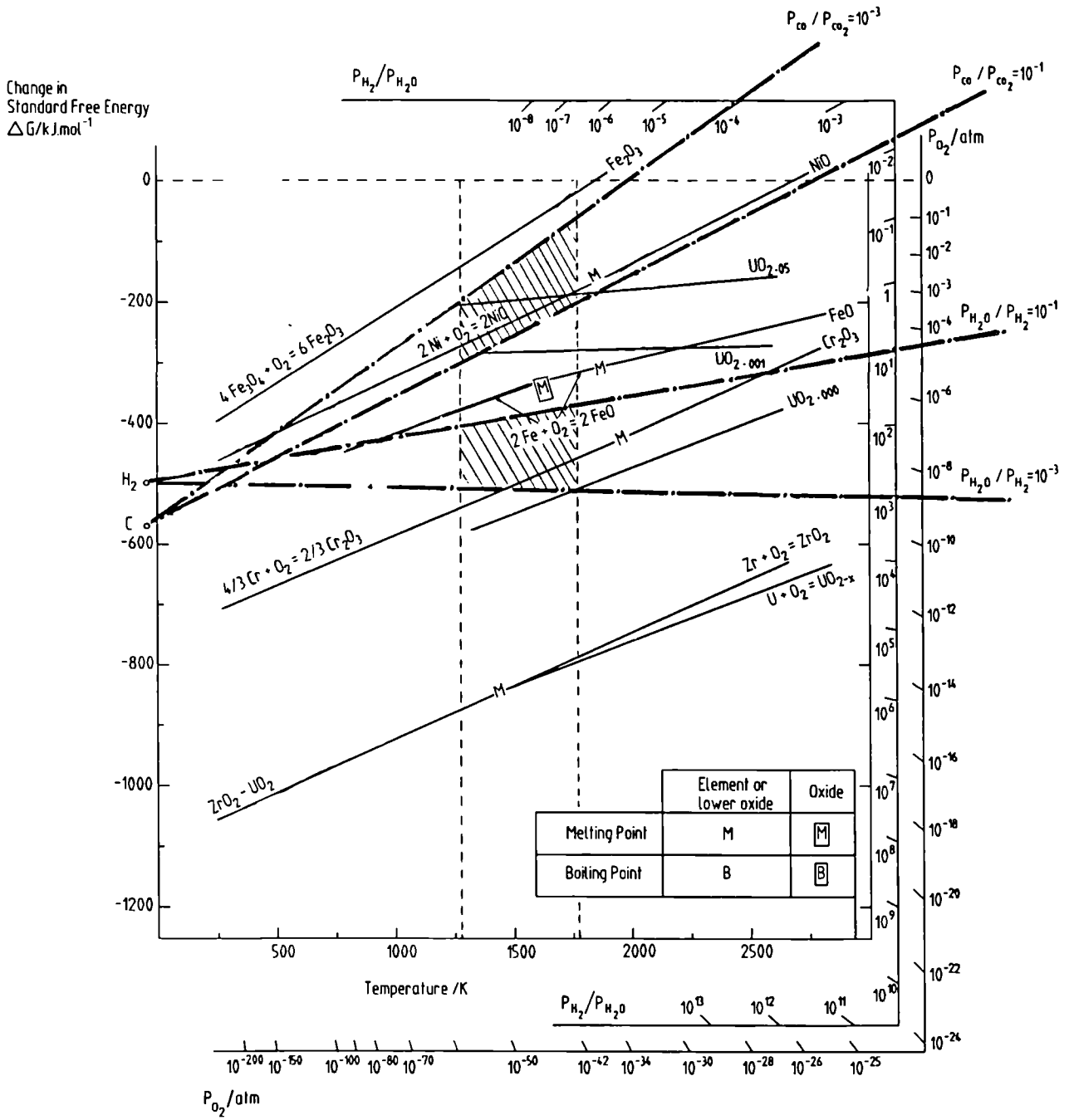


Fig.4.36 Free Energy Ellingham Diagram (ΔG_{O_2} vs. T) showing the domains of the atmospheres in respect of uranium oxides of various stoichiometries.

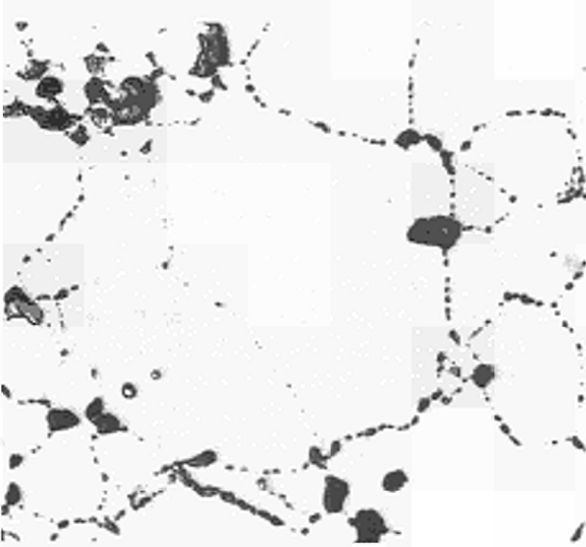


Fig.4.37 Micrograph of BN 3-241 after pre-cooking at 1000 °C and then staircase anneal to 1500 °C under reducing (H_2O/H_2) atmosphere.

larger grain size of the ABB fuel (20 μm mean diameter vs. 13 μm for BN fuel) also seems to restrict pore growth by

- doubling the mean diffusion path for gas atoms to a grain boundary and by
- halving the grain boundary surface available per unit volume for pores.

Under oxidising conditions the greatly enhanced numbers and sizes of intragranular pores (see Fig.4.38 and Fig.4.39) imply a substantially increased gas mobility or possibly the

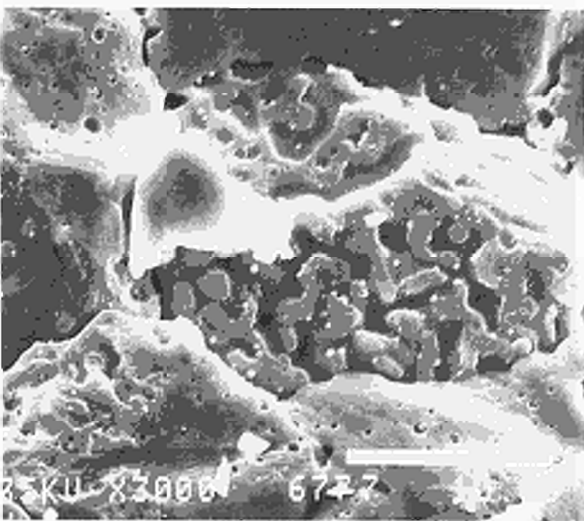


Fig.4.38 SEM-micrograph of BN 3-241 fuel after direct heating to 1500 °C under oxidising (CO/CO_2) atmosphere.

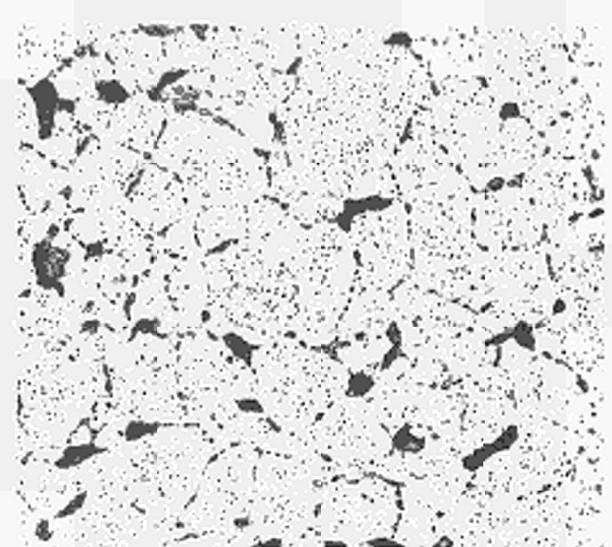


Fig.4.39 Optical micrograph of BN 3-241 after direct heating to 1500 °C under oxidising (CO/CO_2) atmosphere.

existence of more nucleation sites in the UO_2 . This may result from an altered lattice structure.

Conclusions

From the above results three main conclusions may be drawn:

- As grain size increases, there is a large decrease in the fission gas releases that result from the heat treatment because of the reduced grain boundary surface.
- There was a considerable increase in fission gas release at longer oxidising annealing times (6 hours). At these longer durations the oxygen mobility is increased.
- Pre-cooking at 1000 °C for 48 h under reducing conditions causes the disappearance of the U_4O_{9-x} type-phases in the as-received material. Precooking appears to have a "memory effect" that increases intragranular porosity in subsequent 1500 °C heat treatments.

References

- [1] Coquerelle M., Walker, C.T., Proc. of an IAEA Technical Committee Meeting, IWGRPT/36 held in Studvik, Sweden (1990), 110.
- [2] Ronchi C., J. Nucl. Mater. 84 (1979) 55-84
- [3] Ronchi C., Matzke, H.J. J. Nucl. Mater. 45 (1973) 15-28

Chemistry of the UO₂ Fuel Periphery - Properties of Cs-U-O-Compounds

Introduction

UO₂ power reactor fuels irradiated to a burn-up of 50.000 GWd/t and more display new aspects of fuel chemistry. The strong local burn-up increase at the fuel periphery induces fission product accumulation and a reaction between Cs and UO₂ at the cladding/fuel interface. A modification of the fuel cladding mechanical interaction can be anticipated.

A collaboration between E.D.F. and the Institute has been established with the aim to investigate these effects.

The first phase of the investigation is limited to

- the synthesis of Cs₂UO₄ and the study of its thermal stability,
- an investigation of the chemical compatibility between Cs₂UO₄ and ZrO₂, Cs₂CO₃ and ZrO₂,
- the study of the mechanical properties of Cs₂UO₄.

Synthesis of Cs₂UO₄ and thermal stability

Cs₂UO₄ can be prepared according to the following reactions:

- (1) $3 \text{Cs}_2\text{CO}_3 + \text{U}_3\text{O}_8 + 0.5 \text{O}_2 \longrightarrow 3 \text{Cs}_2\text{UO}_4 + 3 \text{CO}_2$
- (2) $\text{UO}_2 + \text{Cs}_2\text{CO}_3 + 0.5 \text{O}_2 \longrightarrow \text{Cs}_2\text{UO}_4 + \text{CO}_2$
- (3) $\text{U}_3\text{O}_8 + 3 \text{Cs}_2\text{O} + 0.5 \text{O}_2 \longrightarrow 3 \text{Cs}_2\text{UO}_4$

Reaction (1) has been chosen because the starting materials Cs₂CO₃ and U₃O₈ are stable and easy to handle, their low density favour a high degree of homogeneity of the mixtures and therefore a good reaction yield is to be expected. On the contrary, Cs₂O is difficult to handle and to prepare as a pure powder.

A mixture of U₃O₈ and Cs₂CO₃, pressed in pellet form, was heated in air at 670 °C for 24 hours. The intermediate and final products were analysed by X-ray diffraction. The Cs₂UO₄ prepared

according to the reaction (1) was submitted to a heat treatment in order to determine its thermal stability. The experiments were carried out under various atmospheres using a thermobalance. A significant weight loss under argon atmosphere starting around 850 °C indicated a decomposition process. X-ray analysis of the annealed products displayed the transformation of Cs₂UO₄ into another cesium uranate with the nominal composition Cs₂U₂O₇. It is assumed that the formation of Cs₂U₂O₇ occurred according to the following reaction:



The weight loss was mainly caused by the evaporation of Cs₂O and was used to estimate the reaction ratio α (α is the ratio between the weight variation at time t and the total weight variation) (Fig.4.40).

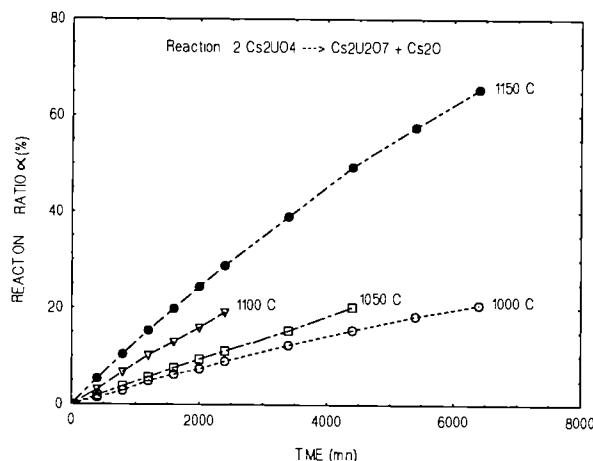


Fig.4.40 Reaction ratio α as a function of time at different temperatures

The activation energy of this reaction will be calculated from long duration annealings and will be reported in the next TUAR.

Chemical interaction

As the burn-up increases, the initial gap disappears progressively and the fuel periphery comes in contact with the partially oxidised inner surface of the zircaloy-4 cladding material. Several tests have been made to study the compatibility of Cs₂UO₄ with ZrO₂.

Cs₂UO₄ and ZrO₂ powder have been compacted to ensure a good contact between the two com-

pounds. The samples were heated at 670 °C under helium atmosphere for one week. Optical analysis of the specimen showed that no reaction occurred at the interface between the two compounds. Similar tests confirmed that Cs_2CO_3 did not react with ZrO_2 at 670 °C under air or helium.

Additional experiments are planned with longer annealing times.

Preparation of sample for mechanical testing

Preliminary experiments have been started in order to find the best sintering conditions for Cs_2UO_4 powder. A Cs_2UO_4 pellet, 6 mm in diameter and 3 mm in height, was heated at 800 °C under nitrogen containing ~0.5 % oxygen. The green density of the pellet was 83 % of the theoretical density. The sintering temperature was chosen taking into account the fact that at 850 °C the Cs_2UO_4 starts to decompose. Intermediate density measurements showed that no densification occurred even after 50 hours at 800 °C. SEM analysis of the fracture surface (Fig.4.41) indicated that the grains are very

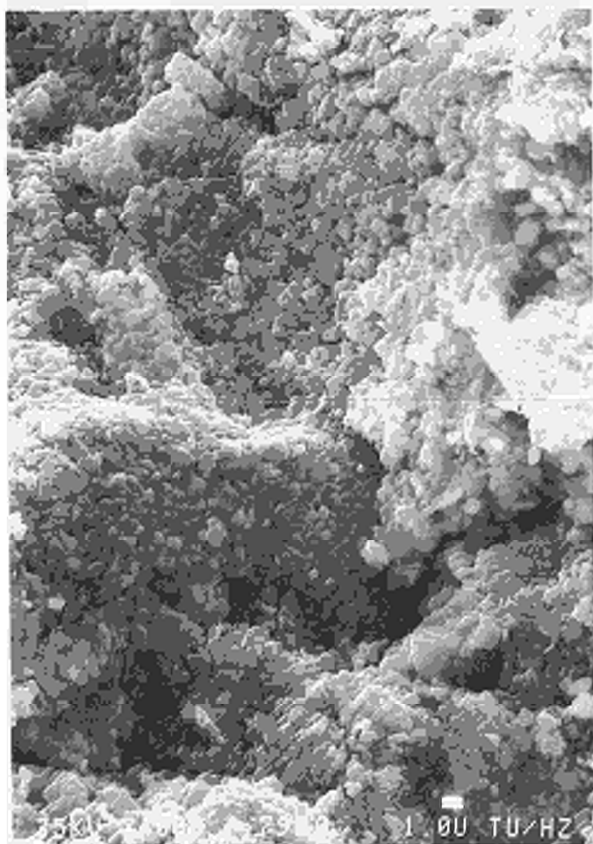


Fig.4.41 SEM of a fracture surface of a compacted Cs_2UO_4 powder heated 50 hours at 800 °C

small (about 1 μm) and that the structure is porous. Hot-pressing of the Cs_2UO_4 powder will be carried out to obtain higher densities.

Further experiments will be undertaken to study the mechanical behaviour of pure Cs_2UO_4 or Cs_2UO_4 doped with Zr or Mo.

Modelling of the Underground Water Contamination in a Spent Fuel Repository

Objectives

In the frame of safety studies for the spent fuel storage program, a hypothetical accident is assumed to happen, namely that water/steam comes in close contact with the spent fuel. The temperature range assumed for such an accident is 200-500 °C, and under these conditions fuel oxidation and leaching processes are expected to occur.

For understanding the chemical processes involved during leaching, a broad data basis is needed, and an experimental program has been defined and is in progress at the Institute including leaching tests as well as the study of the oxidation kinetics of the spent fuel.

In order to facilitate a comprehensive review of all related experiments the interest of having a modeling frame which could interpret, reproduce and extrapolate the experimental results is obvious.

The programme comprises two stages:

- the calculation of the isotope inventory of the fuel, the location of the isotopes and to which extent they could come in contact with the external leaching agent (water/steam)
- the calculation of the progress of fuel leaching by diffusion and reaction with the leachant.

Method

The second stage has to be supported by experimental data which are not available to a sufficient extent, thus the work performed in 1992 concerned only the first stage. By means of the

FUTURE and MITRA programs (developed at ITU), the following calculations were performed:

- By using FUTURE the restructuring of a fuel pellet including densification under irradiation, crack formation, pore size and pore location were calculated.
- By using MITRA the local isotope distribution was determined, taking into account the yield and decay laws as well as the migration within the grain according to the diffusion laws and the fuel restructuring as calculated above.

For that purpose the fuel pin was supposed to have undergone a 3-cycle irradiation history in three different reactor positions corresponding to a linear power of 186W/cm, 320W/cm and 270W/cm, with a cooling period of 34 days between each cycle. After the last cycle the fuel is supposed to be stored during 1000 years.

For these calculations the fuel was divided into three radial zones: one central, one intermediate and one external zone. Their respective volumes are: $V_{tot}/9$, $3V_{tot}/9$ and $5V_{tot}/9$.

Results

Under these conditions FUTURE indicates that the fuel pellet is found to be in contact with the cladding at the end of the irradiation. In the external zone the grain size is the same as for the fresh fuel while it has grown into the central zone. The volatile fission products are mainly redissolved in the matrix in the external zone, precipitated as bubbles (either within the grain or on the faces) in the intermediate zone, and appear as connected intergranular porosity in the central zone. In the latter zone the open porosity is roughly 50 %.

From this restructuring model we have calculated the probability for an isotope to migrate to the grain face and escaping to the outer limits of its zone and thereafter to the fuel periphery and the leachant. The results are plotted in Fig.4.42. At the end of 1000 years storage, the calculation shows a very low probability for the species located in the external zone to be release from the fuel. The species located in the two other fuel zones have a probability roughly 10 times greater to come into contact with the leachant.

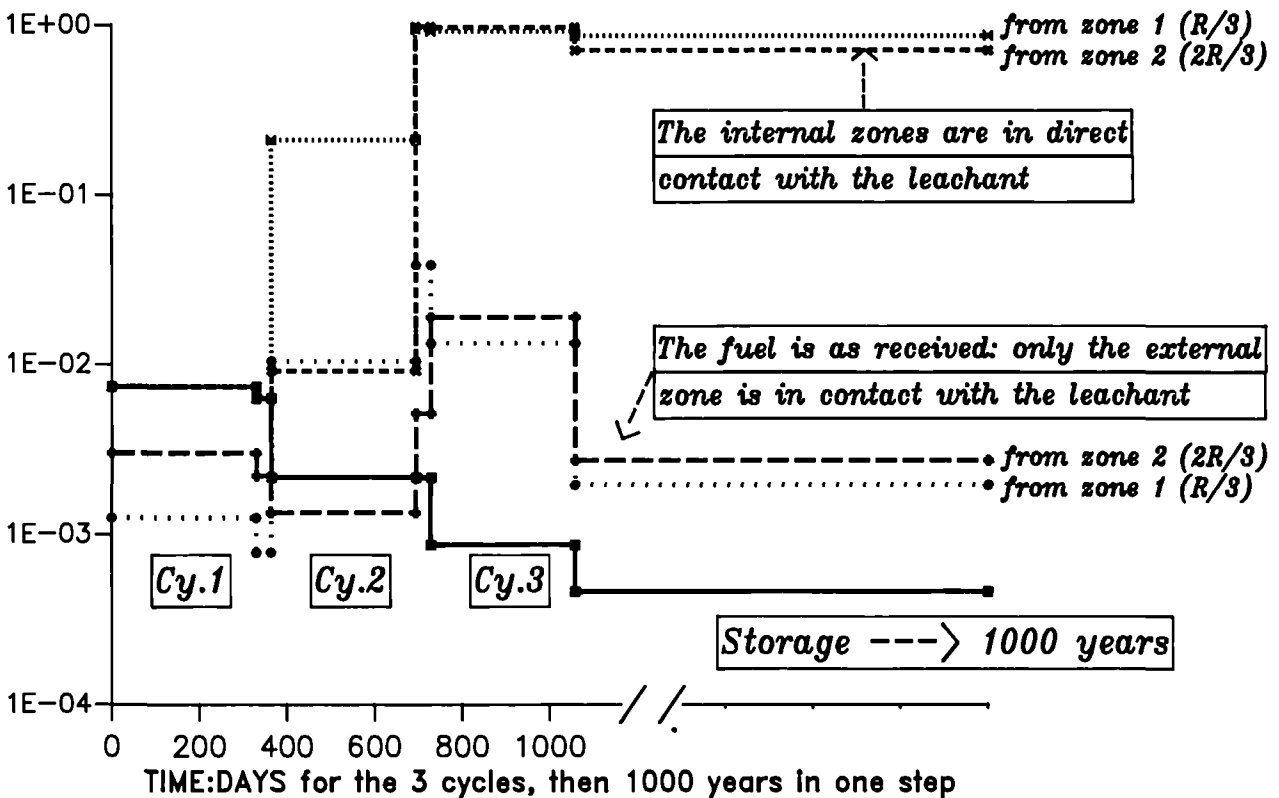


Fig.4.42 Probability for an atom migrated to the grain faces to come in contact with the leachant

The calculation of the release of isotope located in the central zone when the outer zone is already leached indicates similar release probabilities for the intermediate and the central zones.

A similar exercise was undertaken by using FUTURE and MITRA but extended now to all fission products. Some results of the mass transfer are illustrated in Figs.4.43 and 4.44. The lower line(s) correspond(s) to the amount that could come into contact with water/steam in the case of the as irradiated fuel. The upper lines represent the contribution of each of the three zones if they are sequentially peeled off by the water/steam action.

Future work

The advantage of these two modelling tools is that both, fuel restructuring and inventory, can be represented. Coupled with kinetics and chemical data on the oxidation/leaching pro-

cesses we could estimate reasonable upper limits of fission product transfer to the groundwater in the frame of the storage safety studies. Such calculations could be repeated for some selected irradiation histories.

A limited amount of work has to be done on the FUTURE and MITRA programs to improve their flexibility and the management of the huge amount of data that can be obtained. The actinide distribution should be included. However, in order to quantify the source term during a spent fuel storage accident, experimental data concerning the leaching and oxidation processes of the fuel are a prerequisite for a parametric study. From this study the fission-product and actinide source terms could be estimated in ground water under specified conditions (low/high burn-up fuel, time of the accident, chemical conditions).

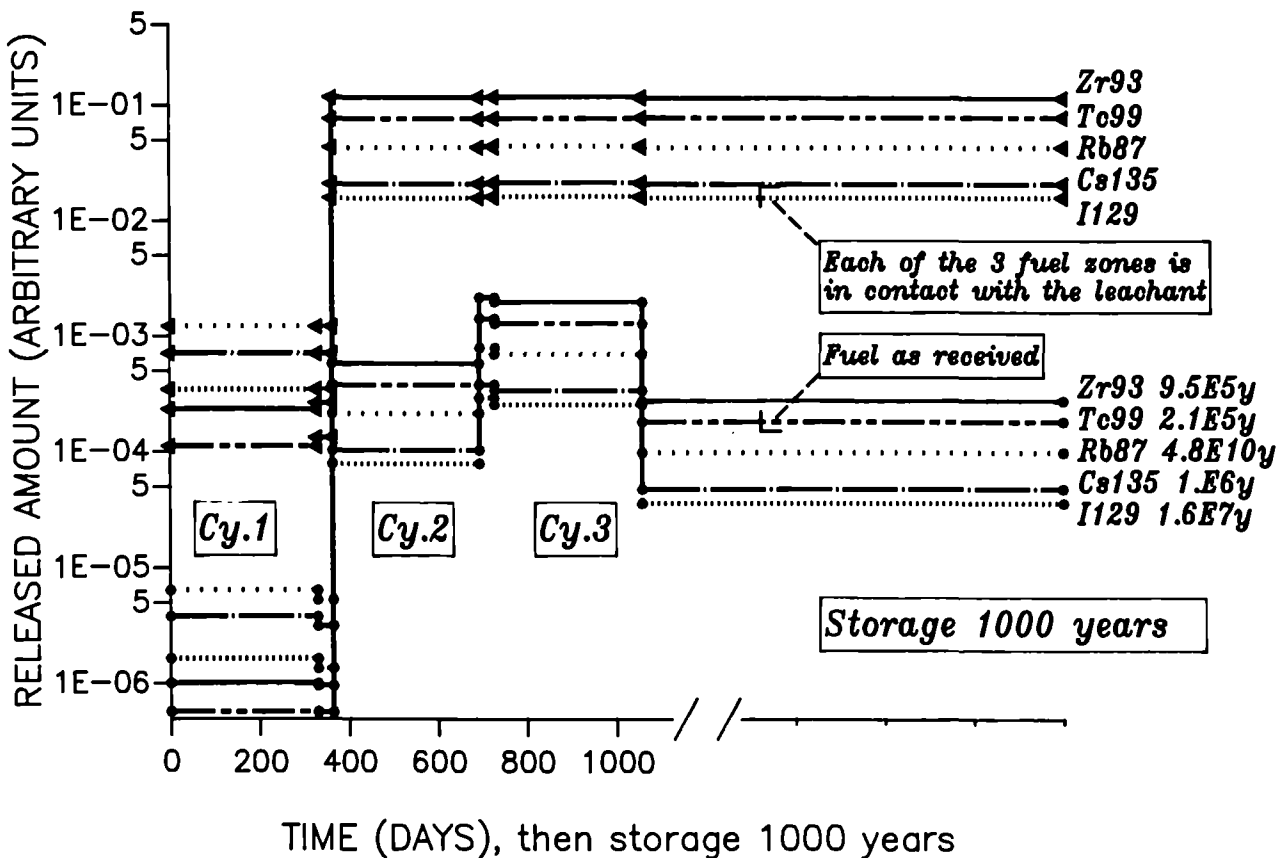


Fig.4.43 Probable amount of long-life isotope in contact with the leachant (arbitrary units)

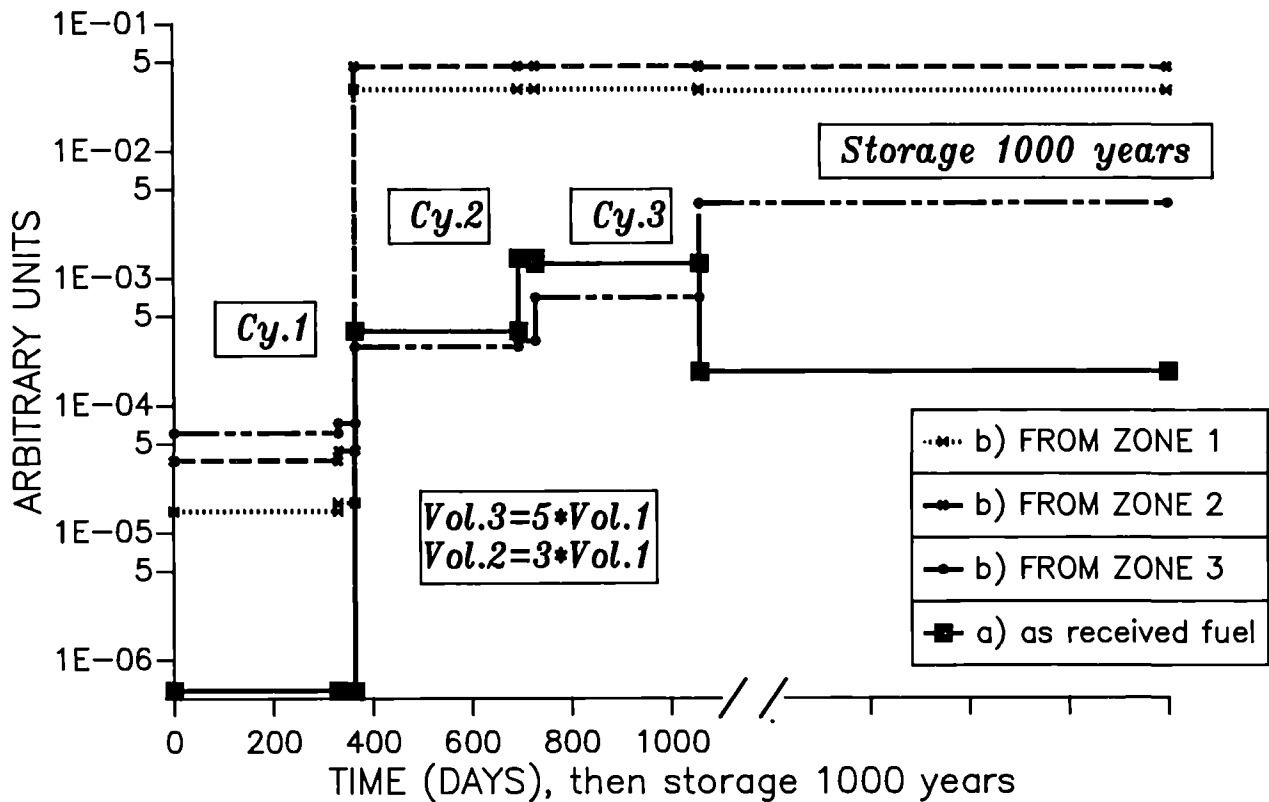


Fig.4.44 Transported amount to the leachant (arbitrary units)

Non-Destructive Assay for Spent Fuel Characterisation

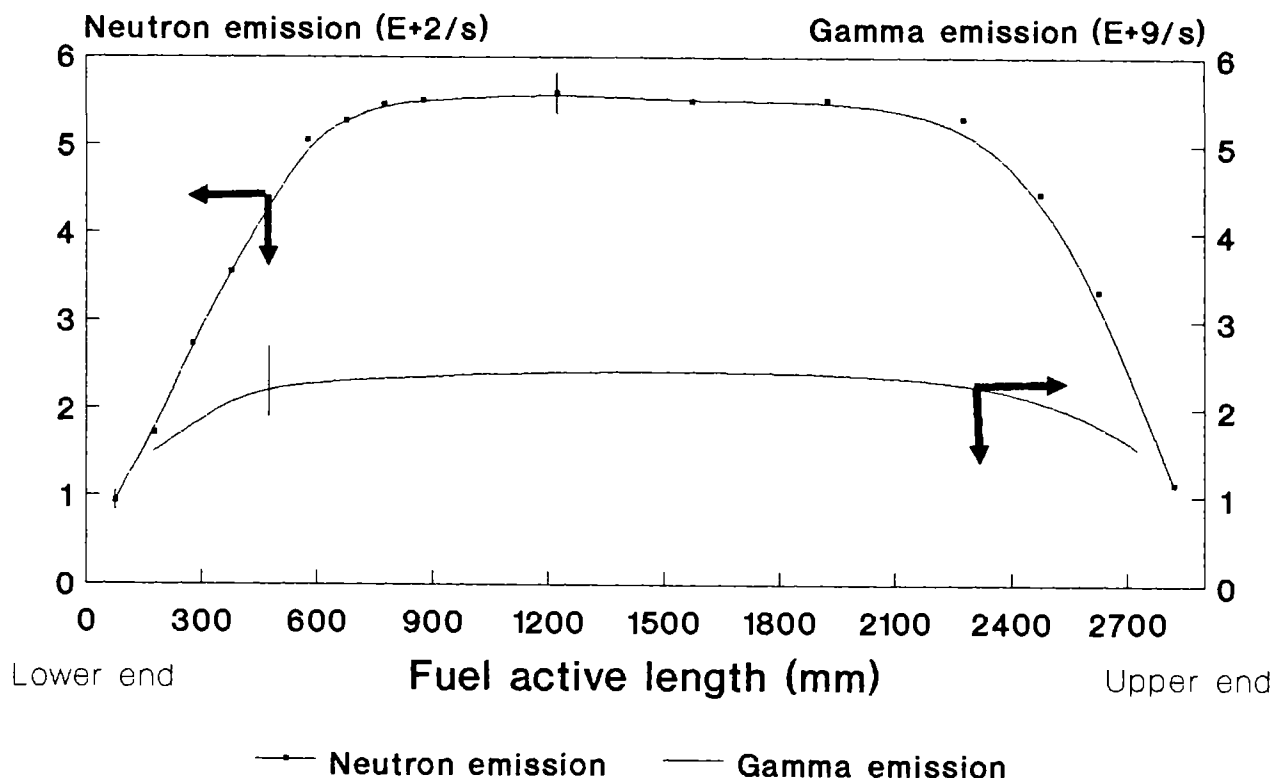
Equipment for non-destructive assay has been developed for the characterisation of individual spent fuel pins in a β - γ hot cell, (TUAR-91, p. 121). The spent fuel is characterised in terms of burn-up and radiotoxicity potential by passive neutron interrogation and gamma spectroscopy. Passive neutron interrogation is performed by a semi-cylindrical array of neutron detectors embedded in a polyethylene moderator. Gamma spectroscopy is performed by a HPGe detector situated outside the hot cell, with γ -radiation collimated by a hole through the cell wall. Quantification of the experimentally measured neutron and gamma signatures is accomplished using Isotopic Correlations (TUAR-92 p. 108).

The NDA of spent fuel has been demonstrated through the analyses of different LWR spent fuel pins[1]. The neutron and gross gamma profiles, as a function of distance along a fuel pin are shown in Fig.4.45. Such curves form the ba-

sis from which the information required to characterise a fuel is obtained through isotopic correlations. The average burn-up for different pins has been predicted to within 6 % of the value declared by the operators. Pellets taken halfway along the region of peak burn-up from two of LWR pins were destructively analysed (DA) for local burn-up determination. On the basis of the ^{148}Nd measurement by Isotope Dilution Mass Spectrometry, the results are:

	DA measurement	NDA prediction
Pellet 1 :	44.8 GWd/tU	46.5 GWd/tU
Pellet 2 :	54.8 GWd/tU	55.8 GWd/tU

Spent fuel characterisation has been performed within a number of applications. The neutron and gamma distribution profiles were determined for the GNS project related to direct disposal of spent fuel at the Gorleben site (see corresponding text in this report). The gross neu-



Burnup 40.3 GWd/tU

Fig.4.45 Axial distribution of neutron and gamma emissions from an LWR spent fuel.

tron and gamma measurements from minor actinide-containing spent fuels (SUPERFACT fuels) were measured for dosimetry aspects associated with such fuels (see corresponding text in this report).

Gross neutron and gamma measurements were performed on spent fuels of different initial enrichment and final burn-up in order to study, in association with KORIGEN, the buildup of higher nuclides during irradiation in a thermal reactor. This is an on-going study related to the effect of these parameters on a fuel cycle comprising handling of such fuels, enrichment costs, material behaviour per unit burn-up and radiotoxicity potential. (Results of this study will be available for the next issue of TUAR).

Further studies include the use of gross neutron measurements as a normalisation parameter on KORIGEN calculations in relation to LWR-UPu fuel. These studies will be coupled with DA isotopic analyses in order to study the effect of initial plutonium enrichment on the KORIGEN predictions. Gross neutron measurements will be finally employed to predict, through isotopic

correlations, the local inventory of a segment which will subsequently undergo leaching and hence yield information on leach rates.

The present neutron collar used for passive neutron interrogation is being extended to include a miniature semiconductor detector for simultaneous gamma spectrometry. Finally, the possibility to install a system in order to perform gamma emission tomography on spent fuel in the hot cell will be investigated. Such a system would yield information on the FP activity across the radius of the fuel.

1.5 Actinide Research

Introduction

The central objective of actinide research in ITU and in its numerous collaborations is the elucidation of the electronic structure of actinide metals and actinide compounds, in particular of the behaviour of the 5f electrons. The dualism between localized and itinerant characteristics as it is particularly clearly demonstrated in the actinide series, is a key problem in these studies.

These goals are approached by experiment and theory. Experimental studies are either selective investigations on the basis of theoretical or other experimental information which indicates that a particular material and method are promising, or they can involve a systematic approach to a whole class of compounds. Theoretical calculations can indicate to the experimentalist where he can expect to find important results, and on the other hand try to combine experimental evidence from different sources into a general picture. An important basis for the experimental study is the preparation of polycrystalline and single crystal samples of actinides of high specific activity, and their careful characterization by x-ray diffraction, chemical, and electron microprobe analysis.

Preparation and Characterization of Actinide Metals and Compounds

Work on preparation, crystal chemistry and physical properties of large families of isostructural compounds continued during the reporting period. Progress in the study of the following groups of materials will be reported:

- Magnetic compounds with the ThMn_{12} structure
- Compounds with the 1:1:1 composition
- Compounds with the 2:2:1 composition
- Quasicrystals
- Compounds with the 1:13 composition
- Compounds with the 1:2:3 composition

The compounds prepared and encapsulated for physical property measurements during 1992 are listed in Tab. 5.1.

The new intermetallic compounds prepared and characterised in the reporting period are listed in Tab. 5.2.

The investigation of the AnX_3 compounds with the AuCu_3 structure type is continued by the preparation of NpIn_3 , NpGa_3 and $\text{Np}(\text{Sn}_{0.8}\text{Ge}_{0.2})_3$ for Mössbauer spectroscopy.

The systematic study of the AnM_2Al_3 compounds ($\text{An} = \text{Np}, \text{Pu}, \text{U}_x\text{Np}_{1-x}$ and $\text{M} = \text{Ni}, \text{Pd}$) was started in order to compare their physical properties with the heavy fermion system UPd_2Al_3 . All AnM_2Al_3 compounds prepared crystallise in the hexagonal CaCu_5 structure type.

Magnetic compounds of the ThMn_{12} structure type

During 1992, a study of ternary uranium-iron based compounds of the ThMn_{12} structure type was started in cooperation with the Chemistry Department of the ICEN-LNETI in Sacavem, Portugal. These tetragonal compounds of high iron content are good candidates for permanent magnets. New intermetallic phases with a rare earth and with this structure have already been discovered ($\text{SmFe}_{11}\text{Ti}$, $\text{YFe}_{10}\text{V}_2$). With the 5f elements a much larger magnetic coercivity may occur due to the larger 5f-3d electronic coupling.

The work was started with the $\text{UFe}_{12-x}\text{Al}_x$ and $\text{UFe}_{12-x}\text{Si}_x$ systems, where, according to the literature, the ThMn_{12} -type structure was found to exist. The phase diagram of the ThMn_{12} -type compounds was investigated. In the range $6.2 \leq x \leq 8.2$ the $\text{UFe}_{12-x}\text{Al}_x$ system melts congruently. In the $\text{UFe}_{12-x}\text{Si}_x$ system no congruent melting was observed. In the range $\text{UFe}_{8.7}\text{Si}_{3.3}$ - $\text{UFe}_{11.5}\text{Si}_{0.5}$ the ThMn_{12} -type phase coexists with an intergranular silicon-iron rich phase. $\text{UFe}_{9.2}\text{Si}_{1.8}$ seems to melt congruently.

After the metallographic study of $\text{UFe}_{12-x}\text{Al}_x$, the $\text{UZn}_{12-x}\text{Fe}_x$ system was examined. In this system only a small part of the zinc can be substituted. The iron-rich samples ($X < 8$) were not homogeneous. Detailed magnetization measurements in single phase polycrystalline UFe_4Al_8 were performed in the range 4-300 K and under fields up to 5 T.

A Czochralski apparatus for growing single crystals of actinide based hard magnets was built and several crystals with compositions

Tab.5.1 Samples prepared, characterised and encapsulated in 1992 for the indicated measurements.

Neutron Scattering	CEN Grenoble	NpBi NpTe	M-SC M-SC
Resistivity	CEN Grenoble	NpTe NpSe NpSb NpP	M-SC M-SC M-SC M-SC
Susceptibility	CEN Grenoble	NpTe NpSe U ₅ Sb ₄	M-SC M-SC M-SC
Magnetism	Univ. Amsterdam	U ₂ M ₂ In (M=Co,Rh,Ir) U ₂ M ₂ Sn (M=Co,Ni,Pt)	AcM AcM
Mössbauer Spectroscopy	CEN Grenoble, TU München	NpSe NpAl ₂ NpIn ₃ , NpGa ₃ (U _{0.5} Np _{0.5})Pd ₂ Al ₃ (U _{0.7} Np _{0.3})Pd ₂ Al ₃ Np ₂ M ₂ In (M=Co,Rh,Ni,Pd,Pt)	M-Powder AcM-Powder AcM-Powder AcM-Powder AcM-Powder AcM-Powder

AcM=Arc Melting

M=Mineralisation

SC=Single Crystal

UFe_{12-x}Al_x (6.2 ≤ x ≤ 8.2) were pulled, oriented and prepared for the measurement of physical properties. Physical property measurements on single crystals are in progress.

Study of a new family of actinide ternary intermetallic compounds

Studies of large isostructural groups of compounds provide important information on the development of the electronic structure of actinide intermetallics, especially on the hybridization of 5f states with electron states of ligands. We report here on a new family of compounds of the type An₂M₂X. It crystallizes in the U₃Si₂ structure type. 22 new uranium and neptunium compounds of this type were prepared (Table 5.3) by arc-melting a mixture of the components.

One compound of this family (U₂Co₂Al) was observed in the ternary phase diagram U-Co-Al. This compound melts incongruently. Object of this work is the synthesis of analogous compounds with In and Sn as p elements. They are formed congruently. The compounds are characterized by X-ray diffraction, by magnetization measurements at T = 4.2 K and, for the Np-containing compounds, by Mössbauer spectroscopy at 4.2 and 79 K.

U₂M₂In, Np₂M₂In and U₂M₂Sn were prepared by arc melting of stoichiometric amounts of metals under a purified Ar atmosphere. The samples are checked by metallography. Small single-crystalline fragments could be obtained. They were used for the X-ray structure determination, performed on a Enraf-Nonius CAD-4, four circle diffractometer. In some cases X-ray

Tab.5.2 Crystallographic data of new actinide intermetallic compounds.

Compounds	Space group	Structure type	Lattice parameters (pm)	Z
PuOsAl	P6 ₃ /mmc	MgZn ₂	542.6(1) 863.0(1)	4
PuCoAl	P $\bar{6}$ 2m	Fe ₂ P	678.5(9) 392.1(3)	3
PuRuAl	P6 ₃ /mmc	MgZn ₂	539.9(1) 848.8(2)	4
PuFeAl	P6 ₃ /mmc	MgZn ₂	525.2(2) 852.3(6)	4
PuRhAl	* Pnma	Ge ₈ Mn ₅ Pd ₁₁	698.9(1) 414.7(1) 1573.5(2)	8
PuIrAl	Pnma	Ge ₈ Mn ₅ Pd ₁₁	692.4(1) 414.0(1) 1572.5(2)	8
NpIrSn	* P $\bar{6}$ 2m	Fe ₂ P	737.6(3) 399.2(1)	3
NpPd ₂ Al ₃	* P6/mmm	CaCu ₅	539.0(1) 419.1(1)	1
PuPd ₂ Al ₃	* P6/mmm	CaCu ₅	540.2(1) 419.4(1)	1
NpNi ₂ Al ₃	* P6/mmm	CaCu ₅	522.8(2) 400.5(2)	1
Np _{0.5} U _{0.5} Pd ₂ Al ₃ *	P6/mmm	CaCu ₅	537.9(1) 419.0(1)	1
Np _{0.3} U _{0.7} Pd ₂ Al ₃ *	P6/mmm	CaCu ₅	537.5(1) 419.1(1)	1
NpIn ₃	Pm3m	AuCu ₃	461.25(5)	1
NpGa ₃	Pm3m	AuCu ₃	425.51(1)	1
Np(Sn _{0.8} Ge _{0.2}) ₃ *	Pm3m	AuCu ₃	455.1(1)	1

* from X-ray single crystal analysis.

Tab.5.3 Lattice parameters of new An_2M_2X intermetallic compounds.

Compounds	Lattice parameters		Compounds	Lattice parameters	
	a (pm)	b (pm)		a (pm)	b (pm)
U_2Co_2In *	736.1(2)	343.1(1)	U_2Co_2Sn	729.0(5)	351.2(5)
U_2Ni_2In *	737.4(2)	357.2(1)	U_2Ni_2Sn	723.4(6)	370.6(5)
U_2Rh_2In *	755.3(2)	360.5(1)	U_2Rh_2Sn	751.1(5)	363.5(3)
U_2Pd_2In *	763.7(1)	375.2(1)	U_2Pd_2Sn *	760.2(2)	378.5(1)
U_2Ir_2In	759.6(9)	358.2(5)	U_2Ir_2Sn *	756.6(1)	360.1(1)
U_2Pt_2In *	767.9(3)	370.3(2)	U_2Pt_2Sn	753.3(9)	365.1(2)
Np_2Co_2In	732.2(1)	351.5(1)	Np_2Co_2Sn *	726.2(2)	356.5(1)
Np_2Ni_2In *	736.4(2)	359.0(1)	Np_2Ni_2Sn *	729.3(2)	366.1(1)
Np_2Rh_2In *	752.4(2)	364.9(1)	Np_2Rh_2Sn *	750.2(3)	366.8(1)
Np_2Pd_2In	765.3(1)	379.9(2)	Np_2Pd_2Sn *	762.2(4)	381.6(2)
Np_2Pt_2In	767.5(2)	371.6(2)	Np_2Pt_2Sn *	765.6(2)	373.0(1)

* from X-ray single crystal analysis.

powder diffraction was used for the determination of the lattice parameters.

Magnetization measurements at 4.2 K have been performed at the High-Field Installation of the University of Amsterdam in semi-continuous fields up to 38 T. To avoid an influence of texture of the bulk pieces, the samples were in the form of randomly oriented powder particles fixed by frozen alcohol.

Some Np_2M_2In compounds were studied at 4.2 K and above the ordering temperature with Mössbauer spectroscopy using the ^{237}Np 5/2 - 5/2 transition. The ^{241}Am metal source was always kept at 4.2 K. The sample was ground and encapsulated in an Al disc with a neptunium density of 180 mg/cm².

All compounds investigated were found to crystallize in the U_3Si_2 -type (space group $P4/m\bar{b}m$) structure. The projection of the structure along the c axis is shown in Fig.5.1. The atomic positions are the following ($x = 0.389$):

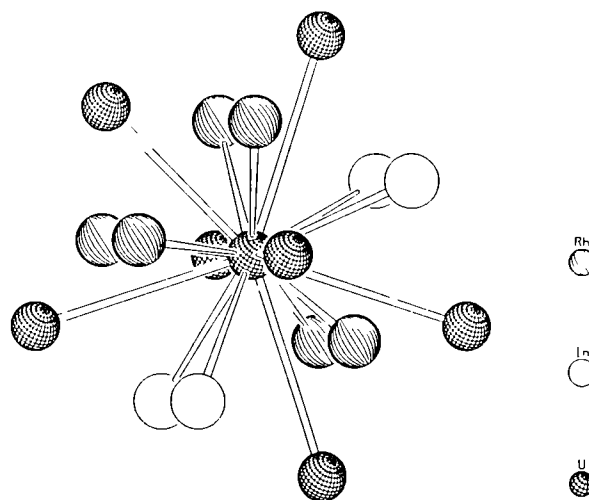


Fig.5.1 Structure of U_2Rh_2In . Representation of surroundings of U atoms viewed along a direction close to the c-axis .

U1 in 2a : 0, 0, 0
 U2 in 4h : x, x+1/2, 1/2
 Si in 4g : x, x+1/2, 0

In An_2M_2X compounds the actinide atoms occupy only the 4h positions, whereas the X atoms occupy the 2a positions and transition metal atoms T the Si-positions 4g. The structure consists of two alternating types of basal-plane sheets separated by $c/2$, one containing only actinides, the other accommodating M and X atoms. Each An atom has three types of nearest actinide neighbours. There are two nearest neighbours along the c-axis separated by $d_{An-An}(1) = c$, i.e. $d_{An-An}(1) = 340 - 370$ pm. In the basal plane, there is one nearest neighbour at the distance $d_{An-An}(2)$ slightly larger than (1) for U_2M_2In compounds, and probably slightly smaller than (1) for U_2M_2Sn compounds, where the details of atomic positions have not been refined yet. For Np_2M_2In , the distances (1) and (2) are approximately equal. Finally, there are four other nearest actinide neighbours in the plane, with $d_{An-An}(3)$ of about 490 pm.

Fig. 5.2 shows the high-field behaviour of U_2Pd_2In , U_2Co_2In and U_2Ni_2In at 4.2 K. The first one, displaying a metamagnetic transition which starts at about $B = 25$ T, has undoubtedly an antiferromagnetic ground state. The second one displays a linear magnetization curve with a corresponding moment of only 0.05 $\mu_B/f.u.$ induced in a field of 20 T. Therefore we can assume

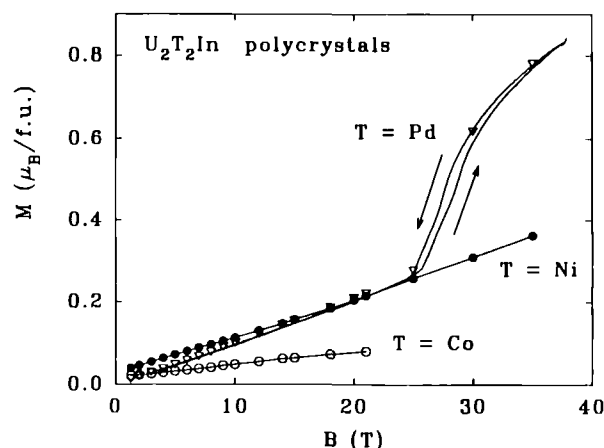


Fig.5.2 Magnetization curves of selected U_2T_2In compounds at 4.2 K.

that U_2Co_2In is non-magnetic, its magnetic susceptibility being of only $1.8 \cdot 10^{-8} m^3/mol$. U_2Ni_2In , which displays a weak upturn in the $M(B)$ dependence and reaches a larger value of magnetization in $B = 35$ T (corresponding to $0.37 \mu_B/f.u.$) can be either an antiferromagnet with a metamagnetic transition above the experimentally accessible range, or an exchange-enhanced paramagnet with spin-fluctuation features.

The compounds Np_2T_2In ($T = Co, Rh, Ni, Pd, Pt$) were investigated by Mössbauer spectroscopy. The results are listed in Tab. 5.4. All com-

Tab.5.4 Hyperfine parameters and line width of the Np_2M_2In compounds.

Compound	T(K)	$B_{hf}(T)^a$	$\Delta B_{hf}(T)^b$	$e^2qQ(mm/s)$	FWHM(mm/s) ^c	IS(mm/s) ^d
Np_2Co_2In	80	----	----	9.8(4)	2.7(1)	-16.3(5)
	4.2	143(2)	7(2)	6.0(3)	3.3(1)	-16.4(5)
Np_2Rh_2In	80	----	----	20.1(3)	2.7(1)	-12.9(5)
	4.2	286(2)	21(2)	4.5(3)	2.9(1)	-13.1(5)
Np_2Ni_2In	45	----	----	10(4)	3.2 ^e	-10.4(1)
	4.2	337(1)	4(2)	3.0(2)	3.2(1)	-11.1(1)
Np_2Pd_2In	45	----	----	15.8(8)	4.1(2)	0.4(1)
	4.2	299(1)	37(4)	-6.8(9)	4.9(4)	0.4(1)
Np_2Pt_2In	45	----	----	32.6(4)	4.9(1)	-6.6(1)
	4.2	312(1)	47(4)	-15.2(8)	4.7(3)	-6.3(1)

Hyperfine parameters and line width of the Np_2T_2In compounds measured by Mössbauer spectroscopy

- Mean value of the Gauss distribution of magnetic hyperfine fields
- Full width at half maximum of the Gauss distribution of magnetic hyperfine fields
- Full width at half maximum of the resonance line
- Isomer shift relative to $NpAl_2$; our ^{241}Am -metal source has a shift of -14 mm/s against $NpAl_2$
- FWHM was fixed at the low temperature value and the fit was improved by addition of a second site (7%) with parameter values: $e^2qQ \equiv 0$, FWHM $\equiv 3.2$ mm/s, IS $\equiv -17.6$ mm/s

pounds show magnetic order at 4.2 K. At 80 K no magnetic hyperfine splitting is present in $\text{Np}_2\text{Rh}_2\text{In}$ and $\text{Np}_2\text{Co}_2\text{In}$. The corresponding spectra can be fitted with a single quadrupolar hyperfine pattern, which means, that all the Np ions see the same local surroundings in the paramagnetic phase. This also applies for $T = \text{Pd}$ and Pt at 45 K. However, in the case of $\text{Np}_2\text{Ni}_2\text{In}$, a second subspectrum with a different isomer shift and a relative intensity of -7% had to be included in order to give a reasonable fit. This subspectrum could either be explained by a second crystallographic phase or by another Np site in the crystal.

At 4.2 K an additional magnetic hyperfine splitting appears with an accompanying reduction of the quadrupole interaction parameter e^2qQ .

In the following the $\text{Np}_2\text{T}_2\text{In}$ compounds will be discussed in two separate groups, the Co - group with 9 electrons in the outer s - and d - shell of the T - atoms $T = \text{Co}, \text{Rh}$, and the Ni - group with $T = \text{Ni}, \text{Pd}, \text{Pt}$ and one more valence electron in the corresponding shells of the T - atom.

If we compare $\text{Np}_2\text{Co}_2\text{In}$ with $\text{Np}_2\text{Rh}_2\text{In}$, we notice a much stronger hyperfine field for the Rh-compound, which also shows a higher isomer shift and quadrupole splitting. The reduction of the magnetic moments in the case of Co can be well understood as a consequence of the stronger 5f-d hybridization. This is comparable with effects observed in other actinide-d intermetallics. The larger mean magnetic 5f-moment in $\text{Np}_2\text{Rh}_2\text{In}$ is a consequence of the weaker delocalization of the 5f-states as compared to the Co case. This picture is supported by the variation of the isomer shift IS between the Rh- and the Co-compound. In the Rh-case the more localized 5f-electrons reduce the s-electron density at the nucleus $\rho(0)$ by higher screening effects as compared to $\text{Np}_2\text{Co}_2\text{In}$. A similar tendency was observed in the NpX_3 compounds (with X taken from group IIIa and IVa elements of the periodic table), where 5f-ligand hybridization strongly influences IS.

If we go down the Ni - group of the periodic table from Ni to Pd and to Pt we observe a similar increase of IS but the values are all higher as compared to the Co - group. According to the interpretation of the variation of IS given above, the 5f-d hybridization increases when going up the periodic table in both groups. When turning from Co to Ni and Rh to Pd, i.e. adding one valence electron, IS rises by ~ 6 mm/s, which corresponds to a reduction of the 5f-delocalization.

This reflects the expectation, that adding one d-electron pulls the d-band further below the Fermi level and consequently weakens the 5f-d hybridization. A similar trend of 5f - d hybridization can be observed in UX_3 compounds with $X = \text{Pd}, \text{Pt}$ and Rh, Ir .

Compounds with the 1:1:1 composition

To continue the systematic investigations of the AnMX compounds, six Pu compounds and NpIrSn were prepared and characterised by X-ray diffraction. Single crystal X-ray diffraction analysis shows that the compounds crystallise in three structure types (Fe_2P , MgZn_2 and $\text{Ge}_8\text{Mn}_5\text{Pd}_{11}$). The projection of the new structure of PuRhAl along the b axis is represented in Fig. 5.3. Mössbauer spectroscopy and magnetic measurements (magnetization and susceptibility) were performed on a number of the 1:1:1 compounds.

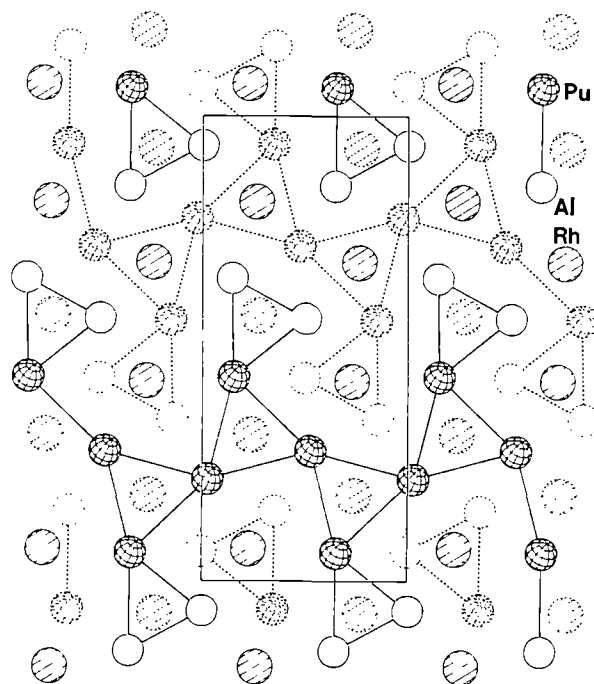


Fig.5.3 Projection of the PuRhAl structure along the b axis (solid atoms at $y = 0.25$ and dashed atoms at $y = 0.75$).

The Mössbauer measurements have been performed on the NpTAl compounds with the ZrNiAl structure type (that is, $T = \text{Co}, \text{Ni}, \text{Rh}, \text{Ir}, \text{Pt}$ as well as NpNiGa). All these compounds are magnetically ordered at 4.2 K. The magnetic Mössbauer spectra at this temperature are com-

plicated, they suggest the presence of magnetic modulated structures or spin fluctuations. Nevertheless, it has been possible to realise a fit of the spectra with two gaussian distributions of the hyperfine field. Then, the strength of the fields increases according to the sequence (Tab. 5.5): (NpCoAl) < NpNiAl < NpNiGa < NpRhAl < NpIrAl < NpPtAl.

The isomer shifts at 30K (48K for NpIrAl) show the following tendency (Tab. 5.6): (NpCoAl) < NpIrAl < NpRhAl < NpNiAl < NpNiGa < NpPtAl.

According to the low point symmetry of the crystallographic Np position ($m2m$), the asymmetry

factor equals or is close to unity except for NpCoAl ($\eta = 0.651$) and NpPtAl ($\eta = 0.232$). The quadrupole interaction parameter e^2qQ is rather large with values around 40 mm/s, it is positive for NpNiAl and NpNiGa and negative for the other compounds.

Magnetisation and susceptibility measurements have also been performed. All the compounds ordered antiferromagnetically (except perhaps NpIrAl). The transition (Néel) temperature is given in Tab. 5.7.

PuTAl compounds crystallise with various structures, allowing comparison. In order to reduce the influence of the size effect due to the

Tab.5.5 Simulation of Mössbauer spectra of NpTAl compounds with the ZrNiAl structure in their magnetic state.

Specimens (4,2K)	$B_{hf}(T)$	$\sigma(T)$	$e^2qQ(mm/s)$	η	θ	$\delta(mm/s)$	FWHM(mm/s)	Ri(%)
NpNiAl	223(4)	8(1)	42(1)	1,00	73(1)	-9,6(1)	3,8(2)	66
	156(1)	7(1)	40(2)		90(1)	-9,8(1)		34
NpNiGa	228(1)	12(1)	42(2)	1,00	97(6)	-7,6(1)	3,3(2)	61
	170(1)	17(1)	38(3)		90(2)	-7,8(1)		39
NpRhAl	229(1)	20(1)	-36(2)	0,88	24(3)	-11,4(1)	4,2(3)	57
	170(1)	24(2)			123(2)	-11,2(2)		43
NpIrAl	259(1)	7(1)	-36(2)	1,00	-170(7)	-13,4(1)	4,1(3)	68
	176(3)	35(3)			109(5)			32
NpPtAl	284(1)	30(1)	-35(1)	0,23	10(4)	-5,7(1)	48(3)	73
	178(1)	80(2)			48(3)	27		

σ is the standard deviation of the two gaussians; θ is the angle between the principal axis of the hyperfine field and the electric field gradient. The isomer shift δ is given with respect to $NpAl_2$.

Tab.5.6 Fit of the paramagnetic spectra of the NpTAl compounds with the ZrNiAl structure.

Specimens	$\delta (mm/s)$	$ e^2qQ (mm/s)$	η	FWHM (mm/s)
NpCoAl	-14,03(6)	49.0(2)	0,65(1)	3,40(3)
NpIrAl (48K)	-12,78(6)	34(2)	1,00(4)	3,91(4)
NpRhAl	-10,26(6)	39,2(2)	0,88(2)	3,76(4)
NpNiAl	-9,27(5)	42(1)	1,00(3)	3,73(3)
NpNiGa	-7,39(6)	38(1)	1,00(2)	3,56(4)
NpPtAl	-5,37(6)	39.2(2)	0,23(2)	4,60(5)

Tab.5.7 Néel temperatures

Compounds	NpCoAl	NpNiAl	NpNiGa	NpIrAl	NpPtAl
$T_N(K)$	7	21	16	$32 > T_N > 48$	12

transition metal, the real distances are divided by the sum of the metallic radii (coordination number 12). This method leads to the trends shown in Fig 5.4. In particular, it can be seen that the PuRhAl structure appears as a transition structure between ZrNiAl and TiNiSi structure.

Characterization of NpBe₁₃ compounds

Since high pressure Mössbauer experiments, as well as neutron diffraction measurements are planned on the heavy fermion compound NpBe₁₃, the preparation of high quality samples is of utmost interest. According to ref [1], the magnetic properties of NpBe₁₃ are extremely sensitive to the Be content. Samples with small Be excess turned out to be nonmagnetic down to 2 K. Be-deficient samples showed a magnetic transition around 4.9 K with one magnetic Np site, although the crystallographic data of these two types of samples were identical. The compounds that have been prepared for Mössbauer

measurements always contained some impurities [1]. A new sample, which was made in Los Alamos, showed only one crystallographic phase according to X-ray characterization and Mössbauer measurements at 80 K. However at 1.2 K the Mössbauer spectrum reveals two magnetic sites of the Np atom, one being magnetically split, the other being nonmagnetic. According to the interpretation given above the compound contains two different magnetic phases, one with excess Be displaying no magnetic order down to 1.2 K, the other with Be deficiency and a magnetic phase transition below 5 K. A new series of compositions NpBe₁₂, NpBe₁₃, NpBe₁₄ has been made recently to investigate the sensitivity of the Be contents towards magnetic behaviour. Preliminary X-ray diffraction studies on powder samples have shown no differences whatsoever. According to the interpretation of reference [1] this would mean, that higher Be contents (but with unchanged lattice constant) increase the 5f-ligand hybridization and destroy magnetism. A systematic Mössbauer study of NpBe_{13+x} ($x = -1, 0, +1$) at ambient and elevated pressure could reveal the influence of the

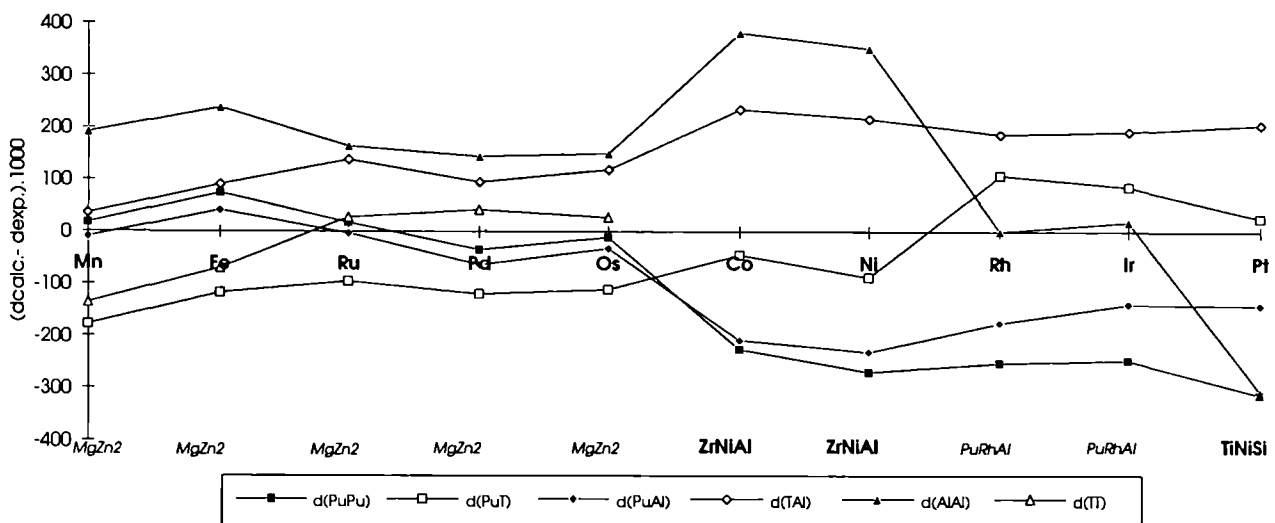


Fig.5.4 Difference between the distances calculated on the basis of the metallic radii (CN = 12) and the real distances in the PuTAl compounds.

variation of 5f-ligand hybridization caused by two different effects ("chemical" and physical pressure) on T_{ord} and the magnetic moments. Ambient pressure Mössbauer experiments at 1.2 K and single crystal X-ray measurements at room temperature are under way.

Reference

- [1] J. Gal, F.J. Litterst, W. Potzel, J. Moser, U. Potzel, G.M. Kalvius, S. Fredo, and S. Tapuchi, *Phys. Rev. B* **36** (1987) 2457.

Synthesis and characterization of quasicrystalline materials

We have previously studied many samples of ternary Al-Cu-U, Al-Cu-M (M = Ru, Rh, Re, Ir) and quaternary Al-Cu-Ru-U alloys prepared by various solidification methods [1; TUAR-91, pp 136-142]. This year we have investigated the quasicrystalline structure of conventionally solidified ternary $\text{Al}_{80-x}\text{Cu}_{20}\text{M}_x$ (M = Ru, Rh, Re, Ir) alloys with $x = 7.5, 15, 20, 22.5$ at. % by EDX, DTA and magnetic measurements. Bulk samples of 20-200 mg were used for the magnetic measurements.

A SQUID-Magnetometer (Quantum-Design) within the group of Prof. Politis from the Nuclear Research Centre Karlsruhe (KfK) was employed to measure the temperature dependence of the magnetic susceptibility, χ (T), between 5 K < T < 300 K in the following manner: The specimens were first cooled from room temperature to 5 K. Then, a minimum external magnetic field of $H = 1000$ Oe was applied, for all subsequent measurements. χ (T) was recorded for the complete temperature cycle of 5-300-5 K. In addition, the magnetization as a function of field, M (H), was measured up to 50 KOe in the field range $-50 \text{ kOe} \leq H \leq 50 \text{ kOe}$ at $T = 50$ K. The magnetic properties of the samples show many features in common with single Al-Cu-Fe icosahedral quasicrystals described by Matsuo et al. [2].

Using the empirical criteria of Tsai et al. [3] based on the theory of Hume-Rothery et al. [4] we have investigated by calculation the formation of a quasicrystalline phase in the $\text{Al}_{90-x}\text{Tc}_{10}\text{M}_x$ (M = transition metal) system, where the criterion of the stability ($p = e/a \approx 1.75$) is fulfilled [5]. Subsequently, we were able to produce several binary $\text{Al}_{100-x}\text{Tc}_x$ ($x = 5, 10, 15, 18.5$ at. %), and ternary $\text{Al}_{90-x}\text{Tc}_{10}\text{M}_x$

(M = Mn, Ru, Rh, Pd, Re, Ir, Pt) alloys at various concentrations x , by conventional solidification methods. The characterization of the quasicrystalline state in these alloys by X-rays, EDX, DTA, SEM and TEM is currently in progress. Dilatometric measurements in the ternary Al-Cu-M (M = Ru, Rh, Re, Ir) system are also under preparation.

References

- [1] N. Athanasiou, I. Ray, J.C. Spirlet and C. Politis; "Synthesis and Characterization of Quasicrystalline Materials"; 22^{ième}s Journées des Actinides, Méribel, France, 22-25 April 1992;
- [2] S. Matsuo, T. Ishimasa, M. Mori and H. Nakano; *J. Phys.: Condens. Matter* **4** (1992) 10053.
- [3] A.P. Tsai, A. Inoue and T. Masumoto; *Mater. Trans. JIM* **30** (1989) 666.
- [4] W. Hume-Rothery, R.E. Smallman and C.W. Haworth; "The Structure of Metals and Alloys"; 5th Edition; Institute of Metals North American Publ., Brookfield (1988).
- [5] N. Athanasiou; Dr. Thesis, Eng. Sci. Dep. Univ. of Patras (in preparation).

Structure of $(\text{L}^*\text{Tc}(\text{CO})_2)_2(-\text{N}_2)$ with $\text{L}^* = \text{HB}(3,5\text{-Me}_2\text{C}_3\text{N}_2)_3$

The compound $(\text{HB}(3,5\text{-Me}_2\text{C}_3\text{N}_2)_3\text{Tc}(\text{CO})_3)$ reacts after UV irradiation in tetra-hydrofuran with elementary nitrogen to give the air-stable N_2 -bridged binuclear complex $(\text{HB}(3,5\text{-Me}_2\text{C}_3\text{N}_2)_3\text{Tc}(\text{CO})_2)_2(-\text{N}_2)$. The crystal and molecular structure of this first N_2 -bridged technetium complex has been determined by single crystal X-ray diffraction. The compound crystallises in the monoclinic space group C2/c with the cell parameters $a = 2,032.6(6)$, $b = 1,454.7(4)$, $c = 1,427.0(5)$, $\beta = 103.95(2)^\circ$ and $Z = 4$. The crystal structure of the N_2 -bridged binuclear complex $(\text{HB}(3,5\text{-Me}_2\text{C}_3\text{N}_2)_3\text{Tc}(\text{CO})_2)_2(-\text{N}_2)$ is represented in Fig. 5.5. The co-ordination polyhedron about the Tc atom is a slightly distorted octahedron formed by the three nitrogen atoms of the tridentate pyrazolyl borate ligand, the two carbons of the carbonyl groups and the N atom of N_2 bridging the Tc atoms. The N-N distance in N_2 is 116.0 pm and the Tc-N-N angle is 174.0° .

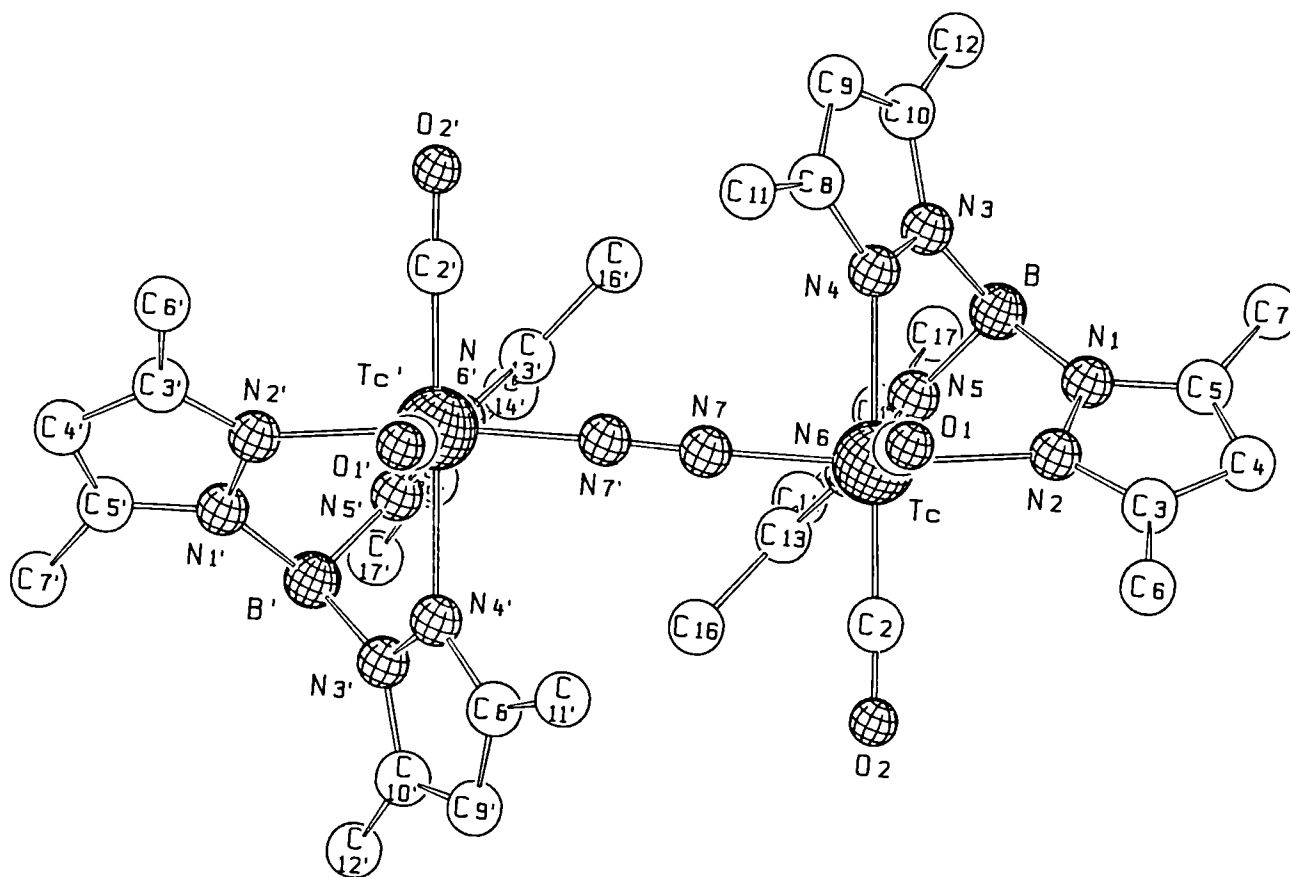


Fig.5.5 Structure of $(\text{HB}(3,5\text{-Me}_2\text{C}_3\text{N}_2)_3\text{Tc}(\text{CO})_2)_2(-\text{N}_2)$

Solid State Physics Studies on Actinide Systems

Estimated magnetic ordering temperature of uranium dioxide

When the 5f states are localized, the 5f moments interact indirectly through exchange interactions with the valence electrons. The exchange interactions of the atoms depend in general upon both orbital and angular properties but the *isotropic* part of the exchange interaction depends only upon radial integrals for a 5f-shell. In the local spin density approximation (LSDA) [1,2] the *spin polarization - or magnetic - energy* may be expressed in terms of radial exchange integrals [3,4], $J_{ll'm_l m_{l'}}$, by

$$E_{SP}^{LSDA} = -\frac{1}{4} \sum_{l,l'} J_{ll'm_l m_{l'}} \quad (1)$$

The LSDA exchange integrals for the 5f states of actinide atoms are plotted in Fig. 5.6 where they are compared with the similar exchange integrals from Hartree Fock theory. The reason that the f-d exchange integrals decrease across each series is the contraction of the 5f-shell, which decreases the overlap with the d-states. The overlap between 5f and 6d densities occurs over a relatively small region of space corresponding to the outer part of 5f density and the inner part of the 6d density. As the 5f shell contracts the region of overlap decreases [5].

In actinides where the 5f states are localized they may be treated, to a good approximation, as part of the atomic core. As an example we have taken UO_2 . The total number of 5f electrons is known to be equal to 2 since uranium in UO_2 is quadrivalent. UO_2 orders as a type one antiferromagnet. Since the 5f states are localized we assume that they can only interact via the valence charge and spin densities, in which case we have the following model.

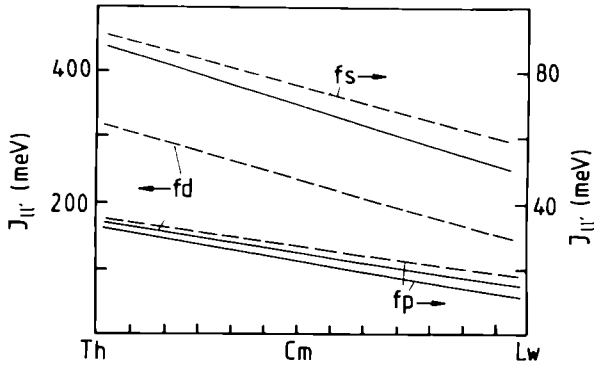


Fig.5.6 Calculated exchange integrals across the actinide series for free atoms. The full lines are the LSDA exchange integrals and the dashed lines are the Hartree Fock exchange integrals.

The valence bands in UO_2 are of primarily oxygen 2p character. However the oxygen 2p states hybridize with the 6d states of the uranium. The valence bands therefore contain a 6d admixture and there is a finite 6d charge density at the uranium site. The 5f magnetic moments polarize the 6d density via the local exchange interactions described above. We calculate the 5f-6d exchange interaction J_{5f-6d} to be 11.1mRy at a lattice constant of 6.3Å and 14.9mRy at a lattice constant of 5.4Å which is close to be experimental equilibrium. The exchange interactions therefore increase with decreasing volume. The interatomic interactions are mediated by the induced 6d spin density. In the presence of the 6d spin density it takes a finite energy to flip a 5f spin at a particular site. The local 6d spin densities are induced by the 5f spin densities at all sites and, through the exchange interaction with the 5f electrons, provide the molecular field in which the 5f electrons find themselves.

In order to simulate the molecular fields we have made self-consistent spin polarized calculations for antiferromagnetic UO_2 , with a type one configuration for values of the 5f spin between zero and 2. The 5f spin up and spin down occupation numbers were determined by

$$n_{5f} = n_{5f}^+ + n_{5f}^-$$

$$\mu_{5f} = n_{5f}^+ - n_{5f}^-$$

where n_{5f}^+ and n_{5f}^- are the up and down spin occupation numbers, n_{5f} is the total number of 5f electrons and μ_{5f} is the 5f spin moment. Clearly the occupation numbers n_{5f}^+ , n_{5f}^- are part of the input to the calculations and are not determined ab initio as are the partial occupation numbers

of the conduction electron states. Of course, since UO_2 is an antiferromagnetic insulator the computed total valence band spin is zero. At each oxygen site the total spin is also zero. But we calculate a finite induced 6d spin moment at each uranium site parallel to the 5f spin moment at that site. The induced 6d moment was found to be linearly proportional to the uranium spin. The calculated 6d moment, μ_{6d} is $\mu_{5f} 0.03\mu_B$ at a lattice constant of 6.3Å and $\mu_{5f} 0.029\mu_B$ at a lattice constant of 5.4Å.

The importance of the above result is that it enables the susceptibility, χ_{5f}^{6d} , of the 6d spin to the 5f spin to be calculated quite simply. The exchange splitting of the 6d states by the 5f spin is given by $\Delta_{6d} = J_{5f-6d}\mu_{5f}$. The 6d susceptibility, χ_{5f}^{6d} is

$$\chi_{5f}^{6d} = 2 \frac{\mu_{6d}}{\Delta_{6d}}$$

All of the quantities required occur quite naturally in the calculations and we find

$$\chi_{5f}^{6d} \approx 3$$

at a lattice constant of 6.3Å and

$$\chi_{5f}^{6d} \approx 2$$

at a lattice constant of 5.4Å.

When the 6d susceptibility is known a simple mean field theory [6] may be used to estimate the magnetic ordering temperature. The Helmholtz free energy of the valence bands above the ordering temperature is expanded

$$\Delta F = F_d(\mu_d, T) - F_d(0, T) = \frac{1}{2} A(T)\mu_{6d}^2 + \dots (2)$$

where

$$A(T) = \frac{1}{\chi_{5f}^{6d}} - \frac{J_{5f-6d}^2 (g-1)^2 J(J+1)}{3kT} \quad (3)$$

is the effective field acting on the valence bands. For a second order transition the ordering temperature is obtained by setting $A(T)$ to zero. The g-factor is taken from experiment to be 0.8 [7]. For UO_2 at a lattice constant of 5.4Å we find $T_N = 29K$. The measured ordering temperature is slightly higher (31K) but the transition is first order due to lattice distortion [8]. The value calculated here for a second order transition is therefore a lower bound. The ordering temperature should be proportional to

$$X_{5f}^{6d} J_{5f-6d}^2$$

if the g -factor is independent of temperature. Furthermore X_{5f}^{6d} is proportional to the reciprocal of J_{5f-6d} if the induced 6d moment, μ_{6d} , is independent of lattice constant - which we find to be almost true. The ordering temperature is therefore proportional to J_{5f-6d} and increases with decreasing lattice constant. The latter statement constitutes a prediction from theory which it would be interesting to check.

Since reasonable results have been obtained for UO_2 the method described will be applied to other actinide compounds in the near future.

References

- [1] W. Kohn and L.J. Sham; *Phys. Rev.* **140** (1965) A1133.
- [2] U. von Barth and L. Hedin; *J. Phys.* **C5** (1972) 1629
- [3] O. Gunnarsson; *J. Appl. Phys.* **49** (1978) 1399.
- [4] M.S.S. Brooks and B. Johansson; *J. Phys.* **F13** (1983) L197.
- [5] JRC Karlsruhe Ann. Rep., (1991) 145.
- [6] D. Bloch, D.M. Edwards, M. Shimizu and J. Voiron; *J. Phys.* **F5** (1975) 1217.
- [7] J.M. Fournier and R. Troc in *Handbook on the Physics and Chemistry of the Actinides*; eds. A.J. Freeman and G.H. Lander (North Holland, Amsterdam) vol. **2** (1985), p. 29.
- [8] J. Faber and G.H. Lander; *Phys. Rev.* **B14** (1976) 1151.

Neutron and synchrotron X-ray scattering

Introduction

The temporary shutdown (until early 1995) of the reactor of the Institute Laue Langevin in Grenoble caused a severe disruption in our neutron scattering programme, particularly for our projects on transuranium samples. Permission and the necessary safety precautions are not available at some of the other sites (e.g. Saclay and Rutherford Lab, UK). Nevertheless, we have continued performing detailed experiments on interesting uranium compounds and the year was notable for a successful polarised-neutron experiment on URuAl (at Saclay), the discovery of a new phase transition in USb (at Brookhaven), and the measurement of unusual critical scattering in USb_{0.8}Te_{0.2} (at Risø).

The magnetic X-ray scattering (all performed at the Brookhaven Synchrotron) went well this year with the completion of the study of the complex phase transitions in U_{0.85}Th_{0.15}Sb and extensive work on NpAs. In the latter material the resonance scattering is so strong that we have been able to observe magnetic critical scattering. To our considerable surprise we observe effects on a quite different length scale to that seen with neutron scattering. This work is integrated below in the section on "critical effects" - we find that the techniques of neutron and X-ray magnetic scattering are truly complementary, and we need to discuss the physics involved rather than emphasise the technique.

Publications: Some 19 papers were published in 1992 from the neutron and synchrotron effort. In these are 8 papers in the open literature and 11 papers published in Conference Proceedings (including 4 invited papers, and 7 papers from the ICNS Conference in Oxford). All these, together with our many collaborators, are listed in the Appendices. The principal investigator was also involved with writing two Chapters for a forthcoming Book to be published by North-Holland, of which he is an editor. P. Raison successfully completed his doctorate degree.

Hybridization effects in intermetallic compounds

Last year we reported on hybridisation effects in a 1:1:1 compound URhAl, which is a ferromagnet at low temperature. An important aspect of this structure is that the uranium atom has two different d electron neighbours. One (Rh_I) is in the same ab plane of the hexagonal structure as the uranium, and the other neighbour (Rh_{II}) has a bond that includes a displacement of $c/2$ (i.e. it has a major component along the c axis). The distances U-Rh_I and U-Rh_{II} are both $\sim 2.92\text{\AA}$. The study of URhAl found that a strong hybridisation occurred between the U and Rh_I sites, but not between the U and Rh_{II}. Because URhAl is a ferromagnet, and exchange effects may be a factor in determining the polarisation of the Rh d electrons, we extended the study to URuAl. This compound is a paramagnet, so that the experiment is performed by inducing a small moment with an applied magnetic field, and measuring the magnetization density. The experiment was performed at Saclay and is a collaboration also with the University of Amsterdam. The results and comparison between the two materials are shown in Tab. 5.8.

Tab.5.8 Moments and ratios of moments (in Bohr magnetons) in $UTAl$, where $T=Rh$ or Ru in an applied field of 5 T as determined by polarised neutrons. The last row gives the ratio of the orbital moment μ_L to the spin moment μ_S . The free-ion value of this quantity is -2.5.

	URhAl	URuAl
Uranium moment	0.94(3)	0.042(3)
d metal (Site I)	0.28(2)	0.019(3)
Ratio (Site I/Uranium)	0.30(2)	0.45(8)
d metal (Site II)	0.03(2)	0.001(3)
Ratio (Site II/Uranium)	0.03(2)	< 0.05
μ_L/μ_S of uranium	-1.81(7)	-2.5(3)

Although the moments on the different sites are much smaller in the case of URuAl than in the case of URhAl, we see from the table that the ratios of the Ru and Rh moments to that on the uranium are essentially the same for the two compounds. Thus the hybridization between the U $5f$ and T metal d electrons (which is given by the ratios) is independent of the exchange (given by the magnitude of the moments). Moreover, the strong anisotropy reflected in the different hybridization with the T_I and T_{II} sites is also the same in both materials.

Phase transitions in NaCl-type uranium compounds

Studies of USb

We attempted a difficult experiment (performed at the reactor at Brookhaven National Laboratory) to separate the magnetic lattice effects in the well-known uranium antiferromagnet USb. A large crystal was prepared in ETH, Zürich. The experiment required the use of polarised neutrons and a special analyzer. Quite unexpectedly, we found a new (mysterious) phase transition in USb at 140K, some 72K below the Néel temperature (T_N). Fig. 5.7 shows the depolarisation of neutrons as a function of temperature as measured at BNL. Such an effect is totally unexpected in a pure antiferromagnet (and we have always considered USb such a system) and suggests that there are more subtleties in the structure than we had previously realised. The depolarisation of the neutrons at low temperature also prevents the original experiment from being completed. We have noted that muon experiments by Kalvius et al have also shown

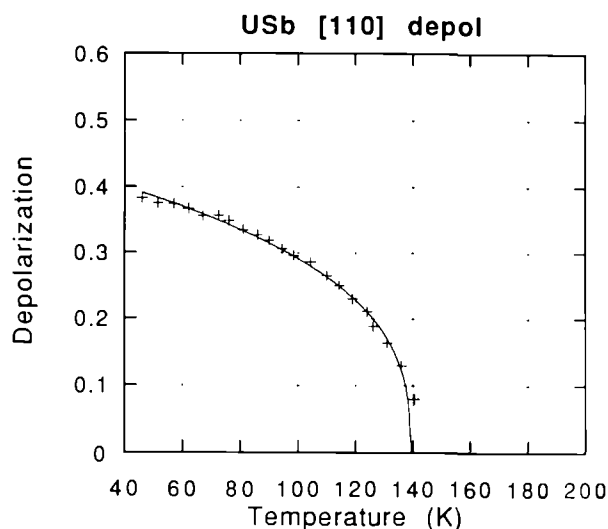


Fig.5.7 Temperature dependence of the depolarisation of neutrons scattered from a single crystal of USb. T_N of this material is 212K.

unusual effects at this temperature, and we are planning a series of joint neutron/muon experiments to further elaborate this phase transition.

Magnetic structures in $U_{0.85}Th_{0.15}Sb$

In a study involving magnetisation and neutron (both at CEN-Grenoble) and X-rays (at the Brookhaven synchrotron) we have made a thorough investigation of the magnetic properties of this Th doped derivative of USb. The combination of these three techniques (performed using the same crystal in each measurement) has allowed us to demonstrate that the moments at low temperature on adjacent uranium sites are not of the same magnitude. Furthermore, the near-surface structure (as seen by the X-rays, which have a very large absorption) is subtly different from that of the bulk. Models for the different arrangement of magnetic moments are shown in Fig. 5.8. A further interesting effect is that when the material develops a ferromagnetic component (at 160K) and distorts rhombohedrally there is a 'buckling' of the surface morphology that derives from the magneto-elastic interaction. This is seen clearly in the X-ray diffraction pattern as a broadening of the effective mosaic of the crystal, and is illustrated in Fig. 5.9.

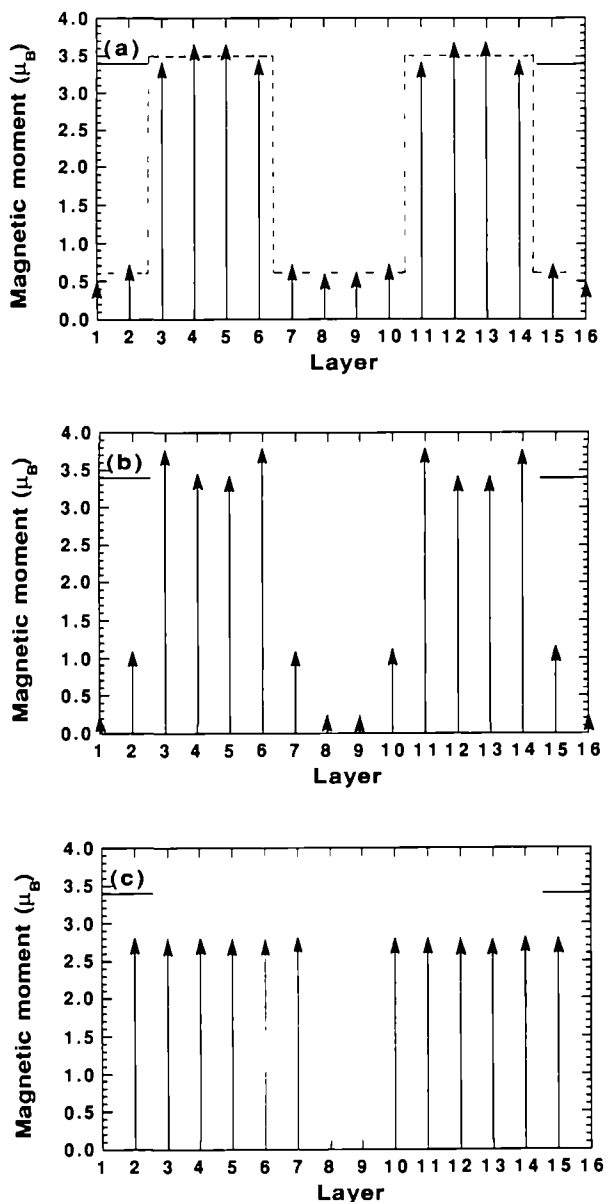


Fig.5.8 Models of the magnetic configuration at low temperature in $U_{0.85}Th_{0.15}Sb$. The horizontal line at $3.4 \mu_B$ is the maximum possible moment gJ for a $U f^3$ state. In each case two complete magnetic repeat units are shown. (a) Result of combining observed neutron structure factors. The square-wave modulation is shown as a broken line. (b) Result of adding the observed $q=1/2$ component, which results in a distortion of the square wave. (c) The $6+, 0, 0$, structure. The X-ray intensities suggest a near-surface magnetic structure of this form that is more strongly modulated than that deduced from the neutron intensities, which represent the bulk of the material.

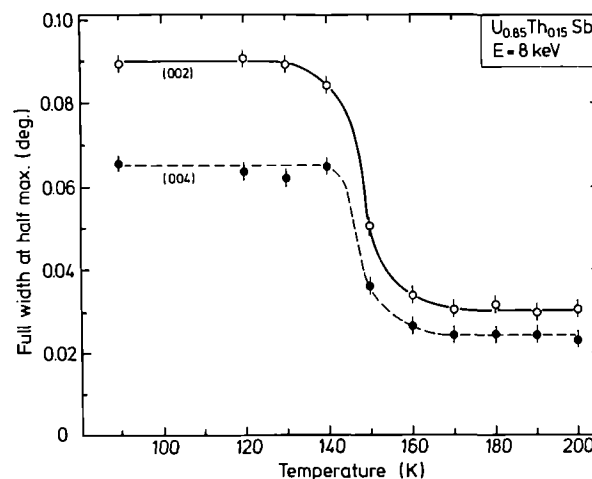


Fig.5.9 Transverse widths of the (002) and (004) reflections as a function of temperature taken with the high-resolution X-ray configuration. The larger effect for the (002), which has the smaller scattering angle, shows that the mosaic distribution of the near-surface region is strongly disturbed at the onset of ferromagnetism ($T_C=160K$).

Critical scattering and phase transitions in NpAs

Using X-ray resonant scattering (at the Brookhaven Laboratory Synchrotron, USA) we have performed a series of experiments to examine both the magnetic structure and the correlations that occur just above the ordering temperature (T_N) in single crystals of NpAs. Particularly important is the extremely good resolution of this technique. With the very fine collimation of the photon beam emerging from the synchrotron we can envisage the exploration of correlations on the length scales of $10,000 \text{ \AA}$ in X-ray diffraction. This is an order of magnitude better than possible with neutrons, and clearly will bring a new microscopic tool to bear on the area of precursor effects near phase transitions. However, the penetration of such photon beams into the materials is very small, so that the technique is one of surface sensitivity (no more than a few thousand \AA). Some of the data showing the temperature dependence of the correlations near T_N in NpAs is shown in Fig. 5.10. From data such as these we can extract the inverse correlation range k , which is simply related to the observed half-width at half maximum of the Lorentzian curves shown in Fig. 5.10. The real-space correlation width is simply $\xi=1/k$. The results for both the neutron and X-ray experiments on

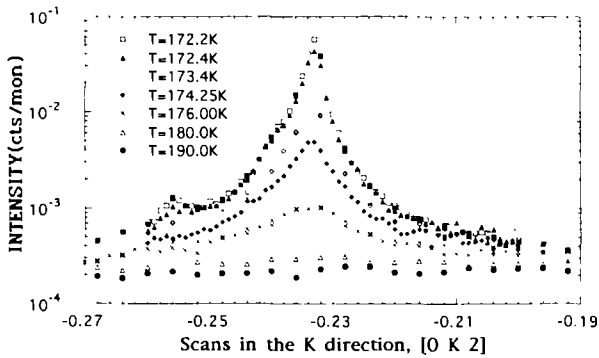


Fig.5.10 Experimental data taken with synchrotron X-rays showing the magnetic critical scattering just above $T_N=172.1K$ in NpAs. The resolution of the instrument is shown as the vertical bars. Note the logarithmic scale for intensity.

NpAs are shown in Fig. 5.11. Three points are immediately obvious. (a) The neutron and X-ray results are different; in particular as we improve the resolution we apparently see a sharper component, suggesting a much longer real-space length scale. (b) The temperature dependencies of these correlation lengths (as judged by the slopes of the lines) are different. (c) The X-ray determined correlation length tends to saturate at a finite order, suggesting that the magnetic order never really becomes 'infinitely long range' (which would correspond to $\kappa=0$). None of these points are understood at this time. Very similar effects have been seen by a group at Brookhaven working on holmium. Although our observations are probably not particular to actinides, they do illustrate how an effect – the resonant magnetic X-ray scattering, which is unique in his strength to $5f$ systems – can be of interest in areas of general physics.

Critical scattering and phase transitions in $USb_{0.8}Te_{0.2}$

The magnetic phase diagram of the $USb_{1-x}Te_x$ system was first established some ten years ago. Our interest recently has turned to aspects of the phase transitions. In particular, in a series of neutron experiments at Risø National Laboratory, Denmark, we have measured the correlations that occur at temperatures just above the antiferromagnetic ordering temperature T_N . The data are then deconvoluted with the experimental resolution function to give the widths, and as above, the inverse correlation width. These inverse correlation widths are plotted as a function of reduced temperature (as in Fig. 5.11

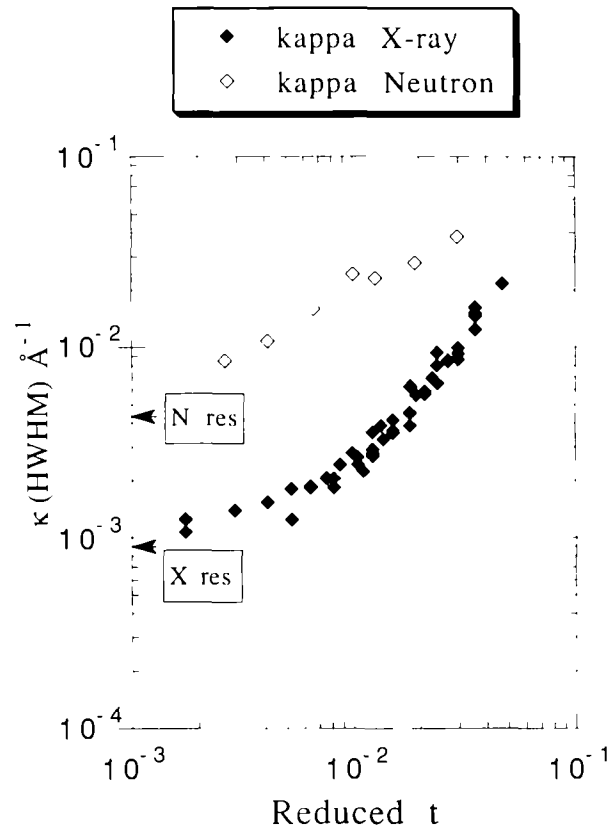


Fig.5.11 Values for the inverse correlation width (derived from the half-width of the peaks in Fig. 5.10) as a function of temperature as derived by neutrons (open points) and X-rays (closed points) for the development of magnetic order in NpAs. The different resolutions of the two techniques are indicated on the ordinate axis. The reduced temperature $t=(T-T_N)/T_N = 172.1K$ where T_N is the ordering temperature.

for NpAs) in Fig. 5.12. Here we have examined the two different directions, parallel and perpendicular to the direction of the propagation of the magnetic modulation. It is known from work on USb that there is a difference between these two correlation lengths, and that this is related to the anisotropy in the hybridization that occurs in these actinide systems. (The anisotropy here has exactly the same microscopic origin as that described in the first paragraph above). The behaviour of the inverse correlation length shows, as expected, a logarithmic dependence, and the slope of the line is in accord with theory. We now plan to study this material by the X-ray technique that has been applied to NpAs, and this will take place in 1993.

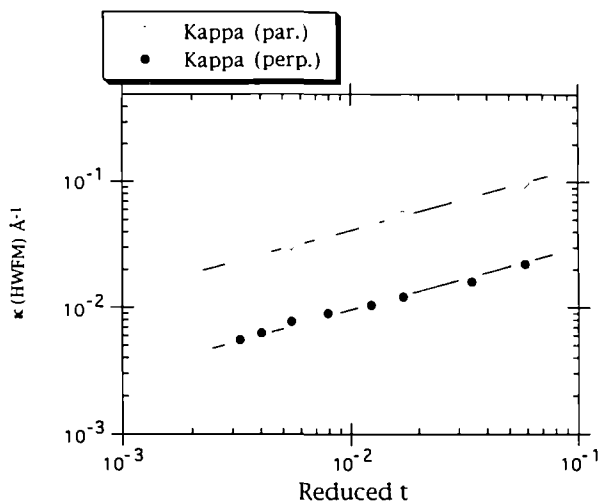


Fig.5.12 Values for the inverse correlation widths (similar to the previous figure) for $USb_{0.8}Te_{0.2}$ as derived from neutron experiments. The two different directions correspond to those parallel (open points) and perpendicular (closed points) to the propagation of the magnetic modulation direction. The straight lines are fits with $\kappa = t^\nu$ with $\nu = 0.50$, where t is the reduced temperature $t = (T - T_N)/T_N$ and $T_N = 204.54K$

Collaborative studies of U_5Sb_4

This new U-Sb phase was recently synthesized at ITU. The crystal structure was determined by X-ray diffraction and can be described as a stacking of U-Sb layers of atoms perpendicular to the hexagonal c-axis. There are two distinct crystallographic sites (labeled I and II) for both U and Sb atoms. The U coordination in this compound is rather unusual. The U_{II} atoms form chains along the c-axis with a short U-U distance of 3.10\AA , comparable to the interatomic distance in metallic uranium. It is therefore possible for the $5f$ orbitals to hybridise along the chains. The magnetic properties of this compound are being examined by a number of different techniques; these include Mössbauer spectroscopy, magnetization and susceptibility measurements (collaboration with the CEN-Grenoble), high-field magnetization, AC-susceptibility, resistivity and specific heat (collaboration with the University of Amsterdam), and neutron scattering (collaboration with the CEN-Grenoble and LLB-Saclay).

The Mössbauer spectra (Fig.5.13) show that U_5Sb_4 orders magnetically. Magnetization and susceptibility measurements determine this compound to be a highly anisotropic ferromag-

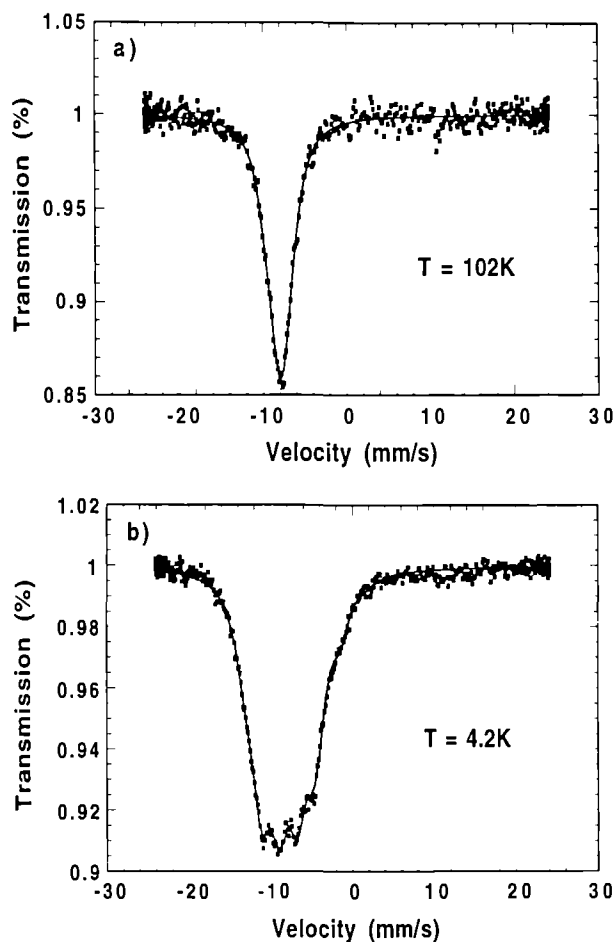


Fig.5.13 ^{121}Sb Mössbauer spectra showing the hyperfine splitting at the Sb atom transferred from the uranium site in the ordered state of U_5Sb_4 . Spectra taken at (a) $T = 102K$, (b) $T = 4.2K$.

net with a Curie temperature of $86K$ and a moment of $1.70 \mu_B$ /(U atom) in a field of 5 Tesla along the easy c axis. The response in the ab plane is much smaller, is linear in field, and gives $0.1 \mu_B$ /(U atom) in the same field. A pronounced remanence and an almost rectangular hysteresis loop were observed at low temperature. The low-field susceptibility was found to behave peculiarly. After zero-field cooling, a maximum develops in the heating cycle of the thermomagnetic curves (Fig. 5.14). This maximum becomes broader and shifts to lower temperatures with increasing applied field. Similar behavior has already been observed in a number of other anisotropic rare-earth and actinide ferromagnets. A possible explanation could be the development at low temperature of a compensated 180° domain structure with narrow domain walls. The reduced mobility of these domain walls could be the origin of the high coercivity (6 kOe at $6K$).

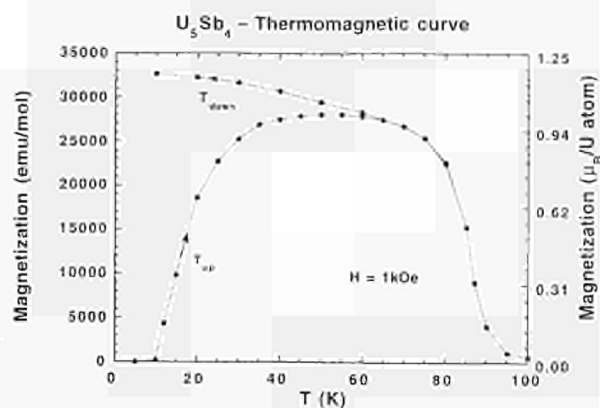


Fig 5.14 Thermomagnetic cycle of a single crystal of U_5Sb_4 . The crystal was first cooled in zero field to 6K, then a field of 1kOe was applied along the c-axis. The crystal was heated to 100K and cooled. The heating and cooling curves are labeled T_{up} and T_{down} , respectively.

To confirm the nature of the magnetic ground state, neutron experiments were performed on single crystals. Reciprocal lattice scans found no antiferromagnetic peaks and confirmed the existence of a ferromagnetic component in zero field. The neutron data could be fit with a simple model in which the two U sites carry a moment of $1.7(1)\mu_B$ oriented along c. A recent polarised-neutron experiment confirmed that, in spite of the short $U_{II}-U_{II}$ distance, the U_I and U_{II} atoms have comparable magnetic moments. A detailed analysis of the data is now in progress.

Studies of ionic systems

A carefully planned experiment at the Rutherford Laboratory (UK) on a sample of $^{242}PuO_2$, which had been prepared at Los Alamos National Laboratory, was canceled at the last minute by the Laboratory Director. Further work on transuranium samples will not be attempted there.

Studies of the neutron inelastic scattering of UF_4 and NpF_4 were completed at Argonne National Laboratory, and the low-energy crystal-field levels, of importance in understanding magnetic and thermodynamic properties, were established. In the process neutron elastic experiments were used to characterise the structure of UF_4 . An unexpected contraction of the volume was found when heating from low temperature. Studies of ThF_4 are now planned to test whether the behaviour is related to the $5f$ electrons, and possible covalent bonding.

The studies of UCp_3Cl were completed (Thesis work of P. Raison) and this work has been submitted in 4 consecutive papers to "Molecular Physics". A highlight of this work is the relationship between the static distortion of the structure and the steric hindrance of the motion of some, but not all, of the Cp rings. This aspect of the low-temperature structure, which results in weak hydrogen-chlorine bonds, is illustrated in Fig. 5.15.

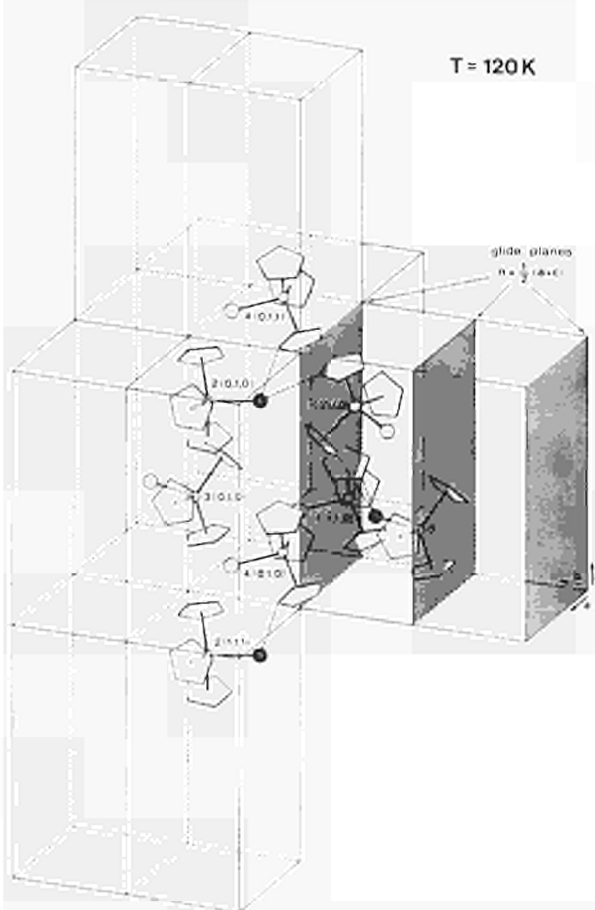


Fig 5.15 Representation of the structure of UCp_3Cl at 120K as determined by a crystallographic refinement of the neutron intensities from a single crystal. The large open circles are the chlorine atoms. The dashed lines from these to the H atoms at the corners of the Cp rings indicate the short Cl-H distances that develop at low temperature. Parentheses describe molecules translated respectively along the a, b, or c directions. For example, molecule 3(0,1,0) corresponds to the third molecule of the unit cell translated once in the b direction. The short Cl-H distances that develop cause a hindering of the dynamical rotation of the relevant Cp rings. This is the process that causes 1/3 of the Cp rings to stop rotating below the 245K phase transition.

Photoelectron studies (UPS and XPS) of O₂, CO₂, CO and C₂H₄ adsorption on Pu metal

Photoelectron spectroscopy was used to study the reactivity of Pu metal with O₂, CO₂, CO and C₂H₄ at 77 K and 296 K. The sample used in this study was a high-purity electrorefined Pu stabilized in the δ -phase by addition of 1 wt. % Ga. To clean the surface, heating/ Ar⁺ ion sputtering cycles were used. Although sputtering removed Ga preferentially, its presence at the surface could still be detected. The gas dosages are given in units of langmuirs (1L = 10⁻⁶ Torr s).

The UPS valence band spectrum of a clean surface of Pu metal presents the following features: a narrow emission line at the Fermi level (E_F), which is attributed to itinerant 5f states and a small peak at 0.74 eV below E_F (Fig. 5.16, curve 0L). This last feature can be attributed to the existence of a small amount of δ -Pu at the surface. This assignment is based on the following facts: a) most of Ga, used to stabilize the δ -phase, is removed during the sputtering procedure. However, even after heavy sputtering, 40 % of Ga could still be detected which leads us to consider that some δ -character is still retained; b) scraping of the sample accentuates the existing structure at 0.74 eV and narrows the 5f emission line at E_F .

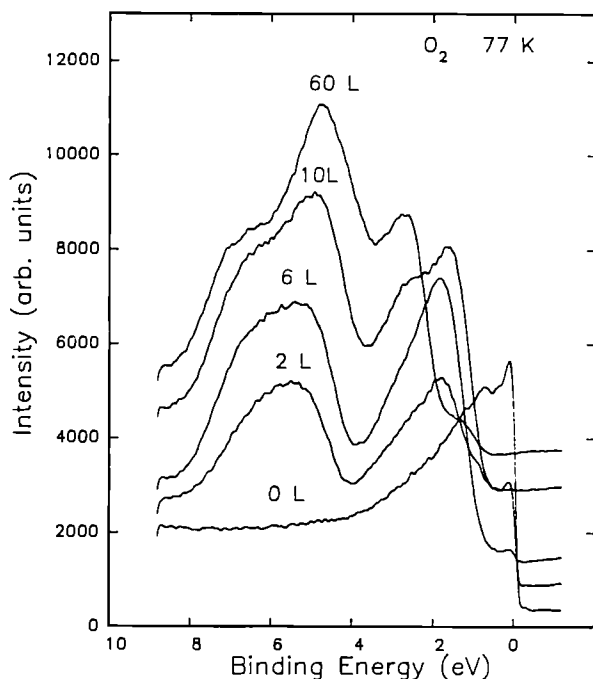


Fig. 5.16 UPS-HeII spectra of O₂ adsorption on Pu at 77 K.

Adsorption of O₂

At 77 K, O₂ reaction with Pu metal shows the following features: for low dosages (<6 L) two emission lines at 1.4 eV and 5.6 eV are observed (Fig. 5.16). The peak at 5.6 eV is attributed to the O 2p emission line. At higher dosages a shoulder is developing at the higher BE (binding energy) side of this line. Increasing oxidation leads to a progressive decrease of the emission at E_F . At 8 L O₂, this emission is no longer detected. The emission line at 1.4 eV is assigned to the Pu 5f⁵ state of Pu₂O₃ [1,2]. At 10 L another emission line at 2.4 eV is observed. This emission line is assigned to the Pu 5f⁴ state of PuO₂ [1,2]. The increase of dosages changes the ratio of these lines and leads also to a shift of the O 2p line to lower BE. At 60 L, the peak attributed to Pu₂O₃ has vanished. UPS showed, for both temperatures, successive reduction of PuO₂ to Pu₂O₃. All these results are interpreted as follows: O₂ in contact with the surface dissociates and forms Pu₂O₃. Further exposure to O₂ leads to the formation of PuO₂. At 296 K, similar features are observed. However, the development of these features occurs at higher dosages. XPS measurements confirm, for both temperatures, the initial formation of Pu₂O₃ followed by PuO₂ [1,2]. This behaviour is different from that of U that only forms UO_{2-x} [3].

Adsorption of CO₂

CO₂ adsorption at 77 K (Fig. 5.17) displays at low dosages an increase of the O 2p emission line at 5.6 eV and a simultaneous decrease of the emission at E_F . However, this process is slower compared to O₂ adsorption (Fig. 5.16). At 4 L, three new emission lines at 2.5 eV, 11.2 eV and 13.2 eV and at 400 L two further emission lines at 9.2 eV and 14.8 eV are observed. The two lines at 11.2 eV and 13.2 eV are attributed to orbitals of carbonate formed at the surface [4]. The two lines at 9.2 eV and 14.8 eV and the dominant line at 13.2 eV are due to physisorbed CO₂ [5]. For dosage up to 100 L an increase in the intensity of the emission lines at 11.2 eV and 13.2 eV is observed. However, at 400 L the emission at 11.2 eV is even weaker than for 100 L. The following interpretation is suggested: initially Pu₂O₃ is formed, after which CO₂ reacts with Pu₂O₃ to form carbonates. After saturation, CO₂ physisorbs on top of the carbonate layer. Unfortunately, one of the orbitals of the carbonate has its emission line in the same spectral range (13.2 eV) as the emission from physisorbed CO₂. Therefore both carbonate lines grow simulta-

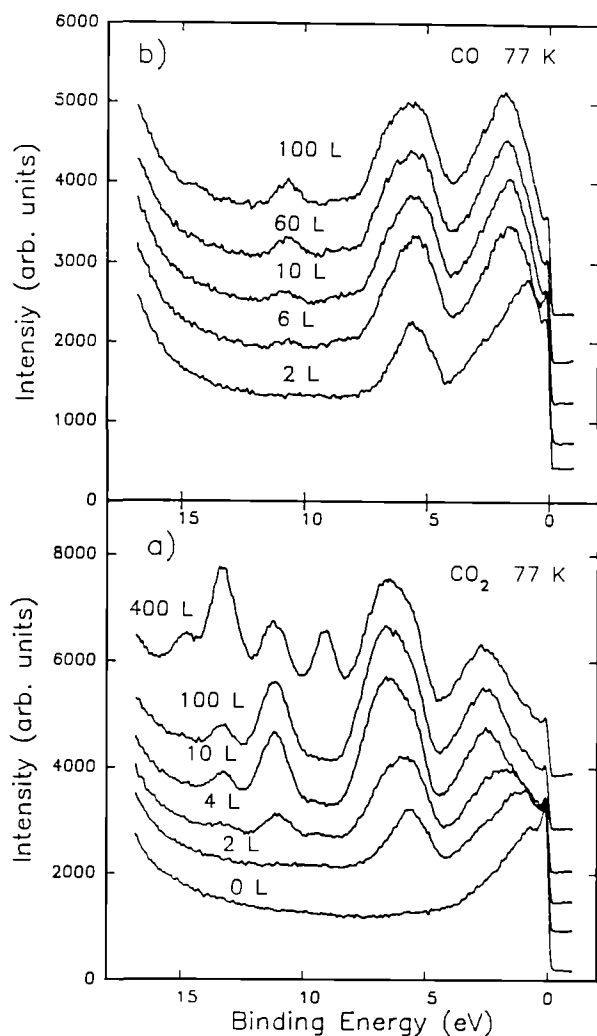


Fig.5.17 a) UPS-HeII spectra of CO_2 adsorption on Pu at 77 K; b) UPS-HeII spectra of CO adsorption on Pu at 77 K.

neously in the early stages of adsorption. When carbonate formation is finished, the line at 13.2 eV continues its growth due to physisorption of CO_2 [5]. The emission line at 2.5 eV (4 L) is assigned to Pu $5f^5$ states of Pu_2O_3 . At 296 K, CO_2 adsorption shows a similar behaviour as at 77 K, however, no physisorption of CO_2 is observed. XPS measurements confirm the UPS results.

Adsorption of CO

At 77 K, CO adsorption (Fig. 5.17) leads to the growth of an O 2p emission line at 5.4 eV. For higher dosages two emission lines at 8.6 eV and 10.6 eV appear. These lines are assigned to orbitals of chemisorbed CO [6]. A decrease of the emission at E_F was also found. In addition an emission line at 1.7 eV is observed, which is at-

tributed to the Pu $5f^5$ state of Pu_2O_3 [1,2]. At 296 K, the O 2p line occurs at 5.8 eV. For dosages higher than 8 L, two emission lines at 11 eV and 13.1 eV are observed. These features are attributed to carbonate formation [7]. A decrease of the intensity at E_F and of the Pu $5f^5$ state of Pu_2O_3 is also found. XPS Pu 4f core line spectra confirm this.

Adsorption of C_2H_4

C_2H_4 adsorption studies at 77 K (Fig. 5.18) display for exposures up to 100 L, the growth of two main lines at 1.0 eV and 3.8 eV. For higher dosages (>100 L) four very weak emission lines between 6.0 eV and 11 eV and a small decrease of the emission at E_F are observed. The emission line at 3.8 eV is attributed to the C 2p state [8]. This carbon line is either due to the formation of plutonium carbide or to the chemisorption of carbon. The emission lines observed for dosages higher than 100 L are attributed to the physisorption of C_2H_4 [9]. The emission line at 1.0 eV is the most important one. We tentatively attribute it to the formation of PuH_2 . This assignment is based on the following facts: 1) the surface is free of oxygen (confirmed by UPS); 2) carbon features appear at energies higher than 3 eV. Thus we assume a reaction of Pu with H, ob-

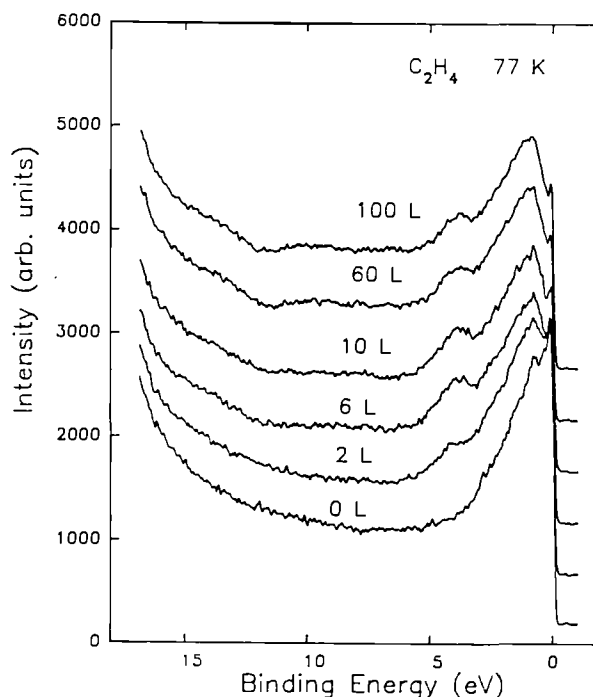


Fig.5.18 UPS-HeII spectra of C_2H_4 adsorption at 77 K.

tained after the dissociation of C_2H_4 . At 296 K the features observed are similar to those at 77 K except that no physisorption of C_2H_4 occurs.

Conclusion

When comparing the results obtained with the four gases on Pu and U metal several statements can be made: the initial adsorption of all gases results in dissociation. However, the following products are formed on Pu and not on U: for O_2 two different types of oxides are formed; for CO_2 and CO , carbonates are formed; for C_2H_4 the formation of PuH_2 is proposed. These differences in behaviour may be partially related to a stronger 5f electron localization in Pu but are probably also due to the morphology of oxide and/or carbon layers which grow on the surface.

References

- [1] J. R. Naegele, J. Ghijsen and L. Manes, in "Actinides Chemistry and Physical Properties" (Structure and Bonding 59/60), Ed. L. Manes (Springer, Berlin, 1985) p. 199
- [2] D. Courtaix, J. Chayrouse, L. Heitz and R. Baptist, *Solid State Commun.* **39** (1981) 209
- [3] a) T. Gouder, C. A. Colmenares, J. R. Naegele and J. Verbist, *Surf. Sci.* **235** (1989) 280;
b) T. Gouder, C. Colmenares, J. R. Naegele, J. C. Spirlet and J. Verbist, *Surf. Sci.* **264** (1992) 354
- [4] J. Wambach, G. Odorfer, H.-J. Freund, H. Kuhlenbeck and M. Neumann, *Surf. Sci.* **209** (1989) 159
- [5] a) D.W. Turner, A.D. Baker and C.R. Brundle, *Molecular Photoelectron Spectroscopy*, Wiley, New York (1970); b) H.-J. Freund, H. Kossman and V. Schmidt, *Chem. Phys. Letters* **123** (1986) 377
- [6] R. Miranda, K. Wandelt, D. Riger and R.D. Schenell, *Surf. Sci.* **139** (1984) 430
- [7] J. Wambach, G. Odorfer, H.-J. Freund, H. Kuhlenbeck and M. Neumann, *Surf. Sci.* **209** (1989) 159
- [8] F. Steinbach, J. Kiss and R. Krll, *Surf. Sci.* **157** (1985)
- [9] D. G. Streets and A.W. Potts, *J. Chem. Soc. Faraday Trans. II* (1974) 1505

Mössbauer spectroscopy

Introduction

Meanwhile three Mössbauer spectrometers have been installed at the Institute, two for measurements at ambient and high pressure up to ~ 80 kbar and at temperatures between ~ 1.3 K and 80 K and one for sample characterization at 4.2 K and from 80 K up to room temperature. The source can be kept below 15 K even at high absorber temperatures. This is a prerequisite to achieve reasonable recoil-less free fractions for the Mössbauer resonances used in actinide research.

In actinides the Mössbauer effect can in principle be observed with several isotopes, but only ^{237}Np and ^{243}Am allow the hyperfine parameters of all kinds to be investigated with excellent resolution. Up to now we have used the ^{237}Np resonance with a 60 keV transition. ^{237}Np Mössbauer spectroscopy in combination with X-ray diffraction at ambient and high pressures is a powerful tool to study the magnetic 5f moments (which are proportional to the magnetic hyperfine field), the transition temperature, the charge state and degree of delocalization (via the isomer shift) as well as the anisotropy of the crystal (electric quadrupole interaction) as a function of the lattice parameter in Np intermetallics. Furthermore this method allows us to distinguish different crystal or magnetic sites of the Np atom, different crystal and magnetic phases, and it may thus be used for sample characterization.

In most of the heavy fermion compounds a direct f-f overlap of the actinide or lanthanide atoms is of minor importance. For that reason during the last year we have begun our programme of the systematic investigation of magnetism in compounds with dominating 5f-ligand-s,-p hybridization (NpBe_{13} , NpX_3 compounds) as well as 5f-d hybridization (1:2:3 compounds as NpPd_2Al_3), where the rather big Np-Np distances exclude a prevailing direct 5f-5f overlap. A strong influence of 5f-d hybridization is also expected in the 2:2:1 compounds, of which we have measured the $\text{Np}_2\text{T}_2\text{In}$ group (with T = Co, Rh, Ni, Pd, Pt) in cooperation with CENG.

Mössbauer spectroscopy of NpPd₂Al₃

We have studied NpPd₂Al₃, the Np analogue to the heavy-fermion system (HFS) UPd₂Al₃, by means of Mössbauer spectroscopy. Both NpPd₂Al₃ and UPd₂Al₃ crystallize in the hexagonal PrNi₂Al₃ structure (space group P6/mmm). Intensive research has focused on UPd₂Al₃ since its discovery as a HFS [1] stems from the fact that superconductivity ($T_c = 2$ K) coexists with antiferromagnetic order ($T_N = 14$ K), the uranium carrying the substantial ordered moment of $0.85 \mu_B$ [2]. This is larger by a factor of about 50 than in the previously established cases URu₂Si₂ and UPt₃.

To our knowledge no transport or specific heat data exist for NpPd₂Al₃. Hence we can not say whether it is also a HFS and whether superconductivity exists. The Mössbauer spectra, however, clearly establish the presence of magnetic ordering. A phase transition was found at $38 (\pm 1)$ K. It is of second order. The paramagnetic spectrum consists of a pure quadrupole pattern. Full rotational symmetry ($\eta = 0$) is maintained. The magnetic spectra had to be fitted with an overlay of three magnetic patterns including quadrupole interactions. The hyperfine parameters resulting from these fits at low temperatures, together with those at 80 K, are summarized in Tab. 5.9. The presence of three magnetic sites with different occupations points towards a modulated structure. The relatively small number of sites, and the absence of a subspectrum with very small fields suggest that the modulation is fairly squared and commensurate at low temperatures. Spectra above 30 K require more intensity of the small field and the linewidth (FWHM) increases. It is likely that the modulation changes. The maximum saturation hyperfine field corresponds to an ordered moment on Np of $1.67 \mu_B$, which is about twice the moment

on U in antiferromagnetic UPd₂Al₃. The fact that the magnitude of eq is the same above and below T_N means that the spins point in the same direction as the electric field gradient, probably along the c -axis.

The isomer shift relative to NpAl₂ is +10 mm/s. On the basis of the systematics developed for a wide variety of Np intermetallics [3] one can conclude that the Np³⁺ ion with the Hund's rule groundstate ⁵I₄ is present. From susceptibility data at elevated temperatures a U⁴⁺ charge state was deduced in UPd₂Al₃ [4].

The saturation hyperfine field in NpPd₂Al₃ (Tab. 5.9) is only about 2/3 of the Np³⁺ free-ion field. It is thought that the main cause for the reduction comes from crystalline electric field (CEF) interactions.

In summary, it appears that the Np analogue of the HFS UPd₂Al₃ has a more pronounced ionic and hence a stronger magnetic character.

References

- [1] C. Geibel et al., Z. Phys. B 84 (1991) 1.
- [2] A. Krimmel et al., Z. Phys. B 86 (1992) 161.
- [3] G.M. Kalvius et al., Hyperfine Interactions 72 (1992) 77.
- [4] A. Grauel et al., Phys. Rev. B, to be published.

NpX₃ compounds under high pressure

Since in these compounds the Np-Np spacing is far above the Hill limit [1], 5f delocalization is mainly caused by hybridization of 5f electrons with ligand valence electrons, in s- and p-

Tab.5.9 Hyperfine parameters and linewidths of NpPd₂Al₃.

T (K)	$B_{\text{hf}}[1]$ (T)	Int[1] (%)	$B_{\text{hf}}[2]$ (T)	Int[2] (%)	$B_{\text{hf}}[3]$ (T)	Int[3] (%)	eq (10^{18} V/cm ²)	S^a (mm/s)	FWHM (mm/s)
80	—	—	—	—	—	—	+ 2.27(4)	+ 10.9(1)	2.8(1)
20	342(2)	32(3)	296	56(3)	118(3)	12(2)	+ 2.29(4)	+ 9.5(3)	2.6(1)
4.2	360(1)	37(3)	316(1)	55(3)	121(3)	8(2)	+ 2.30(3)	+ 10.4(2)	2.1(1)

^a isomer shift is given relative to NpAl₂.

orbitals [2]. These compounds provide a unique opportunity to understand pure 5f-electron hybridization with ligand s- and p- electrons, in contrast to direct 5f-5f-overlap and to mixed 5f-electron with ligand s-, p- and d-electron hybridization. This is an important question, because for example in most of the heavy fermion systems the rather large f-f-distance excludes direct f-f-overlap and in some of them only f-ligand s- and p-mixing is expected to be present (CeAl₃, UBe₁₃, NpBe₁₃).

We have studied NpSn₃ previously by ²³⁷Np Mössbauer spectroscopy at pressures up to 6.2 GPa [5]. Among the NpX₃ series, NpIn₃ is a very interesting compound. Analogous to UX₃ we expect a lower 5f ligand hybridization and thus more localized 5f orbitals than with NpSn₃. The Mössbauer spectrum at 4.2 K shows a superposition of several discrete magnetic hyperfine patterns including low - moment and even nonmagnetic contributions [3]. The nature of this superposition is not yet known and the question arises, whether the partial reduction of ordered moments is driven by a Kondo mechanism, as in NpSn₃, or whether NpIn₃ is already a fully localized magnet. To study this question, we have started an investigation at ambient pressure between 1.3 K and 10 K, and at a pressure of 4 GPa between 1.3 and 4.2 K. Furthermore we studied the change of the magnetic behaviour and the ordering temperature at ambient and elevated pressure by the thermal scan method.

The spectra measured at 4.2 K at ambient and under elevated pressure of Fig. 5.19 clearly show, that the non-magnetic Mössbauer line disappears at 4 GPa. B_{hf} (I_{max}) increases only slightly. IS decreases by 1.4 mm/s. The quadrupole interaction is small ($e2qQ < 6$ mm/s). The spectrum measured at 1.3 K and 4 GPa shows no deviation from the magnetic structure and the corresponding moment found at 4.2 K, i.e. the moments are already close to saturation at 4.2 K. A nonmagnetic line does not appear below this temperature.

If we compare the variation of B_{hf} , T_{ord} , IS with pressure for NpIn₃ and for NpSn₃, we observe a similar tendency between ambient pressure and 4 GPa or 4.4 GPa, respectively, for the two compounds (Fig. 5.20 and Tab.5.10). Our comparison shows, that NpIn₃ exhibits a pressure behaviour similar to NpSn₃, which is typical for localized magnets. The ordering temperature rises considerably, whereas the hyperfine field rises only slightly (~10% only), and the electron density at the Np nucleus increases [6].

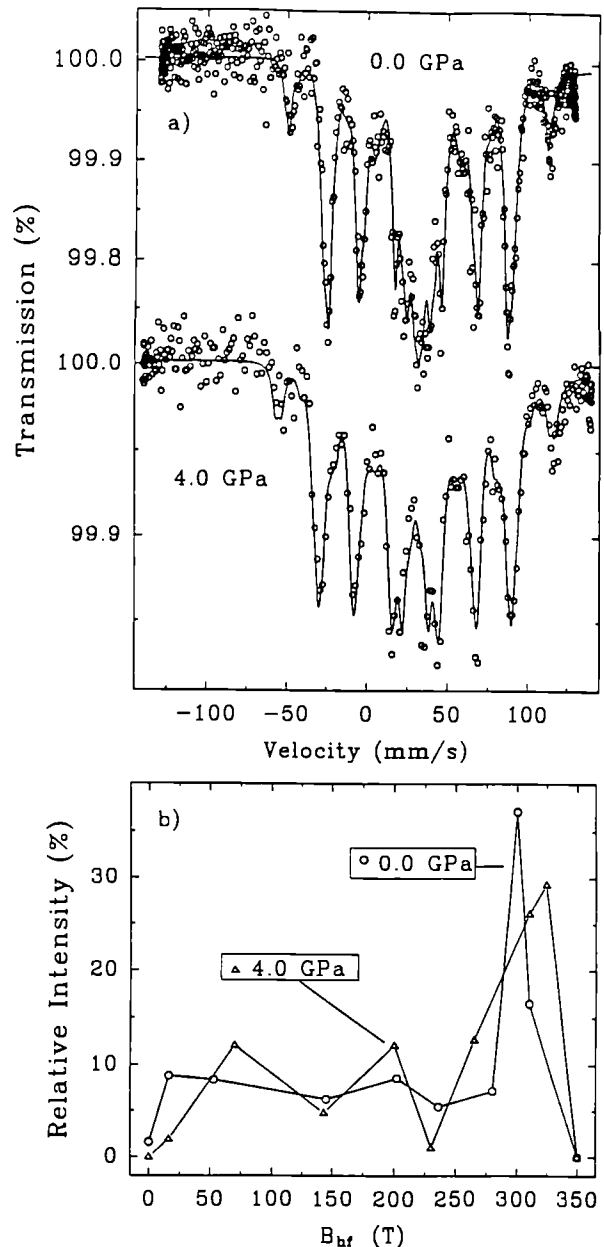


Fig.5.19 a) ²³⁷Np Mössbauer absorption spectra of NpIn₃ at 4.2 K and various pressures. b) Distribution of magnetic hyperfine fields obtained from the fits of the spectra shown in a).

Within the picture of orbital 5f-moments coupled by anisotropic hybridization, in both compounds external pressure may slightly change the crystal field splitting, bandwidth and the ordered moments, the overwhelming effect, however, is a strong increase of the exchange interaction and a stabilization of magnetism.

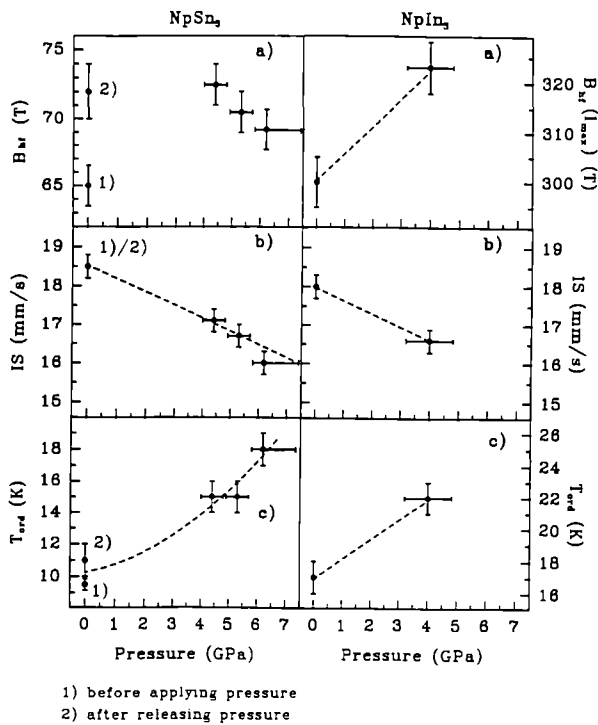


Fig.5.20 Comparison of the pressure dependence of a) the magnetic hyperfine field B_{hf} , b) the isomer shift IS relative to $NpAl_2$, c) the ordering temperature T_{ord} for $NpSn_3$ and $NpIn_3$. In $NpSn_3$ a small hysteresis effect of B_{hf} and T_{ord} was observed [4].

Tab.5.10 Change of isomer shift IS , relative change of magnetic hyperfine field B_{hf} and of the ordering temperature T_{ord} between ambient pressure and 4.0(8) GPa, 4.4(5) GPa for $NpIn_3$ and $NpSn_3$, respectively.

Compound	$NpSn_3$	$NpIn_3$
ΔIS (mm/s)	-1.4(5)	-1.4(5)
$\frac{\Delta B_{hf}}{B_{hf}}$ (%)	10(3)	~ 5
$\frac{\Delta T_{ord}}{T_{ord}}$ (%)	50(10)	30(6)
Pressure difference (GPa)	4.4(5)	4.0(8)

References

- [1] H.H. Hill, in: Plutonium 1970 and Other Actinides, W.N. Miner, Ed., Met. Soc. AIME, 1971, p. 2
- [2] D.D. Koelling, B.D. Dunlap and G.W. Crabtree, Phys. Rev. B **31** (1985), 4966
- [3] J. Gal, I. Yaar, S. Fredo, I. Halevy, W. Potzel, S. Zwirner and G.M. Kalvius, Phys. Rev. B **46** (1992), 5351
- [4] M.R. Norman and D.D. Koelling, Phys. Rev. B **33** (1986), 3803
- [5] G.M. Kalvius, S. Zwirner, U. Potzel, J. Moser, W. Potzel, F.J. Litterst, J. Gal, S. Fredo, I. Yaar and J.C. Spirlet, Phys. Rev. Lett. **65** (1990), 2290
- [6] W. Potzel, J. Moser, G.M. Kalvius, C.H. de Novion, J.C. Spirlet, and J. Gal, Phys. Rev. B **24** (1981), 6762

High Pressure Studies on Actinide Systems

Effect of pressure on the optical response of Th_3P_4 and U_3P_4

Th_3P_4 and U_3P_4 are typical members of the family of Th_3P_4 type compounds which comprises a large number of lanthanide and actinide pnictides and chalcogenides of 3:4 stoichiometry. X-ray diffraction study of Th_3P_4 and U_3P_4 up to 40 GPa [1] showed that the crystal structure does not change in this pressure range. Variation of physical properties under pressure can thus be studied in these compounds without interference from structural changes.

Triuranium tetraphosphide is a diamagnetic semiconductor, while the uranium compound is ferromagnetic below 138 K [2]. Their optical reflectivity at ambient pressure has been determined by Schoenes et al. [3]. These authors also derived densities of state for the compounds. The electronic properties and magnetic anisotropy of U_3P_4 were explained on the basis of hybridization between 5f orbitals of uranium and 3p orbitals of phosphorus [4]. This p-f mixing raises the energy of the valence p states which then overlap the conduction band.

Optical reflection under pressure was measured in the spectral range 0.5 to 4 eV up to 38 GPa for Th_3P_4 and up to 39 GPa for U_3P_4 . Reflectivities were determined at the sample-diamond interface. The data from the X-ray powder diffraction study [1] were used to scale the oscillator

strengths. The evolution of optical reflectivity of Th_3P_4 with pressure is shown in Fig 5.21a. Fig. 5.21b and 5.21c give, for the selected pressures of 10.1 GPa and 38.2 GPa (highest pressure reached), the optical conductivity and the real and imaginary parts of the dielectric constant. Most of the electronic transitions observed between 0.5 and 4 eV in Th_3P_4 and U_3P_4 at ambient pressure are only weakly affected by pressure. Some of them are slightly shifted to lower or higher energies.

Comparing the spectra of the two compounds at ambient pressure [3], or at moderate pressure as obtained in the present work, the most prominent difference is the upturn in reflectivity and conductivity towards the lowest energies observed for U_3P_4 which contrasts with a steady decrease in the same energy range for Th_3P_4 . This upturn in reflectivity confirms the metallic

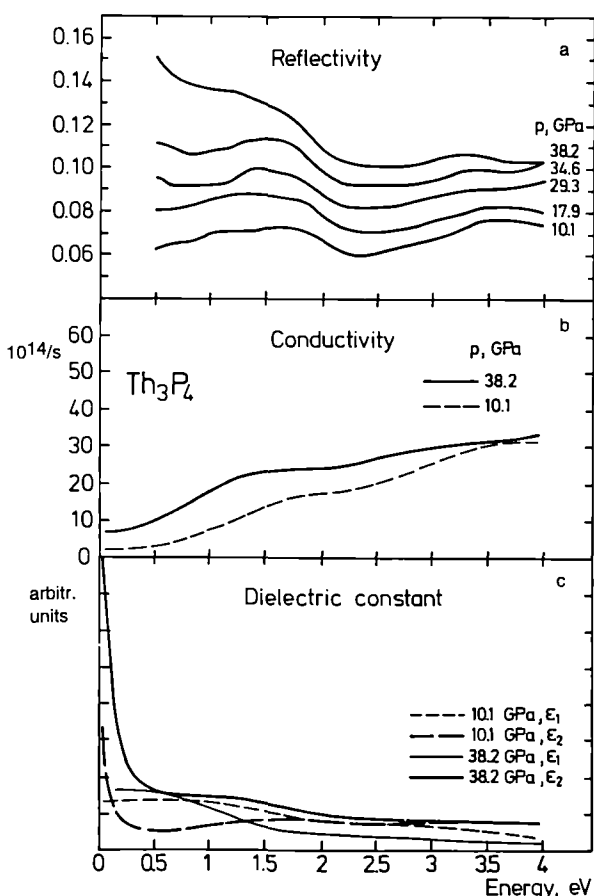


Fig.5.21 Evolution with pressure of optical reflectivity (a), optical conductivity (b) and real and imaginary parts of the dielectric constant (c) for Th_3P_4

character of U_3P_4 . As seen in Fig. 21a, the reflectivity curve for Th_3P_4 at 38 GPa shows a very similar upturn towards the lowest energies. This indicates that Th_3P_4 goes metallic at this pressure. In contrast, the conductivity of Th_3P_4 steadily decreases towards the lowest energies even at 38 GPa. Along the same lines, the energy decrease with pressure in the conductivity features of Th_3P_4 (Fig. 21b) supplies additional evidence of pressure-induced increase in f occupation and, as a consequence, of metallic character in the latter compound. One can conclude that a pressure of 38 GPa creates sufficient $5f$ occupation to allow for p - f mixing and thus induce metallic character in a similar way as this has been assumed for U_3P_4 at ambient pressure.

References

- [1] L. Gerward, J. Staun Olsen, U. Benedict, H. Luo, F. Hulliger; High Pressure Research 4 (1990) 357-359
- [2] W. Trzebiatowski, R. Troc; Bull. Acad. Polon. Sci., Ser. Sci. Chim. 11 (1963) 661
- [3] J.J. Schoenes, M. Küng, R. Hauert, Z. Henkie; Solid State Comm. 47 (1983) 23-27
- [4] T. Suzuki, S. Takagi, N. Niitsume, K. Takegahara, T. Kasuya, A. Yanase, T. Sakakibara, M. Date, P.J. Markowski, Z. Henkie; High Field Magnetism, M. Date, ed., North Holland Amsterdam 1983, pp. 183-187

The electrical resistance of USe under high pressure

Resistivity measurements by Schoenes et al. [1] on the uranium chalcogenides show for US above the Curie temperature a linear temperature dependence ascribed to the phonon contribution to the electrical resistivity. USe has such a linear behaviour too, but the temperature coefficient is smaller than the one of US. UTe finally has a maximum in the resistivity above the Curie temperature followed by a logarithmic decrease to higher temperature, which was interpreted by Schoenes et al. in terms of a dense Kondo behaviour [1,2].

Measurements of the electrical resistance of UTe under pressure show a strong increase of the Curie temperature to a maximum of 180 K at 7.5 GPa [3]. A decrease of the Curie temperature of US with increasing pressure was found by magnetisation measurements [4,5]. As the

resistivity behaviour of USe appears to be intermediate to UTe and US [1], and the high pressure behaviour of UTe is reminiscent of that of US [3], we performed high pressure resistance measurements on USe, the intermediate substance in the series of the uranium chalcogenides.

With increasing pressure the resistance decreased at all temperatures. Above 4 GPa the rate of decrease of the resistance with pressure was noticeably smaller than at low pressures. Up to 4 GPa the Curie temperature (derived from the maximum in dR/dT) increases to 192 K (Fig. 5.22). Above 4 GPa the Curie temperature

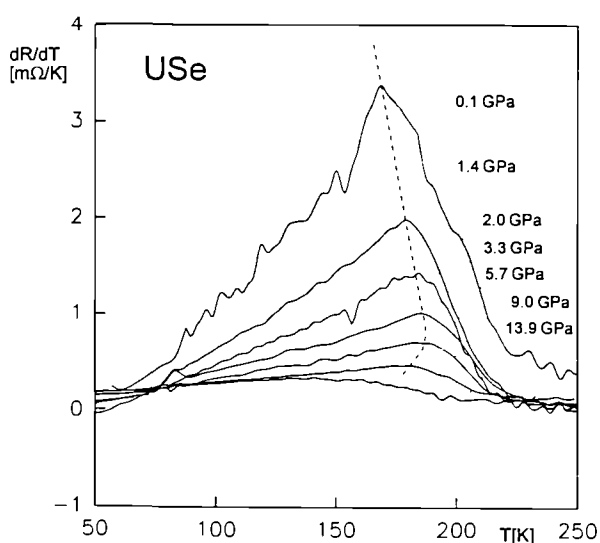


Fig.5.22 dR/dT of USe at selected pressures from 0.1 GPa to 13.9 GPa; the dashed line connects the estimated Curie temperatures.

decreases with increasing pressure. An overview of the pressure dependence of the Curie temperature of USe is given in Fig. 5.23.

At low pressures we observe an increase of the Curie temperature to a maximum of 192 K around 4 GPa (Fig. 5.23). At pressures above 4 GPa the Curie-temperature decreases with increasing pressure. This behaviour of the Curie-temperature is reminiscent of that observed for UTe [3], which has a maximum of the Curie temperature around 7.5 GPa. For UTe we based our interpretation on the coexistence of ferromagnetic inter-atomic exchange and anti-ferromagnetic intra-atomic Kondo coupling: Suppressing the Kondo coupling with increasing pressure led to an increase of the Curie tempera-

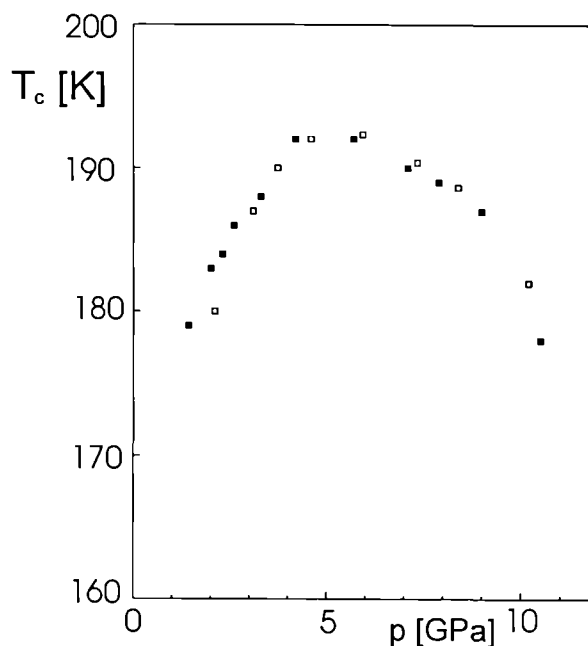


Fig.5.23 Pressure dependence of the Curie temperature of USe; open and full symbols: 2 different samples

ture. Schoenes et al. [1] tentatively ascribed the relatively small temperature coefficient of the resistance of USe to a similar additional contribution to the electrical resistance with negative temperature coefficient as found in UTe. The comparable behaviour of the Curie temperature supports this interpretation.

In addition, the fact that in USe the crystallographic phase transition starts only around 20 GPa [6] means that the maximum in the Curie-temperature is not influenced by this phase transition in the case of USe, which reinforces our interpretation that the maximum in the Curie-temperature is an intrinsic effect of the low pressure phase in the case of UTe [3].

The decrease of the Curie-temperature at higher pressures in USe as well as in UTe can be explained within an itinerant electron picture, like Fournier et al. [5] interpreted their results of magnetisation of US under pressure. The Curie-temperature of US decreased with increasing pressure [4,5], in accordance with the assumption of iron-like itinerant magnetism. An overview of the magnetic behaviour of the uranium chalcogenides is shown in Fig. 5.24. The U-U distances used in this plot were calculated from the measured pressure values using the pressure-volume relationships obtained from high-pressure X-ray-diffraction measure-

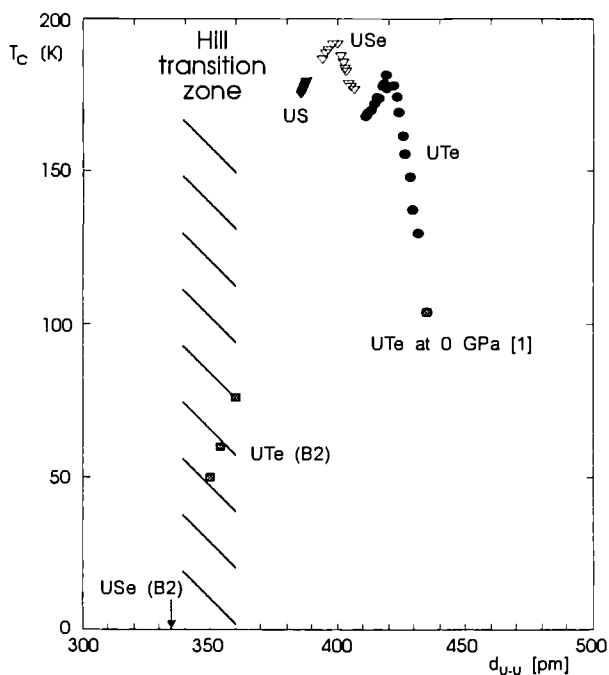


Fig.5.24 Curie temperatures of uranium chalcogenides vs U-U spacing

ments [6,7]. The variation of the Curie-temperature of US was taken from the results of Huang et al. [4]. The trend for the Curie-temperature of the three chalcogenides suggests that magnetism should disappear below the Hill-transition-zone. The observed anomaly in the resistance of the high pressure (B2) phase of UTe, tentatively ascribed to a magnetic ordering, also fits to this behaviour.

At low pressures we find in both compounds a strong increase of the Curie-temperature, which we ascribe to the disappearance of intra-atomic Kondo-coupling, caused by increasing 5f overlap. At higher pressures USe and UTe behave like itinerant ferromagnets as US does already at zero pressure. Increasing pressure leads to a larger 5f bandwidth and therefore to lower Curie-temperatures, or even to non-magnetic behaviour in accordance with the Hill-plot, as we believe at 20 GPa for USe.

References

- [1] J. Schoenes, B. Frick and O. Vogt; Phys. Rev. B30 (1984) 6578
- [2] B. Frick, J. Schoenes and O. Vogt; J. Mag. Mag. Mat. 47&48 (1985) 549

- [3] P. Link, U. Benedict, J. Wittig and H. Wühl; J.Phys.: Condens. Matter 4 (1992) 5585
- [4] C. Y. Huang, R. J. Laskowski, C.E. Olsen and J.L. Smith; Journal de Physique Colloque C4 (1979) 26
- [5] J.M. Fournier, J. Voiron and R. Troc; Solid State Communications 54 (1985) 441
- [6] L. Gerward, J. Staun Olsen, U. Benedict, S. Dabos and O. Vogt; High Pressure Research 1 (1989) 235
- [7] J.M. Léger, I. Vedel, A.M. Redon, J. Rossat-Mignod and O. Vogt; Solid State Com. 66 (1988) 1173

Pressure-induced phase transition in alpha-plutonium

With the heavier actinides Am to Cf, pressure induces phase transformations to structures of lower symmetry, accompanied by volume decreases from 6 to 21 %. The decrease in symmetry, together with the observed decrease in atomic volume, indicate that these transitions correspond to the delocalisation of the 5f electrons. In the earlier actinides, which have their 5f electrons already in an itinerant state, pressure can not induce this type of phase transition. A phase transition in alpha-plutonium was thus not expected, except for very high pressures.

In a paper on a high-pressure study of thorium, Akella et al. [1] briefly mention a pressure-induced structural change of plutonium from monoclinic to hexagonal close packed. To check for this reported high-pressure phase, we studied plutonium metal by X-ray diffraction at room temperature up to 62 GPa. Several samples of the same batch of plutonium metal were studied, most in the energy-dispersive mode and one in the angle-dispersive mode with the position-sensitive detector. The results of the different runs were in good agreement, although variations in relative intensities were observed. These are thought to be due to the sample size (of the order of 10 micrograms) which is not sufficient to guarantee completely random distribution of crystallites.

Above 40 GPa, new peaks appearing in the diffraction spectra indicated the formation of a high-pressure phase. The diffraction data do not fit the hexagonal close packed structure proposed by Akella et al. [1] because the latter structure does not explain 4 weak to medium intensity diffraction lines that appear in most of our spectra. We propose instead another hexagonal structure which can be derived from the monoclinic alpha-plutonium structure by slight shifts of the atomic positions and can be seen as a distortion of a hexagonal close-packed cell.

A projection of the proposed structure along the c -axis is shown in Fig. 5.25. The shaded area in Fig. 5.25 indicates how a hexagonal close-packed cell has to be distorted to yield the proposed cell. The space group is $P6_3/m$ (no. 176) with atoms in special positions $2d$ ($2/3, 1/3, 1/4$) and $6h$ ($x, y, 1/4$ with $x=0.2, y=0.333$), $Z=8$. Only the point symmetry of the position $2d$ changes to 6, whereas the other atoms still have the point symmetry of m . The lattice constants are: $a = 543.7$ pm, $c = 449.3$ pm, $c/a = 0.826 = 1.652/2$, at 55 GPa, and $a = 537.77$ pm, $c = 445.51$ pm, $c/a = 0.828 = 1.657/2$, at 62 GPa.

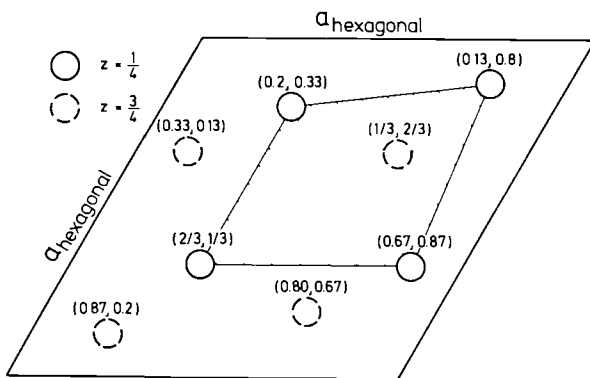


Fig.5.25 Projection along c of the high-pressure structure of plutonium. The shaded area represents a distorted hexagonal close-packed cell.

The relationship between alpha-plutonium and the high-pressure structure is visualised in Fig. 5.26. Based on this structure, Fig. 5.27 shows lattice parameters and volume as a function of pressure. The volume decreases by 1 to 2 % at the phase transition. It is noteworthy that the volume of the high-pressure phase exhibits an approximately linear decrease with pressure, indicating a value of the pressure derivative B'_0 close to zero. The transformation to a hexagonal cell is completed at 47 GPa. When releasing pressure, hysteresis to transformation is observed down to 5 GPa, where the metal becomes again single-phase monoclinic.

Fitting the pressure-volume data to different equations of state yielded good agreement between the different equations, allowing to adopt average values of $B_0 = 43(2)$ GPa and $B'_0 = 15(2)$.

The present study on plutonium suggests that the neighbouring metal neptunium could well

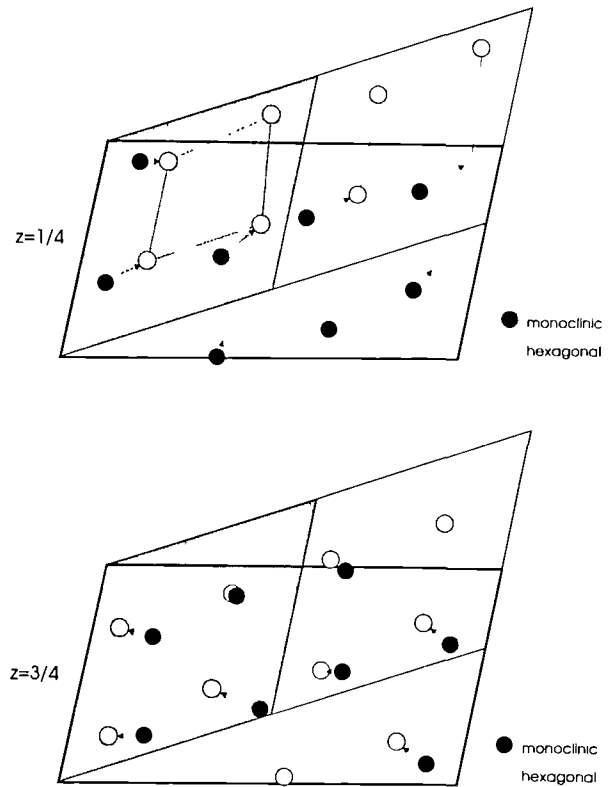


Fig.5.26 Relationship of the high-pressure structure of plutonium with alpha-plutonium

exhibit a phase transition at a pressure somewhat higher than 52 GPa. It thus seems useful to extend the study of the compression of neptunium to higher pressures.

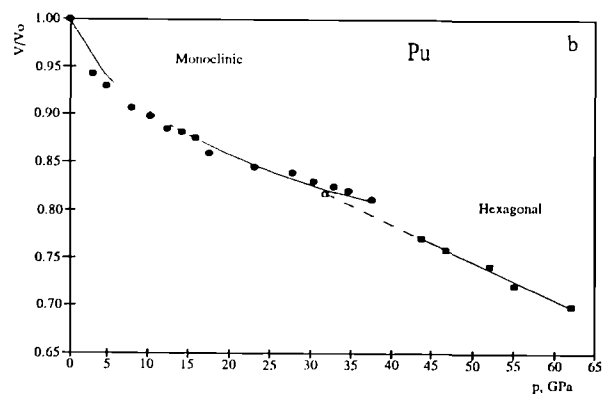


Fig.5.27 Relative volume of plutonium as a function of pressure

Reference

- [1] J. Akella, Q. Johnson, G.S. Smith, L.C. Ming; High Pressure Research 1 (1988) 91-95

Updated diagrams for pressure-induced phase transitions in 5f and 4f metals

All lanthanide and actinide metals have been studied by high-pressure X-ray diffraction in the past 20 years, except actinium, because of its extremely intense radioactivity, and except the heavy actinides einsteinium to lawrencium where either no solids exist or, in the case of Es, study of solids is complicated by fast decay and important decay heat.

The field of investigation has been recently extended by the study of selected f elements at higher pressures, in some cases above 100 GPa (see, e.g., refs 1 and 2), and by the study of binary alloys between f elements that are neighbours in the Periodic Table (see, e.g., refs. 3 and 4). In addition, the only lanthanide element that had never been studied by these methods owing to its radioactivity, promethium, has undergone high-pressure X-ray diffraction study [5], as has a Pm-Sm alloy [6]. These recent results will briefly be reported and included in updated versions of the two general diagrams.

Probably the most interesting result of these investigations at extreme pressures is the formation, around 100 GPa, of a body-centred tetragonal phase in samarium [1], designated bct 1 in Fig. 5.28a. Samarium undergoes, with increasing pressure, the transformations to the dhcp, ccp and distorted ccp (trigonal) phases which are in general observed for the trivalent lanthanide metals and the heavy actinide metals. Around 32 GPa, it transforms to a monoclinic phase [7].

The formation of a low-symmetry structure such as this monoclinic phase is, according to a widely accepted - though not rigorously proven - correlation, taken as strong indication of an onset of f itinerancy. Along the same lines, a tetragonal structure, having relatively high symmetry, should be correlated to more localised f electrons, and the degree of delocalisation should first increase at the trigonal-to-monoclinic, and then decrease again at the monoclinic-to-bct transition if a gradual correlation is assumed.

This situation parallels that in cerium metal (Fig. 5.28a) where transformations from ccp to monoclinic to body-centred tetragonal are observed with increasing pressure.

Such an "oscillation" of delocalisation during a monotonous pressure increase has not a very high probability. The simple correlation between degree of symmetry and degree of itinerancy probably does not hold. There are, in addition, other indications for a more complicated relationship.

First, protactinium has a body-centred tetragonal structure, of a type different from that in Sm and Ce (designated bct 2 in Fig. 5.28b). Its high density, on the other hand, and theoretical calculations indicate some participation of its two 5f electrons in the metallic bonding.

Second, the recent observation of a body-centred tetragonal phase of the "bct 1" type as it exists in Ce and Sm, formed from the ccp phase of thorium around 100 GPa (see Fig. 5.28b) was interpreted as a sign of 5f bonding [2]. This interpretation assumes that the slight loss of symmetry accompanying the transition from ccp to bct is already correlated to 5f bonding. In the case of thorium, in contrast to cerium and samarium, no monoclinic phase intermediate to ccp and bct was found.

A third example probably exists in the case of plutonium. (see above). Fig. 5.28b shows that monoclinic plutonium, which is considered to be a prototype for a low-symmetry structure correlated with itinerant 5f electrons, transforms to a more symmetric hexagonal structure around 40 GPa (see above). The same is true for a $\text{Pu}_{0.75}\text{Am}_{0.25}$ alloy.

The recent results described in the previous sections have been used to update previously published general diagrams of phase relations under pressure. The updated diagrams are shown in Fig. 5.28. They consist of interconnected binary phase diagrams of metals which are neighbours in the Periodic Table, and visualize the general trends in phase relations under pressure. They refer to room temperature data only. The thick dots on these diagrams represent the phase transitions which have been experimentally observed. To avoid complication, two-phase regions are not shown.

If the diagrams are superimposed according to equal f counts, there is no resemblance. But if the diagram for the lanthanides is shifted to

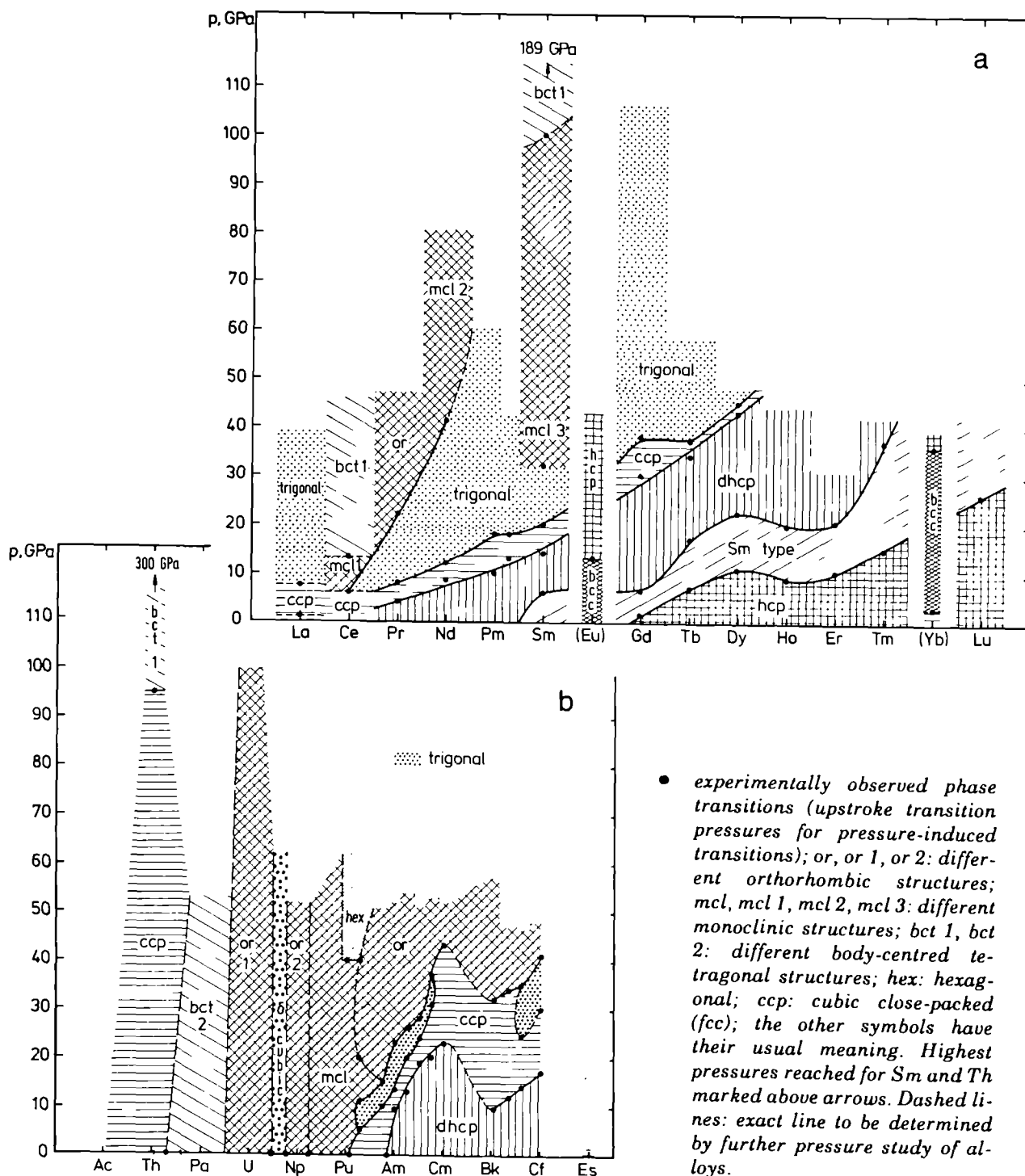


Fig.5.28 General diagrams of the phase relations of the f-metals under pressure, status end 1991. The two diagrams are shifted according to the Z+4 homology.

a. lanthanides. b. actinides.

higher Z by 4 atomic numbers, there is a striking similarity in the structural sequences with increasing pressure and with increasing Z . This comparison between the two diagrams is an illustration of the principle of "shifted homologous relationships" between the transplutonium and the lighter rare-earth metals as suggested by Johansson and Ward.

References

- [1] Y. Vohra, J. Akella, S. Weir and G.S. Smith; *Physics Letters A* **158** (1991) 89-92
- [2] Y.K. Vohra and J. Akella; *Phys. Rev. Letters* **67** (1991) 3563-3566
- [3] S. Dabos-Seignon, E. Gering, U. Benedict, J.C. Spirlet and M. Pagès; *High-Pressure Research* **2** (1990) 255-261
- [4] R.G. Haire, S. Dabos, U. Benedict and C. Dufour; paper presented at the Spring Meeting of the American Chemical Society, Boston, MA, April 23-27, 1990
- [5] R.G. Haire, S. Heathman and U. Benedict; *High Pressure Research* **2** (1990) 273-288
- [6] S. Heathman, R.G. Haire and U. Benedict; to be published
- [7] J.S. Olsen, S. Steenstrup, L. Gerward, U. Benedict, J. Akella and G. Smith; *High Pressure Research* **4** (1990) 366-368

HPXRD study of $AnCl_4$ ($An = Th, U$) single crystals

The present HPXRD study was performed using a Merrill-Bassett diamond-anvil cell [1] with a prepressed Inconel gasket. The crystals of approximately $0.1 \times 0.05 \times 0.05 \text{ mm}^3$ and a ruby splinter as internal pressure reference were mounted in the cell with dried silicone oil as pressure transmitting medium. The lattice parameter refinement and the data collection at different pressures were performed on a CAD4 Enraf-Nonius four circle diffractometer using Mo K radiation.

The plot of the relative volume vs pressure shows a greater compressibility for UCl_4 than for $ThCl_4$. The derivative of the volume decrease is 2.5 \% GPa^{-1} for UCl_4 in comparison to the 1.7 \% GPa^{-1} of $ThCl_4$. For the two compounds the compression is anisotropic with the c axis approximately 3 to 4 times more compressible than the a axis (Fig. 5.29). The full structure refine-

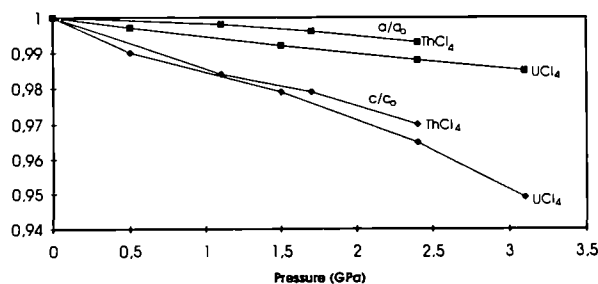


Fig.5.29 Variation of a/a_0 and c/c_0 vs pressure for $ThCl_4$ and UCl_4

ments were carried out in space group $I4_1/amd$ with the An atom at the position $(0, 3/4, 1/8)$ and the Cl atoms at the position $(0, y, z)$. For all pressure steps the y, z co-ordinates for the Cl atoms were refined for $ThCl_4$ and UCl_4 .

The An element is eight-co-ordinated and the Cl atoms form a decahedron with four short An-Cl and four long An-Cl distances. The crystal presents an arrangement of these decahedron units along the a and b axis with the Cl-Cl distances ranging from 307 to 318 pm, where the Cl-Cl distances along the c axis range from 340 to 350 pm. The strong repulsive Cl-Cl interaction in the (ab) plane and the vacancies in the c direction are probably responsible of the observed anisotropic compression. Pressure has no significant effects on the geometry around the An atom. Only a small co-ordination change,

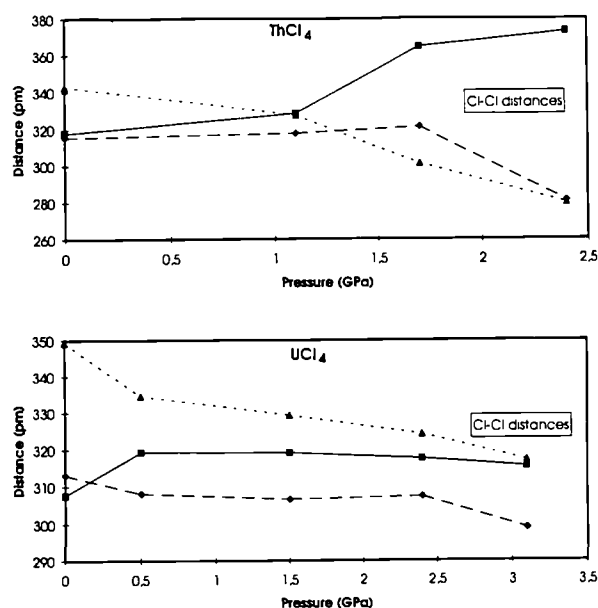


Fig.5.30 Variation of pertinent Cl-Cl distances vs pressure for $ThCl_4$ and UCl_4

from 2×4 to 8 for the ThCl_4 is visible. The largest pressure effect appears in the Cl-Cl interactions, especially for ThCl_4 . UCl_4 shows only a general decrease of Cl-Cl distances and a general shrinking of the crystal. The variation of pertinent Cl-Cl distances vs pressure for ThCl_4 and UCl_4 is represented in Fig. 5.30.

Over the measured pressure range, no phase transitions were observed. The pressure-volume data fitted to a Birch-Murnaghan equation of state yield a bulk modulus and pressure derivatives of, $B_0 = 38$ GPa, $B_0' = 10$ for ThCl_4 and $B_0 = 42$ GPa, $B_0' = 1.5$ for UCl_4 . These values are consistent with the measurements obtained from X-ray powder diffraction data [2].

References

- [1] L.Merrill and W.A. Bassett, Rev. Sci. Instrum.,45 (1974) 290
- [2] J.P. Dancausse, Thesis (University of Orsay,France) 1991

2. Exploratory Research

Acoustic Aerosol Scavenging

Introduction

The aim of the project "Acoustic Aerosol Scavenging" is to investigate the feasibility of using high intensity sound to scavenge particulate material from the air. The basic idea is to agglomerate the fine particles (aerosol) by the use of a sound field, to a size large enough that they precipitate out either due to sedimentation in the gravitational field (i.e. under *static* conditions) or by the action of an externally applied field such as the electric field in an electrostatic precipitator (i.e. under *dynamic* conditions). These agglomeration and precipitation steps form the basis of the scavenging process.

During the reporting period, results at flow rates up to 1000m³/hr have been obtained. These are reported in the section "Support to DG XIII". In this section, we summarize recent experimental investigations on the attenuation of sound energy by aerosols and theoretical activities concerning the optimisation of acoustic cavities for aerosol conditioning. In addition, an analysis of acoustic agglomeration at low frequencies is presented with emphasis on infra-sound scavenging of aerosols.

Attenuation of sound in fog and soot aerosols

Introduction

The attenuation of sound in liquid (fog) and solid (soot) aerosols was investigated initially with the aim of designing a new improved acoustic agglomeration cavity. The results obtained are consistent with appropriate attenuation models.

Experimental facility and procedure

A diagram of the experimental facility is shown in Fig. 6.1. The aerosol was either introduced

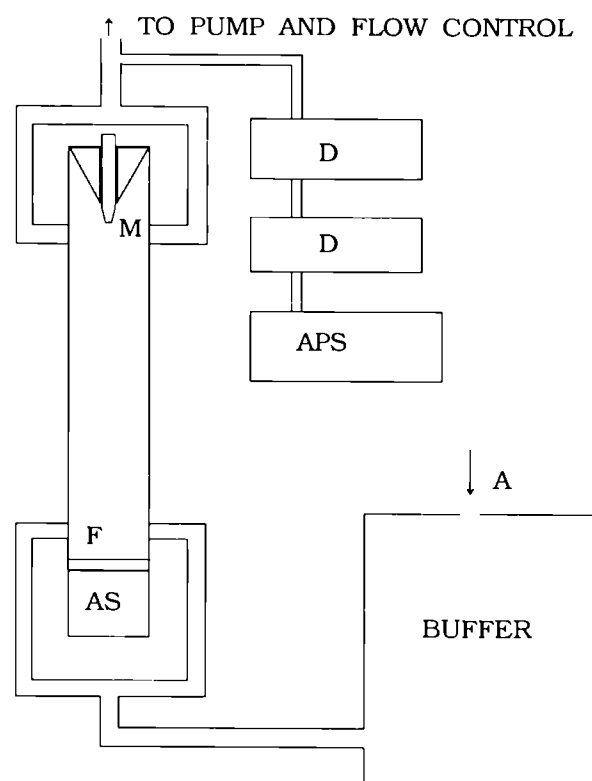


Fig.6.1 Diagram of the experimental facility. When pumping through the test section, the aerosol is continuously mixed by a fan with the fresh air admitted at A. The acoustic signal is monitored by a microphone, M, positioned at the vertex of a conical sound absorbing unit. The aerosol is sampled after the test section. The sound sources (AS) were either loud-speakers or piezo-electric driven stepped plates.

into a buffer (fog) or created directly inside the buffer (soot was generated by burning rubber). The aerosol was then drained from the buffer into the test tube at a constant flow rate. An acoustic source (stepped plate driven by a piezo-electric transducer or loud-speaker) was used to generate an acoustic signal in the test tube (Input powers lower than 10 W were used so that only linear progressive waves were obtained). A microphone, positioned at the vertex of a conical piece constructed from sound-insulating material, was located at the opposite end of the test tube. The characteristic properties of the aerosols were measured continuously during the ex-

periment by an Aerosol Particle Sizer (TSI3310). The Sound Pressure Level (SPL), and successive size distributions of the aerosols were acquired on personal computers every 5 s and 15 s respectively. These signals were corrected for the time lag, due to the different sampling positions in the installation. Time was then eliminated to obtain the relationship between the attenuation coefficient (relative to the SPL in fresh air before the experiment) and the size distribution functions.

The experimental investigation covered a range of frequencies (1-40 kHz for fog, and 2.5-20 kHz for soot). A characteristic experiment lasted 45 minutes, during which the concentration of fog aerosol in the test tube decreased from 10^7 to 10^4 cm^{-3} . (Under similar conditions, the concentration of soot aerosol decreased from $1.5 \cdot 10^6 \text{ cm}^{-3}$ to $3.5 \cdot 10^3 \text{ cm}^{-3}$.)

Characterization of the aerosols

Simple mass balance considerations show that the mass of aerosol in the test tube should follow an exponential decay. This is indeed the case as is illustrated in Fig. 6.2a for a fog aerosol. However, the total particle concentration does not follow this exponential decay at the beginning of the experiment (see Fig. 6.2a). This is due to ageing of the aerosol. As is shown in Fig. 6.2b where the statistical parameters of the size distributions, (\bar{d}_g, σ_g) are plotted as a function of time during the experiment. Both of these parameters increase until the concentration is sufficiently low to hinder further brownian agglomeration. When this concentration is reached, the total particle concentration exhibits an exponential behaviour with time (see Fig. 6.2a). In contrast the characteristics (\bar{d}_g, σ_g) of the soot aerosol were constant with time, and the total concentration of particles decreased exponentially throughout the experiment. The distribution function as measured by the APS is believed to be correct, but the absolute concentrations are probably underestimated. Therefore an in depth analysis of the data for soot aerosol is more complicated as the absolute aerosol mass is unknown by a factor related to the sensitivity of the device for soot particle detection.

Experimental attenuation coefficient

The experimental attenuation coefficient α as a function of particle concentration N_T is shown

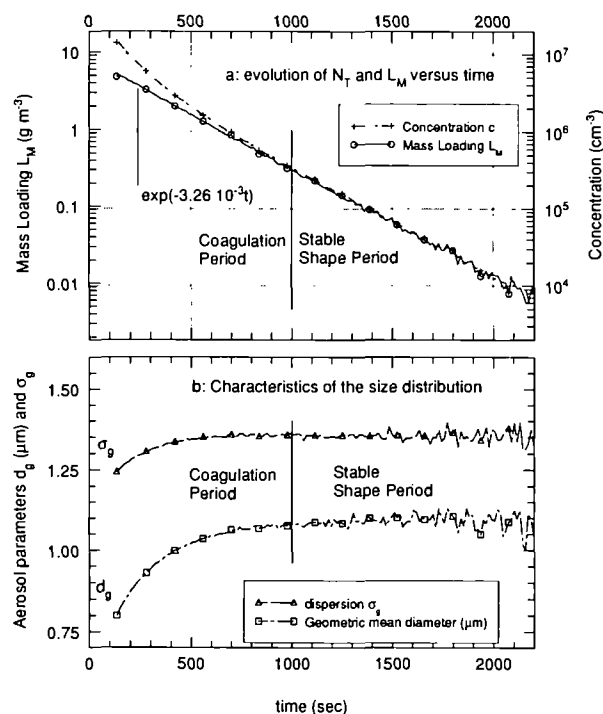


Fig.6.2 FOG: Comparison of the evolution of mass loading and total concentration of particles as a function of time (a). After a given time, a size distribution constant in shape is established, as is shown by the evolution of \bar{d}_g and σ_g with time (b).

in Fig. 6.3 and Fig. 6.4a for fog and for soot aerosols respectively. The curvature of the attenuation coefficient α as a function of N_T for fog aerosol can be explained by the evolution of the size distribution during each run. Indeed, if the experimental size distributions are used as input to the theoretical model described below, this behaviour can be reproduced. The apparent scatter in α at high N_T is also attributable to differences in the initial size distribution [1]. For the soot aerosol, the observed scatter in the experimental data (see Fig. 6.4a), is due to the low level of attenuation characteristic of soot (i.e. the signal to noise ratio is poorer), and to temperature changes caused by the aerosol generation process.

Comparison with theory

The attenuation of sound energy by an aerosol stems from a number of different phenomena. For soot the classical theory of Temkin and Dobbins [2,3], which only takes thermal and viscous dissipation into account, is sufficient to inter-

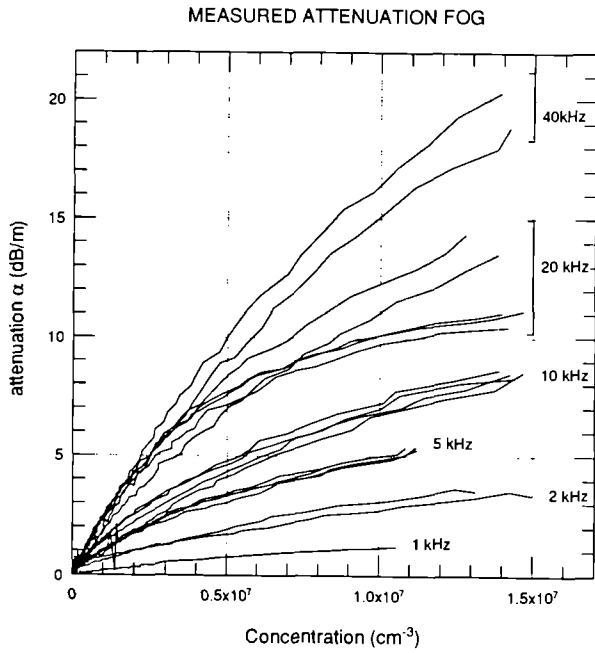


Fig. 6.3 FOG: Attenuation coefficient, α , as a function of the total particle concentration. The scatter observed at individual frequencies is explained by different initial properties of the aerosol.

pret the data. For a given mass concentration C_M of particles of a given radius R , the coefficient of attenuation is expressed by:

$$\alpha_{TD}(R) = \frac{\omega C_M(R)}{a_0} \left(\frac{\omega \tau_d(R)}{1 + (\omega \tau_d(R))^2} + (\gamma - 1) \frac{C'_p}{C_p} \frac{\omega \tau_t(R)}{1 + (\omega \tau_t(R))^2} \right) \quad (1)$$

where $\omega = 2\pi f$ and:

$$\tau_d = R^2 \frac{2\rho'}{9\mu} \quad (2)$$

(dynamic relaxation time of the particle)

$$\tau_t = R^2 \frac{\rho' C'_p}{3k} \quad (3)$$

(thermal relaxation time of the particle)

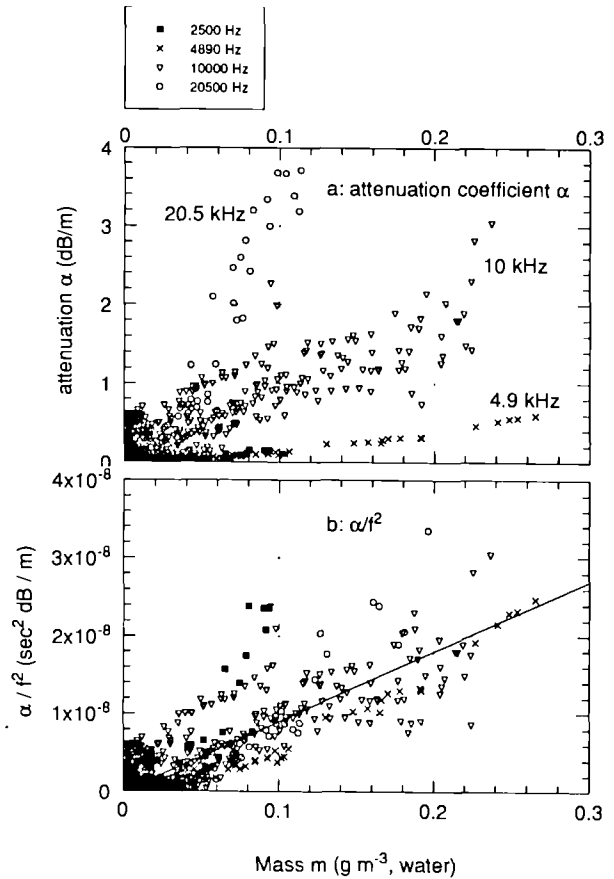


Fig. 6.4 SOOT: a- Attenuation coefficient, α , for different frequencies, as a function of equivalent mass of water. b- a plot of α/f^2 shows that experimental points are grouped around the same straight line.

where μ and k are the dynamic viscosity and the thermal conductivity of the gas, C_p and γ the specific heat capacity and the specific heat ratio of the gas, ρ' and C'_p the density and the specific heat capacity of the particle. For a polydisperse aerosol, this expression must be integrated over the full size range.

For soot, ($\bar{d}_g = 0.65 \mu\text{m}$, $\sigma_g = 1.3$), the characteristic dynamic and thermal times are $\tau_d = 1.3 \cdot 10^{-6} \text{ s}$ and $\tau_t = 9.7 \cdot 10^{-6} \text{ s}$. Within the investigated frequency range (2.5-20 kHz), the sound attenuation coefficient should exhibit the asymptotic behaviour predicted by theory i.e. the coefficient of attenuation, α , is directly proportional to the square of the frequency, f .

A plot of α/f^2 versus equivalent mass of water is shown in Fig. 6.4b. The experimental points are grouped around the same straight line, indicating that the attenuation coefficient α is indeed

proportional to f^2 and the expected asymptotic behaviour is found.

For fog, the interpretation of the experimental data requires a refinement to the theory of Temkin and Dobbins (provided by the model of Cole and Dobbins [4]). The refined model takes the transfer of mass between the vapour and the droplets into account. This phenomenon arises due to the periodically changing pressure around the droplets. Since any phase change is associated with heat release or absorption, the mass transfer contribution is intertwined with the thermal dissipation term. The expression of α_{CD} is then not as simple as for the Temkin and Dobbins theory. It is noteworthy, however, that in the Cole and Dobbins model a new characteristic time,

$$\bar{\tau} = \frac{\tau_t}{C_f}, \quad (4)$$

is introduced, where

$$C_f = \frac{C_M}{1 + C_M} \sim C_M \quad (5)$$

(the mass concentration, C_M , is the ratio of particulate mass to the mass of gas in a unit volume of the mixture). Since $C_f \sim 10^{-3}$, this new time $\bar{\tau} \sim 10^3 \tau_t$, introduces a relaxation phenomenon which plays a major role in the low frequency regime.

For the fog aerosol, the experimental data can be compared directly with theory, provided that the physical constants of the aerosol are known. By averaging the set of experimental size distribution functions measured at three different particle concentrations, three characteristic size distributions were generated. These characteristic functions were then used to compute the attenuation as a function of frequency at these three concentrations. The theoretical attenuation corresponding to individual experimental measurements were also been computed from individual size distributions. The results in term of the theoretical attenuation per wavelength, $\alpha\lambda$, as a function of frequency, are shown for these three particle concentrations, in Fig. 6.5.

Best agreement with theory over all frequency ranges is obtained using the Cole and Dobbins model which includes the mass transfer effect. This dissipation mechanism is particularly important for frequencies less than 10 kHz.

Conclusion

These investigations have shown that the attenuation of sound by a soot aerosol can be described by the theory of Temkin and Dobbins. For a liquid aerosol, the mass transfer effect as discussed by Cole and Dobbins must be included. This effect explains the larger than expected attenuation of sound at low frequency. Since industrial aerosols are usually multicomponent and multiphase, the expected attenuation should be estimated using the theory of Cole and Dobbins particularly if agglomeration using low frequency is planned.

Optimization of acoustic cavities for aerosol conditioning

Introduction

Fundamental to the design of suitable acoustic chambers for aerosol conditioning is the decision to use either a progressive or standing wave configuration for a fixed energy input from the sound source. Since the acoustic agglomeration rate is proportional to the product of the average amplitude of the wave and the residence time of the aerosol in the acoustic field, it is not clear which configuration is fundamentally better. Using progressive waves (PW), the lower average amplitude is offset by a longer residence time. Using standing waves (SW), the average amplitude can be considerably higher than in the PW (the treatment volume is now limited by the plate spacing between sound source and reflector) at the expense, however, of a smaller residence time.

The efficiency of an acoustic cavity

Consider aerosol flowing with speed v in the z -direction, between two infinite parallel walls separated by a distance D as shown schematically in Fig. 6.6. Between the planes $z=0$ and $z=Z$, the aerosol is subjected to a high intensity acoustic field. At any instant in this region the total aerosol particle concentration n is governed by the differential equation (in a Lagrangian reference frame) $Dn/Dt = -Kn$ consistent with the orthokinetic mechanism of acoustic agglomeration [5]. The underlying physical mechanism of agglomeration is that of small particles, fully entrained in the sound wave, colliding with heavy particle collection or scaveng-

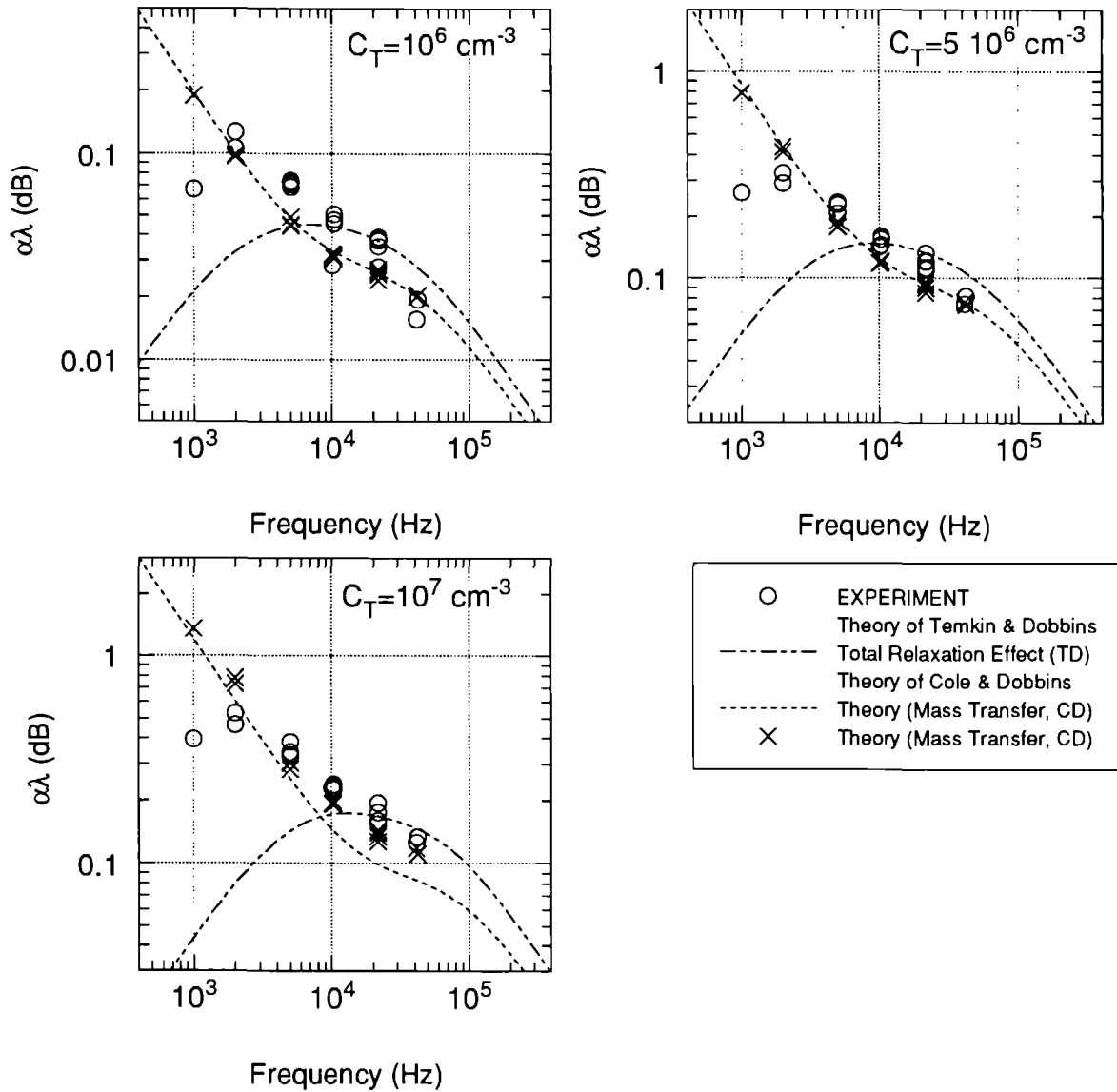


Fig.6.5 FOG: Experimental attenuation per wave-length, compared with the theories of Cole and Dobbins (CD) and of Temkin and Dobbins (TD). Note the increased contribution to attenuation at low frequency, when mass transfer is included.

ing centres. The rate of change of the small particles is proportional to both the concentration of small particles and heavy particles. For the case of interest here the concentration of small particles is much larger than that of the heavy particles. In addition, the number of heavy particles is constant throughout the agglomeration process, depending only on their concentration in the initial aerosol distribution [6]. The resulting first order differential equation for the particle concentration implies that the agglomeration coefficient depends essentially on the sound wave amplitude A and the initial aerosol particle concentration (since this determines the number of heavy 'seed' particles) i.e. $K = K(A, n(t=0))$.

By integration of the above equation between $z = 0$ and $z = Z$, the efficiency of the cavity (defined by $\epsilon \equiv 1 - n(Z)/n(0)$) is obtained i.e.

$$\epsilon = \begin{cases} 1 - \exp \left[-A_{ac} \frac{\langle A(x,0) \rangle}{A_L} a(0)D \right] & \text{for } \frac{a(0)}{a(z)} = 1 \\ A_{ac} \frac{\langle A(x,0) \rangle}{A_L} a(0)D & \text{for } \frac{a(0)}{a(z)} = \frac{n(0)}{n(z)} \end{cases} \quad (6)$$

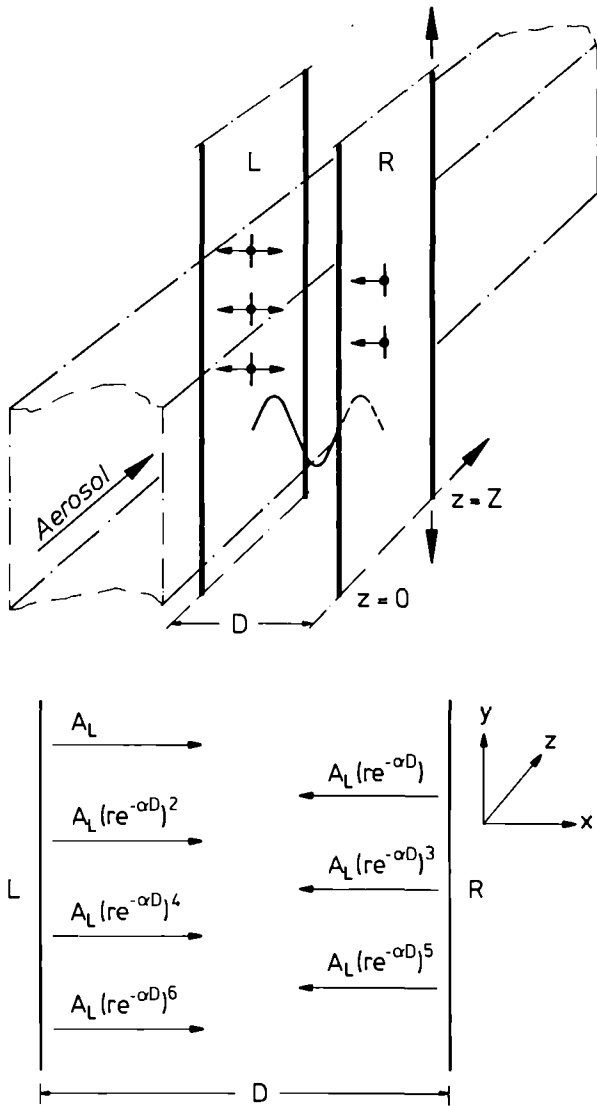


Fig.6.6 Schematic diagram of aerosol flow through an acoustic cavity with wall separation D . The cavity wall L emits a wave of amplitude A_L which undergoes attenuation by the aerosol and reflection at the wall R . These processes give rise to an infinite number of waves emerging from L and R which have to be summed to obtain the amplitude at various points in the cavity.

where $A_{ac} = K(A_L, 0)\tau_{res}/\alpha(0)D$ is the acoustic agglomeration number and $\tau_{res} = Z/v$ is the residence time of the aerosol in the cavity. For a constant volume flow rate between the walls, the residence time is directly proportional to the wall separation D i.e. τ_{res}/D is constant. It follows that for any particular application, A_{ac} should be approximately constant, dependent only on the volume flow rate. The above expressions for the efficiency, of the cavity can be combined to give

$$\epsilon = (1 + \beta) \left[1 - \exp \left[\frac{-A_{ac} \langle A(x,0)/A_L \rangle \alpha(0)D}{1 + \beta} \right] \right] \quad (7)$$

where β is the attenuation parameter. When heavy particle attenuation dominates, $\beta \rightarrow 0$. When fine particle attenuation dominates $\beta \rightarrow \infty$. In the next section we investigate the properties of $\langle A(x,0)/A_L \rangle \alpha(0)D$ in the above relation. In the following analysis, the subscripts referring to aerosol concentration at $z=0$ are dropped.

The amplitude variations of a standing wave ($r = 1$) and a progressive wave are shown in Fig. 6.7a for $\alpha D = 0.2$ (low attenuation) and $D/\lambda = 6$. For small αD , the amplitude varies as $\cos(\Phi_2 - \Phi_1)/2$ (the average value of this quantity over one cycle is $2/\pi$). In Fig. 6.7b the same waves are shown for $D/\lambda = 0.5$, i.e the plate spacing is the smallest possible for a standing wave. It should be noticed that although the value of D/λ has change by more than a factor ten, the averaged value $\langle A/A_L \rangle$ is almost identical in both cases. This is due to the fact that $\langle \cos \Phi \rangle$ over one or many cycles is the same. At higher values of αD , the waves are more attenuated as can be seen in Figs. 6.7c and 6.7d.

For a progressive wave $\langle A/A_L \rangle \alpha D (= 1 - \exp(-\alpha D))$ varies between 0 and 1 as expected. For a standing wave, the quantity $\langle A/A_L \rangle \alpha D$ can be now be calculated by numerical integration of the areas under the curves of Fig. 6.7 for various values of αD . The results are shown in Fig. 6.8. For the standing wave, at small values of αD , the averaged amplitude $\langle A/A_L \rangle$ is equal to $(2/\pi)(\alpha D)^{-1}$ such that the product $\langle A/A_L \rangle \alpha D \rightarrow 2/\pi$. Thus although the residence time is tending towards zero (for a fixed volume flow rate τ_{res} is proportional to D) the averaged amplitude is increasing at the same rate such that the product is a constant. At large values of αD , the values for the standing and progressive waves tend to the same value as is to be expected.

In Fig. 6.9 the efficiency of the acoustic cavity is shown for various values of A_{ac} and αD . The exponential relation has been used here since this leads to a lower estimate of the efficiency. From this figure it is clear that at high values of αD (i.e. $\alpha D > 1$) the efficiencies of standing and progressive wave configurations are equal (as expected) and depend only on the value of A_{ac} . At

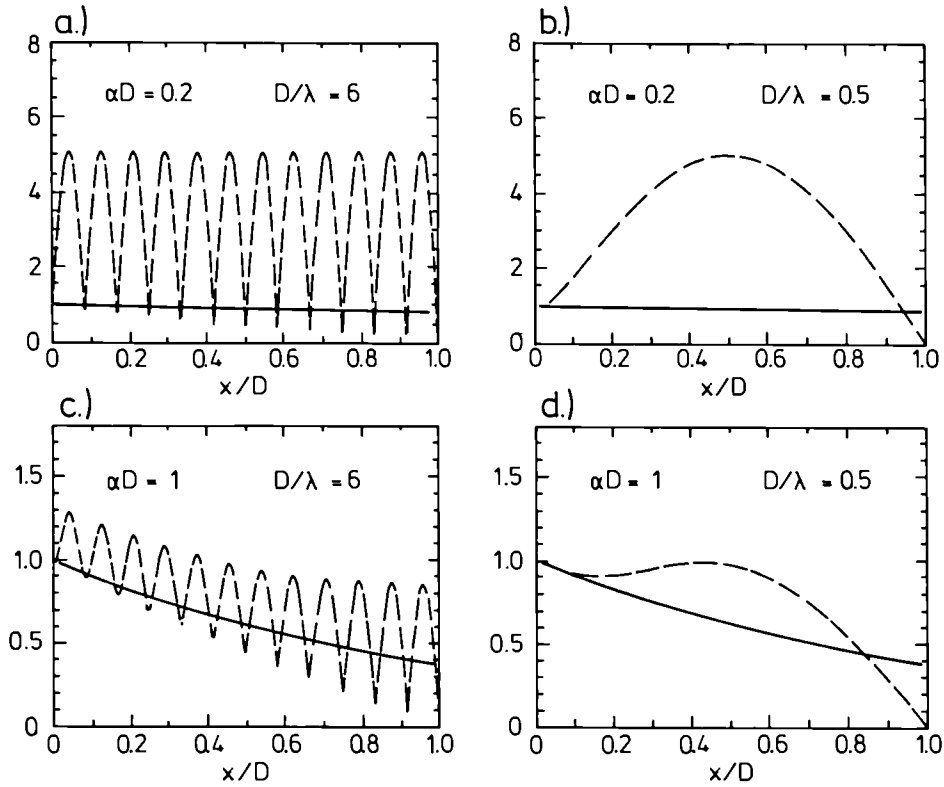


Fig.6.7 The normalized wave amplitude A/A_L as a function of normalized position x/D in the cavity for various values of αD and D/λ . The broken and continuous curves represent standing and progressive waves respectively.

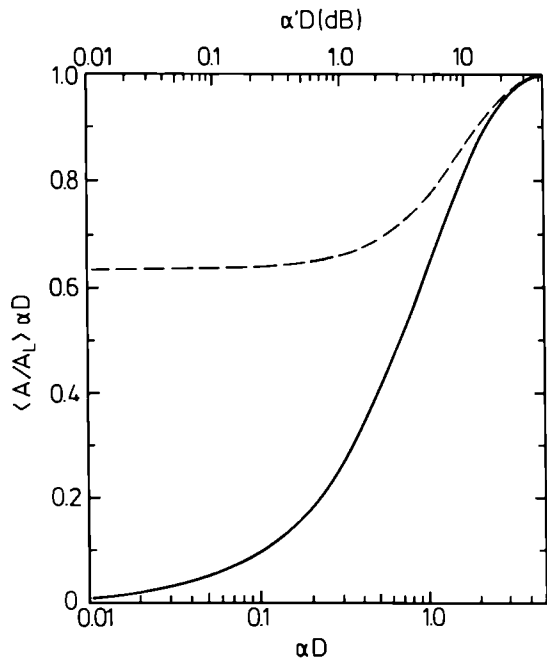


Fig.6.8 The value of $\langle A/A_L \rangle \alpha D$ as a function of αD . The broken and continuous curves are for the standing and progressive waves respectively. For convenience, the top axis gives the values of αD where α' is the attenuation coefficient measured in units of dB m^{-1} .

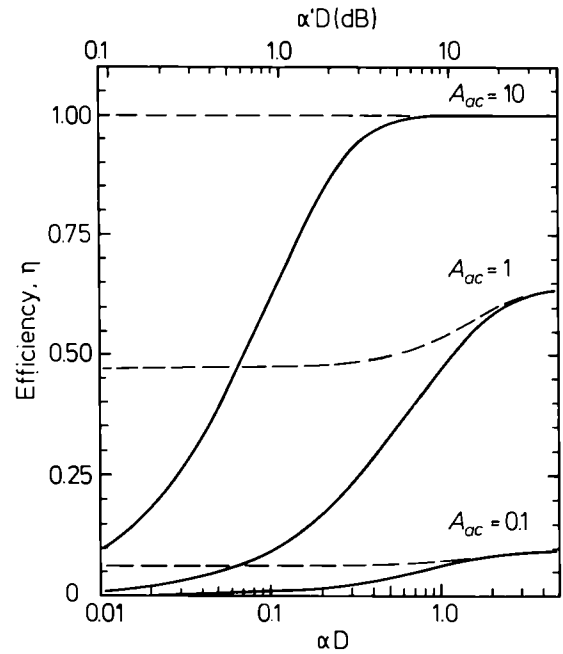


Fig.6.9 The efficiency of an acoustic cavity as a function of αD for various values of A_{ac} . The broken and continuous curves are for the standing and progressive waves respectively. The top axis gives the values of αD where α' is the attenuation coefficient measured in units of dB m^{-1} .

small values of attenuation ($\alpha D < 1$), the standing wave configuration is *apparently* more efficient than the progressive wave configuration. This is due to the higher averaged amplitude of the standing wave since the residence time is the same in both cases. To obtain the progressive wave, however, it has been assumed that the wave energy which arrives at the wall R is lost from the cavity. This wave energy could, of course, be reflected back into the cavity (along a different path so as not to interfere with the original wave). After each traversal of the cavity the wave energy would be reflected (at an angle) further downstream or upstream. Under these conditions one should use the limiting value of efficiency ϵ for $\alpha D \gg 1$ for the progressive wave. Consider the case of $\alpha D = 0.1$ and $A_{ac} = 1$: From Fig. 6.9 the efficiency of the standing wave is $\approx 47\%$. For the progressive wave configuration, for the same value of plate spacing D, one could reflect the energy along the z direction. In this case the limiting value for the efficiency ($\alpha D \gg 1$) should be used i.e. 63% which is higher than the value for the standing wave. An acoustic cavity has been designed based on such considerations [7].

It can therefore be concluded that, apart from technical simplicity of a progressive wave configuration over that of a standing wave, the progressive wave configuration will lead also to a slightly higher conditioning efficiency. Care should be taken at very low frequencies ($\ll 1\text{kHz}$) where the dimension of the cavity are such that one cannot use the limiting efficiency for $\alpha D \gg 1$ for the progressive wave - here one should use the actual value of αD together with the results in Fig. 6.9. However under usual conditions the efficiency of the cavity will be determined by the value of A_{ac} for both PW and SW configurations (the dependence on αD being weak).

Relation between static and dynamic agglomeration experiments

In contrast to the *dynamic* agglomeration experiments, in which the aerosol passes once through the acoustic module at a fixed volume flow rate, *static* agglomeration experiments refer to the agglomeration of aerosol in a constant volume chamber or cavity. Although the volume of aerosol is constant the aerosol is not static but circulates in the chamber due to acoustic streaming, use of a fan etc., to ensure efficient mixing and uniform particle density throughout the volume. The distance between the sound source and the chamber wall is denoted by X.

The particle concentration throughout the chamber at any time is denoted by $n(t)$. This particle density is decreasing due to the fact that in front and to the back of the transducer a volume of P/α , where P is total area of the radiating surface and $1/\alpha$ is the approximate range of the field in the aerosol, is being acoustically treated. The *static* agglomeration coefficient K_{st} at any time t is evaluated using the relation.

$$K_{st} = - \frac{1}{n(t)} \frac{dn(t)}{dt} = K(A_L, 0) < \frac{A}{A_L} > \frac{P}{P_C} \quad (8)$$

Where $K(A_L, 0)$ is the intrinsic agglomeration coefficient for aerosol of concentration $n(t)$ with sound wave of amplitude A_L . The quantity P/P_C accounts for the cross sectional area of the chamber (P_C) being different from that of the sound source (P). Of particular interest here is the static agglomeration coefficient evaluated at $t = 0$. From the previous analysis, at low starting concentration $n(0)$, $< A/A_L > = 2/(\pi\alpha X)$. At very low particle concentration $< A/A_L >$ should therefore tend to infinity. In practice, however, at low concentrations the attenuation is no longer determined by the aerosol but by non-linear absorption in the air. Hence $< A/A_L > = 2/(\pi\alpha X) = \text{constant}$. Attenuation under these conditions is independent of the aerosol concentration. Hence

$$\text{for } n(0) \text{ low:} \quad K_{st} \sim \frac{K(A_L, 0)}{\alpha X} \frac{P}{P_C} \quad (9)$$

Where α is constant. It follows that K_{st} is proportional to the starting concentration $n(0)$. At high concentrations $< A/A_L > = (\alpha X)^{-1}$ (progressive wave). Here α is proportional to $n(0)$ such that

$$\text{for } n(0) \text{ high:} \quad K_{st} = \frac{K(A_L, 0)}{\alpha(0)X} \frac{P}{P_C} \quad (10)$$

Since both K and α are proportional to the starting concentration, $n(0)$, K_{st} should be approximately constant. This is exactly what is observed experimentally [6] for the initial agglomeration rate (at later times in the acoustic treatment, the experimental data show that K_{st} increases - this is presumably due to significant modification of the aerosol distribution).

In the above expression for K_{st} it should be noted that $K(A_L, 0)/a(0)$ depends only on the properties of the aerosol and the sound source. As a consequence, results obtained under *static* conditions can be applied under *dynamic* conditions. To do this the (*dynamic*) agglomeration number A_{ac} is written as follows

$$A_{ac} = \left[\frac{K(A_L, 0)}{a(0)} \right] \frac{\tau_{res}}{D} = \left[K_{st} X \frac{P_C}{P} \right] \frac{\tau_{res}}{D} \quad (11)$$

The quantity in square brackets is independent of the configuration (i.e. whether *static* or *dynamic*) it depends only on the basic properties of the aerosol and sound sources. The second term in square brackets can be evaluated from the 'static' experiments ($K_{st} = 0.04s^{-1}$, $X = 1.3m$, $P_C/P \approx 1$). It follows that the residence time, for example, required under dynamic conditions with a plate spacing of $D = 0.5m$, to yield an efficiency of 90% (i.e. $A_{ac} = 2.3$, see previous section) is $\tau_{res} = 22s$. It should be noted here that this high value of residence time is a consequence of the low acoustic power ($\sim 100 W$) used in the *static* experiments [6].

Conclusion

Based on the orthokinetic model of acoustic agglomeration, a mathematical analysis of aerosol flow through acoustic cavities has been presented. The key parameter in this analysis is the dimensionless acoustic agglomeration number A_{ac} which is the ratio of the residence time of the aerosol in the cavity to the agglomeration timescale. The analysis presented allows only for orthokinetic agglomeration. Care should be taken in applying these results to experimental situations where other mechanisms e.g. hydrodynamic, turbulent, may be active. In addition, it has been assumed that only agglomeration occurs in the acoustic cavity and that there is no precipitation to the walls. Based on these restrictions, it has been shown that there is no benefit to be obtained from the use of standing waves. Progressive waves are easier to implement and will result in better agglomeration efficiency than for standing waves. In addition, it has been shown how results obtained under *static* conditions can be related to *dynamic* flow conditions. The *static* experiments are simpler and considerably less expensive to set up in the laboratory than their *dynamic* counterparts which relate to industrial applications.

Infrasound scavenging of aerosol

Introduction

From our experience over the past few years, we know that the agglomeration of micron sized aerosol particles by ultrasound at 20kHz and sound pressure levels between 150 and 160 dB is a fast and effective process. We also have learned the main disadvantage of ultrasound i.e. that the attenuation of the sound wave energy by the aerosol is very high - of the order of 5dB/m at particle concentrations around $10^6 cm^{-3}$. To overcome this problem of attenuation it is clear one should use low frequency sound. But how does this change the speed of the agglomeration process? In the following sections, I present the results of calculations of the coagulation kernel taking account of the particle collision efficiencies at the frequencies of 2kHz, 200Hz, and 20Hz. The results are compared to the same calculations made at 20kHz for which there is also experimental data.

The coagulation kernel

The number of aerosol particles with volumes in the range $v+dv$ in the volume element $d\mathbf{r}$ at time t is given by $n(v, \mathbf{r}, t)dv d\mathbf{r}$ where $n(v, \mathbf{r}, t)$ is the particle distribution function. In general, the balance equation for $n(v, \mathbf{r}, t)$ includes terms for convection, diffusion, evaporation and condensation, source, and coagulation processes. If we neglect, for the moment, the spatial variation of the particle distribution function and consider only the process of coagulation, the governing equation is given by [8]

$$\begin{aligned} \frac{dn(v, t)}{dt} = & -n(v, t) \int_0^\infty K(u, v)n(u, t)du + \\ & \frac{1}{2} \int_0^v K(u, v-u)n(u, t)n(v-u, t)du \end{aligned} \quad (12)$$

where $n(v, t)dv$ is the number of particles with volume between v and $v+dv$, and $K(u, v)$ is the collision kernel i.e. the number of collisions per unit time between particles of volumes u and v . The first term on the right describes the rate at which particles of volume v are 'lost' due to collisions with particles with volume u - for all val-

ues of u . The second term describes the rate at which particles of volume v are 'created' due to collisions between particles of volume u and v , for all values of u (the factor $1/2$ ensures that collisions are not counted twice).

In the orthokinetic mechanism of agglomeration, the acoustic field is used to increase the collision probability between particles of different sizes. The small particles, through viscous coupling with the gas, move forwards and backwards with an amplitude equal to that of the sound wave. The larger particles, due to their inertia, are relatively unaffected by the wave. The resulting differential entrainment leads to an increase in the collision rate between particles.

The coagulation kernel for orthokinetic acoustic agglomeration is given by [8,9]

$$K(a,b) = K(u,v) = \frac{2U_g (a+b)^2 \omega |\tau_a - \tau_b|}{\left(1 + \omega^2 \tau_a^2\right)^{1/2} \left(1 + \omega^2 \tau_b^2\right)^{1/2}} \quad (13)$$

where U_g is the gas displacement velocity amplitude, a and b the particle radii, ω is 2π times the wave frequency f , and τ is the particle relaxation time. In Fig. 10a, the 'geometrical' kernel $K(a,b)$ at 20kHz, has been evaluated for particles of radius a in the range 0.1 to 10 μm colliding with 'seed' particles of diameters of radius $b = 1.5, 2, 2.5, 3, 5, \text{ and } 10 \mu\text{m}$ (the distinction between particles to be scavenged and seed particles is arbitrary - the actual seed particles in a given situation will depend on the aerosol distribution and the frequency of the sound wave).

It can be seen that for particles of radius less than 1 μm , the collision kernel with seed particles in the range 1.5 - 10 μm depends strongly on the diameter of the seed particle but not on the diameter of the particles to be scavenged. Notice also that the seed particles themselves can agglomerate with larger diameter particles with a probability comparable to the that of the agglomeration of fine particles and seeds (primary orthokinetic process). Thus the coagulation kernel for this process has a similar magnitude to that of the primary orthokinetic process - but due to the smaller number of seed particles, the overall rate for this process is less than that for the primary process.

In the derivation of this coagulation kernel two important effects have not yet been considered. The first is the collection efficiency E which arises due to fluid forces. A large particle moving relative to a fluid causes the fluid to flow around

it. A small particle fully entrained in the fluid also has this tendency to flow around the larger particle thereby reducing the collision rate.

The second factor which has been omitted in the above analysis is the refill factor α . If the particle velocities were completely described by the relations given above then all small particle within approximately one amplitude A distance from the large particles would coagulate in the first cycle of the sound wave. Thereafter, there would be no further coagulation due to the fact that the cylindrical volume of length $2A$ and diameter equal to that of the large particle (or the 'reduced' diameter if one includes fluid effects) is now swept clean of small particles. Due, however, to diffusion, convection, turbulence, and additional acoustical effects this volume will refill with particles. This phenomena is characterized by the refill factor α . Including these effects, the coagulation kernel can now be written as

$$K^*(a,b) = \alpha EK(a,b) \quad (14)$$

In the present analysis it is assumed that $\alpha = 1$.

The collision efficiency

The collection of small particles on a collector is governed by the Stokes number Stk . This number is the ratio of two characteristic timescales, i.e. $Stk = \tau_a/\tau$ where τ_a is the particle relaxation time described above and τ characterizes the fluid flow near the collector i.e. $\tau = D/v$ where D is a characteristic dimension of the collector and v the flow velocity. When Stk is small, the particles will follow the streamlines of the flow past the collector. When Stk is large, the particles due to their inertia cannot follow fast changes of streamline direction and will tend to impact on the collector. In the present case, the 'collector' is the larger particle which is not fully entrained in the oscillatory motion of the fluid. The characteristic timescale for flow around such a particle is clearly $\tau = b/|V_a - V_b|$. Hence the Stokes number is given by

$$Stk = \frac{\tau_a}{\tau} = \frac{2\rho a^2 |V_a - V_b|}{9\eta b} \quad (15)$$

The collection efficiency can be expressed in terms of the Stokes number in the form [10]

$$E = \left(\frac{Stk}{Stk + \beta} \right)^\delta \quad (16)$$

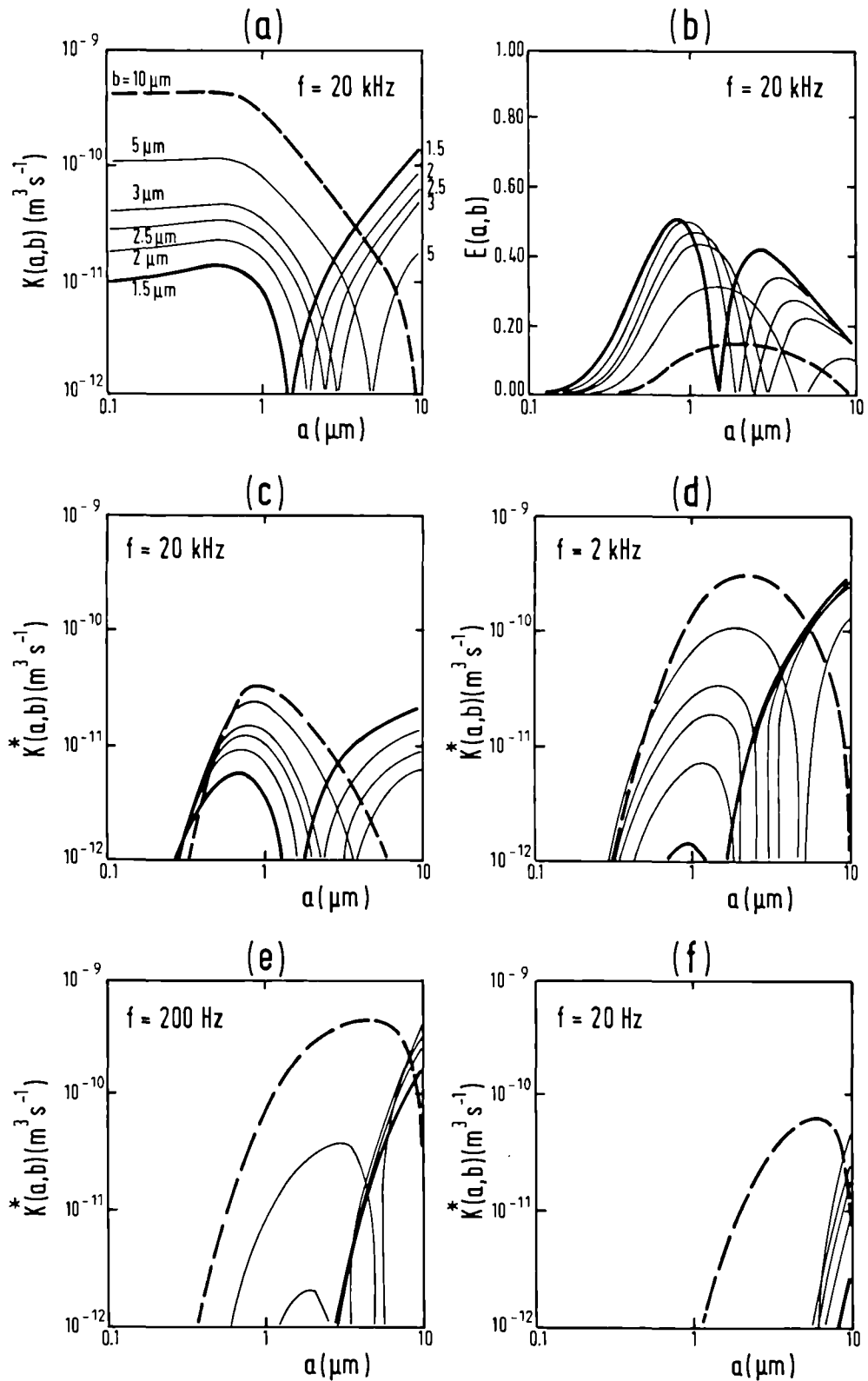


Fig.6.10 Aerosol coagulation and efficiency kernels at $\text{SPL} = 150 \text{ dB}$: (a) geometric kernel K at 20 kHz , (b) efficiency kernel E at 20 kHz , (c) - (f) the coagulation kernels $K^* = EK$ at 20 kHz , 2 kHz , 200 Hz , and at 20 Hz . The thick continuous and broken curves refer to the $1.5 \mu\text{m}$ and $10 \mu\text{m}$ particles respectively. The thin continuous curves refer to the intermediate particle sizes $2, 2.5, 3,$ and $5 \mu\text{m}$.

where β and δ are parameters which can be adjusted to fit the experimental data. For viscous flow around the sphere (Reynolds number $Re < 1$), the data is best fit by $\beta = 0.65$, and $\delta = 3.7$. For potential flow ($Re \gg 1$), $\beta = 0.25$, and $\delta = 2$. For acoustic agglomeration the particle Reynolds number is usually less than 10 such that the viscous flow assumption can be made. The particle collision efficiencies at 20 kHz and 150 dB are shown in Fig. 6.10b. The collision efficiency $E(a,b)$ has been evaluated for particles of radius a in the range 0.1 to 10 μm colliding with 'seed' particles of radius $b = 1.5, 2, 2.5, 3, 5,$ and 10 μm . Clearly, the collisions are strongly dependent on both the radii a and b of the particles. The coagulation kernel data shown in Fig. 6.10c have been obtained by multiplying the geometrical kernel data (Fig. 6.10a) by the collision efficiency data (Fig. 10b). This provides a more realistic kernel for orthokinetic acoustic coagulation. The effect of frequency can be seen by comparing the results of Figs. 6.10c-6.10f where the coagulation kernel K^* has been evaluated at 20 kHz, 2 kHz, 200 Hz and 20 Hz respectively.

A summary of the calculations is given in Tab. 6.1. It can be seen that agglomeration at low frequencies is perfectly feasible within the orthokinetic model of agglomeration provided one uses seed particles as scavenging centres. The agglomeration rate is given by

$$dn(a)/dt \sim -[K^*(a,b)n(b)]n(a) \quad (17)$$

where the quantity $[K^*(a,b)n(b)]$ is the agglomeration coefficient. For reasonably fast agglomeration one requires $[Kn] \geq 0.1 \text{ s}^{-1}$ (i.e. $n(a)$ decreases by more than 60% in 10 s). For seed particle concentrations $n(b) \sim 10^4 \text{ cm}^{-3}$, this requires $K^* \sim 10^{-11} \text{ m}^3 \text{ s}^{-1}$. As can be seen from Tab. 6.1, this can be achieved by suitable choice of the parameters a, b , and f .

Conclusions

It is not sufficient to consider only the coagulation kernel resulting from purely geometrical collisions between particles oscillation in a sound wave. The effects of fluid forces on the particle motion can reduce the geometrical collision rate by orders of magnitude and, therefore, must be included to obtain a realistic coagulation kernel.

Inclusion of the effects of fluid forces in the analysis results in a coagulation kernel which can be extremely sensitive to the particle diameters. In Tab. 6.1, it can be seen that a change of a fac-

Tab.6.1 Sensitivity of the coagulation kernel $K^*(a,b)$ to the particle radii a and b .

Frequency	a(μm)	b(μm)	$K^*(a,b)$ at SPL=150dB (m^3s^{-1})
20kHz	0.5	1	1×10^{-12}
	0.5	10	1×10^{-12}
	1	10	8×10^{-12}
	2	10	4×10^{-12}
2kHz	0.5	1	6×10^{-15}
	0.5	10	2×10^{-12}
	1	10	5×10^{-11}
	2	10	2×10^{-10}
200Hz	0.5	1	3×10^{-19}
	0.5	10	9×10^{-13}
	1	10	3×10^{-11}
	2	10	2×10^{-10}
20Hz	0.5	1	7×10^{-24}
	0.5	10	5×10^{-16}
	1	10	6×10^{-14}
	2	10	3×10^{-12}

tor 2 in the particle radius results in a change of more than one order of magnitude in the value of the coagulation kernel. This extreme dependence on particle diameter needs to be checked experimentally. If correct, it raises the possibility of particle sieving using acoustic fields. Finally, we have shown that infrasound scavenging of micron size aerosol particles is feasible provided one uses suitable seed particles. Agglomeration rates within an order of magnitude of those obtained using ultrasound should be achievable.

References

- [1] J. Somers, Ph. Capéran, Internal Report K0293167
- [2] S. Temkin, R. Dobbins, J. Acoust. Soc. Am. 40 (1966) 317.
- [3] S. Temkin, R. Dobbins, J. Acoust. Soc. Am. 40 (1966) 1016.
- [4] J.E. Cole, R. Dobbins, J. Atmos. Sci. 27 (1970) 426.
- [5] Mednikov, E. P. (1965) *Acoustic Coagulation and Precipitation of Aerosols*. Consultants Bureau, New York.
- [6] Magill J., Ph. Capéran, J. Somers, K. Richter, G. Rodriguez-Corral, E. Riera-Franco de Sarabia, and J.A. Gallego-Juarez, Frequency dependence of the acoustic agglomeration rate of a glycol fog. *J. Aerosol Sci.* 22 (1991) 27-30.

- [7] Magill J., J. McGinley, K. Richter, Akustische Kammer für die Aerosolbehandlung von Abgasen, Euratom patent no. 87850, Luxembourg (1991).
- [8] M.M.R. Williams and S.K.Loyalka, *Aerosol Science Theory and Practice: With Special Applications to the Nuclear Industry*, Pergamon Press, 1991, p. 212-215.
- [9] S. Temkin, unpublished report 1989.
- [10] F. Löffler, *Staubabscheiden*, Georg Thieme Verlag Stuttgart, 1988, p.109-110.

3. Scientific-Technical Support to Community Policies



Introduction

Support to DG XIII

Acoustic Aerosol Scavenging

Introduction

The main aim of this work has been the investigation of acoustic aerosol pre-conditioning as a means to increase the efficiency of an electrostatic precipitator (ESP). These devices are widely used in off-gas cleaning in many industrial processes (power generation, steel production, etc.). Although high separation efficiencies for particles with diameters greater than a few microns are achieved, these devices remove finer particles with diameters less than 1 μm much less effectively. Given the greater health risk posed by such particles, an improvement in their separation efficiency is clearly desirable. Acoustic conditioning of the aerosol induces particle agglomeration so that these fine particles can be separated more effectively by an ESP. The investigations presented here have involved the participation of the Instituto de Acústica, Madrid, and Apparatebau Rothemühle, Wenden, FRG (an electrostatic precipitator manufacturer).

During the course of the year, a proposal for further support of this project was presented to the "Technische Vereinigung der Großkraftwerkbetreiber" (VGB-Forschungstiftung). This proposal was discussed at a meeting with the responsible committee of the VGB (Arbeitsausschuß Luftreinhaltung/Entstaubungs-Anlagen) in Karlsruhe in February 1992. Subsequently modifications as requested by VGB were made and the proposal was re-submitted. A final decision is awaited.

Other proposals for funding of this project were presented to the National Dairy Products Re-

search Centre, Fermoy, Co. Cork, Ireland and to Peiniger GmbH, Leverkusen. The former are interested in improving the separation efficiency of cyclones used in milk-drying process while the latter company wishes to reduce the dust content in the air generated while cleaning surfaces of buildings by sand blasting.

The project "Acoustic Aerosol Agglomeration" was presented on the stand organised by DG XIII at the INTERKAMA exhibition held in Düsseldorf (5-10. Oct. 1992).

Installation for agglomeration tests under dynamic conditions

Experiments to investigate the effect of acoustic pre-treatment of an aerosol on the efficiency of an electrostatic filter were performed in a specially constructed installation [1,2]. Although two sound sources (21 kHz) were located in the acoustic modules (square cross-section of side length 500 mm) most experiments were performed with a single source in operation. The electrostatic precipitator was cylindrical in form (diameter = 400 mm, length = 1.6 m), and was fitted with an axial saw-tooth spray electrode. Flow rates between 150 and 1500 m^3/hr could be achieved. This corresponds to flow velocities of 0.17-1.7 m/s in the acoustic module and 0.33-3.33 m/s in the ESP.

Aerosol generation and measurement

The aerosol was generated by the evaporation and condensation of a commercial liquid marketed under the name Safex. The aerosol has a size distribution which is approximately log-normal with a geometric mean particle diameter, d_g , of 0.8 μm and a geometric standard deviation, σ_g , of 1.4.

Aerosol concentration and size distributions were monitored using a TSI aerodynamic particle sizer (APS) following dilution of the aerosol by a factor of 10000. The aerosol was sampled by a probe (iso-kinetic at 500 m^3/hr) directed into the flow.

Improvement of the separation efficiency of an ESP by means of acoustic pre-conditioning at a flow rate of 560 m³/hr

The particle size distribution of the aerosol was measured under the following conditions:

1. with the acoustic source and ESP switched off
2. with a single acoustic module (21 kHz, 400 Watts) in operation
3. with only the ESP (voltage = 60 kV) in operation and
4. with both the acoustic source (21 kHz, 400 Watts) and ESP (voltage = 60 kV) switched on.

The results are shown in Figs.7.1a and 7.1b in terms of number and mass distributions. The total particle concentration and mass loading of the untreated aerosol were $2 \times 10^6 \text{ cm}^{-3}$ and 1350 mg/m^3 respectively. The data show that acoustic agglomeration induces a re-distribution of the aerosol mass and a concomitant reduction in particle concentration. The efficiency of the electrostatic precipitator, η_{ESP} , and acoustic electrostatic precipitator combination, η_{EAP} , as a function of particle size is then given by

$$\eta(d) = 1 - T(d) \quad (1)$$

where $T(d)$ is the diameter dependent transfer function for any device and is given by

$$T(d) = N_{\text{out}}(d)/N_{\text{in}}(d) \quad (2)$$

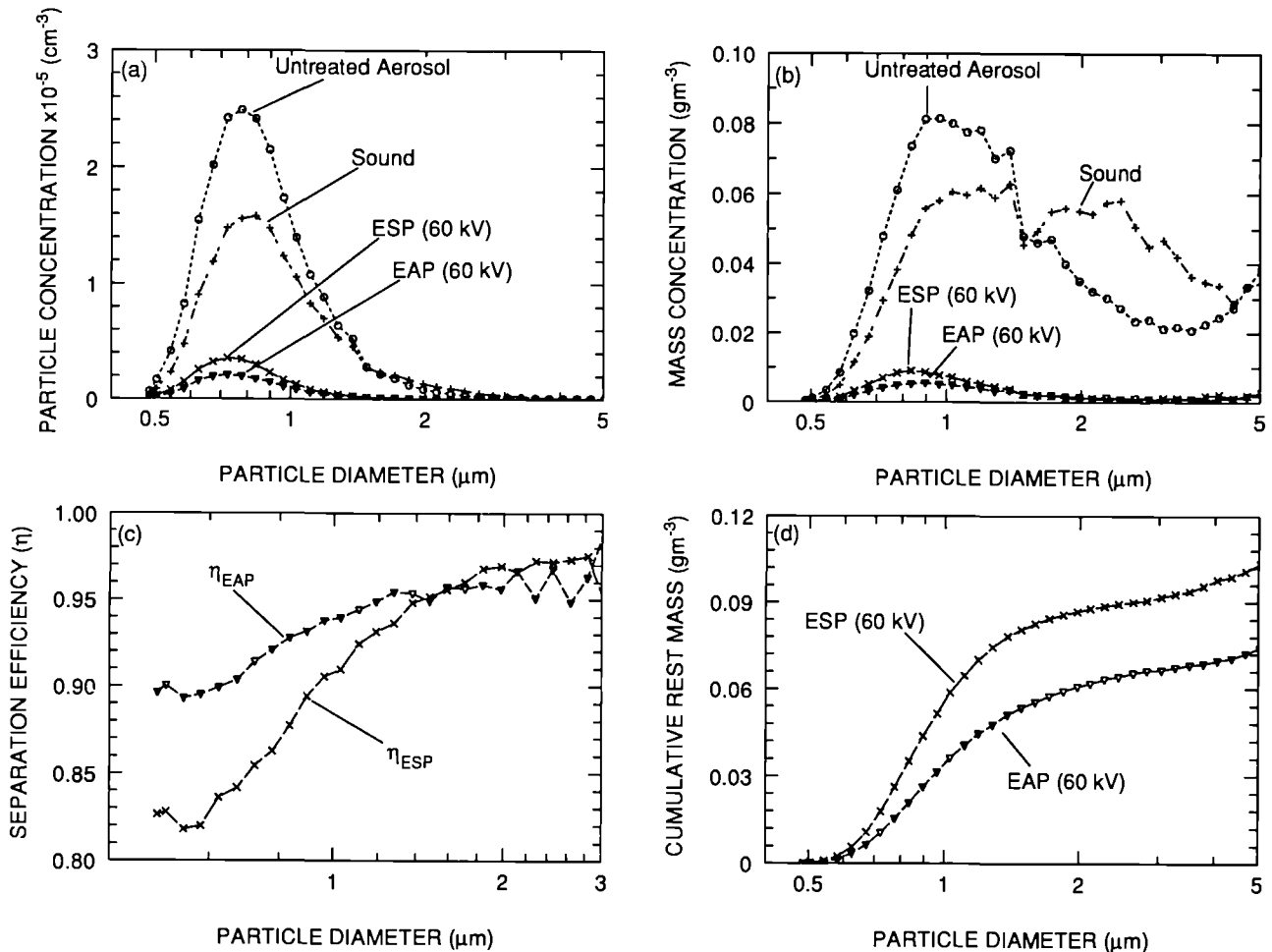


Fig.7.1 Characteristics of an electro-acoustic precipitator operating at a volume flow rate of 560 m³/hr. The particle concentration and mass loading of the untreated aerosol were $2 \cdot 10^6 \text{ cm}^{-3}$ and 1350 mg/m^3 respectively. A single sound source (21 kHz) operating at 400 Watts input power was used.

where $N_{in}(d)$ and $N_{out}(d)$ are the concentration of particles of diameter d entering and leaving the device. The efficiencies of the ESP, η_{ESP} , and EAP, η_{EAP} , determined in this way are shown in Fig.7.1c. Acoustic pre-conditioning of the aerosol increases the separation efficiency of the ESP for 0.8 μm particles from 87 to 92 %.

The cumulative rest mass as a function of particle diameter is shown in Fig.7.1d for the ESP and EAP. The ESP reduces the cumulative mass below 5 μm from 1350 mg/m^3 to 103 mg/m^3 . With the acoustic module in operation, the EAP reduces the rest mass by a further 29 mg/m^3 to 74 mg/m^3 .

Acoustic agglomeration efficiency as a function of particle concentration and flow rate

The agglomeration rate and the residence time of the aerosol in the acoustic conditioning cavity are the key parameters which determine the efficiency of the acoustic agglomeration module. The former depends sensitively on the particle size distribution and concentration, and the frequency and intensity of the sound field, while the latter depends not only on the flow rate but also on the effective length, L_A , of the acoustic treatment module.

Dependence of acoustic agglomeration on particle concentration

Assuming that the main acoustic agglomeration mechanism is the ortho-kinetic effect, the agglomeration rate, dN_t/dt , is given by

$$\frac{dN_t}{dt} = -KN_t \quad (3)$$

where N_t is the total particle concentration and K the agglomeration coefficient. By including the attenuation of sound energy by the aerosol in the above expression, the agglomeration efficiency at short residence times, $\eta_A^0 (= \Delta N/N = -K\Delta t)$, is given by [3]

$$\eta_A^0 = \eta_{sat}^0 \left[1 - \exp(-\gamma L N_t^0) \right] \quad (4)$$

where η_{sat}^0 is the saturation agglomeration efficiency reached when the initial particle concen-

tration, N_t^0 , is high and L is the perpendicular distance in front of the radiating plate in which acoustic agglomeration is effective. The parameter γ is the attenuation of sound by an aerosol with a given size distribution normalised to the particle concentration. Independent measurements [3] made at 21 kHz and low acoustic power give $\gamma \approx 9 \times 10^{-9} \text{ dB}\cdot\text{cm}^2$ for the aerosol used in this work.

The measurements of the agglomeration efficiency, η_A^0 , as a function of aerosol concentration using a single transducer operating at 400 Watts and a flow rate of 560 m^3/hr are shown in Fig.7.2. Fitting of the data to equation 4 gives the effective acoustic treatment length in front of the radiating plate, $L \approx 1.26 \text{ m}$. As the source was inserted into a square cross sectional cavity (side length = 500 mm) at an angle of 60° , the length of the effective acoustic module, L_A , is 0.63 m. Thus a flow rate of 560 m^3/hr corresponds to a residence time of the aerosol in the acoustic cavity of 1.01 s.

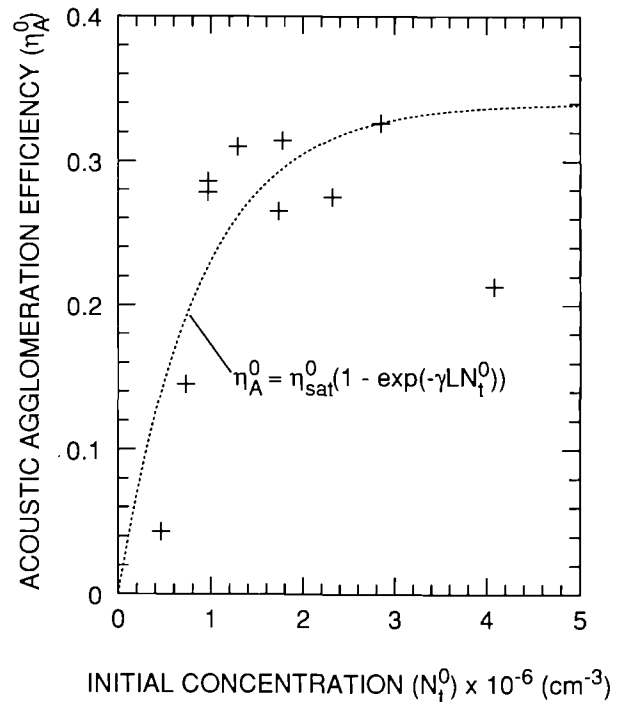


Fig.7.1 Characteristics of an electro-acoustic precipitator operating at a volume flow rate of 560 m^3/hr . The particle concentration and mass loading of the untreated aerosol were $2 \cdot 10^6 \text{ cm}^{-3}$ and 1350 mg/m^3 respectively. A single sound source (21 kHz) operating at 400 Watts input power was used.

Dependence of acoustic agglomeration on the volume flow rate

The efficiency of the acoustic agglomeration module, η_A , in terms of total particle concentration is plotted as a function of volume flow rate in Fig. 7.3. The particle concentration of the untreated aerosol was $2\text{--}3 \times 10^6 \text{ cm}^{-3}$. As two transducers (operating at 250 and 400 Watts) located in separate modules were used, the effective length of the acoustic treatment module was 1.26 m.

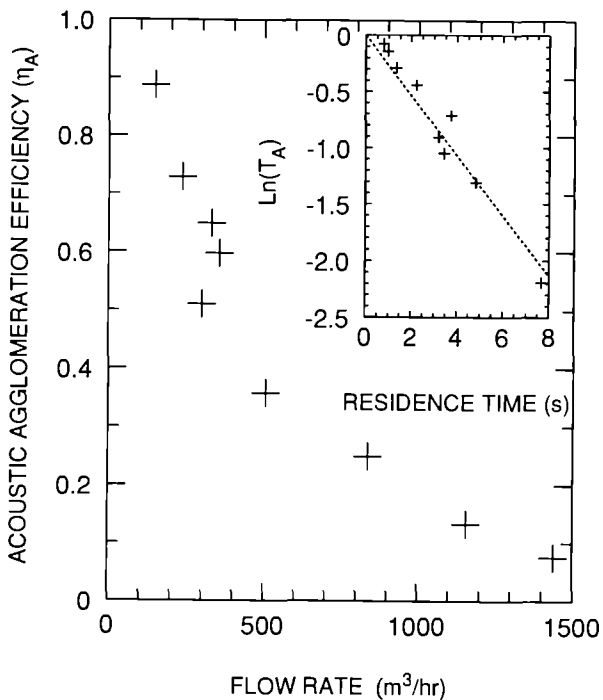


Fig.7.3 Acoustic agglomeration efficiency, η_A , achieved by two sources operating at 250 and 400 Watts as a function of flow rate. The particle concentration was $2\text{--}3 \cdot 10^6 \text{ cm}^{-3}$. In the inset the data are transformed via equation (5) to enable the determination of the agglomeration coefficient, K .

Integration of equation (3) gives

$$\ln\left(\frac{N_{\text{out}}}{N_{\text{in}}}\right) = \ln(T_A) = \ln(1 - \eta_A) = -Kt \quad (5)$$

where T_A is the transfer value of the acoustic module in terms of the total particle concentration. A plot of $\ln(T_A)$ versus the acoustic treatment time, t , shown in the inset to Fig.7.3,

yields a straight line of slope $K = 0.27 \text{ s}^{-1}$. That K is approximately one order of magnitude higher than the value obtained previously in experiments made under static conditions [4] is expected for two reasons. First, the static experiments were performed at lower input power (100 Watts as opposed to 400 and 250 Watts in the dynamic experiments). Secondly, the effect of dilution due to the ratio between the effective acoustic treatment volume and the volume of the experimental chamber reduces the value of K determined in the static experiments.

Efficiency of the ESP and EAP as a function of flow rate

The efficiency of the ESP as a function of flow rate is shown in Fig.7.4. (The particle concentration of the untreated aerosol was $2\text{--}3 \times 10^6 \text{ cm}^{-3}$ and the ESP was operated at a voltage of 40 kV).

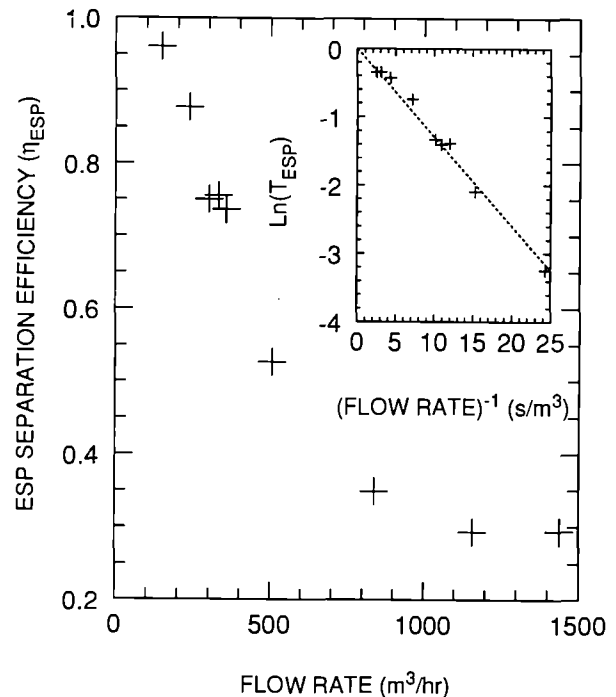


Fig.7.4 Efficiency of the electrostatic filter, η_{ESP} , at an operating voltage of 40 kV as a function of flow rate. The particle concentration was $2\text{--}3 \cdot 10^6 \text{ cm}^{-3}$. In the inset the data are transformed via equation 7 to enable the determination of the drift velocity, w .

A theoretical expression for the efficiency of an electrostatic precipitator is given by the Deutsch equation

$$\eta_{\text{ESP}} = 1 - \exp \left[-wA_{\text{ESP}}/V \right] \quad (6)$$

where A_{ESP} is the surface area of the collection electrode (2.1 m^2), V the volume flow rate through the filter and w the drift velocity of the charged particle in the electric field. Rearrangement of equation 6 gives

$$\ln(1 - \eta_{\text{ESP}}) = \ln(T_{\text{ESP}}) = -wA_{\text{ESP}}/V \quad (7)$$

where T_{ESP} is the transfer value of the ESP averaged over the particle size range measured. A plot of $\ln(T_{\text{ESP}})$ against $1/V$ yields a straight line of slope $-A_{\text{ESP}} \cdot w$ (see inset to Fig.7.4). Given the collection area of the filter, an average value of $w = 6 \text{ cm/s}$ is determined.

As discussed above the redistribution of the aerosol mass achieved by acoustic aerosol conditioning increases the efficiency of the ESP. It is possible to calculate the expected efficiency of the electro-acoustic precipitator assuming that the characteristic transfer functions of the acoustic and ESP modules combine linearly. Thus

$$\eta'_{\text{EAP}} = 1 - (T_{\text{ESP}} \cdot T_{\text{A}}) \quad (8)$$

where η'_{EAP} is the calculated efficiency of the EAP. As shown in Fig.7.5, the measured efficiency of the EAP as a function of flow rate is higher than the value derived using equation (8)

There are at least two secondary effects which could cause this behaviour. First the redistribution in mass caused by the acoustic source increases the probability of inertial losses in the duct. In the data presented here, however, this was not the case. Secondly, the particle concentration decrease achieved by acoustic treatment of the aerosol decreases the space charge in the filter. This causes the effective electric field at the spray electrode to increase, which in turn improves filtration efficiency even though the mass loading remains constant. The increased current drawn by the filter when the acoustic source is in operation (see Fig.7.6) indicates that the space charge is indeed decreased when the aerosol is subjected to acoustic pre-treatment.

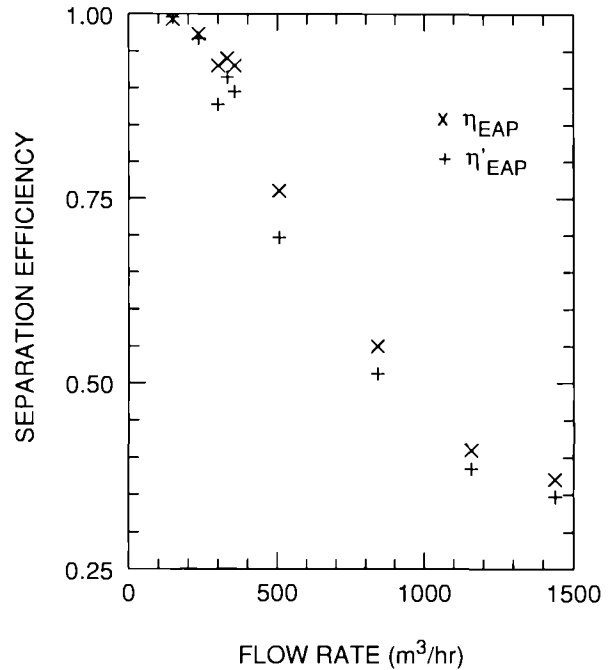


Fig.7.5 Comparison of the measured, η_{EAP} , and calculated, η'_{EAP} (see equation (8)), efficiency of the electro-acoustic precipitator as a function of flow rate. The particle concentration was $2\text{-}3 \cdot 10^6 \text{ cm}^{-3}$ and the ESP was operated at a voltage of 40 kV.

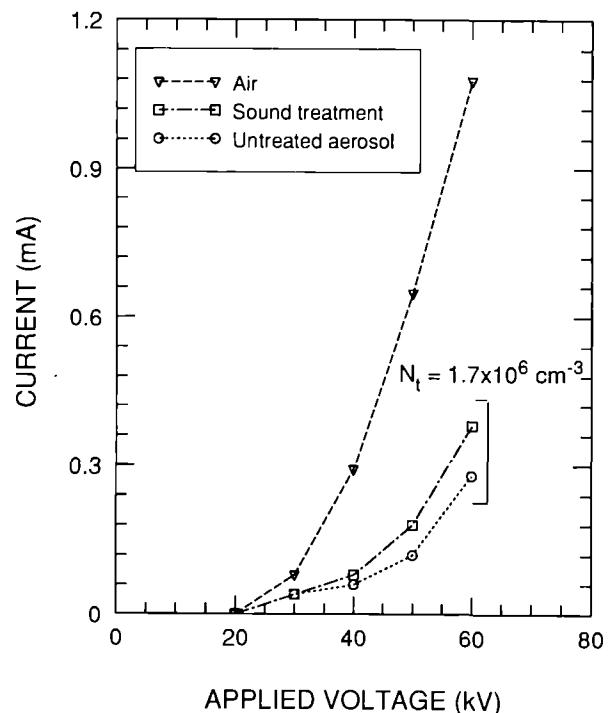


Fig.7.6 Current - voltage characteristic of the ESP in air and in aerosol with and without acoustic pre-conditioning. The flow rate and particle concentration were $560 \text{ m}^3/\text{hr}$ and $1.7 \cdot 10^6 \text{ cm}^{-3}$ respectively.

Conclusions

These experiments have shown that treatment of an aerosol with sound can induce a significant increase in the efficiency of an electrostatic precipitator. The efficiency of the ESP and acoustic agglomeration modules exhibit a similar dependence on the volume flow rate. Under these experimental conditions, about 1 kW of acoustic power per 1000 m³ of treated gas would be required to increase the particle separation efficiency of the ESP from 90 to 95%.

Future investigations on the acoustic agglomeration of both liquid and solid aerosols will concentrate on the influence of the applied frequency and standing waves on the agglomeration rate. A new aerosol measurement device will enable the characterisation of the effect of sound treatment on respirable particles with diameters lower than 0.5 µm. The results should make possible the design of an optimised acoustic cavity and the means to predict the optimum frequency or frequencies to agglomerate a given aerosol. With this information, scaling the process up to capacities of 10-20000 m³/hr and installation under industrial environments *vis-a-vis* high temperature, corrosive gases etc. is a medium term aim.

References

- [1] TUAR 90 page 160, TUAR 91 page 192
- [2] J. Magill, Ph. Capéran, J. Somers, K. Richter, S. Fourcaudot, P. Barraux, P. Lajarge, E. Riera Franco de Sarabia, G. Rodriguez-Corral, J.A. Gallego-Juarez and N. Seyfert, *J. Aerosol Science* **23** (1992) 803
- [3] J. Somers, Ph. Capéran, Internal Report K0293168
- [4] J. Magill, Ph. Capéran, J. Somers, K. Richter, E. Riera Franco de Sarabia, G. Rodriguez-Corral and J.A. Gallego-Juarez, *J. Aerosol Science* **22** (1991) 27.

Support to DG XVII

On-Site Laboratories

Progress of the Sellafield on-site laboratory

Introduction

The reasons lying behind the development of a Nuclear Safeguards Analysis laboratory on-site at Sellafield were outlined previously (TUAR 91, 168). The progress made this year will be given here.

Design

The final design was completed and provides the basis for the safety applications which have to be made subsequently for the construction of the laboratory. In this design the layout of the laboratory has been defined as have the services required, the apparatus including the glove boxes provided by the Institute, the procedures to be followed and the number of samples to be analysed. Clearly some of these parameters are estimates and will be more accurately defined later, but the application for laboratory construction will be based on this design.

Construction application

A pre-construction safety case will be made on our behalf by BNFL in the course of next year. A main part of this is the 'hazards of operation' study (HAZOP), in which the services and construction are viewed in a formal manner for the consequences following possible malfunctions, accidental or not. A large number of details were required for this study involving the processes in the glove boxes and the services and connections to the glove boxes in particular. Procedures have been written for all forms of analysis and also for diverse actions such as receipt of samples and disposal of waste. The procedures as submitted are accepted as defining the actions to be carried out in the laboratory. Changes to the procedures which will inevitably occur following experience in the methods and

other design changes must be declared formally and possibly incur new HAZOPs studies.

Apparatus testing and development

Development is being carried out in four areas:

- testing of the input (IDMS) glove box,
- implementation of NDA apparatus,
- construction of a glove box for titration and NDA,
- development of the computer system.

1. The glove box for IDMS conditioning of input samples has been in use in routine measurements whereby the weakness of the design and areas necessary for improvement in particular have been looked at. Details of the component testing are given below.
2. A combined neutron coincidence/gamma spectrometer for PuO₂ samples has been installed. Details of a joint international experiment to characterise the detector system are given below. The K-edge absorptiometer has also been improved: the computer program has been improved, a quality control system which checks the value of a number of experimental parameters has been introduced and a second gamma detector for determining the Pu isotopes was installed.
3. The data access system for the calculation of the results of the analysis has been extended. It is expected that this system can replace the present dependence on the main-frame computer early next year. The connection between the automatic titration apparatus and the central lab computer has been finished and results are routinely sent by this route. This and the other computer developments are dealt with in more detail later in this article.
4. The glove box for the titration, including K-edge absorption, neutron coincidence / gamma spectrometry and dissolution of solid samples is under construction. The necessity to have all these functions in one box in a relatively restricted area has meant that several compromises have had to be made. This glove box will be completed early next year and tested with U and later Pu material.

The state of development is dealt more fully below.

Training of personnel

In March 1992, theoretical training for the "Laboratoria In Situ (LIS)" personnel started. Weekly lectures or seminars followed by discussions as well as theoretical exercises have been held. During the theoretical and the practical courses material related to the different lectures and exercises was distributed to the participants in order to let them take part in discussions and to test their level of understanding.

During the first part of the theoretical course, the topic "*fuel cycle*" was discussed.

The main characteristics and operational functions of nuclear reactors have been illustrated, with regard to the reasons by which a change in reactor operation can influence the nature of the sample after irradiation.

Reprocessing treatment as well as operational modes of reprocessing plants, in particular the plant in Sellafield, were also covered.

At the end of these lectures a visit was made to the "*Nuclear Technology*" laboratories of the Institute, where ceramics and fuel rods for reactors are prepared.

Introductory lectures on the general inorganic chemistry of uranium and plutonium and some of their most important compounds, on their chemical separation and on the analytical techniques used for their determination were given. The basic principles of nuclear chemistry were also revised.

The goal of the introductory part on chemistry, since the background knowledge of the LIS crew was quite heterogeneous, was to arrive at a basic knowledge of chemistry.

The personnel more skilled in chemistry have been requested to prepare short, but more detailed notes on some of the subjects discussed during the lectures.

During the second part of the course, started on 21 September and which will finish in 1993, the analytical techniques and procedures used in the LIS, such as: titration, mass-spectrometry, non-destructive analysis (K-edge and hybrid K-edge, neutron counting), α - and γ -spectrometry, are being discussed in more detail. Attention will also be given to the technical characteristics and performance of the instrumentation employed in the LIS with particular attention to the operator difficulties.

The experts of the four methods employed in the LIS (titration, non-destructive analysis, IDA, and mass-spectrometry), under the guidance of the Institute staff are preparing manuals of

these procedures, to be available for all the LIS team, so that all the personnel have the necessary information and knowledge of the procedures employed in the LIS.

For the operators of each different technique, specialised practical training courses held by the Institute staff and external experts, have been also started.

A four-day (30 June - 3 July 1992) specialised course was held by Canberra-Packard staff, concerning the use and maintenance of the K-edge and hybrid K-edge apparatus. In this course software and hardware principles as well as the electronic component operations were explained to the participants from a theoretical as well as a practical point of view. The LIS personnel which will concentrate on this technique are continuing practical experiments in our laboratories in the framework of different programmes to improve their skill before starting, in September 1992, the maintenance of the K-edge installed in La Hague.

French language courses, at two different levels of knowledge, have been organised in-house for LIS personnel from October 1992.

In the Institute, the work for three LIS teams, each composed of four operators, has been organised simulating the actual operational situation in the on-site laboratories. A weekly meeting is held where both the leader of the team operating during the current week and the leader of the team which will operate in the following week participate. This is in order to discuss the problems which might arise and to improve the organisation and coordination between the different teams.

Development of components

Construction of a portable compact K-edge absorptiometer

Following a request from DCS Luxembourg, a transportable glove box for a compact K-edge apparatus has been developed. The glove box is for DCS inspectors to determine U concentrations in solutions at reprocessing sites. The device contains the following:

- two fingers in the glove box base projecting under the box for the K-edge and gamma spectrum measurements,

- a light construction so that it is transportable in a relative small van,
- all necessary equipment, including computers, detectors with liquid nitrogen cooling, nuclear electronics, apparatus for measurement of density, vacuum pumps etc.

The equipment must be stable enough to withstand transport shocks. Aluminium has been used for most of the construction: for the glove box frame and base and glove rings as well as the dewar supports. The glove box base and fingers are made of stainless steel for strength. The glove box panels are made of polycarbonate because of its strength. Under the table, wheels are provided for transport and feet to stabilize the box during the measurements. The detectors are swung into the measurement position by a system which allows the operator to do this easily. The apparatus is then locked in position. The ability to do this was found very important for the transport and also to allow a detector to be changed if defect.

Inside the glove box, racks are provided for sample vials and cuvettes. Tools including pipettes, tongs etc. for the chemical manipulations are kept in a small, lockable, stainless-steel box for the transport. The glove box panels are also protected during the transport by metal plates which are held in position by screws. Samples are bagged in and out of the glove box.

At present the glove box is in the final construction stage: late delivery of detectors has caused a delay. After construction and testing of the apparatus it will be taken to La Hague for testing on-site.

A further box has been requested by DCS, somewhat larger and including a balance, densitometer and a microwave oven for dissolution of solid samples.

Expert system for the evaluation of safeguards measurement results

An expert system has been developed to evaluate analysis results. The system is under test at present.

The system is installed on the central MicroVAX computer where all the measurement results of the analyses are collected (isotope measurements from mass spectrometry, element concentrations from titration, isotopes measured by alpha spectrometry and the calculated precision of measurement). The tests are made on the data of the current measurement. After the

measurements, the expert system gives diagnostics on their validity. The verdict is then put to the analyst for validation. If the results are not accepted the output of the expert system can be used to isolate the measurement error.

In the present version, the expert system is built from a set of about 200 rules divided into categories dependent on their function. There are 4 principal groups of applications associated with the different analytical methods and elements analysed. In our case, isotope dilution mass spectrometry (IDMS) and potentiometric titration are the methods utilised for U and Pu. The knowledge rules of the expert system embrace the following categories:

- elements and isotopes measured,
- techniques and instruments utilised for the measurements,
- results from the individual instruments,
- measurement precisions from the instruments,
- results and precisions calculated by the database program on the VAX,
- acceptable limits for the measurements and their precisions,
- error diagnostics.

The expert system operates by determining the set of rules for a sample analysis and applying them to obtain a diagnostic statement. In the present state of development the system can produce statements to the effect that a particular measurement should be repeated or that the measurement conditions should be altered to obtain more satisfactory conditions. The intrinsic quality of the measurements cannot at present be judged because only the measurement values are transmitted. However in the future supplementary information will be transmitted to the results database pertaining to the condition and trustworthiness of the measurement. This will permit the expert system to have access to this information and with the aid of new rules form a judgement of the standard of the measurement.

After installation, initially for IDMS results, the expert system has been extended to include the results of titration for U and Pu. Other methods, such as non-destructive techniques and K-edge absorptiometry will be included next. The system will function the same, however with a wider application range.

The ability to call up results according to specific criteria, e.g. measurement type, means that statistical tests can be built in to the system. At present this is being applied to the

quality control of standard materials. Control charts of the measured values are automatically produced to allow trends and outliers to be determined. The expert system can also call on mathematical routines or statistical tests. It is planned, for instance to apply tests to a series of measurements to detect outliers. It is expected also to be able to consider the standard deviations obtained for a measurement method from the analyses and by comparison with other results determine for instance the presence of contamination, resulting for example in the advice to check a glove box, or deterioration in a particular instrument which should be checked and serviced. The expert system cannot do this at present but it is hoped to introduce this feature in the near future.

Data evaluation on the safeguards measurements

The new evaluation system for Safeguards measurements: the data collection via a PDP-11/73 computer and storage and evaluation on a MicroVax was described previously (TUAR 91, 174). It has been extended to include new types of analysis and the calculation of existing types has been refined. Special procedures for quality control measurement results have been developed.

The measurement data from titration is now automatically transferred to the data acquisition system. An improved method of correction of the titration data has been incorporated.

The results of the calculations on the MicroVax are being compared with those calculated on the main-frame IBM 3090 computer and are now being tested to ensure errors have not been made in the calculation programmes. The results are produced in such a form that they can be sent directly to Luxembourg using the electronic mail connection and it is envisaged that the results will be exclusively calculated on the MicroVax at the start of next year.

A system of costing has been included to allow an overview of hours worked and a check on the time spent analysing a sample in the Institute. Various monthly or yearly reports are possible. Preparations are being made for further statistical evaluation of the measured data. The necessary information is made available for example as a weekly report of work completed for Safeguards measurements. It is planned to make this an automatic part of the system in the future.

A program system to train personnel who need to use the database system has been written. It is separate from the system used for routine measurements and has its own account. The operator undergoing training does not have access to the full system for security reasons. A manual with instructions for the training system has also been written. Operators can thus be made conversant with the system before using it on current data.

The system will be developed in the following year to widen the quality control measurements, to include calculations of error propagation and to extend the system to other types of measurement. The Vax will be linked to the laboratory network for the transmission of results.

Progress of the La Hague (LSS) on-site laboratory

Introduction

Since May 1992 representatives of COGEMA, SGN, of the CTI, DCS, Luxembourg and this Institute have met several times to discuss and define the on-site laboratory (LSS) which is planned to be built in the reprocessing centre of COGEMA at La Hague to carry out analytical measurements in the frame of Fission Material Control. The start of the laboratory is foreseen for the end of 1996.

General agreement was made on the following points:

- the type and number of samples to be analysed,
- the equipment necessary for this task,
- the analytical methods to be employed,
- the infrastructure requirements.

The laboratory is conceived to analyse a total of about 1000 samples per year, from the reprocessing units UP3 and UP2-800. For obvious safety reasons a layout similar to that planned for the on-site lab at Sellafield and to that in the analytical laboratory at Karlsruhe has been retained. However some changes to the analytical methods to be employed had to be made to respect the regulations in force at La Hague: the determination of U and Pu by potentiometry has been replaced by gravimetry, and the separation of U and Pu by solvent extraction for IDMS by ion exchange.

The non-destructive methods have been given

priority to minimise the liquid and solid wastes produced by the LSS.

Conception

The LSS comprises the following :

1. A high active area with 3 hot cells and associated equipment:
 - In the first cell U and Pu from the 'cuves d'adjustage bilan' (500 per year) and the preceding part of the production (120 per year) from the UP3 and UP2-800 units are measured using a hybrid K-edge apparatus.
 - The second cell is foreseen for treatment of waste from the measurement process and for excess material.
 - The third cell is for the analyses by hybrid K-edge apparatus for U and for Pu in solutions of Pu nitrate (200 per year) from the dissolution of aged Pu material.
2. An area of lower activity where a chain of glove boxes is installed:
 - A box in which an analytical robot is used for the preparation of diluted samples for isotopic analysis.
 - A glove box for the analysis of Pu in Pu oxide (200 per year) by neutron/gamma counting and gravimetry.
 - A glove box for dissolution of MOX samples from the MELOX unit, for subsequent IDMS analysis.
 - A glove box for analysis of U nitrate by K-edge absorptiometry (140 per year).

The LSS will be constructed in two storeys of the annex of the central UP3 building. It will be 370m² in size, not including services and changing rooms.

Conclusion

The project to construct an on-site laboratory at La Hague is in the first design phase with the goal of defining as well as possible everything which is necessary for the construction of the laboratory and the limits of responsibility and the interfaces between COGEMA, SGN and EURATOM.

Data transfer between mass-spectrometers and PDP 11/73

One of the main parts of the on-site laboratories which promises to bring advantages of reliability and control of the measurements is the integration of the mass-spectrometers into the laboratory computer system. This has been foreseen both for input to and output from the mass-spectrometers via serial connections to the central PDP 11/73 computer. Three mass-spectrometers (Finnegan-MAT) are installed at present, each with a Hewlett-Packard PC for real-time control of the measurement procedures, calculation of results and their transmission to the central computer.

The mass-spectrometers analyse samples deposited on filaments either manually or automatically by an analytical robot. In the latter case all the information concerning the sample is stored on the central computer and then inputted manually to the mass-spectrometer by the operator before starting the analysis. A computer program has now been written which sends the data automatically from the central computer to the mass-spectrometer, thus eliminating possible errors arising from the manual input of data.

The results from the mass-spectrometer are held on disk on the mass-spectrometer control computer and are subsequently transferred to the central laboratory computer.

At present three communication lines to the PDP 11 are permanently occupied for the transfer from the mass-spectrometers and three identical applications programs for the transfer (one for each mass-spectrometer) run on the computer. These programs must always be ready for data transfer and take up computer resources, thus slowing its response time. For this reason a program has been written which combines the functions of the individual programs, thus minimising system resources on the PDP 11.

In this new scheme the output from each mass-spectrometer is brought into an input on a 8-line asynchronous multiplexer on the PDP 11. One of the methods provided by the TSX-Plus system to service interrupts for non-standard devices has been utilised. (TSX-Plus provides a real-time program support facility that allows multiple real-time programs to run concurrently with normal time-sharing operations.) As a result no communication lines are occupied and only one application is running at a time. Moreover, the application is active only when a mass-

spectrometer is actually sending or receiving data, its execution being suspended in between. When an interrupt caused by a mass-spectrometer occurs, the program identifies which line is interrupting and proceeds then to accept or send data according to the request of the mass-spectrometer. All data are transferred in blocks. At both ends of the transmission line checksums are performed to insure that the transfer was correctly effectuated.

If a mass-spectrometer sends an interrupt while the PDP is serving another line, the occurrence of the interrupt and its line identification are recorded to allow the PDP, once free, to service the new request automatically.

The program has led to an improvement in response of the central PDP-11 computer to the data transfer from the mass-spectrometers used for measurement of U and Pu isotope ratios.

Testing of components for the on-site laboratory

Two of the glove boxes which will be installed in the on-site laboratory, Sellafield are in the later stages of development. The glove box containing an analytical robot for the IDMS procedures is being extensively used and tested on real samples and the glove box for the titration and NDA analysis of product samples is in the final design stage.

The components, apart from the robots themselves, which are set up or constructed in the Institute are made to undergo a series of tests to prove their ruggedness before the installation in the on-site laboratory.

Tests have been made on the following components in the IDMS glove box:

- provision of vacuum to the alpha chamber,
- dispenser and vortex mixer,
- filament preparation.

The time required to reach an adequate vacuum for the alpha counter was found to be longer than 1/2 hour. Because the procedure has to wait for the alpha spectrometer results before calculating the optimum amounts of solution to be placed on the mass spectrometry filaments, the waiting time extends the whole procedure. Tests showed however that the alpha chamber itself and the vacuum connections were leak tight and that the only method of reducing the vacuum was to shorten the lines between the pump and the alpha chamber.

The method was therefore changed so that an initial count is made on the planchettes,

sufficient to determine the concentration of the solution and when the vacuum is sufficient, a longer count is made for the alpha spectrum.

By the dispenser, which supplies under robot control measured amounts of nitric acid, and also TBP solution for the extraction, it had been found that the connecting tubing was leaking and that drops of the solutions were falling onto the floor. The system was redesigned, using teflon tubing (resistance to organic solution) and by having a drop catcher under the dispenser, leading directly to waste reservoirs.

The filament preparation device is crucial for the overall reproducibility of the IDMS method. The deposition of the drops and the drying was optimised. Multiple tests were carried out to ensure that the drops were deposited adequately and for the first time video cameras were installed to record the procedure. Thus the deposition of drops on individual filaments could be controlled later. The application of video cameras has been found to be very useful and it is being seriously considered that such cameras be installed permanently to control critical points of the procedure, such as extraction or filament preparation.

Two components of the titration box in particular have been investigated. An alternative washing procedure using simple manipulations with the robot was introduced for the polyethylene titration beakers. These beakers are reused and must be cleaned of all traces of the previous titration. The wash method conceived initially involved a spray method which however used too much water thus causing waste problems and did not meet the highest criteria of reliability. The new wash method was tested and proved adequate. The total amount of liquid waste per titration is reduced to 80 ml with this method.

The AgO dispenser has been tested by dispensing and weighing with the robot in overnight runs. The precision of dispensing was shown to be sufficient for the titration procedure.

Maintenance of the Hybrid K-Edge Apparatus at La Hague

The maintenance of the hybrid K-edge absorptiometer, installed in November 1989 in the reprocessing centre, La Hague, to allow the

independent analysis of U and Pu in dissolver solutions of the UP3 unit, has been carried out regularly by personnel of the Institute each month.

A change of the Cd-109 source was deemed necessary because its activity ($T_{1/2} = 462$ d) had become too low to be used for the stabilisation of the K-edge spectrum.

A break in the cooling supply pipe for the X-ray generator required service by the manufacturer (Canberra).

The electronic parts were moved behind the hot cell, following a request of COGEMA. COGEMA expects thus to be able to build a new hot cell for the reception of the UP3 and UP2-800 units.

None of these problems disturbed significantly the Safeguards measurements.

Two members of the teams for on-site measurements have been trained specifically for the measurement techniques with this type of apparatus at the Institute and the central laboratory at La Hague and have begun regularly to travel to the La Hague centre to check the correct functioning of the apparatus and to discuss with EURATOM inspectors possible problems which occurred.

International Experiment to Test the Application of a Neutron Coincidence Counter - Gamma Detector for the Measurement of PuO₂ Samples

Introduction

A major part of the samples measured in the planned on-site laboratory at Sellafield will be done non-destructively. Only about 10 to 20% of all samples will be destructively analysed. Plutonium oxide samples in gramme quantities are traditionally measured by calorimetric or neutron coincidence methods. A development new to this design was to measure the total Pu by a combination of neutron coincidence and gamma spectrometry, whereby the neutron coincidence would measure the ²⁴⁰Pu equivalent and the gamma spectrometry the Pu isotopic vector and thus allow the total Pu to be calculated.

The design was a development of standard neutron coincidence detection with the geometry of the neutron detectors so arranged that a high purity germanium gamma detector (HPGG)

could be brought close to the material and simultaneously measure the gamma spectrum. The electronics of the neutron detector would use the shift register, JSR-12 design of Los Alamos and the gamma spectrometer the program MGA to determine the Pu isotopics.

The tested apparatus will be installed in-situ under the so-called titration box, where Pu product samples will be measured by titration, K-edge absorptiometry/gamma spectrometry and n-coincidence/gamma spectrometry. To test the capabilities, an experiment was designed and a special glove box constructed for the instrument. Samples of PuO₂ were prepared and sealed in plastic (polyethylene) and stainless-steel screw-capped vials at IRMM Geel. The experiment described here concerned the measurement of these samples and comparison with the certificated values provided by the Institute for Reference Materials and Measurements, Geel.

The experiment was carried out with the cooperation of workers from LANL, DCS Luxembourg, IRMM Geel and with observers from Canberra Electronics and JRC Ispra.

Experimental

The layout of the counter is shown in Fig.7.7. The 18 He-3 neutron detectors are arranged vertically in high density polyethylene to thermalise the neutrons and improve their detection. The HPGG detector is also mounted vertically so that it views the underside of the sample which is inserted in a well or finger in the floor of the glove box. The sensitivity of the neutron detectors was specified to be constant over a length much longer than that of the vials to render the counter relatively insensitive to the sample position and size. Liquid nitrogen cooling, required by the HPGG detector was provided to the detector by a cryostat finger of unusual geometry to fit the positioning of the neutron tubes. The counters and mounting were provided by Canberra Electronics.

15 samples of various weights were provided by IRMM: 10 in polyethylene and 5 in stainless-steel vials. At the time of the design

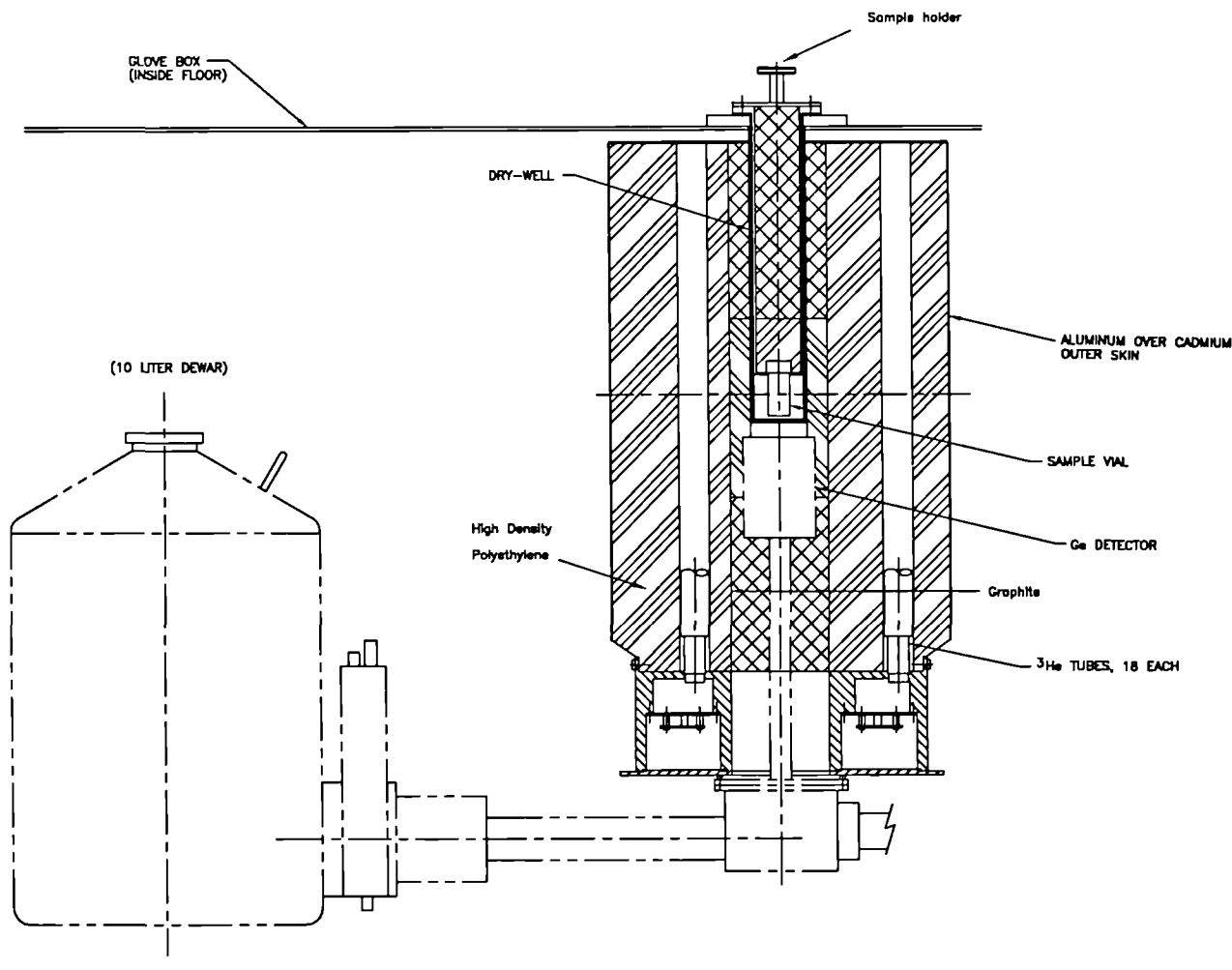


Fig.7.7 Layout of the neutron-gamma counter under the glove-box.

specification it was not certain which material would be used at Sellafield and it was deemed useful also to measure the sensitivity of the neutron counter to the vial material. The overall accuracy on the mass of PuO₂ in the vials is specified as 10⁻⁴. The isotopic abundances of the Pu was also specified by IRMM.

Neutron counting

Vials were brought into the glove box and stored in borated high-density polyethylene to reduce background effects while counting. Initial experiments had shown effects on the 0.1% level from samples held in the glove box. All samples were counted for about 10 hours. The software counted a sequence of 30 second counts so that post-counting statistics could be used to remove outliers. Over such periods of time, statistical errors down to 0.1% were obtained for the samples over 4 g in weight.

The purpose of the long counts (10 hours) was to determine the ultimate accuracy of the method against the certified values. Short counts of 2 to 4 hours were also carried out to investigate the effect of sample changing, of packing effects in the powder samples, of geometrical effects in the filling of the capsules and positioning effects from loading the vials. No statistical positive effects were found from the above listed causes, although this does not rule out effects at the 0.1% level. Variations at this level will be investigated later. A later trial was also made with the addition of moisture to a vial to check the sensitivity of the method to the presence of H₂O.

Throughout the experiment the weights of the vials were measured relative to a blank vial and compared with those specified at IRMM Geel. A change in weight at the beginning of the experiment was assumed to be from moisture losses in the vial labels due to the different atmospheres in the glove boxes here and in Geel.

An initial fit of the real or coincident neutron counts to the certified PuO₂ contents was made for the sample in plastic vials: the curve is given in Fig.7.8. The fit shows a slight quadratic function arising from neutron multiplication effects in the samples: A maximum effect is found at about 5 g content, when the height of the powder in the vials equals that of the width. Above this value, extra PuO₂ contributes proportionately less to the neutron multiplication. The fit is good, yielding a

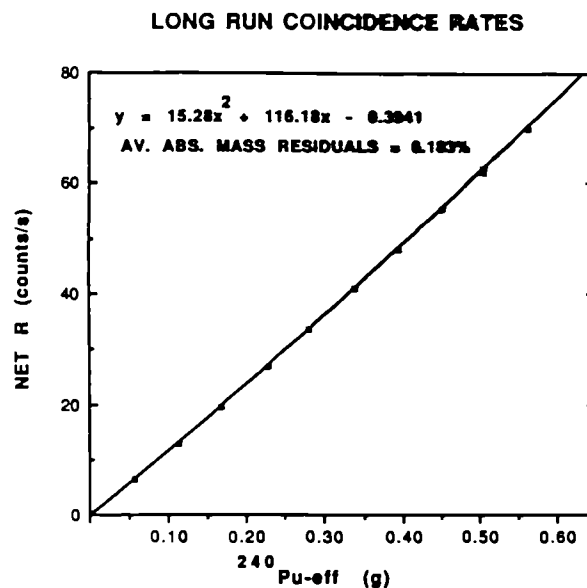


Fig.7.8 Count-rate (reals) as a function of effective ²⁴⁰Pu

predicted error for PuO₂ weight at the centre of the curve of 0.183%. The statistical error is 0.147% which demonstrates that other error sources are less than 0.1%.

Gamma counting

Gamma spectra were accumulated during the experiment. The Pu isotopes were the same for all samples and of an unusually high enriched ²³⁹Pu compared with samples expected in the situation of a reprocessing plant. The isotopic vector calculated by MGA was quite satisfactory however. During the gamma counting, the detector exhibited instabilities which prevented it from reaching the resolution expected. It was suspected that the cause was moisture accumulating in the preamplifier which is mounted by the detector to reduce noise but which is therefore thermally isolated by the polyethylene shielding of the neutron detector.

A further problem which has yet to be addressed is the gamma contribution from ²⁴¹Am - which is expected to be much higher in 'real' reprocessing samples than in the standards used in this experiment. To reduce the deadtime in the detector, shielding of indium or tin will be used. This shielding will have a relatively small effect on the neutron counting. However the size of this effect will have to be determined.

Conclusions

The neutron counting on a series of standard samples showed that the goal of measuring total Pu to better than 1% by this method will very likely be achieved. Under the circumstances of this experiment, typical accuracies of < 0.2% were achieved. The calculation of the total Pu content is dependent on knowing the Pu isotopic vector, and this can be measured at the same time by gamma spectrometry. All this can be carried out on relatively small PuO₂ samples (< 10 g) which allows us to lower the amount of total Pu in the laboratory and thus the operator dose at the same time.

The counter is being used regularly to accustom the operators to it and to check its long-term stability. It is planned to use a series of PuO₂ samples, prepared at the Institute and containing Pu of different isotopic compositions to confirm these results, to optimise the gamma as well as the neutron counting, and to compare the results found on the same samples by titration and possibly K-edge absorption as well.

Installation and Applications of an ICP-Mass Spectrometer Coupled On-Line to an Ion Chromatograph

Introduction

During the last decade the analytical technique of Inductively Coupled Plasma Mass Spectrometry (ICP-MS) has been extensively applied in different fields of research, such as clinical chemistry, biochemistry, geochemistry as well as environmental studies [1-4].

On account of its high sensitivity and multi-isotopic capabilities the technique of ICP-MS has also been employed for the characterisation of spent nuclear fuels [5].

Samples of relatively low activity, such as diluted solutions arising from the dissolution of spent fuels, can be handled in a glove box and both elemental and isotopic information can be quickly gathered for the most of the fission products and actinides. However, the methodologies applied for the analysis of nuclear samples by ICP-MS differ from those employed for natural elements.

This is because of the different and, in many cases, unknown isotopic abundances in nuclear samples. From this point of view, the determination is nuclide-specific rather than element-orientated. As well as this, isobaric interferences from neutron capture reactions, the consequence of the irradiation of the fuel, and from β -decay of relatively long-lived radionuclides, occur. Therefore, for the complete characterisation of nuclear material the analysis must be preceded by chemical separation, which can be time-consuming and hazardous.

The on-line coupling of a chromatographic system with an ICP-MS installed in glove box is described here. Examples of the analysis of heavy fission products (Cs, Ba, lanthanides), separated on-line by Ion Chromatography are presented.

Experimental

Instrumentation

An Elan 5000 ICP-MS instrument (Sciex, Canada) and a 4500i high pressure chromatographic pump (Dionex, USA), modified in order to handle radioactive materials in a glove box, were used.

The diagram in Fig. 7.9, shows the installation of the system in the glove box. The quadrupole mass filter, ion lenses and channel electron-multiplier detector are outside the glove box. All vacuum line connections to the two rotary pumps are provided with absolute filters to avoid radioactive contamination in the pumps. The mass spectrometer is connected to the plasma through an opening in the left-side stainless-steel wall of the glove box where the sampling interface is attached. The plasma torch, nebulizer, chromatographic column, pneumatic injector valve, peristaltic pump and autosampler are inside the glove box. The eluent, coming from the chromatographic pump outside the glove box, is passed into the injection valve and then into the chromatographic column. If no chromatographic separation has to be performed, the sample is sucked through the peristaltic pump directly into the nebulizer. When chromatographic separations are carried out before the ICP-MS detection, the effluent from the chromatographic column is directly injected in the nebulizer. In both cases the waste from the nebulizer is stored in a vessel inside the glove box.

A mixed-bed ion-exchange column CS5 (Dionex, USA) and a 100 μ l loop were employed.

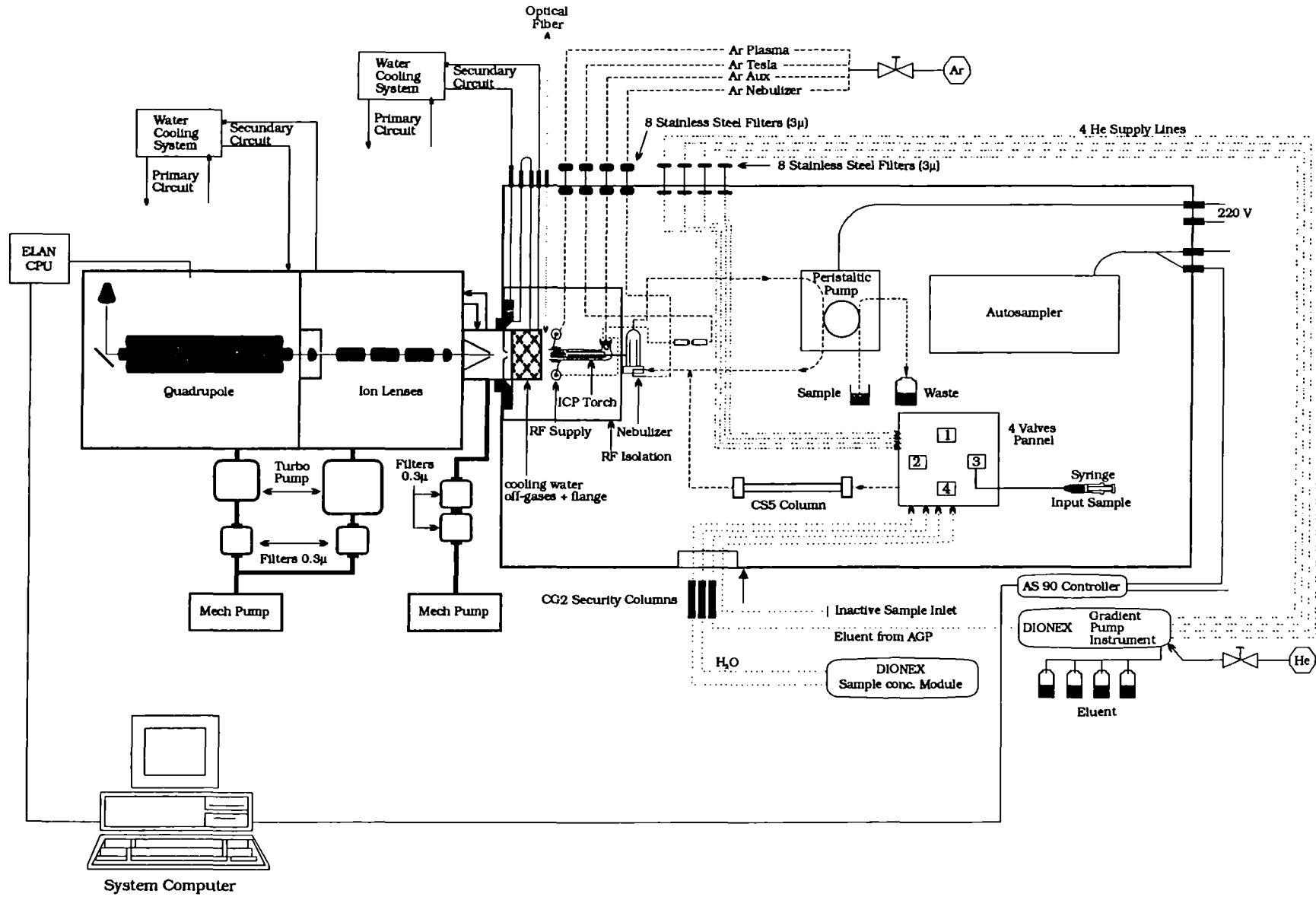


Fig.7.9 Schematic diagram of the ICP-MS installed in the glove box and coupled to the ion chromatograph

Reagents

Stock solutions of natural elements were obtained from Spex as 1000 ppm standards and diluted daily as necessary with 1% nitric acid to the required concentrations. Nitric acid, oxalic acid, diglycolic acid and lithium hydroxide (Merck, Suprapur grade) as well as ultra pure water (18 MegaOhm/cm resistivity at 25°C) obtained by treating Milli-Q water in a UHQ system (Elga, U.K) were used throughout.

Eluent solutions

The eluent solutions consisted of oxalic acid and diglycolic acid both 100 mM and dissolved in 190 mM lithium hydroxide.

Results and discussion

The complete determination of the abundance of fission products in spent fuels by ICP-MS is hindered by isobaric interferences of nuclides originating from β -decay and neutron capture reactions (Tabs.7.1 and 7.2).

Tab.7.1 Isobaric interferences by β -decay

Source isotope	Half-life	Decay product
Kr 85	10.76 a	Rb 85
* Sr 90	28.5 a	Zr 90
Zr 93	1.5 E6 a	Nb 93
Tc 99	2.1 E5 a	Ru 99
* Ru 106	368 d	Pd 106
Pd 107	6.5 E6 a	Ag 107
I 129	1.57 E7 a	Xe 129
* Cs 134	2.06 a	Ba 134
Cs 135	2 E6 a	Ba 135
* Cs 137	30.17 a	Ba 137
* Ce 144	285 d	Nd 144
* Pm 147	2.62 a	Sm 147
Sm 151	93 a	Eu 151
* Eu 155	4.96 a	Gd 155

* Isotopes which will produce significant interference after 5 years cooling time (Kr and Xe are lost during dissolution of the sample)

Two ICP-MS spectra of the distribution of fission products for two fuels irradiated under different conditions are shown in Fig.7.10. For both spectra, the peak located at mass 119, from U^{2+} , is common. Greater differences are evident for the high mass range (Cs, Ba and lanthanides), where the occurrence of relatively long-lived β -

Tab.7.2 Isobaric interferences by neutron capture

Source isotope	Isotope produced	Interference on
Y 89	Y 90 \rightarrow Zr 90	Sr 90 (28.5 a)
Mo 95	Mo 96	Zr 96
Tc 99 (2.1 E5 a)	Tc 100 \rightarrow Ru 100	Mo 100
Rh 103	Rh 104 \rightarrow Pd 104	Ru 104
Ag 109	Ag 110 \rightarrow Cd 110	Pd 110
Pr 141	Pr 142 \rightarrow Nd 142	Ce 142
Nd 143	Nd 144	Ce 144 (285 d)
Pm 147 (2.62 a)	Pm 148 \rightarrow Sm 148	Nd 148
Sm 149	Sm 150	Nd 150
Eu 153	Eu 154 (8.8 a)	Sm 154
Tb 159	Tb 160 \rightarrow Dy 160	Gd 160

* Isotopes which will produce significant interference after 5 years cooling time (Kr and Xe are lost during dissolution of the sample)

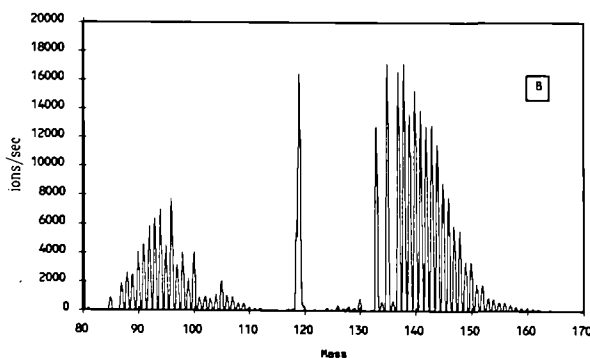
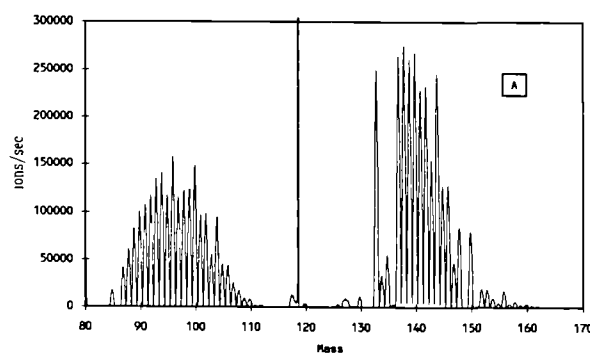


Fig.7.10 ICP-MS spectra of fission products in spent nuclear fuel: a) uranium oxide irradiated in a thermal reactor, b) uranium-neptunium oxide irradiated in a fast neutron reactor

emitters is coupled with high neutron capture cross-sections. The net result is the presence of isotopes of different elements at the same nominal mass (e.g. ^{137}Cs and ^{137}Ba for the β -decay case and ^{148}Nd and ^{148}Sm for the case of neutron capture reactions).

Neutron capture reactions are absent in Fig.7.10b as can be observed for the quasi-gaussian distribution of the high mass fission products. However, commercial fuels correspond typically to Fig.7.10a.

In order to obtain a complete picture of the fission product inventory, for characterisation purposes, a chemical separation of the elements has to precede the ICP-MS measurement. Elements to be separated from each other include Cs from Ba, Ce from Nd, Nd from Sm, Pm from Sm, Sm from Eu and Sm from Gd.

For the separation, carried out in the glove box, an agglomerated ion-exchange resin, Dionex CS5, was used. This type of resin contains an internal core particle, consisting of polystyrene-divinylbenzene of moderate cross-linking (2-5%), to which is attached a monolayer of small diameter particles which carry the functional groups comprising the fixed ions of the ion-exchange [6]. Provided the outer layer of functionalized particles is very thin, the agglomerated resin exhibits excellent chromatographic performance due to the very short diffusion path available to solute ions during the ion-exchange process. The CS5 column, used in this investigation, consists of anion- and cation-exchange sites both of which are available during the elution.

For the separation of the lanthanide series, using a pure cation-exchanger such as the CS3 column (Dionex) together with a-hydroxyisobutyric acid (HIBA) as eluent medium, the elution sequence is from Lu^{+3} to La^{+3} . Under these experimental conditions [7], the elements of interest in our investigation elute after 12 min. and are also not well resolved. Employing a mixed-bed ion-exchanger, such as CS5, and elu-

ent media forming anionic complexes with the lanthanides, the sequence of elution is reversed compared with the elution performed by a pure cation-exchanger. Also Cs and Ba can be separated from each other and from the lanthanide series by cation-exchange process on CS5 column.

Using the chromatographic conditions reported in Tab.7.3, the chromatographic separation obtained for the elements considered here, before their ICP-MS measurement, is shown in Fig.7.11. The lanthanides tested, are eluted in the sequence La, Ce, Pr, Nd, Sm, with Cs in between Ce and Pr. Increasing the ionic strength of the eluent - using for instance 700 mM nitric acid - Ba is also eluted at the end of the chromatogram.

Conclusions

After having achieved the chemical chromatographic separation by the procedure described, the methodology of isotopic dilution analysis can be applied by spiking the sample with natural elements. Except for La, Pr and Pm, all fission products from Cs to Gd can be determined by this way. La and Pr can be determined by calibration and/or standard additions and Pm by using the response curve of the instrument for the other lanthanides, as no standards are available. Using the technique described above, the direct determination - for instance - of fuel burn-up by ICP-MS based on ^{148}Nd is now possible without interference from ^{148}Sm .

Tab.7.3 Chromatographic conditions

Column	HPLC-CS5, 250 x 50 mm			
Loop volume	100 μl			
Flow rate	1 ml/min			
Eluent 1	100 mM Oxalic acid, 190 mM Lithium hydroxide			
Eluent 2	100 mM Diglycolic acid, 190 mM Lithium hydroxide			
Eluent 3	distilled water			
Gradient				
Time (min)	%1	%2	%3	Comment
0.0	60	30	10	start
0.5	60	30	10	injection
3.4	60	30	10	start of gradient
15.0	30	30	40	end of gradient

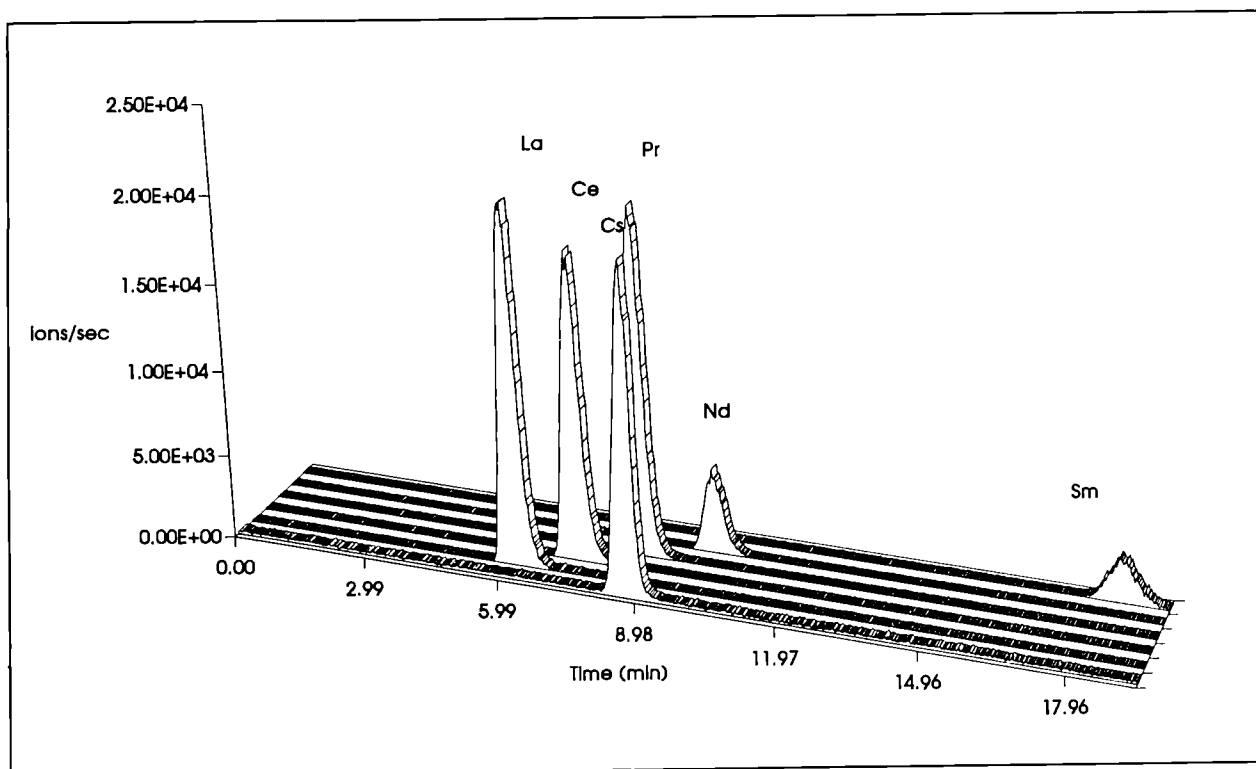


Fig.7.11 Chromatographic separation of six elements with ICP-MS detection. Separation performed according to the conditions of Tab. 7.3

References

- [1] A.L. Gray, 'Inductively coupled plasma source mass spectrometry' in 'Inorganic Mass Spectrometry', Wiley and sons, New York, 1998, p. 257
- [2] G.M. Hieftje and G.H. Vickers, *Anal. Chim. Acta* **216** (1989) 1
- [3] R.S. Houk and J.J. Thomsos, *Mass Spectrom. Rev* **7** (1988) 425
- [4] J.E. Cantle, 'Analytical Chemistry Instrumentation', W. R. Laing Ed., Lewis Publishers Inc., 1986, p. 3
- [5] J.I. Garcia Alonso, J.-F. Babelot, J.-P. Glatz, O. Cromboom and L. Koch, *Radiochimica Acta*, in press
- [6] P.R. Haddad and P.E. Jackson, 'Ion Chromatography, principles and applications', Elsevier, Amsterdam, 1990, p. 56
- [7] S.S. Heberling, J.M. Riviello, M. Shigen and A.W. Ip, *Research and Development* **9** (1987) 74

Glow Discharge Mass Spectrometer (GDMS) : Installation

At the end of 1991 a GDMS instrument (Fisons, VG 9000) was purchased. This instrument provides unrivalled performance in the analysis of solids, where traditionally a combination of several techniques are required, with elemental coverage across the entire periodic table (except hydrogen) and a range of detection from 100% to parts per trillion.

The main characteristics of the instrument consist of: detection limit approaching 0.001 ppb wt; rapid multi-element analysis of solid samples; major, minor, trace and ultratrace determination in one analysis cycle; full elemental coverage including C, N, O, P, S; high accuracy; low matrix effects: thin layer analysis to micron levels; depth profiling with a resolution below 0.1 mm; precision of 1% on major, 1-10% on minor and trace elements; isotope ratio capability; automated handling.

The GDMS VG9000 combines the advantages of

a proven DC plasma ion source with the high resolution (double focusing - mass and energy) of a reverse Nier Johnson mass spectrometer. The glow discharge source produces a highly stable beam of singly charged ions with negligible molecular or multi-charged species. The mass spectrometer has exceptional ability to resolve low level interference species from elemental peaks. This allows full elemental coverage with excellent sensitivity.

The argon plasma within the source sputters neutral species from the sample surface which are subsequently ionised within the plasma. It is this feature which gives the glow source its independence from the sample matrix effects, allowing excellent quantification without the use of matrix-matched standards.

The dual-mode ion detector system is computer controlled and has a dynamic range in excess of eleven orders of magnitude, allowing major, minor, trace and ultratrace measurements to be performed in one analysis cycle.

In 1992 our technical department, in collaboration with the instrument producer, completely redesigned the instrument for installation in a glove box. During the construction the producer made the main modifications consisting of a new type of ion source, a new interlock system for the sample insertion in the ion source as well as a new type of discharge cell.

The modified instrument was delivered by the company in October 1992 and subsequently installed in the Institute workshop. The instrument was tested for four weeks and its performance was checked on the basis of fourteen different parameters.

The parameters tested are reported in Tab.7.4 where a comparison between the specifications and the actual value obtained for these parameters is reported before the installation in a glove box.

Parameters tested:

- Source vacuum (the vacuum in the source is performed by a cryopump);
- Analyser vacuum (the vacuum in the analyser is performed by two turbo pumps);
- Mass resolution (defined as M/DM at 5% peak height, using a 25 mm source defining slit) was measured for three different elements: copper, aluminium and gold;
- Transmission;
- Matrix current. This parameter gives an indication of the efficiency of the ion source. It is very important in our instrument to test its performance because the ion source has been completely redesigned;

- Beam transmission stability. This parameter was measured over two different durations of time: 10 and 30 minutes using 20 and 30 scans respectively;
- Peak position stability. This parameter is referred to the variations of the peak centre position and was measured over 30 minutes;
- Mass calibration. This parameter has been tested over the range mass from boron to lead;
- Mass marking;
- Ion counting efficiency;
- Reproducibility. This parameter was measured for major, minor and trace elements defined as the 10-50%, 0.1% and 0.5-1 ppm concentration levels respectively;
- Accuracy. This parameter was measured for major, minor and trace elements;
- Abundance Sensitivity (AS). This parameter gives an indication of the tailing of the peak. For instance, using a copper matrix and a resolution higher than 4000, the abundance sensitivity as measured at mass 62 should be lower than 1 ppm relative to the mass 63. Abundance Sensitivity can be calculated, in the case of copper, as following:

$$AS = (\text{actual baseline at mass 62}) / (\text{Maximum height at mass 63}) \times 10^6 \text{ ppm}$$
- Gas background. This parameter was measured using the NBS sample 685W gold, after a pre-sputter time using a cryocooled cell. Very good background levels were obtained for all gases tested.
 After these tests the instrument was dismantled in order to be installed in a glove-box by our workshop staff. Its installation will be finished next year.

Verification of Tank Volume Measurements by Neodymium Tracing and IDMS

Introduction

In a reprocessing plant the usual calibration method for accountability tanks consists of adding weighed portions of water to the tank and measuring the hydrostatic pressure exerted by the liquid column by a high precision manometer. An independent verification of the volume (or weight) of a batch of fissile material could be of interest for Safeguards purposes.

Tab.7.4 Comparison between the specifications and the actual values before the installation in a glove box

Parameters	Standard Performance Specifications	Actual value obtained before installation
source vacuum	$< 3 \times 10^{-8}$ mbar	2.4×10^{-8} mbar
analyzer vacuum	$< 3 \times 10^{-8}$ mbar	1.8×10^{-8} mbar
mass resolution	> 400	6940 for Al 6624 for Cu 5466 for Au
transmission	$> 50\%$	75%
matrix current	$> 1 \times 10^{-10}$ A	6.2×10^{-10} A
beam transmission stability	10 min., $< 3\%$ RSD 30 min., $< 5\%$ RSD	2.51 3.87
beam position stability	30 min., < 30 ppm RSD	13
mass calibration	± 10 millimass units	8
mass marking	< 500 ppm	< 100 ppm
ion counting efficiency	$> 75\%$ background < 1 count/s	80.74% background < 1 count/s
reproducibility	major elements $< 3\%$ rsd minor elements $< 5\%$ rsd trace elements $< 10\%$ rsd	1.6% 2.6% 1.8%
accuracy	major elements $< 5\%$ rsd minor elements $< 10\%$ rsd trace elements $< 20\%$ rsd	2.5% 2.7% 2.1%
abundance sensitivity	< 1 ppm	0.38 ppm
gas background	Carbon < 10 ppm Nitrogen < 10 ppm Oxygen < 5 ppm	3.6 ppm 4.3 ppm 0.7 ppm

Such a verification method could be based on the application of a suitable tracer. In this technique a tracer isotope of a selected element is added to the tank, the content is thoroughly mixed and sampled. The concentration of the tracer element is then determined by isotope dilution mass spectrometry in the laboratory.

Background

A few years ago the Institute took part in an inter laboratory experiment dealing with the tracer technique. Natural lutetium was employed for volume verification in a mock-up

tank; the experiment called Caldex was organized by DWK, Hannover, Germany (TUAR 90, 151).

This exercise, the results of which have not yet been published, was very successful and showed the potential of the method. The analytical errors were very small and the agreement with the usual volume calibration method was excellent.

However, the conditions for this test were ideal. Earlier tracer experiments on active input tanks have often failed, due to uncertainties in the addition and mixing-in of the tracer, although the measurements themselves were very precise [1, 2].

Experimental

In the last quarter of 1992 a tracing experiment was organized by DG XVII at the La Hague UP2 plant, and carried out by personnel from the Institute.

Natural neodymium was used as tracer in the input tank. It was added at a concentration of about 50 g/l, the dilution factor in the tank being between 3000 and 10 000. The samples were spiked with Nd-150 (92% pure) at the plant for isotope dilution mass spectrometry in the Institute.

Two experiments each at 3 volume levels between 6 and 20 cubic meters were designed:

- A Addition of the neodymium tracer to the batch of nitric acid, mixing and sampling (i.e. tracing anew for each volume and rinsing of the tank in between the additions), and
- B addition of the tracer to the batch of acid and diluting further with acid to get 3 different volumes (i.e. tracing once, without rinsing between the levels). Design B was a check on the calibration curve made by the operator/inspection team just before the tracer experiments with neodymium.

Blank values (i.e. acid without tracer) were also investigated in both experiments.

The pretreatment of the samples in the laboratory prior to mass spectrometric measurements consisted of evaporation to dryness and re-dissolution in weak acid to condition the samples for mass spectrometry; the tracer and the ^{150}Nd spike were measured separately, as well.

Furthermore, a check of the possible bias of the measurement system could be made, in that the tracer solution was diluted very carefully in the laboratory and spiked with the same spike as used for the plant samples. In these later measurements the data on the spike concentration are unimportant, as they cancel in the calculation: at a ratio between dilution factors, that from the plant (unknown) and from the laboratory, provides the key to the tank volume.

One advantage of the use of neodymium as a tracer is the existence of many isotopes of that element, allowing (quasi) independent calculations of the tank volume to be done based on several different isotope ratios (e.g. $^{142}\text{Nd}/^{150}\text{Nd}$, $^{143}\text{Nd}/^{150}\text{Nd}$ etc).

The variety of isotopes introduces on the other hand certain deficiencies in the measurement process: Not all the ratios taken are in the

optimum range, to yield good precision. The relatively large mass distances from the principal spike isotope (^{150}Nd) for some of the isotopes may also act as a restraint and may give rise to mass discrimination effects; the main part of this however is compensated for by the total evaporation technique used for the measurements. In the mass-spectrometer a multiple cup collector is used.

Under these constraints and employing 4 different set of ratios it was possible to separate out the "calculation error" from the overall error; an error component assignable to the calculation of the volume could thus be identified.

A further error component separately accessible from the two designs (A and B, above) was the sampling and mixing error, the existence of which could provide the clue to the failure of some of the earlier efforts made on the tracer technique.

Through a properly designed duplication of measurements the instrumental error of the ratio measurements (the analytical error) could also be evaluated.

The experiment is presently under final evaluation and the results will be published elsewhere. No numerical data are therefore given here, but the conclusions below could be drawn.

Conclusions

1. The blank values were at least 10000 times lower than the level of the neodymium concentrations in the tank.
2. The analytical error was in all cases negligible compared to other error sources.
3. A difference between the experiments A and B indicates a significant sampling and mixing error in experiment A.
4. The "calculation error" varies with the isotope ratio considered, and is about twice the analytical error in the best cases. Certain ratios should not be used in the calculation.

References

- [1] H. Bokelund, Eurochemic Technical Report ETR 266, 1970
- [2] P.R. Trincerini, Report EUR 12623, 1990

Work for Third Parties

Introduction

In 1992, new contracts with third parties worth 441.6 kECU have been concluded. This brought the total volume of contract work under execution on December 31, 1992 up to 17 107,5 kECU. Additional studies for external clients, totalling 662,90 kECU were under negotiation by the end of 1992.

Examples of contract work concerning conditioning, conversion, post-irradiation analysis, and reprocessing of nuclear fuels, nuclear transmutation of long-lived nuclides and the preparation of alpha emitters for radio-therapeutical applications are given below.

Conditioning of C-Containing MOX and Carbide Pellets

9.5 kg pellets (2 kg Pu, 6 kg U) containing large amounts of carbon were transformed to U-Pu oxide by controlled combustion and oxidation. The pellets, delivered by Siemens, were homogenized and analysed before treatment. After the elimination of carbon, the material, again homogenized and analysed, was shipped back for recovery of the fissile material.

Conversion of Uranyl- and Pu Nitrates in Solution to Oxides

About 28 l uranyl nitrate solution containing 10 g U / 1.5 kg U-235 and minor amounts of Pu were conditioned, precipitated and transformed to oxide on request by the Institut für Heiße Chemie (IHCh) of the Kernforschungszentrum Karlsruhe (KfK). The material was precipitated as ADU and calcined. After homogenization and analyses the material was returned to KfK.

For the same Institute 4 l of Pu solutions with about 700 g Pu were precipitated as oxalate, calcined, analysed and returned to KfK.

At the same time a large number of test samples containing fissile material were rearranged and conditioned for transport to a reprocessing

plant. All these specimens have been used over the last few years in various experiments performed in collaborations between ITU and KfK.

Post-Irradiation Examination of LWR Fuel Rods

In the frame of the contract with KWU/Siemens, non-destructive and destructive examinations of power reactor fuel rods were continued (see TUAR '91).

In 1992,

- 28 fuel rods from the Neckarwestheim reactor (GKN II) with UO₂ fuel,
 - 14 fuel rods from the Gösigen reactor in Switzerland (KKGg) with UO₂ fuel,
- and
- 5 material test pins (MTS) from Gösigen for Zr-alloys corrosion studies

were received for analysis at the Institute.

A list of the examinations carried out on these pins is given in Tab.8.1.

In addition, 19 fuel rods from the GKN II reactor and 17 fuel rods from the KKGg reactor were conditioned and transported back to the reactor pool.

Post-Irradiation Examination of Phebus PF Project Fuel Rods

Phebus PF is an international project to study fission gas release in severe accident situations under realistic conditions in which the Institute participates by doing modelling work, and performing non-destructive examination of fuel rods already irradiated in BR3 reactor in Mol, Belgium.

In 1992, 51 rods corresponding to batches 1 and

Tab.8.1 Post-irradiation analysis carried out with power reactor fuel pins for KWU/Siemens

Type of analysis	KWO	KKGg	MTS	GKN II	ISOTOP.	KKKG-VII	MTS	TOTAL
Visual examination and photo documentation						8		8
Fuel rod length						8		8
Fuel rod profilometry						8		8
Eddy current defect testing of rods						8		9
Eddy current oxide layer thickness measurement		5	6			8	2	21
Rod axial gamma-scanning						6		6
Mechanical fuel-clad gap measurement				1				1
Fission gas puncturing and analysis		14		18		7		39
Determination of rod free volume		5		8		7		20
Metallography	5	10						15
Ceramography	3	8						11
Radiochemical burn-up analysis	1							1
Isotopic analysis of Np-237					2			2
SEM on cladding samples		2						2
Microprobe of irradiated fuel sample	3							3
Dismantling		3		1				4
Conditioning for back transport		17		19				36

2, were analysed at the Institute. The non-destructive testing carried out was:

- A) 1. visual examination and photography 51 rods
 2. eddy current defect testing 51 rods
 3. axial γ -scanning 51 rods
 4. fuel rod length determination. 51 rods
- B) 1. eddy current oxide thickness measurement 6 rods
 2. profilometry 6 rods

In addition the following destructive examinations were made on 2 rods:

1. prior γ -spectroscopy at max. power position on NDT bench
2. puncturing and fission gas analysis
3. fuel ceramography (optical microscopy porosity and grain size measurements and SEM-EDX analysis) at:
 - a) maximum power position
 - b) mid power position
4. radiochemical and isotopic fuel analysis (ICP-MS, quantitative γ -spectroscopy) for burn-up determination at maximum power position.

The primary source term of the PHEBUS experiment FTPO-test was computed with the FUTURE-MITRA-CHEMIF software chain whose basic feature is to provide the released amount of the fission product nuclides in their various isotopic occurrences and based on the evolution of the fuel restructuring.

Production of ^{225}Ac and ^{213}Bi for Labelled Monoclonal Antibodies

Introduction

The cytotoxic effect of incorporated alpha emitters has been known for a long time. Interest in the therapeutical application of radionuclides against certain forms of cancer has increased since the availability of monoclonal antibodies which can act as a transport agent for the radioisotopes.

The advantage of this technique is that approxi-

mately 1000 times less total radiation dosage is required to kill tumours compared with external radiation methods.

The feasibility of ^{225}Ac for therapeutic applications

^{225}Ac , together with its daughter nuclides (Fig.8.1) is a serious contender for this application for the following reasons [1, 2]:

- The nuclide can be produced ready for application on a sufficiently large scale and its daughters are easily detected and measured by alpha- and gamma-spectrometry.
- There is no radon isotope in the decay chain which could cause problems in handling large amounts of the material.
- There are no high energy gamma emitters in the decay chain.
- If required, the alpha-emitting daughter ^{213}Bi with a half-life of 46 minutes instead of ^{225}Ac (10 day half-life) can be used.

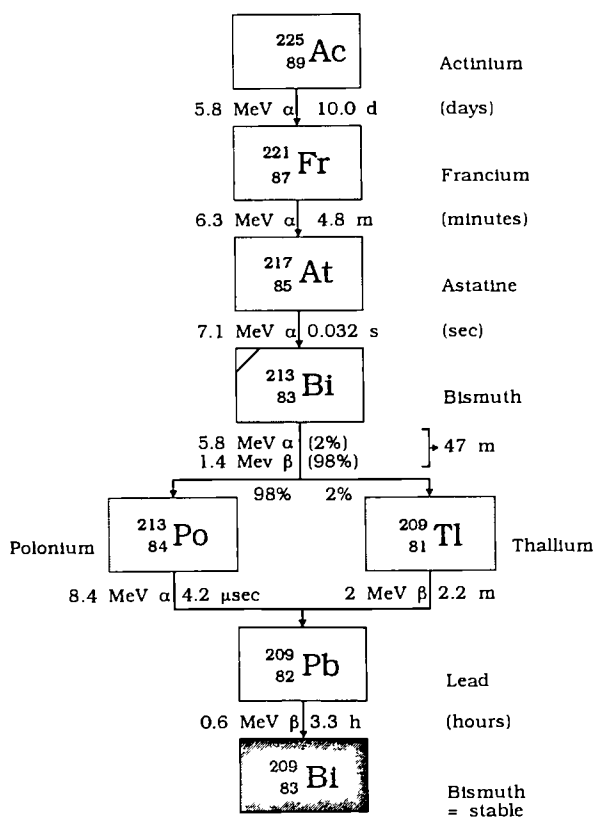


Fig.8.1 Radioactive decay chain of ^{225}Ac

^{225}Ac Production

The generator of choice for a continuous supply of ^{225}Ac is its precursor ^{229}Th . This nuclide decays with a half-life of 7340 years via ^{225}Ra (half-life = 15 d) into ^{225}Ac .

There are 2 different possibilities to form the ^{229}Th source in sufficient quantities for the future potential demand for ^{225}Ac :

1. From ^{233}U already available in large amounts from the earlier irradiation of ^{232}Th in thermal reactors. The amount of available ^{233}U is in the order of hundreds of kilograms. (^{233}U is contaminated with ^{232}U which decays into ^{228}Th . The separation of ^{225}Ac from the mix of ^{228}Th and ^{232}Th is complicated by a relatively long-lived radon daughter of ^{228}Th as well as the presence of hard gamma-rays in the decay chain.)
2. By successive neutron capture in ^{226}Ra . Sufficient ^{226}Ra is available in Europe and in the USA for this purpose. A patent application has already been published on this production route [3].

Separation of ^{225}Ac from ^{229}Th and ^{213}Bi from ^{225}Ac

Several schemes for milking ^{225}Ac from the parent ^{229}Th are possible which enable very high purity ^{225}Ac to be obtained (i.e. with no detectable thorium or radium contamination) and without notable loss of the ^{229}Th source material.

The separation scheme used in this work employed two columns, the first with titanium phosphate (PHOTI D, 0.1 - 0.5 mm, NIRUCHEM SA, BG) and the second with DOWEX 50 WX 8 (100 - 200 mesh).

The ^{229}Th is fixed on the PHOTI D - column resin and is eluted with (three bed volumes) 0.5M HNO_3 . Both columns are connected in series so the ^{225}Ac is fixed directly on the second column (possibly mixed with Ra). In order to separate ^{225}Ra (^{224}Ra), the second column is washed with 2M HNO_3 (five bed volumes) and subsequently the ^{225}Ac is eluted with 4M HNO_3 using three bed volumes (Fig.8.2). The function of DOWEX resin is thus the purification of ^{225}Ac . The separation process is continuously monitored by gamma-spectrometry (Fig.8.3).

The purity of the final products was determined by ICP-MS. This method has the advantage of being able to determine inactive as well as active impurities.

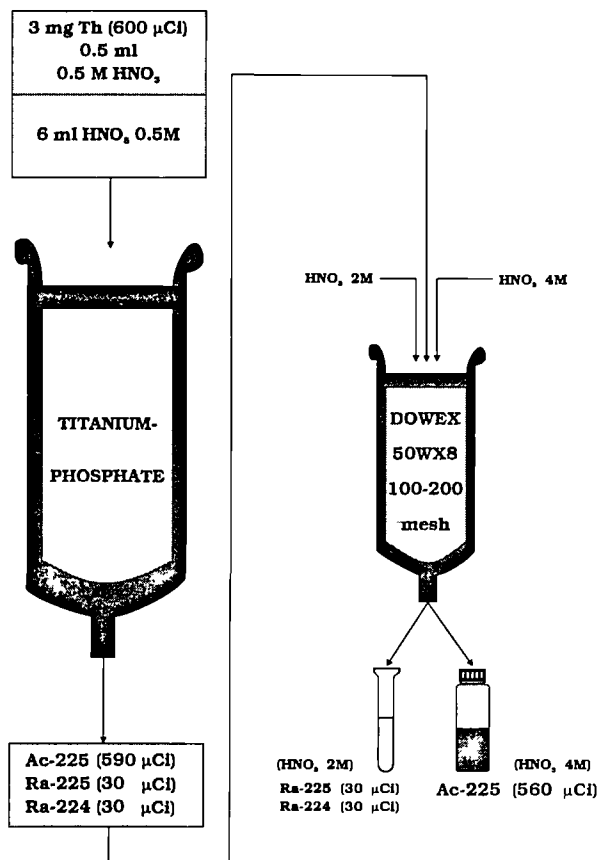


Fig. 8.2 Flow diagram of ^{225}Ac separation from the parent ^{229}Th

Conclusions

The methods outlined here promise to open up the use of ^{225}Ac as a source material of alpha particles for application in radioimmune therapy at prices which compare favourably to other already existing therapeutic treatments.

References

- [1] M.W. Geerlings, F.M. Kaspersen (AKZO N.V.) Radioimmunotherapy using α -particle emission. Patent: PCT/EP 90/00990
- [2] M.W. Geerlings, F.M. Kaspersen, C. Apostolidis, R. van der Hout "The feasibility of Actinium-225 as source of α -particles in radioimmunotherapy" accepted for publication in Nuclear Medicine Communications
- [3] J. van Geel, J. Fuger, L. Koch (Commission of the European Communities, JRC Karlsruhe) A method for producing ^{225}Ac and ^{213}Bi . Patent: PCT/EP 91/00306; 91 102 260.6

Irradiation of Minor-Actinide Containing Alloys (CRIEPI)

During the reporting period, two candidate fuels: $\text{U}_{67}\text{Pu}_{19}\text{Zr}_{10}\text{MA}_2\text{RE}_2$, $\text{U}_{61}\text{Pu}_{19}\text{Zr}_{10}\text{MA}_5\text{RE}_5$ were characterised sufficiently, allowing the feasibility study for their irradiation in PHENIX - carried out by CEA, Cadarache - to arrive at a positive conclusion.

The following parameters in particular were determined and compared with those of a standard fuel without minor actinides: density, melting point, Young's modulus as a function of temperature and Poisson coefficient. In order to assess the fuel behaviour under normal and accidental conditions, the following simulation tests were conducted:

- redistribution of MA-RE-U-Pu-Zr in a thermal gradient,
- fuel and cladding interaction with sodium metal as a function of temperature,
- determination of the eutectic temperature of the fuel/cladding mixture.

The present knowledge was deemed adequate by CEA and an irradiation contract was drawn up which will define further the fuel fabrication specifications. This irradiation is scheduled for October 1994.

The samples will be placed in 3 rigs for 3 different burn-ups, whereby the arrangement will be the normal PHENIX device. The rigs are installed in sub-assemblies (carriers). Each rig contains 16 standard oxide pins and 3 metallic pins (1 reference U-Pu-Zr pin, 1 pin with 2% and 1 pin with 5% minor actinides and rare-earths).

Study of Reprecipitation Phenomena from Dissolver Solutions of Highly Burnt Nuclear Fuels

The study of the reprecipitation phenomena in dissolved spent fuel solutions has been terminated successfully. Three samples of highly burnt nuclear fuel were dissolved in nitric acid of different concentrations and the residue was immediately separated by centrifugation and filtration. The solutions were kept at different temperatures, half at room temperature and half at 50 °C.

The dissolver solutions were filtered after 20, 68 and 164 hours, the filtered fines dissolved and analysed by ICP-MS.

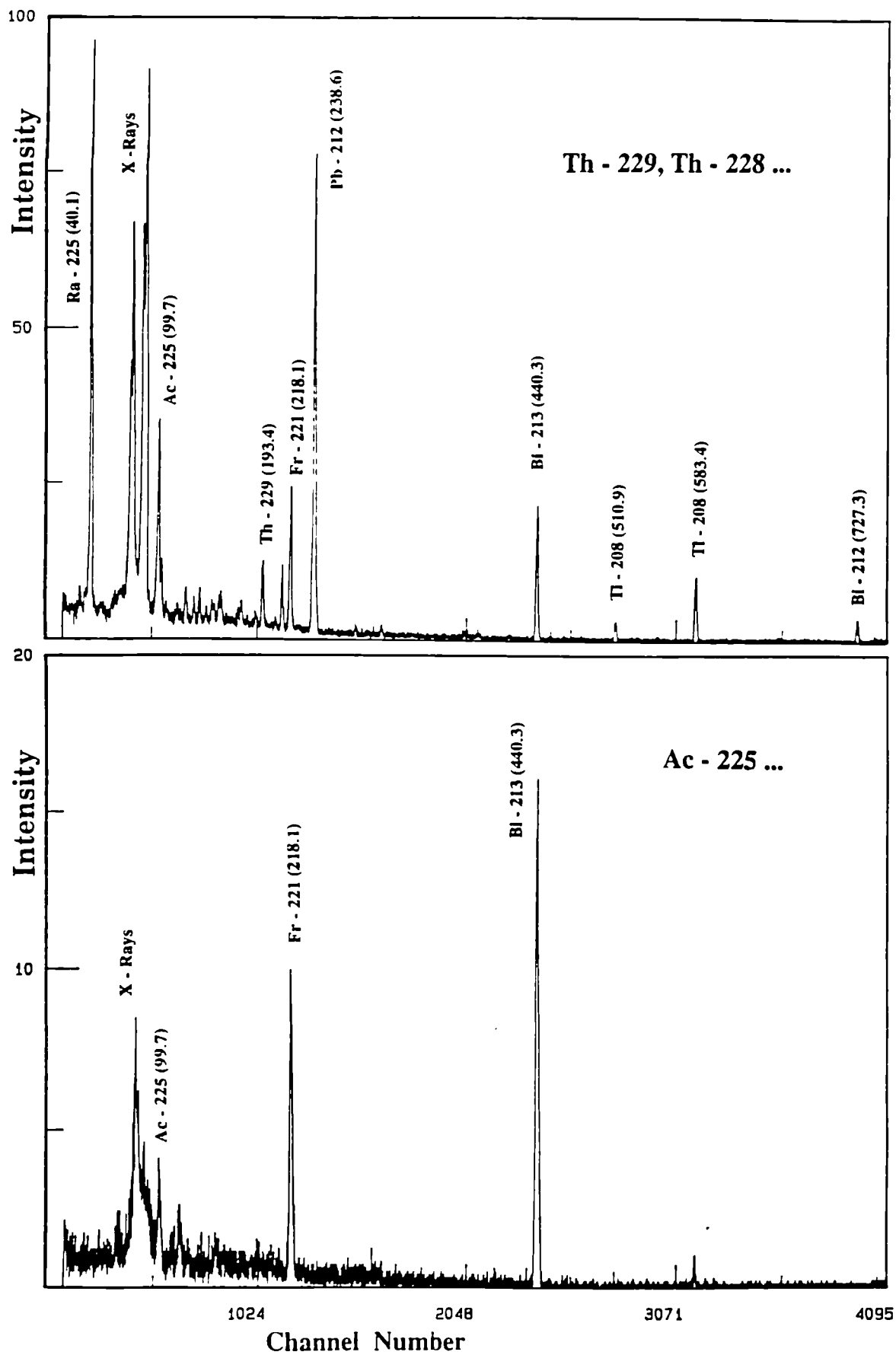


Fig.8.3 Gamma-spectra of column elution fractions

A significant influence of the parameters studied (time, acidity) on the amount and the composition of the precipitate was found. The results will be presented in April 1993 at the Meeting of the Atomic Energy Society of Japan.

The results in comparison to literature data proved that the fuel used for this study and also for the previous one on dissolution characteristics of high burn-up fuel (TUAR 91, 198) differs from commercial fuel and shows significant differences in its dissolution and reprecipitation behavior. Thus on request of CRIEPI, JRC Karlsruhe has submitted a proposal for a similar study on commercial high burn-up fuels.

Development of a Passive Neutron Detector for Nuclear Material Measurements in the Pilot Conditioning Plant Gorleben

A passive neutron detection device was developed by GNS (Gesellschaft für Nuklear Service mbH) supported by KfK/INR, APA (Anlagen Planung Alzenau GmbH) and MAB (Münchener Apparatebau für Elektronische Geräte GmbH) for Safeguards purposes at the Gorleben Pilot Plant where conditioning of spent fuel will be performed prior to its direct disposal in a geological repository [1].

Hot tests of the equipment under realistic conditions were performed in the hot cells of the Institute where spent fuel rods are available, with the cooperation of MAB. The distribution of neutron and gamma emissions along the fuel length was determined using passive neutron and gamma interrogation (TUAR 91, 121). These distributions were used to verify the burn-up of the fuel rods that was declared by the operators and for evaluation of the data obtained during the hot tests.

References

- [1] E. Leitner and R. Weh, 13th ESARDA Symposium on Safeguards and Nuclear Material Management, Avignon, France, May 14-16 (1991)

ANNEXES

Annex I

Publications 1992

1. Conferences

Conference papers published in 1992 in journals or special conference proceedings volumes may appear also under paragraph 2 (Books and Periodicals)

IAEA Technical Committee Meeting on Reactor Materials Behaviour under Severe Accident Conditions
March 16 - 19, 1992, Aix-en-Provence (F)

Bottomley, P.D.W., Coquerelle, M.
 Fuel Debris Analysis of TMI-2: Fuel and Structural Materials Behaviour

203rd National Meeting of the American Chemical Society
April 5 - 10, 1992, San Francisco, California (USA)

Fuger, J., Goffart, J., Bettonville, S., Jemine, X.
 Indenyl-f-Element Thermochemistry

12th General Conference of the Condensed Matter Division of the European Physical Society
April 6 - 9, 1992, Prague (CSFR)

Lander, G.H., Stirling, W.G.
 Magnetic X-Ray Scattering
 (Proceedings Physica Scripta T45 (1992) 15-21)

22ièmes Journées des Actinides
April 22 - 25, 1992, Méribel (F)

Apostolidis, C., Meyer, D., Rebizant, J., Maier, R., Kanellakopoulos, B., Marques, N., Pires de Matos, A.
 Crystal and Molecular Structure of Bis{Hydrotris(Pyrazol-1-yl)borate} - Actinoid(IV) - Dichlorides of Thorium, Uranium and Neptunium, (HBPz₃)₂AnCl₂

Athanasίου, N., Ray, I.L.F., Spirlet, J.C., Politis, C.
 Synthesis and Characterization of Quasicrystalline Materials

Benedict, U.
 Pressure-Induced Structural Transitions in Actinides and Lanthanides

Bouillet, M.N., Sanchez, J.P., Tomala, K., Burlet, P., Rebizant, J., Spirlet, J.C., Vogt, O.
 Magnetic Properties of NpSb_{0.95}Te_{0.05} from ¹²¹Sb Transferred Hyperfine Field Measurements

Burlet, P., Jirman, L., Sechovsky, V., Havela, L., Divis, M., Kergadallan, Y., Spirlet, J.C., Rebizant, J., Brück, E., de Boer, F.R., Nakotte, H., Suzuki, T., Fujita, T., Maletta, H.
 Magnetic Phase Diagram of UNiGa

Dancausse, J.P., Benedict, U.
 Review on X-Ray Diffraction Studies under Pressure of Actinide Dioxides

Dancausse, J.P., Heathman, S., Benedict, U., Gerward, L., Staun Olsen, J., Hulliger, F.
 Structural Transition Study of UC₂ under High Pressure

Goncalves, A.P., Henriques, R.T., Bonfait, G., Almeida, M., Spirlet, J.C.
 Preparation, Characterization and Single Crystal Growth of Iron-Actinide Compounds with ThMn₁₂-Type Structure

Langridge, S., Stirling, W., Lander, G.H., Rebizant, J., Spirlet, J.C.
 Resonant Magnetic X-Ray Scattering of NpAs

Link, P., Benedict, U., Wittig, J., Wühl, H.
 High-Pressure Resistance Study of UTe and USe

Meyer, D., Dancausse, J.P., Rebizant, J., Apostolidis, C., Kanellakopoulos, B., Benedict, U.
 Single Crystal High Pressure Studies on Actinide Chlorides (XCl₄, X = Th, U)

Paixão, J.A., Lander, G.H., Tang, C.C., Stirling, W.G., Gibbs, D., Blaise, A., Burlet, P., Brown, P.J., Vogt, O.
 Magnetization, Neutron, and Resonant Magnetic X-Ray Study of U_{0.85}Th_{0.15}Sb

Rebizant, J., Bednarczyk, E., Kergadallan, Y., Meyer, D., Moens, A., Peron, M.N., Rijkeboer, C., Sari, C., Spirlet, J.C.

Preparation and Structure of New Ternary Intermetallic Compounds of Actinides

Sanchez, J.P., Tomala, K., Rebizant, J., Spirlet, J.C.

Magnetic Properties of Stoichiometric NpCo_2 from Mössbauer Spectroscopy

Severin, L., Johansson, B., Brooks, M.S.S.
Magnetism in AnFe_2 Laves Phase Compounds from ab initio Calculations

Spirlet, J.C., Rebizant, J., Kergadallan, Y., Kalbusch, J., Moens, A., Rijkeboer, C.
Progress in the Preparation and Characterization of Actinide Compounds

IAEA Technical Committee Meeting on Fission Gas Release and Fuel Rod Chemistry Related to Extend Burn-up April 27 - May 1, 1992, Pembroke (CDN)

Coquerelle, M., Bottomley, P.D.W.
Hot Cell Fission Gas Release Studies on UO_2

Lucuta, P.G., Verrall, R.A., Matzke, Hj.
Thermal Conductivity and Gas Release from SIMFUEL

IAEA Meeting on Fission Gas Release and Fuel Rod Chemistry Related to Extended Burn-up April 28 - May 1, 1992 Chalk River (CDN)

Mogensen, M., Bagger, C., Toftegaard, H., Knudsen, P., Walker, C.T.
Fission Gas Release Below 20 kWm^{-1} in Transient Tested Water Reactor Fuels at Extended Burn-up

Arbeitskreis Thermophysik May 14 - 15, 1992, Wien (A)

Tasman, H.A.
Wärmeleitfähigkeit von SIMFUEL (UO_2 Kernbrennstoff mit simuliertem Abbrand)

International Conference on Rare Earths '92

June 1 - 5, 1992, Kyoto (J)
(Proceedings in J. Alloys and Compounds)

Benedict, U. (invited)
Pressure-Induced Phase Transitions in 5f and 4f Metals and Compounds

Fuger, J. (invited)
Thermodynamics of the Transuranium Elements and Their Compounds. Comparison with the Lanthanides

Peterson, J.R., Heathman, S., Benedict, U.
Energy Dispersive X-Ray Diffraction Analysis of NdBr_3 at Pressures of up to 52 GPa

Wastin, F., Fuger, J., Kanellakopoulos, B., Rebizant, J., Spirlet, J.C., Sechovsky, V.
Magnetic Study of New PuMt_2Si_2 (Mt: 3d, 4d or 5d Transition Metal) Inter-metallic Compounds

OECD/NED Specialist Meeting on Simulators and Plant Analyzers June 8 - 10, 1992, Lappeenranta (SF)

Lassmann, K.
TRANSURANUS: A Fuel Rod Analysis Code Ready for Use in Simulators and Plant Analyzers

Partitioning and Transmutation of Minor Actinides - Working Group Meeting on Targets and Fuels June 23 - 24, 1992, Karlsruhe (D)

Koch, L.
Evaluation of P&T Research

Koch, L., Nicolaou, G., Wellum, R.
The KNK II Minor Actinide Irradiation Experiment

Koch, L., Betti, M., Garcia Alonso, J.I., Glatz, J.-P., Kammerichs, K., Nicolaou, G., Wellum, R.
Chemical Analysis at ITU

Babelot, J.-F., Koch, L., Matzke, Hj., Spirlet, J.-C., Sari, C., Inoue, T., Kurata, M.
Minor Actinide-Containing Alloy Fuels to be Irradiated in PHENIX

Babelot, J.-F., Koch, L., Inoue, T., Kurata, M.
The CRIEPI Irradiation Experiment

Babelot, J.-F., Koch, L.
Minor Actinides Laboratory and Parameters
Required for Target Fabrication
Glatz, J.-P., Apostolidis, C., Bokelund, H.
Dissolution and Partitioning

*Koch, L., Garcia Alonso, J.I., Kammerichs, K.,
Nicolaou, G., Wellum R.*
The SUPERFACT Irradiation Experiment
Coquerelle, M., Nicolaou, G.
 α , γ - Hot Cell Facility for Post-Irradiation
Examination of MA Fuels

Glatz, J.-P., Bokelund, H.
Equipment for Material Recovery

**International Conference on Advances in
Corrosion and Protection**
June 28 - July 3, 1992, Manchester (UK)

Bottomley, P.D.W., Coquerelle, M.
Electrochemical Experiments on UO₂ Corrosion
in Aqueous Solutions
(Proceedings in Corrosion Science)

**Gordon Research Conference on Particle-
Solid Interactions**
July 6 - 10, 1992, Holderness, N.H. (USA)

Matzke, Hj.
Chemical and Physical Effects in Waste
Matrices Caused by Particle Impact and
Implantation

**Annual Meeting of the Electron Microscopy
Society of America (EMSA)**
August 16 - 21, 1992, Boston, Massachusetts
(USA)

Farthing, I., Love, G., Scott, V.D., Walker, C.T.
A New and Versatile Computer Program for
Correcting EPMA Data

**8th International Symposium on the
Thermodynamics of Nuclear Materials
(STNM-8)**
August 16 - 21, 1992, Snowbird, Utah (USA)
(Proceedings in J. Nucl. Mater.)

Fuger, J.
Problems in the Thermodynamics of the
Actinides in Relation with the Back-End of the
Nuclear Fuel Cycle

Matzke, Hj., Vernaz, E.
Thermal and Physicochemical Properties
Important for the Long Term Behavior of
Nuclear Waste Glasses

**Spectrum '92 - International Conference on
Hazardous and Radioactive Waste
Management**
August 23 - 27, 1992, Boise, Idaho (USA)

van Geel, J., Koch, L., Orlowski, S.
Partitioning and Transmutation of Long-Lived
Radio-Nuclides

**Hiroshima Workshop on Transport and
Thermal Properties of f-Electron Systems**
August 30 - September 2, 1992, Hiroshima
(J)

*Amanowicz, M., Ayache, C., Kitazawa, H.,
Kwon, Y.S., Ohe, Y., Rebizant, J., Spirlet, J.C.,
Rossat-Mignod, J., Suzuki, T., Kasuya, T.*
Low-Temperature Magnetotransport of the
Intermetallic Actinide Compound NpPt₃
(Proceedings in Special Volume, Plenum
Publishing Corp.)

**13th International Conference on X-Ray
Optics and Microanalysis**
August 31 - September 4, 1992, Manchester
(USA)

Farthing, I., Love, G., Scott, V.D., Walker, C.T.
A Versatile Computer Program for Improving
The Precision of Quantitative Electron Probe
Microanalysis

Bottomley, P.D.W., Daguzan-Lemoine, F.
An Electro-analytical Examination of the Gas
Retention in a Ramped (U, Pu)O₂ Irradiated
Fuel

European Aerosol Conference
September 6 - 11, 1992, Oxford (UK)
 (Proceedings in J. Aerosol Sci. 23 Suppl 1 (1992))

Magill, J.
 On the Optimization of Acoustic Cavities for
 Aerosol Conditioning
 pp. S67-S70

*Magill, J., Capéran, Ph., Somers, J., Richter, K.,
 Fourcaudot, S., Barraux, P., Lajarge, P.,
 Gallego, J.A., Riera, E., Rodriguez, G.,
 Seifert, N.*
 Characteristics of an Electro-Acoustic
 Precipitator (EAP)
 pp. S803-S806

van Geel, J., Magill, J., Schmidt, H.E.
 A Survey of Aerosol Research in European
 Community Programmes
 pp. S9-S13

*Baierl, T., Drosselmeyer, E., Polzer, G.,
 Seidel, A., Thiele, H., Wilczek, W.*
 Cytotoxic Effects of High T_c Superconducting
 Materials: Modification by Phospholipids and
 Release of Pro-inflammatory Mediators
 pp. S527-S530

**8th International Conf. on Ion Beam
 Modification of Materials (IBMM-8)**
September 7 - 11, 1992, Heidelberg (D)

*Turos, A., Matzke, Hj., Wielunski, M.,
 Nowicki, L.*
 Radiation Defects in the Oxygen-Sublattice of
 UO_2 Single Crystals
 (Proceedings in Nucl. Instr. and Methods B)

**International Conference on Strongly
 Correlated Electron Systems**
September 7 - 11, 1992, Sendai (J)
 (Proceedings in Physica B)

*Kitazawa, H., Ayache, C., Amanowicz, M.,
 Kwon, Y.S., Ohe, Y., Rossat-Mignod, J.,
 Rebizant, J., Spirlet, J.C., Suzuki, T., Kasuya, T.*
 Hall Effect and Magnetoresistance of the
 Intermetallic Actinide Compound $NpPt_3$

Lander, G.H. (invited)
 Neutron and Synchrotron X-Ray Scattering
 Experiments on Actinides

*Mendik, M., Wachter, P., Spirlet, J.C. Rebizant,
 J. (invited)*
 The Intermediate-Valent Pu
 Monochalcogenides : Negative Elastic
 Constants

*Sanchez, J.P., Ayache, C., Blaise, A., Bouillet,
 M.N., Burette, P., Oddou, J.L., Rossat-Mignod, J.,
 Bakker, K., Franse, J.J.M., Rebizant, J., Spirlet,
 J.C.*
 Magnetic Properties of $NpPt_3$

*Zwirner, S., Spirlet, J.C., Rebizant, J., Potzel,
 W., Kalvius, G.M., Steibel, Ch. Steglich, F.*
 Mössbauer Spectroscopy of $NpPd_2Al_3$

**3rd International Conference on Nuclear
 and Radiochemistry**
September 7 - 11, 1992, Vienna (A)

*Lausch, J.R., Garcia Alonso, J.I., Glatz, J.-P.,
 Koch, L., Walker, C.*
 Analysis of Fines from Dissolution of
 Commercial LWR Fuel

*Garcia Alonso, J.I., Thoby-Schultendorff, D.,
 Giovannone, B., Koch, L.*
 Analysis of Long-Lived Radio Nuclides

*Wellum, R., Brandalise, B., Koch, L., van Geel,
 J.*
 Robotized Conditioning of Radioactive Samples
 for Isotope Analysis

Koch, L., Nicolaou, G., van Geel, J.
 Transmutation of ^{237}Np and ^{241}Am by Fast
 Neutrons into Less Radiotoxic Nuclides

*Garcia Alonso, J.I., Glatz, J.-P., Kameyama, T.,
 Koch, L., Pagliosa, G., Tsukada, T., Yokoyama,
 H.*
 Dissolution Behaviour of Highly Burnt Fuel

*Apostolidis C., Koch, L., Molinet R., van Geel, J.,
 Geerlings, M.W.*
 Production of ^{225}Ac and ^{213}Bi for Labelled
 Monoclonal Antibodies

3rd International Conference on Plasma Source Mass Spectrometry
September 13 - 18, 1992, Durham (UK)
 (Proceedings in Applications of Plasma Source Spectrometry, Royal Soc. of Chemistry, 1993)

Betti, M., Garcia Alonso, J.I., Sato, T., Arboré, P., Koch, L.
 Analysis of Highly Radioactive Liquid Samples by ICP-MS

Garcia Alonso, J.I., Garcia Serrano, J., Babelot, J.F., Closset, J.C., Koch, L., Nicolaou, G.
 Laser Ablation ICP-MS on Spent Nuclear Fuels

IAEA Specialist's Meeting on the Use of FBRs for Actinide Transmutation
September 22 - 24, 1992, Obninsk (Russian Federation)

Koch, L.
 Status of Transmutation

Koch, L., Coquerelle, M., Richter, K.
 Minor Actinide-Containing Fuels for Transmutation Purposes

ALS Workshop on Synchrotron Radiation in Transactinium Research
October 1 - 2, 1992, Berkeley, CA (USA)

Lander, G.H.
 Magnetic X-Ray Scattering Experiments at Resonant Energies

Naegele, J.R.
 High-Resolution Electron Spectroscopy of Highly Radioactive Actinides: Consequences for a Future Transuranium Beamline

3rd International Conference on CANDU Fuel
October 4 - 8, 1992, Chalk River, Ontario, (CDN)

Lucuta, P.G., Verrall, R.A., Matzke, H.J., Hastings, I.J.
 Thermal Conductivity of SIMFUEL

4th Workshop Actinides under Pressure
October 12 - 13, 1992, Karlsruhe (D)
 (Proceedings in Physica B)

Brooks, M.S.S., Eriksson, O., Johansson, B., Severin, L., Trygg, J.
 Pressure Effects upon the Magnetization of Actinide Compounds

Haire, R.G., Gensini, M., Heathman, S., Benedict, U.
 The High-Pressure Behavior of Lanthanide and Actinide Pnictides

Link, P., Benedict, U., Wittig, J., Wühl, H.
 The Electrical Resistance of USe and UTe under High Pressure

Mendik, M., Wachter, P., Rebizant, J., Spirlet, J.C.
 The Elastic Constants of the Pu and U Monochalcogenides

Zwirner, S., Potzel, W., Spirlet, J.C., Rebizant, J., Gal, J. Kalvius, G.M.
 NpX₃ Compounds under High Pressure - A Status Report

12th International Vacuum Congress and 8th International Conference on Solid Surfaces
October 12 - 16, 1992, The Hague (NL)

Almeida, T., Cox, L.E., Ward, J.W., Naegele, J.R.
 Gas Adsorption Studies on Pu-Metal by Photoemission Spectroscopy
 (Proceedings in Surface Science)

Conf. on Fuel, High-Level and Alpha-Bearing Radioactive Waste
October 19 - 23, 1992, Antwerpen (NL)

Nicolaou, G., Würz, H., Koch, L.
 LWR Spent Fuel Characterisation by Non-Destructive Assay

Int. Conf. on Design and Safety of Advanced Nuclear Power Plants
October 25 - 29, 1992, Tokyo (J)

Faugère, J.L., Pelletier, M., Rousseau, J., Guérin, Y., Richter, K., Ledergerber, H.
 The CEA He-Bonded Nitride Fuel Design

**Arbeitskreis Thermophysik
November 5 - 6, 1992, Dresden (D)**

Tasman, H.A.
Black Box Mark 3: Neue Elektronik für
Ultraschall-Thermometrie

**OECD/NEA 2nd General Meeting of the
International Information Exchange
Program on Actinide and Fission Product
Separation and Transmutation
November 11 - 13, 1992, Argonne, Ill (USA)**

Koch, L.
Criteria for the Development of Targets and
Fuels in Nuclear Transmutation

*Inoue, T., Kurata, M., Koch, L., Spirlet, J.-C.,
Babelot, J.-F., Sari, C.*
Recycling of Minor Actinides in Metal Fuel
FBRs

**Conference on Magnetism and Magnetic
Materials
December 1 - 4, 1992, Houston, Texas (USA)
(Proceedings in *J. Appl. Physics*)**

Stirling, W.G., Lander, G.H.(invited)
Resonant Magnetic Scattering from 5f Magnetic
Materials

*Nakotte, H., de Boer, F.R., Havela, L.,
Svoboda P., Sechovsky V., Kergadallan Y.,
Spirlet, J.C., Rebizant J.*
Magnetic Anisotropy of UCoGa.

2. Books and Periodicals

(including publications which had been submitted or presented at conferences in 1991 and which appeared in print in 1992)

Almeida, T., Havela, L., Spirlet, J.C., Naegele, J.R.
Gas Adsorption Studies on UNiAl by Photoemission Spectroscopy
Surface Science 269-270 (1992) 1180-1185

Amoretti, G., Blaise, A., Caciuffo, R., Di Cola, D., Fournier, J.M., Hutchings, M.T., Lander, G.H., Osborn, R., Severing, A., Taylor, A.D.
Neutron-Scattering Investigation of the Electronic Ground State of Neptunium Dioxide
J. Phys. Condensed Matter 4 (1992) 3459-3478

Apostolidis, C., Kanellakopoulos, B., Klenze, R., Reddmann, H., Schulz, H., Amberger, H.-D.
Zur Elektronenstruktur metallorganischer Komplexe der f-Elemente
XXIX. Optische und magnetochemische Untersuchungen an Mono- und Bis-Acetonitriladdukten des Grundkörpers Tris-Cyclopentadienyl-Praseodym (III)
J. Organomet. Chem. 426 (1992) 307 - 323

Auluck, S., Gasche, T., Brooks, M.S.S., Johansson, B.
Magnetic and Magneto-Optical Properties of Uranium Sulphide
J. Magn. Magn. Mater. 35 (1992) 104 - 107

Bartscher, W.
Actinide Hydrides
Chapter in Hydrogen Metal Systems
Balaban Publishers, Israel, VCH Weinheim (submitted)

Basalo, C. (ed.), Bottomley, P.D.W. (Translator), Holmes, D.R. (Translation editor)
Water and Gas Mains Corrosion, Degradation and Protection
English Edition published by Ellis Horwood Ltd, London (1992)

Bauer, M., Brooks, M.S.S., Dormann, E.
Orbital Polarization of the Conduction Electrons in Ferromagnetically ordered GdAl₂
Phys. Rev. B (submitted)

Benedict, U., Holzapfel, W.B.
High-Pressure Studies - Structural Aspects
Chapter to be published in Handbook on Physics and Chemistry of the Rare Earths, Special volume Lanthanides/Actinides, North-Holland, Amsterdam
(K. Gschneidner, G.H. Lander, eds.) (submitted)

Benedict, U., Dabos-Seignon, S., Heathman, S., Dancausse, J.P., Gensini, M., Gering, E., Spirlet, J.C.
High-Pressure Phases and Compressibility of Neptunium and Plutonium Compounds in Transuranium Elements - A Half Century, American Chemical Society, Washington, D.C. 1992 (L.R. Morss and J. Fuger, eds.) pp 396 - 403

Benedict, U., Dabos-Seignon, S., Dancausse, J.P., Gensini, M., Gering, E., Heathman, S., Luo, H., Staun Olsen, J., Gerward, L., Haire, R.G.
Actinide Compounds under Pressure
J. Alloys Comp. 181 (1991) 1-12

Blaise, A., Bouillet, M.N., Bourdarot, F., Burlet, P., Rebizant, J., Rossat-Mignod, J.P., Sanchez, J.P., Spirlet, J.P., Vogt, O.
Magnetic Structure and Properties of NpS and NpSe
J. Magn. Magn. Mater. 104 - 107 (1992) 33

Brooks, M.S.S., Johansson, B.
Density Function Theory of the Ground-State Magnetic Properties of Rare Earths and Actinides
Chapter to be published in Ferromagnetic Materials, North Holland, Amsterdam (K.H.J. Buschow, ed.) (submitted)

Brooks, M.S.S., Gasche, T., Auluck, S., Nordström, L., Severin, L., Trygg, J., Johansson, B.
Density Functional Theory of Molecular Fields in R-M Systems,
J. Magn. Magn. Mater. 104 - 107 (1992) 1381

Brooks, M.S.S., Auluck, S., Gasche, T., Trygg, J., Nordström, L., Severin, L., Johansson, B.
Theory of the Curie Temperatures of the Rare-Earth Metals
J. Magn. Magn. Mater. 104 - 107 (1992) 1496

Brown, P.J., Hayden, S.M., Lander, G.H., Zarestky, J., Stassis, C., Honig, J.M.
Observation of Incommensurate Antiferromagnetic Correlations in $\text{La}_{1.8}\text{Sr}_{0.2}\text{NiO}_4$,
Physica B 180 - 181 (1992) 380-382

Burlet, P., Bourdarot, F., Rossat-Mignod, J., Sanchez, J.P., Spirlet, J.C., Rebizant, J., Vogt, O.
Neutron Diffraction Study of the Magnetic Ordering in NpBi,
Physica B 180 - 181 (1992) 131-132

Caciuffo, R., Amoretti, G., Blaise, A., Fournier, J.M., Hutchings, M.T., Lander, G.H., Osborn, R., Severing, A., Taylor, A.D.
Neutron Inelastic Experiments on Actinide Dioxides: Search for Crystal Field Excitations,
Physica B 180 - 181 (1992) 149-152

Chkuaseli, V.F., Matzke, Hj.
Fission Gas Bubble Behaviour in Uranium Dioxide
J. Nucl. Mater. (submitted)

Dancausse, J.P., Gering, E., Heathman, S., Benedict, U., Gerward, L., Staun Olsen, S., Hulliger, F.
Compression Study of Uranium Borides UB_2 , UB_4 and UB_{12} by Synchrotron X-Ray Diffraction
J. Alloys Comp. 189 (1992) 205-208

Dancausse, J.P., Heathman, S., Benedict, U., Gerward, L., Staun Olsen, J., Hulliger, F.
High Pressure X-Ray Diffraction Study of UC_2 Using Synchrotron Radiation
J. Alloys Comp. (submitted)

Delapalme, A., Raison, P., Schweiss, P., Lander, G.H., Rebizant, J., Kanellakopoulos, B.
Studies of $\text{U}(\text{C}_5\text{H}_5)_3\text{Cl}$ - II Temperature Dependence of the Molecular Configurations
Molecular Physics (submitted)
Delapalme, A., Raison, P., Lander, G.H., Kanellakopoulos, B.
Studies of UCp_3Cl - IV Magnetisation Density
Molecular Physics (submitted)

Farthing, I., Lover, G., Scott, V.D., Walker, C.T.
A Modular Universal Correction Procedure for Quantitative EPMA
Microchim. Acta 12 (1992) 117-124

Fuger, J., Khodakovski, I.L., Sergeeva, E.I., Medvedev, V.A., Navratil, J.D. (eds)
The Chemical Thermodynamics of Actinide Elements and Compounds
Part 12: The Actinide Aqueous Inorganic Complexes
International Atomic Energy Agency, Vienna
STI/PUB/424/12 (1992)

Garcia Alonso, J.I., Babelot, J.F., Glatz, J.P., Cromboom, O., Koch, L.
Applications of a Glove-Box ICP-MS for the Analysis of Nuclear Materials
Radioanalytica Chimica Acta (submitted)

Garcia Alonso, J.I., Thoby-Schultendorff, D., Giovannone, B., Koch, L.
Analysis of Long-Lived Radionuclides by ICP-MS
J. Radioanal. Chem. (submitted)

Gasche, T., Auluck, S., Brooks, M.S.S., Johansson, B.
Theory of the Magnetism of Ternary Uranium Compounds
J. Magn. and Magn. Mater. 104-107 (1992) 37

Gouder, T., Colmenares, C.A., Naegele, J.R., Spirlet, J.C., Verbist, J.
Study of CO Adsorption on U, UNi_2 and UNi_5
Surf. Sci. 264 (1992) 354-364

Gouder, T., Colmenares, C.A., Naegele, J.R., Spirlet, J.C., Verbist, J.
A Surface Spectroscopy Study of the Oxidation Properties of UNi_2 and UNi_5
Surf. Sci. 265 (1992) 175-186

Grenthe, I., Fuger, J., Konings, R.J.M., Lemire, R.J., Muller, A.B., Nuyen-Trung, C., Wanner, H., Forest, I. (eds.)
Chemical Thermodynamics of Uranium; Chemical Thermodynamics Series I
NEA/OECD; North-Holland, Amsterdam (1992)

Havela, L., Almeida, T., Naegele, J.R., Sechovsky, U., Brück, E.
High Resolution Photoemission on UPdSn and UNiAl ,
J. Alloys Comp. 181 (1991) 205-210

Havela, L., Sechovsky, V., Naegele, J.R., Almeida, T., Brück, E.H., Nakotte, H., de Boer, F.R.

5f Electron Localisation in UTX Compounds
J. Magn. Magn. Mater. 104-107 (1992) 23

Hayden, S.M., Lander, G.H., Zarestky, J., Brown, P.J., Stassis, C., Metcalf, P., Honig, J.M.
Incommensurate Magnetic Correlations in $\text{La}_{1.8}\text{Sr}_{0.2}\text{NiO}_4$
Phys. Rev. Lett. 68 (1992) 1061-1064

Hocking, W.H., Verrall, R.A., Lucuta, P.G., Matzke, H.
Depth Profiling Studies of Ion-Implanted Cesium and Rubidium in SIMFUEL and Uranium Dioxide
Radiat. Eff. and Defects in Solids 4 (1992) 125

Holland-Moritz, E., Lander, G.H.
Neutron Inelastic Scattering of Actinides and Anomalous Lanthanides
Chapter to be published in Handbook on Physics and Chemistry of the Rare Earths, Special volume Lanthanides/Actinides, North-Holland, Amsterdam
(K. Gschneidner, G.H. Lander, eds.) (submitted)

Joachim, J.E., Apostolidis, C., Kanellakopoulos, B., Maier, R., Marques, N., Meyer, D., Müller, J., de Matos, A.P., Nuber, B., Rebizant, J. et al.
Metall-organische Chemie des Technetiums - VIII. Technetium(I)-Carbonyl Komplexe mit Polypyrazol-1-yl - borato-Liganden im Vergleich mit seinen Mn- und Re-Homologen
J. Organomet. Chem. (submitted)

Joachim, J.E., Apostolidis, C., Kanellakopoulos, B., Maier, R., Ziegler, M.L.
Metall-organische Chemie des Technetiums - IX. Synthese, Charakterisierung und Untersuchung der Verbindungen Hydrotris (1-Pyrazolyl) borato-Technetium(VII) Trioxid und Hydrotris (3,5-Dimethyl-1-Pyrazolyl) Borato-Technetium (VIII) Trioxid
J. Organomet. Chem. (submitted)

Joachim, J.E., Apostolidis, C., Kanellakopoulos, B., Maier, R., Ziegler, M.L., Rebizant, J., Mayer, D.

Metall-organische Chemie des Technetiums - X. Synthese, Charakterisierung und Röntgenstrukturanalyse von η -Distickstoff-Bis (Hydrotris (3,5-Dimethylpyrazolyl) - borato - Technetium Dicarbonyl, $(\text{L}^*\text{Tc}(\text{CO})_2)_2(\eta\text{-N}_2)$
J. Organomet. Chem. (submitted)

Johansson, B., Brooks, M.S.S.
Theory of Cohesion in Lanthanides and Actinides
Chapter to be published in Handbook on the Physics and Chemistry of the Rare Earths, Special volume Lanthanides/Actinides, North-Holland, Amsterdam
(K. Gschneidner, G.H. Lander, eds.) (submitted)

Jones, D.L., Langridge, S., Stirling, W.G., Lander, G.H., Rebizant, J., Spirlet, J.C., Alba, M., Vogt, O.
Critical Scattering Measurements on Neptunium Arsenide
Physica B 180 - 181 (1992) 38-90

Jones, D.L., Stirling, W.G., Lander, G.H., Osborn, R., Taylor, A.D., Mattenberger, K., Vogt, O.
Search for Intermultiplet Transitions in USb
Physica B 180 - 181 (1992) 199-202

Koch, L.
Plutonium and Plutonium Compounds
Chapter in Ullmann's Encyclopedia of Industrial Chemistry
VCH Publishers, Inc., Weinheim Vol. A 21 (1992) 133-142

Lander, G.H.
Metallic Covalency in Actinide Compounds, in Transuranium Elements - A Half Century, American Chemical Society, Washington, D.C. 1992 (L.R. Morss and J. Fuger, eds.) 338-344

Lander, G.H., Shapiro, S.M., Veltier, C., Dianoux, A.J.
Observation of Low-Energy Magnetic Response in the Heavy-Fermion Compound UBe_{13}
Phys. Rev. B 46 (1992) 5387-5391

Lander, G.H., Stirling, W.C.
Magnetic X-Ray Scattering
Plenary Lecture at the European Physical Society Conference, Prague 1992
Phys. Scr. T45 (1992) 15-21

- Lander, G.H.*
Neutron Elastic Scattering of Actinides and Anomalous Lanthanides.
Chapter to be published in Handbook on the Physics and Chemistry of the Rare Earths, Special volume Lanthanides/Actinides, North-Holland, Amsterdam
(K. Gschneidner, G.H.Lander, G. Choppin, L.Eyring, eds.) (submitted)
- Langridge, S., Stirling, W.G., Lander, G.H., Vogt, O.*
Magnetic Excitations in Monodomain Ferromagnetic $USb_{0.8}Te_{0.2}$
J. Alloys Comp. 181 (1992) 194-196
- Liang, Z., Marshall, A.G., Oires de Matos, A., Spirlet, J.C.*
Gas-Phase Uranium Ion Reactions with 2,4,6-Tri-*t*-butylphenol and 1,3,5-Tri-*t*-butylbenzene: Fourier Transform-Ion Cyclotron Resonance Mass Spectrometry
in Transuranium Elements - A Half Century, American Chemical Society, Washington, D.C. 1992 (L.R.Morss and J.Fuger, eds.) 247 - 250
- Link, P., Benedict, U., Wittig, J., Wühl, H.*
High-Pressure Resistance Study of UTe
J. Phys. Condens. Matter 4 (1992) 5585-5589
- Lucuta, P., Matzke, Hj., Verrall, R.A., Tasman, H.A.*
Thermal Conductivity of SIMFUEL
J. Nucl. Mater. 188 (1992) 198
- Maier, R., Kanellakopoulos, B., Apostolidis, C.*
Molekülstruktur und Ladungsverteilung in metallorganischen Verbindungen der 4f und 5f-Elemente II: Dielektrische Untersuchungen an metallorganischen Komplexen
J. Organomet. Chem. 427 (1992) 33-38
- Maier, R., Kanellakopoulos, B., Apostolidis, C., Nuber, B.*
Molekülstruktur und Ladungsverteilung der 4f- und 5f-Elemente
III. Dipolmomente und Ladungsverteilung der 1:1-Addukte der Tris(Cyclopentadienyl) Lanthanoide(III) bzw.-Actinoide(III)
J. Organomet. Chem. 435 (1992) 275-289
- Mattenberger, K., Vogt, O., Rebizant, J., Spirlet, J.C.*
Magnetization Measurements on Single Crystals of Neptunium Monopnictides, in Transuranium Elements - A Half Century, American Chemical Society, Washington, D.C. 1992 (L.R.Morss and J.Fuger, eds.) 378 - 394
- Mattenberger, K., Vogt, O., Rebizant, J., Spirlet, J.C., Bourdarot, F., Burlet, P., Rossat-Mignod, J., Bouillet, M.N., Blaise, A., Sanchez, J.P.*
Magnetic Properties of Single Crystalline NpAs-NpSe Mixed Compounds Studied by Magnetisation, Neutron Diffraction and Mössbauer Measurements
J. Magn. Magn. Mater. 104-107 (1992) 43
- Matzke, Hj.*
Indentation Techniques for the Evaluation of Mechanical Properties of Ceramics and Glasses
Trans. Tech. Publ. Key Engineering Materials 56-57 (1991) 365
- Matzke, Hj.*
Mechanisms and Kinetics of Leaching of UO_2 in Water
Solid State Ionics 49 (1991) 189
- Matzke, Hj.*
Effects of Radiation on Nuclear Materials
J. Energy Soc. Japan 33 (1991) 757
- Matzke Hj.*
Diffusion in Carbides and Nitrides: Unsolved Problems
Chapter in Diffusion in Solids: Unsolved Problems
Trans. Tech. Publ. Switzerland (G. Murch, ed.)
Diffusion and Defect Data 83 (1992) 111-130
- Matzke, Hj.*
On the Rim Effect in High Burnup UO_2 LWR Fuels
J. Nucl. Mater. 189 (1992) 141-148
- Matzke, Hj.*
Radiation Damage-Enhanced Dissolution of UO_2 in Water
J. Nucl. Mater. 190 (1992) 101-106
- Matzke, Hj.*
Diffusion Processes in Nuclear Fuels
Chapter in Diffusion Processes in Nuclear Materials
Elsevier Science Publishers B.V. (1992) (R.P. Agarwala ed.)

- Matzke, Hj., Turos, A.*
Ion Implantation Studies in UO_2 and UN
J. Nucl. Mater. 188 (1992) 285
- Matzke, Hj.*
Radiation Effects in Nuclear Fuel Materials
in Matériaux sous irradiation, Proc. Trans.
Tech. Pub. (submitted)
- Matzke, Hj.*
Ceramics for Energy Production and
Environmental Applications with Emphasis on
Nuclear Energy
Ceram. Acta (submitted)
- Mezzetti, L., Esposito, L., Matzke, Hj., Pilotti, L.,
Tucci, A.*
Biocompatibility of Dental Materials:
Dissolution Behaviour and Related Hardness
Ceram. Acta (submitted)
- Naegele, J.R.*
Chapter on Actinides in Landolt - Börnstein, Vol
23 (New Series) Electronic Structure of Solids,
Photon Spectra and Related Data, Springer,
Berlin (submitted)
- Morss, L.R., Fuger, J.*
Transuranium Elements - Their Impact on
Science and Technology
in Transuranium Elements - A Half Century,
American Chemical Society, Washington, D.C.
1992 (L.R.Morss and J.Fuger, eds.) 2 - 8
- Nordström, L., Brooks, M.S.S., Johansson, B.*
Theoretical Study on the Enhanced
Paramagnetism in CeNi_x ($x = 1, 2$ and 5).
Phys. Rev. B46 (1992) 3458-3464
- Nordström, L., Brooks, M.S.S., Johansson, B.*
Calculation of Orbital Magnetism and
Magnetocrystalline Anisotropy Energy in YCo_5
J. Phys. Condens. Matter 4 (1992) 3261
- Nordström, L., Brooks, M.S.S., Johansson, B.*
Theory of Magnetism of R-Co Intermetallic
Compounds
J. Magn. Magn. Mater. 104-107 (1992) 1378
- Nordström, L., Brooks, M.S.S., Johansson, B.*
Ab initio Calculation of the Orbital Magnetism
and Magnetocrystalline Anisotropy Energy of
 YCo_5
J. Magn. Magn. Mater. 104-107 (1992) 1942
- O'Carroll, C., Lassmann K.*
Numerical Solution for the Nonlinear Diffusion
Equation describing the Transport of Volatile
Fission Products in Nuclear Fuels
Nucl. Technol. 99 (1992) 268-273
- Ogawa, T., Verrall, R.A., Matzke, Hj.*
Release of Ion-Implanted Kr from $(\text{Th,U})\text{O}_2$ -
Effect of Matrix Oxidation
Solid State Ion. 49 (1991) 211
- Paixão, J.A., Lander, G.H., Brown, P.J.,
Nakotte, H., de Boer, F.R., Brück, E.*
Magnetization Density in URhAl - Evidence for
Hybridisation Effects
J. Phys. Condens. Matter 4 (1992) 829-846
- Paixão, J.A., Lander, G.H., Tang, C.C.,
Stirling, W.G., Gibbs, D., Blaise, A.,
Burllet, P., Brown, P.J., Vogt, O.*
Magnetization, Neutron and Resonant X-Ray
Diffraction Studies of $\text{U}_{0.85}\text{Th}_{0.15}\text{Sb}$
Phys. Rev. B (submitted)
- du Plessis, P. de V., Lander, G.H., Strydom,
A.M., Fak, B.*
Phonon Softening in UO_2
Physica B 180 - 181 (1992) 321-322
- Raison, P., Delapalme, A., Lander, G.H., Carlile,
C., Williams, J.,
Kanellakopoulos, B., Apostolidis, C., Rebizant, J.*
Study of Motion of Cyclopentadienyl Rings in
 UCp_3Cl by Quasielastic Neutron Scattering,
Physica B 180 - 181 (1992) 720-722
- Raison, P., Delapalme, A., Kiat, J.M., Schweiss,
P., Kanellakopoulos, B.,
Rebizant, J., Apostolidis, C., Gonthier-Vassal,
A., Lander, G.H., Brown, P.J.*
Studies of $\text{U}(\text{C}_5\text{H}_5)_3\text{Cl}$ - I. Evidence for
Structural Phase Transitions Below Room
Temperature
Molecular Physics (submitted)
- Raison, P., Lander, G.H., Delapalme, A.,
Williams, J.H., Kahn, R., Carlile, C.J.,
Kanellakopoulos, B.*
Studies of $\text{U}(\text{C}_5\text{H}_5)_3\text{Cl}$ - III. Reorientational
Motions of Cyclopentadienyl Rings
Molecular Physics (submitted)

Ray, I.L.F., Thiele, H., Matzke, H.
Fission Gas Behaviour during Transients in High Burn-Up LWR Nuclear Fuel Samples studied by Electron Microscopy in Fundamental Aspects of Inert Gases in Solids, Plenum Press, New York (1991) (S.E.Donnely and J.H.Evans, eds.)

Ray, I.L.F., Thiele, H., Matzke, H.
Transmission Electron Microscopy Study of Fission Product Behaviour in High Burn-Up UO₂
J. Nucl. Mater. 188 (1992) 90

Rebizant, J., Spirlet, M.R., Apostolidis, C., Kanellakopoulos, B.
Structure of Tetrakis(Cyclopentadienyl) Uranium(IV) Acetate Dioxide (U(C₅H₅)(CH₃CO₂)₂)₄O₂
Acta Crystallogr. C48 (1992) 452-454

Ronchi, C., Hiernaut, J.P., Hyland, G.J.
Emissivity X-Points in Solid and Liquid Refractory Transition Metals
Metrologia 29 (1992) 261-271

Sanchez, J.P., Lebech, B., Wulff, M., Lander, G.H., Tomala, K., Mattenberger, K., Vogt, O., Blaise, A., Rebizant, J., Spirlet, J.C., Brown, P.J.
Examination of the Magnetic Properties of NpCo₂
J. Phys. Condens. Matter 4 (1992) 9423-9440

Scheibel, H.G., Friehmelt, V., Matzke, H.
Mechanical Impact of High-Level Waste Glass Canisters: Waste Glass Fracture, Aerosol Release, and Activity Source terms, in High Level Radioactive Waste and Spent Fuel Management, Korean Nucl. Soc. Seoul (1992) (S.C.Slate et al., eds.)

Severin, L., Johansson, B., Brooks, M.S.S.
Mechanisms for Itinerant Magnetism in Intermetallic Compounds
J. Magn. Magn. Mater. 104-107 (1992) 745

Spirlet, M.R., Rebizant, J., Apostolidis, C., Kanellakopoulos, B., Dornberger, E.
Structure of Bis (ammonium) Hexanitratoplutonium(IV) and Bis (ammonium) Hexanitratothorium(IV)
Acta Crystallogr. C48 (1992) 1161-1164

Spirlet, M.R., Rebizant, J., Bettonville, S., Goffart, J.
Structure of Chlorotris (1,2,4,5,6,7-Hexamethylindenyl) Uranium(IV)
Acta Crystallogr. C48 (1992) 1221-1223

Spirlet, M.R., Rebizant, J., Bettonville, S., Goffart, J.
The Crystal Structure of Methyl (1 - 3 - η - 1 - Ethylindenyl)Thorium IV
Acta Crystallogr. C (submitted)

Spirlet, M.R., Rebizant, J., Bettonville, S., Goffart, J.
The Crystal Structure of Tris (Indenyl) Uranium Trifluoroethanolate
J. Organomet. Chem. (submitted)

Spirlet, M.R., Rebizant, J., Apostolidis, C., Kanellakopoulos, B.
Bis(Cyclopentadienyl)Actinide(IV) Compounds - I. The structure of Dichlorobis(Pentamethyl-η⁵-Cyclopentadienyl)Uranium(IV) and Dichlorobis(Pentamethyl-η⁵-Cyclopentadienyl)Thorium(IV)
Acta Crystallogr. C48 (1992) 2135-2137

Spirlet, M.R., Rebizant, J., Apostolidis, C., Kanellakopoulos, B.
Structure of Tris(η⁵-Cyclopentadienyl) Uranium Thiocyanide
Acta Crystallogr. C (submitted)

Stirling, W.G. and Lander, G.H.
X-Ray Magnetic Diffraction from Rare-Earths and Actinides
Synchrotron Radiation News 5 No. 4 (1992) 17-21

Tang, C.C., Stirling, W.G., Lander, G.H., Gibbs, D., Herzog, W., Carra, P., Mattenberger, K., Vogt, O.
Resonant Magnetic X-Ray Scattering in a Series of Uranium Compounds
Phys. Rev. B 46 (1992) 5287-5297

Trygg, J., Brooks, M.S.S., Johansson, B.
Ab initio Calculation of the Magnetism in GdFe₁₂
J. Magn. Magn. Mater. 104 - 107 (1992) 1447

Turos, A., Matzke, H.
Lattice Location of Fission Products in UO₂ Single Crystals
Nucl. Instrum. Methods Phys. Res. B 65 (1992) 315

Turos, A., Matzke, Hj., Chaumont, J., Thomé, L.
Location of Oxygen Atoms in UO₂ Single
Crystals by Resonant Scattering of He Ions
Nucl. Instrum. Methods Phys. Res. B 66 (1992)
280

*Vernaz, E., Loida, A., Malow, G.,
Marples, J.A.C., Matzke, Hj.*
Long-Term Stability of High-Level Waste
Forms
in Radioactive Waste Management and
Disposal, Elsevier (1991) (L.Cecille, ed.)

*Wang, X.L., Stassis, C., Johnston, D.C., Leung,
T.C., Ye, J., Harmon, B.N., Lander, G.H.,
Schulz, A.J., Loong, C.-K., Honig, J.M.*
Neutron-Diffraction Study of the
Antiferromagnetic Form Factor of La₂NiO₄
Phys. Rev. B 45 (1992) 5645-5653

*Wastin, F., Rebizant, J., Spirlet, J.C., Sari, C.,
Walker, C.T., Fuger, J.*
Synthesis and Characterisation of Some New
Transuranium Intermetallic Compounds with
ThCr₂Si₂ and CaBe₂Ge₂ Structure Type
J. Alloys Comp. (submitted)

Yamashita, M., Matzke, Hj., Linker, G.
Tellurium and Palladium Diffusion in the
German Waste Glass VG98/12 Measured with
the RBS Method
Mater. Res. Soc. Symp. Proc. 257 (1992) 183

Yamashita, M., Matzke, Hj.
Self-Diffusion of Na in GP98/12 Waste Glass
under Alpha-Ray Irradiation
in Chemical and Physical Modifications Induced
by Irradiation in Glasses, North Holland,
Amsterdam (1992) (P.Mazzoldi, ed.)

3. Reports

Buijs, K., Chavane, B., Baumgärtner, E.
Contaminated Smoke: A Simulation of the
Heavy Metal Containing Aerosols from Fires in
Plutonium Glove Boxes - Part II
EUR 14494 EN (1992)

Farthing, I., Walker, C.T., Love, G., Scott, V.D.
QUAD2: A Universal Correction Procedure for
EPMA - Users Manual
1992 - K0292160

Ferreira, T.M.
MITRAI Multicomponent Isotope Transport
Interactive
1992 - K0292157

Gagnol, P., Hiernaut, J.P.
Développement de la technique combinée
spectrométrie de masse - effusion de Knudsen
1992 - K0292164

Lassmann, K.
Minutes of TRANSURANUS Modifications
Version 2, Modification 1, Year 1991
(V2M1J91)
1992 - K0292156

Lassmann, K., van de Laar, J., Peter, G.
Analysis of CABRI Experiments using the
TRANSURANUS Code and the Coupled Codes
TRANSURANUS-CAMDYN
1992 - K0292158

Ronchi, C., Hiernaut, J.P., Hyland, G.J.
X-Points in the Spectral Emissivity of Solid and
Liquid Refractory Transition Metals Measured
by Multichannel Pyrometry
EUR 14220 EN (1992)

Ronchi, C.
Joint Project ITU-DGXIII-Keller Pyrowerk
GmbH - Multiwave Pyrometer -
1992 - K0292163

Schmidt, H.E., Richter, J., Ruczka, L. (ed.)
ITU Annual Report 1991
EUR 14493 EN (1992)

Tasman, H.A.
Emission Computer Tomography - A Literature
Review
1992 - K0292159

Tasman, H.A.
Control and Evaluation Electronics for
Ultrasonic Thermometry
1992 - K0292161

*Tasman, H.A., Gueugnon, J.F., Pellotiero, D.,
Sari, C., Walker, C.T.*
Ultrasonic Thermometers for PHEBUS-FPTO:
Material Specifications, Fabrication, Test
Results
1992 - K0292162

4. Patents

Spirlet, J.C., Moens, A., Inoue, T., Kurata, M.
Preparation of zirconium alloys with actinide elements by the direct oxide reduction with lanthanides or yttrium
Patent proposal P/2359 of April 13, 1992

Spirlet, J.C., Moens, A., Inoue, T., Kurata, M.
The separation of lanthanides and actinides by selective oxydation in zirconium alloys
Patent proposal P/2363 of May 5, 1992

Ronchi, C., Heinz, W.
A perfectly isotropic beam-splitting device for multichannel pyrometers
Patent proposal P/2379 of September 3, 1992

Spirlet, J.C., Bartscher, W., Lebrun, M., Moens, A., Inoue, T.
Preparation of a homogeneous mixture of lanthanide metallic phases in UZr, UPuZr, and UPuNpZr alloys
Patent proposal P/2399 of December 9, 1992

Spirlet, J.C., Kalbusch, J., Moens, A., Lefebvre, P., Inoue, T.
Preparation of highly homogeneous zirconium-actinide-lanthanide alloys by mechanical alloying and ball milling
Patent proposal P/2400 of December 9, 1992

Annex II

Collaborations with External Organisations

Argentina

CNEA Buenos Aires: Diffusion in solids (F.Dyment)

Austria

International Atomic Energy Agency, Vienna: Evaluation and Automation of techniques for safeguards analysis

Belgium

University of Liège: Single crystal growth, X-ray diffraction, and analysis (J. Goffart, L. Martinot, M.R. Spirlet)

Canada

AECL Chalk River: Gas release, SIMfuel production and property studies (I.Hastings, P.Lucuta, R.Verrall)

AECL Whiteshell: Behaviour of Rb and Cs in SIMfuel (W.Hocking)

Czech Republic

University of Prague: Magnetic and electrical measurements (V. Sechovsky, L. Havela)

University of Prague: Gas release measurements (V.Balek)

Peoples Republic of China

University of Beijing, Beijing: TRPO separation scheme development

Denmark

Risø National Laboratory: Neutron scattering (B. Lebech)

Technical University Lingby: High-pressure X-ray diffraction (L. Gerward)

University of Copenhagen: High pressure X-ray diffraction (J. Staun-Olsen)

France

CEN, Cadarache: Superfact (DEC)

CEN, Grenoble: Neutron diffraction, magnetic studies, transport properties and Mössbauer studies (A. Blaise, P. Burllet, J.M. Fournier, and J.P. Sanchez)

CEN, Saclay: Neutron diffraction (J. Rossat-Mignod, A. Delapalme)

CNRS, Grenoble: Crystallography of phase transitions (J.C. Marmeggi)

CNRS, Orsay: Basic studies on spent UO₂ fuel (J.C. Dran)

COGEMA, SGN, La Hague: On-site laboratories

Electricité de France: Paris: TRANSURANUS fuel pin code development

FRAMATOME, Paris: TRANSURANUS fuel pin code development

ILL, Grenoble: Polarized neutron diffraction and neutron inelastic scattering (P.J. Brown, C. Zeyen, T. Brueckel)

Inst. Curie, Paris: Mössbauer and high-pressure studies (M. Pagès, A. Tabuteau, A. Cousson, S. Dabos-Seignon)

Germany

Apparatebau Rothemühle, Wenden: Acoustic aerosol scavenging

Hahn-Meitner-Institut, Berlin: Ranges of ions in solids, B-profiles in leached glasses (D.Fink, J.Biersack)

Hahn-Meitner-Institut, Berlin: High-energy ion implantation (S.Klaumünzer)

Keller, Pyrowerk, Hannover: Fast multichannel pyrometry

KfA Jülich, Inst. für Festkörperforschung: Electrical resistivity under pressure (J. Wittig)

KfA Jülich, Institut für Chemische Technologie: Sample characterization (A. Solomah)

KfK, Karlsruhe, Inst. für Heisse Chemie: Susceptibility and crystal preparation (B. Kanellakopoulos)

KfK, Karlsruhe, Inst. für Nukleare Festkörperphysik: Electron spectroscopies (G. Fink)

KfK, Karlsruhe, Inst. für Technische Physik: Electrical resistivity under pressure (H. Wühl)

KfK, Karlsruhe: TRANSURANUS fuel pin code development

KfK, Karlsruhe, INE: Waste characterisation (L.Kahl)

KfK, Karlsruhe, INFP: Radiation damage studies, RBS analyses, channeling, ion implantation (O.Meyer, G.Linker)

KfK, Karlsruhe, Institut für Kernphysik III: On-site laboratory training

KfK Karlsruhe, Institut für Neutronenphysik und Reaktortechnik: Neutron collar development

KfK Karlsruhe, Institut für Kernphysik III: K-edge densitometry

Max Planck Institut für Festkörperphysik Stuttgart: High-pressure reflectivity studies (K. Syassen)

Siemens/KWU, Erlangen: Post-irradiation fuel element examination (R. Manzel)

Technischer Überwachungsverein Baden, Karlsruhe: TRANSURANUS fuel pin code development

Technischer Überwachungsverein Bayern, München: TRANSURANUS fuel pin code development

Technische Universität München: Mössbauer and μ SR studies (M. Kalvius, W. Potzel, L. Asch, S. Zwirner); X-ray absorption spectroscopy (G. Schütz)

Universität Stuttgart, IKE: Source term studies

Universität Stuttgart, IKE: Data bank system THERSYST (G. Neuer, G. Jaroma-Weiland)

Univ. München, Inst. Anorg. Chem.: Single crystal growth and X-ray diffraction (F. Lux, M. Böhme)

Italy

Centro Ceramico Bologna: Leaching studies, Indentation techniques (L. Esposito)

Centro Legnaro/Padova: RBS, Ion implantation, H-analysis on leached waste matrices ((G. Della Mea, V. Rigato)

University of Padova: Analysis of glass surfaces (P. Mazzoldi)

University of Trento: Indentation techniques (R. Dal Maschio)

Japan

Central Research Institute of Electricity Producing Industries (CRIEPI), Tokyo: Preparation and characterisation of minor actinide alloys

Central Research Institute of Electricity Producing Industries (CRIEPI), Tokyo: Dissolution studies on high burn-up fuel

JAERI, Tokai Mura: Basic studies on nitride fuels (T. Ohmichi)

JAERI, Tokai Mura: Inductively-coupled plasma mass spectrometry

Netherlands

AKZO n.v., Arnhem: Production of alpha-emitting nuclides (M. Geerlings)

University of Amsterdam: Low temperature magnetization and resistivity (J. Franse)

Poland

Nuclear Institute, Warszawa: Channeling techniques, Radiation damage studies (A.Turos)

Portugal

LNETI, Sacavem: Physical chemistry of actinides (A.Piros de Matos)

Russia

Academy of Sciences, IVTAN, Moscow: Studies on high-melting materials (A.E.Sheindlin)

Radium Khlopin Institute, St.Petersburg: Installation and field testing of a robotized system for safeguards analysis.

Sweden

University of Uppsala: Solid state theory of actinides (B. Johansson)

Infrasonik AB, Skäppsholmen, Stockholm: manufacture of infraphones

Switzerland

ETH, Zürich: Single crystal growth, magnetic, optical and transport properties, preparation of U and Th compounds (O. Vogt, J. Schoenes, P. Wachter, F. Hulliger, K. Mattenberger)

Paul-Scherrer-Institut, Würenlingen: TRANSURANUS fuel pin code application

Paul-Scherrer-Institut, Würenlingen: Post-irradiation structural investigations by electron microscopy

Spain

CIEMAT, Madrid: TRANSURANUS fuel pin code development

Instituto di Acustica, Madrid: Acoustic aerosol scavenging (J.A.Gallego-Juarez)

United Kingdom

Birkbeck College: neutron and magnetization studies (K. McEwen)

Royal Institute, London: Calculation of fission products in UO₂

Rutherford-Appleton Laboratory: Neutron spectroscopy (R. Osborn, M. Hagen)

University of Birmingham: Preparation of high purity single crystals (D. Fort)

University of Keele: X-ray and neutron scattering (W.G. Stirling, D. Jones, C. Tang)

University of Warwick: X-ray absorption spectroscopy (M.J. Cooper)

University of Warwick: Radiative properties at high temperatures (G. Hyland)

University of Salford: Solid gas precipitates (S. Donnelly)

USA

Argonne National Laboratory: Neutron scattering (C.K. Loong; L. Morss, S. Kern, G. Goodman)

Brookhaven National Laboratory: High-resolution and magnetic X-ray scattering (D. Gibbs, J. Axe, G. Grubel)

Lawrence Livermore National Laboratory: Surface reactions (C. Colmenares)

Los Alamos National Laboratory: Materials preparation and photoemission (B. Cort, J. Ward, L. Cox)

Oak Ridge National Laboratory: Material preparation, high pressure X-ray and optical studies (R.G. Haire, J.R. Peterson)

University of W. Virginia, Morgantown, W.-Virginia: Actinide theory (G.J. Hu, B.R. Cooper)

Purdue University, West Lafayette, Indiana: Magnetisation and sample preparation (G. Honig and J. Spalek)

Annex III

Human Resources

1. Institute's Staff

The evolution of the staff situation in 1992 is given for three reference dates on the table below:

Date	A2-A4	A5-A8	B	C	D	total
01.01.	20	23	83	68	1	195
01.10.	20	25	83	66	1	195
31.12.	22	23	81	66	1	193

2. Visiting Scientists and Scientific Fellows

10 graduate sectorial grantees from the following countries spent in 1992 prolonged periods of time at the Institute:

D (1)	I (1)
ES (2)	P (1)
F (3)	UK (1)
GR (1)	

3. Secondment from other laboratories

2 experts were delegated from other European research establishments to carry out specific tasks at the ITU in 1992, i.e. from CEA Cadarache (F) and CEA Saclay (F).

Annex IV

Organisational Chart

Institute Director	Jacques VAN GEEL
Adviser, acting as Institute Deputy Director	Jean FUGER
Adviser (Programmes)	Hans Eberhard SCHMIDT
Personnel and Administration	Paul BLAES
S/T Services:	
- Technical Physics	Michel COQUERELLE
- Applied Physics	Hansjoachim MATZKE
- Nuclear Technology	Karl RICHTER
- Nuclear Chemistry	Lothar KOCH
- Actinide Research	Ulrich BENEDICT
S/T-Support:	
- Radiation Protection	Klaas BUIJS
- Technical Services	Gérard SAMSEL

Annex V

Glossary of Acronyms and Abbreviations

ABB: Asea Brown Boverly
ADU: Ammonium DiUranate
AISI: American Iron and Steel Institute
ALARA: As Low As Reasonably Achievable
APS: Aerodynamic Particle Sizer
bct: body-centred tetragonal
BN: BelgoNucléaire
BNL: Brookhaven National Laboratory
BNFL: British Nuclear Fuels plc
BOL: Beginning Of Life (of a fuel pin)
BR2: Belgian Reactor 2 (Mol)
CABRI: CEA test reactor in Cadarache (F)
CANDU: CANadian Deuterium Uranium reactor
CASCADE: Cray Automatic System for the CALculation of Defect Energies
ccp: cubic close packed
CEA: Commissariat à l'Energie Atomique (F)
CEC: Commission of the European Communities
CEF: Crystalline Electric Field
CEN: Centre d'Etudes Nucléaires
CENG: Centre d'Etudes Nucléaires, Grenoble
CHEMIF: code to calculate the chemical behaviour of high burn-up fuel
COCAIN: code to calculate the COrrOsion by steam Cloud on An Irradiated Nuclear fuel element
COGEMA: COmpagnie GÉnÉrale des MATières nucléaires
CRIEPI: Central Research Institute of the Electric Power Industry (Japan)
CTI: Comité Technique Interministériel
DCS: Division Contrôle de Sécurité
DG I: Directorate General "External Relations" of the Commission of the European Communities, Brussels
DG XII: Directorate General "Science, Research, and Development" of the Commission of the European Communities, Brussels
DG XIII: Directorate General "Telecommunication, Information Industry, and Innovation" of the Commission of the European Communities, Brussels and Luxembourg
DG XVII: Directorate General "Energy" of the Commission of the European Communities, Brussels and Luxembourg
dhcp: double hexagonal close packed
DIN: Deutsches Institut für Normung
DSC: Differential Scanning Calorimetry
DTA: Differential Thermal Analysis
DWK: Deutsche Gesellschaft für Wiederaufarbeitung von Kernbrennstoffen (Hannover, D)
EAC: European Accident Code
EAP: Electro-Acoustic Precipitator
ECN: Energie Centrum Nederland (Petten, NL)
ECSAM: European Commission's Safeguards Analytical Measurements
EDAX: Energy-Dispersive Analysis with X-rays
EDF: Electricité de France
EDX: Energy-Dispersive X-ray spectroscopy

EFPH: Effective Full Power Hours
EMPA: Electron MicroProbe Analysis (also EPMA)
EPMA: Electron Probe Micro-Analysis
ERDA: Elastic Recoil Detection Analysis
ESP: ElectroStatic Precipitator
ETH: Eidgenössische Technische Hochschule (Zürich, CH)
EURATOM: EUROpean ATOMIC energy community
FBFC: Compagnie Franco-Belge de Fabrication de Combustible
FIMA: Fissions per Initial Metal Atom
FR: Fast Reactor
FRG: Federal Republic of Germany
FUTURE: code for fuel transient calculations
FWHM: Full Width at Half Minimum
GDMS: Glow Discharge Mass Spectrometer
GKN: GemeinschaftsKernkraftwerk Neckar GmbH (D)
HAW: Highly Active Waste
HAZOP: HAZards of OPERATION study
HBC: High Burn-up Chemistry
HEPA filter: High Efficiency Particulate Air filter
HFR: High Flux Reactor (Petten, NL)
HPGG: High Purity low energy Germanium Gamma detector
HPXRD: High-Pressure X-Ray Diffraction
HWR: Heavy Water Reactor
IAEA: International Atomic Energy Agency (Vienna, A)
ICEN: Instituto de Ciencia e Energia Nucleare (Savacem, P)
ICNS: International Conference on Neutron Scattering
ICRP: International Commission on Radiological Protection
ICP-MS: Inductively Coupled Plasma Mass Spectrometry
IDA: Isotope Dilution Analysis
IDMS: Isotope Dilution Mass Spectrometry
IFR: Integral Fast Reactor
IHCh: Institut für Heiße Chemie
IMA: Initial heavy Metal Atoms
IRMM: Institute for Reference Materials and Measurements
ITU: Institute for Transuranium Elements
JAERI: Japan Atomic Energy Research Institute
JRC: Joint Research Centre
KfK: Kernforschungszentrum Karlsruhe (Karlsruhe, D)
KKGs: KernKraftwerk Gösgen (CH)
KNK: Kompakte Natrium-gekühlte Kernenergieanlage Karlsruhe (D)
KORIGEN: KfK development of the ORIGEN Code
KWU: KraftWerk-Union (D)
LAKU: model to calculate fission gas release (KfK)
LANL: Los Alamos National Laboratory
LLB: Laboratoire Léon Brillouin (Saclay, F)
LIS: Laboratory In Situ
LMFBR: Liquid Metal (cooled) Fast Breeder Reactor
LNETI: Laboratorio Nacional de Engenharia e Tecnologia Industrial (Savacem, P)
LOF: Loss Of Flow accident
LSS: Laboratoire Sur Site
LWR: Light Water Reactor
MA: Minor Actinides (Np, Am, Cm)
MAC: Mass Absorption Coefficient
MC: Mixed Carbide fuel
MCA: MultiChannel Analyzer
MCN: Mixed Carbide/Nitride fuel
MELOX: MELange OXides (MOX fuel fabrication plant, Marcoule)
MGA: Program to determine Pu isotopics (gamma spectrometer)

MITRA: code to calculate the release of radio-nuclides
MOX: Mixed OXide fuel
NTS: Material Test Stab
NDA: Non-Destructive Analysis
Nd-YAG: Neodymium-Yttrium Aluminium Garnet laser
NILOC: Nitride Irradiation with LOw Carbon content
NIMPHE: NItrures Mixtes dans PHenix à joint HELium
NRC: Nuclear Regulatory Commission (USA)
ORIGEN: Oak Ridge Isotope GENeration and depletion code
ORNL: Oak Ridge National Laboratory
PHEBUS: French test reactor (Cadarache, F)
PHEBUS-FP: Programme to study fission product release and their distribution
in the primary circuit
PHENIX: French prototype fast reactor
PIE: Post Irradiation Examination
PNC: Power reactor and Nuclear fuel development Corporation
POMPEI: POM PEtten Irradiation experiment to study the structure
of nitride fuel
PUREX: Plutonium and Uranium Recovery by EXtraction
PWR: Pressurized Water Reactor
RADAR: RAting Depression Analysis Routine
RBS: Rutherford Backscattering Spectroscopy
REDOX: REDuction-OXidation
SAP: Sintered Aluminium Powder
SEM: Scanning Electron Microscopy
SGN: Société Générale des matières Nouvelles
SIMFUEL: SIMulated high burn-up UO₂ FUEL (with major non-volatile fission products)
SLDA: Local Spin Density Approximation
SNAM: Societa NAzionale Metanodotti (I)
SPL: Sound Pressure Level
SQUID: Superconducting QUantum Interference Device:
SUPERFACT: Minor Actinide Irradiation in Phenix
TBP: TriButyl Phosphate
TEM: Transmission Electron Microscopy
THF: Tetra Hydro Furan
THORP: THERmal Oxide Reprocessing Plant (Sellafield, UK)
TOP: Transient OverPower
TRABI: project to study TRANsport of BIg particles
TRANSURANUS: Fuel behaviour code (ITU Karlsruhe)
TRIO: Irradiation capsule, HFR Petten
TRPO: TRialkyl Phosphine Oxide
TRU: TRansUranium elements
TSI: Thermal Systems Incorporated
TSX: Time Sharing operating system
TRUEX: TRansUranium EXtraction
TUAR: Annual Report, Institute for Transuranium Elements (ITU, Karlsruhe)
TUBRNP: Trans-Uranus BuRN- uP model
TUCOP: Transient UnderCooled OverPower
UKAEA: United Kingdom Atomic Energy Agency
ULOF: Unprotected Loss Of Flow
UPS: Ultraviolet Photoelectron Spectroscopy
URFRIC: TransURanus FRICtion model
UV: Ultra Violet
VGB: Vereinigung der Grosskraftwerk-Betreiber (D)
XPS: X-ray Photoelectron Spectroscopy

Annex VI

List of Contributors

1. Specific Programmes

Basic Safety Research on Nuclear Fuels

Hj.Matzke, J.P.Hiernaut, K.Lassmann, S. Nicoll, I.Ray, C.Ronchi, H.A.Tasman, H.Thiele, A.Turos

Safety Aspects of Fuel Operation and Handling

K.Richter, K.Buijs, B.Chavane, J.F.Gueugnon, Hj.Matzke,

Actinide Determination and Recycling

L.Koch, H.Bokelund, J.P.Glatz, G.Nicolaou

Characterisation of Waste Forms and of High Burn-Up Fuel

M. Coquerelle, M.Berton, D.Bottomley, J.P.Glatz, Hj. Matzke, C.Messainguiral, G.Nicolaou, C.O'Carroll, S.Sari, J.L.Spino, E.Toscano

Actinide Research

U.Benedict, M.Brooks, G.Lander, J.Naegele, J.Rebizant, J.C.Spirlet, ; P.Link, P.Raison, J.A. de Carvalho Paixao, M.T.Almeida, D.Meyer, N. Athanasiou, Y.Kergadallan

2. Exploratory Research (Acoustic Aerosol Scavenging)

K.Richter, J.Magill, P.Capéran, J.Somers

3. Support to Community Policies

Support to the Directorate General for External Relations

L.Koch, B.Brandalise

Support to the Directorate General for Innovation and Technology Transfer

K.Richter, J.Magill, P.Capéran, J.Somers

Support to the EURATOM Safeguards Directorate

*L.Koch, M.Betti, B.Brandalise, O.Cromboom, D.I.Kühn, M.Ougier, R.Wellum,
D.Wojnowski; B.Deiss*

4. Work for Third Parties

*C. Apostolidis, M. Coquerelle, J .P. Glatz, J.-F. Gueugnon, L. Koch, G. Nicolaou,
K. Richter, J.L. Spino*

Annex VII

Previous Progress Reports of the Institute for Transuranium Elements

TUSR	Period	COM-Nr	EUR-Nr
1	Jan - Jun 1966	1580	
2	Jul - Dec 1966	1522	
3	Jan - Jun 1967	1745	
4	Jul - Dec 1967	2007	
5	Jan - Jun 1968	2172	
6	Jul - Dec 1968	2300	
7	Jan - Jun 1969	2434	
8	Jul - Dec 1969	2576	
9	Jan - Jun 1970	2664	
10	Jul - Dec 1970	2750	
11	Jan - Jun 1971	2833	
12	Jul - Dec 1971	2874	
13	Jan - Jun 1972	2939	
14	Jul - Dec 1972	3014	
15	Jan - Jun 1973	3050	
16	Jul - Dec 1973	3115	
17	Jan - Jun 1974	3161	
18	Jul - Dec 1974	3204	
19	Jan - Jun 1975	3241	
20	Jul - Dec 1975	3289	
21	Jan - Jun 1976	3358	
22	Jul - Dec 1976	3384	
23	Jan - Jun 1977	3438	6475 E
24	Jul - Dec 1977	3484	7209 E
25	Jan - Jun 1978	3526	7459 E
26	Jul - Dec 1978	3582	7227 E
27	Jan - Jun 1979	3657	7483 E
28	Jul - Dec 1979	3714	7509 E
29	Jan - Jun 1980	3822	7857 E
30	Jul - Dec 1980	3846	8230 E
31	Jan - Jun 1981	3898	8447 E
32	Jul - Dec 1981	3927	8777 E
33	Jan - Jun 1982	3990	9581 E
34	Jul - Dec 1982	4048	10251 E
35	Jan - Jun 1983	4094	10266 E
36	Jul - Dec 1983	4117	10454 E
37	Jan - Jun 1984	4150	10470 E
38	Jul - Dec 1984	4165	11013 E
39	Jan - Jun 1985	4201	11835 E
40	Jul - Dec 1985	4263	11836 E

TUAR

86	Jan - Dec 1986	4302	12233 E
87	Jan - Dec 1987	-----	11783 E
88	Jan - Dec 1988	-----	12385 E
89	Jan - Dec 1989		12849 E
90	Jan - Dec 1990		13815 E
91	Jan - Dec 1991		14493 E
92	Jan.-Dec.1992		15154 E

Previous Programme Progress Reports were confidential for a period of two years. Since 1977 they are made freely accessible after that period as EUR-Reports. They can be ordered from the Office for Official Publications of the European Communities, 2 rue Mercier, L-2985 Luxemburg, Tel. 49 92 81, Telex PUBOF LU 1324 b

This report was compiled and edited by H.E. Schmidt, J. Richter, and L. Ruczka.

Inquiries for more details should be addressed to the Programme Office, Institute for Transuranium Elements, P.O. Box 2340, D-76125 Karlsruhe, Phone 07247-84386, FAX 07247-2712

For further information concerning JRC programmes please contact the Directorate General Science, Research and Development of the Commission of the European Communities, 200 rue de la Loi, B-1049 Brussels, Belgium.

2 | 4 0066 426709 410066 426709 410066 426709

